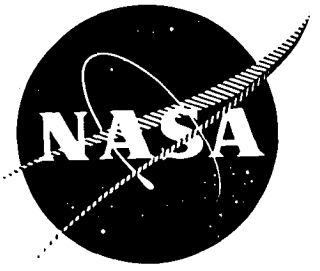

PHYSICAL PHENOMENA IN MERCURY ION THRUSTERS

PREPARED FOR

LEWIS RESEARCH CENTER

NATIONAL AERONAUTICS AND SPACE ADMINISTRATION

GRANT NGR-06-002-112

Annual Report

December 1979

Paul J. Wilbur
Department of Mechanical Engineering
Colorado State University
Fort Collins, Colorado

1. Report No.	2. Government Accession No.	3. Recipient's Catalog No.
NASA CR 159784		

4. Title and Subtitle	5. Report Date
Physical Phenomena in Mercury Ion Thrusters	December 1979
	6. Performing Organization Code

7. Author(s)	8. Performing Organization Report No.
Paul J. Wilbur	
	10. Work Unit No.

9. Performing Organization Name and Address	11. Contract or Grant No.
Department of Mechanical Engineering Colorado State University Fort Collins, Colorado 80523	NGR-06-002-112
	13. Type of Report and Period Covered Contractor Report Dec. 1, 1978 - Dec. 1, 1979
12. Sponsoring Agency Name and Address	14. Sponsoring Agency Code
National Aeronautics and Space Administration Washington, D.C. 20546	

15. Supplementary Notes

Grant Monitor, William Kerslake
Spacecraft Technology Div.
NASA Lewis Research Center
Cleveland, Ohio 44135

16. Abstract

Experimental tests results demonstrating that reductions in screen grid thickness enhance the performance of ion thruster grids are presented. Shaping of the screen hole cross section is shown on the other hand not to affect performance substantially. The effect of the magnetic field in the vicinity of the hollow cathode on cathode performance is studied and test results are presented that show reductions in keeper voltages of a few volts can be realized by judicious application of fields on the order of 100 gauss. The plasma downstream of a SERT II thruster operating without high voltage is studied. A model describing electron escape from the thruster under these conditions is discussed. A model defining the performance of the baffle aperture of an ion thruster is refined and experimental verification of the model is undertaken.

17. Key Words (Suggested by Author(s))	18. Distribution Statement
Electrostatic Thruster Hollow Cathode	Unclassified - Unlimited

19. Security Classif. (of this report)	20. Security Classif. (of this page)	21. No. of Pages	22. Price*
Unclassified	Unclassified	146	

* For sale by the National Technical Information Service, Springfield, Virginia 22161

NASA-C-168 (Rev. 10-75)

N80-17137

TABLE OF CONTENTS

LIST OF FIGURES

LIST OF TABLES

ION OPTICS STUDIES

Graeme Aston

Much of the ion optics work accomplished during this year has been reported recently in Reference 1, which is attached in Appendix B. This work describes the motion of the screen grid plasma sheath as a result of grid system geometry and discharge chamber plasma condition changes. The following topics were however not discussed in this paper. The apparatus and procedure used to collect the data as well as the propellant (argon) were the same as those described in Reference 1.

Screen Grid Thickness Effects

It has been anticipated that, thinning down the screen grid has beneficial effects on the ion beam current and discharge losses. Figure 1 provides physical insight into these effects by showing how the screen hole plasma sheath moves as the screen grid thickness is varied while normalized perveance per hole (NP/H) is held constant. The open, cross hatched and doubly cross hatched rectangles in the upper right hand corner of this figure represent a section of the screen grid webbing. In the figure d_s, which represents the screen hole diameter, was 1.27 cm for all tests and this distance can therefore be used to scale on the figure. Further, t_s represents the screen grid thickness, ℓ_g the screen-to-accel grid separation distance and V_D the discharge voltage. The set of equi-potential contours appearing furthest upstream in Figure 1 are 5 volts below the main discharge plasma potential, the next set is 15 volts below plasma potential and the downstream set is 25 volts below plasma potential. At the -25 volt contour probe measurements suggest that the electron

density is approaching zero. Over the central portion of the screen hole, the Figure 1 results suggest that the plasma feels the presence of the accelerator grid potential very strongly; screen grid thickness and hence screen potential distribution changes have little effect in this region. Conversely, near the screen grid webbing the competing influences of the screen and accelerator grid potentials are both felt and both influence the sheath shape and position. With a thick screen grid (t_s/d_s = 0.18 in Fig. 1) the screen potential is defined well within the plasma and the plasma likewise forms a rather long, well defined sheath adjacent to this potential surface as shown by the solid sheath profile line. As the screen grid thickness is reduced the plasma sheath attempts to move after the screen grid since the screen grid is still a dominate potential surface, though less well defined. However, with sufficient screen grid thickness reduction the shielding effect the screen grid interposes between the discharge plasma and the accelerator grid webbing is reduced to a negligible level. Under these conditions (estimated from other tests not shown to be $t_s/d_s \sim 0.05$), the sheath boundary begins to communicate most strongly with the accelerator grid webbing. Further screen grid thickness reductions have little effect on forcing the sheath boundary to follow after the screen grid. These results would therefore suggest that this value of screen grid thickness ratio would be optimium from a grid performance point of view.

Figure 1 shows that the competing influence of the screen and accelerator potentials gives rise to a sheath potential distribution at the screen grid webbing which tends to direct plasma ions away from the webbing and through the screen hole with decreasing screen grid thickness. This effect is illustrated graphically by electric field vectors in Fig. 1.

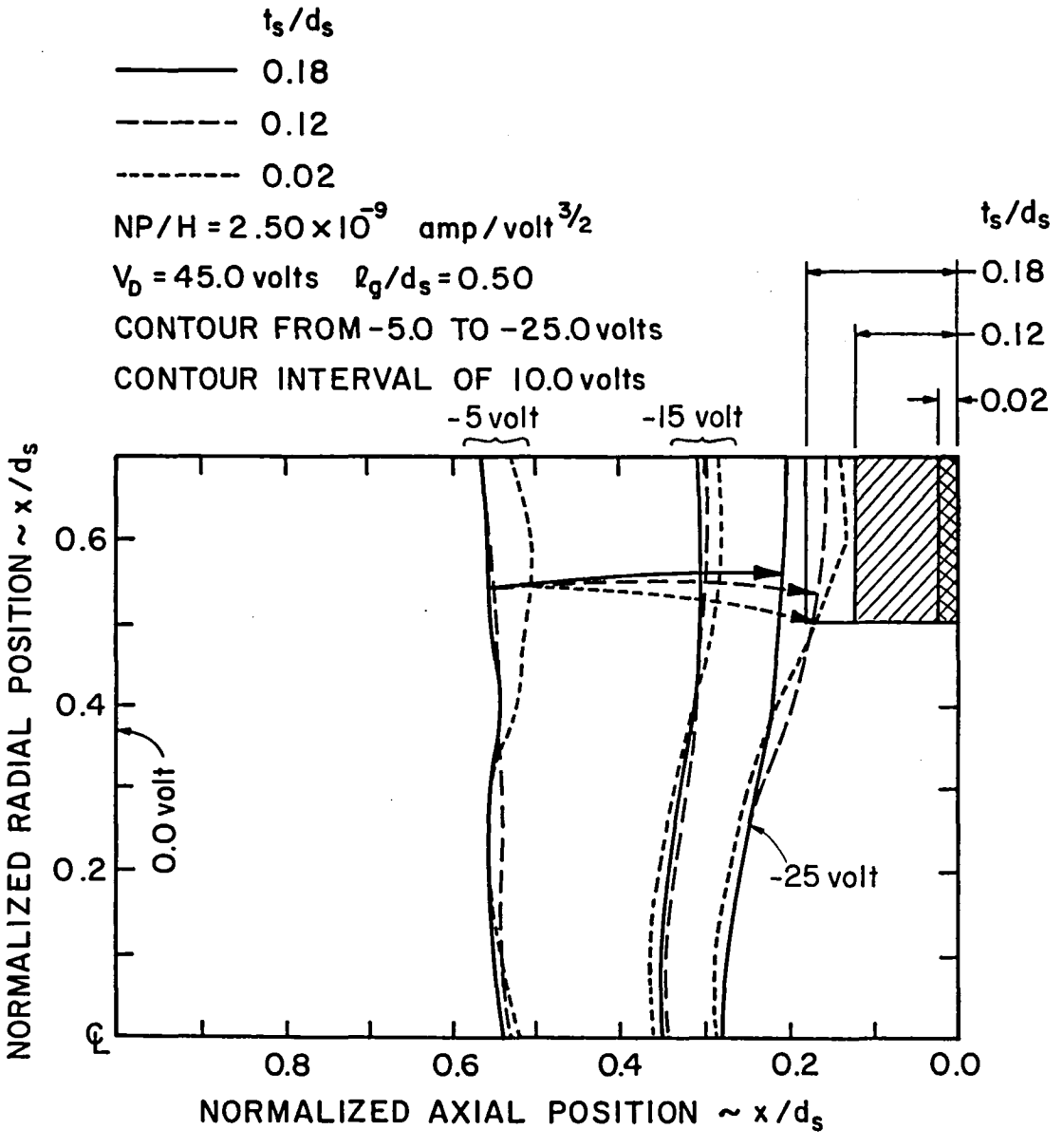

Figure 1. Effect of Screen Grid Thickness on Sheath

The arguments presented above indicate that the position of the central portion of the screen hole plasma sheath would remain essentially unaltered with changes in screen grid thickness. This behavior is verified in Fig. 2 where screen hole sheath profiles are compared for a very thick screen (t_s/d_s = 0.49) and a conventional, thinner screen grid (t_s/d_s = 0.18). Figure 2 shows that the very thick screen grid has pushed those potential lines adjacent to the grid webbing back into the discharge chamber while having very little effect on the central portion of the sheath potential contours. The result is that the screen hole plasma sheath is now inside the screen hole (the sheath probe's shape prevented the probe from entering very far into the screen hole and this is why only a portion of the -15.0 volt contour, for the very thick screen grid, is shown in Fig. 2; however, the trend is clear). Examination of the sheath potential contours adjacent to the very thick screen grid webbing indicates that even ions from within the screen hole might eventually be directed into the webbing and the inside surface of the screen hole. Indeed, the normalized perveance per hole value indicated in Fig. 2, while only about 70% of the maximum value to be expected for the conventional thin screen grid, corresponded to the maximum obtainable normalized perveance per hole for the very thick screen grid.

Figure 3 shows a plot of discharge loss, normalized to the value for t_s/d_s = 0.49, against screen grid thickness. This curve illustrates dramatically the adverse screen web focusing effects introduced with increasing screen grid thickness.

The results shown in Figs. 1, 2, and 3 are strong evidence that ion impingement on the screen grid webbing decreases significantly with screen grid thickness reductions. This has obvious implications for decreased

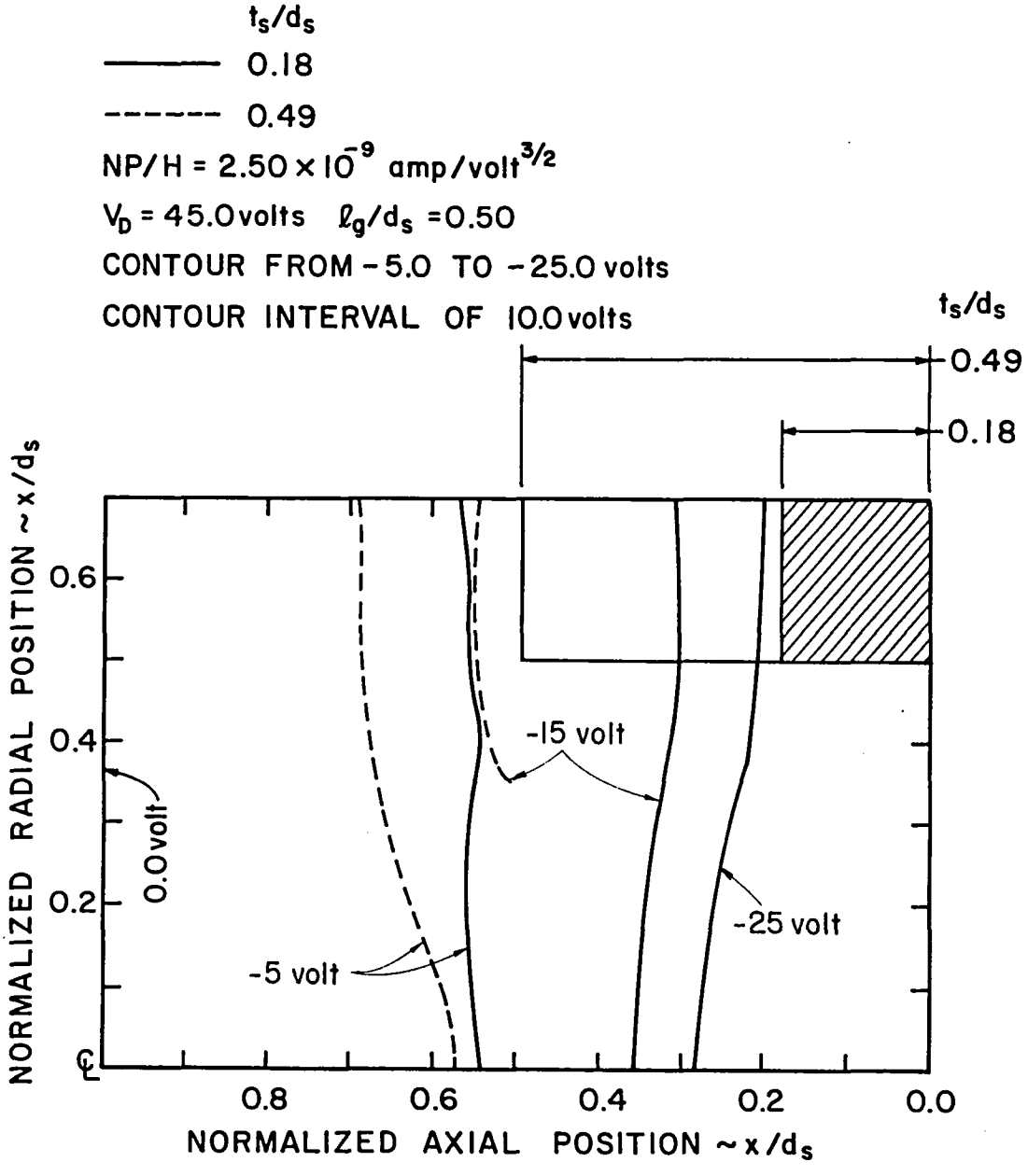

Figure 2. Effect of Screen Grid Thickness on Sheath

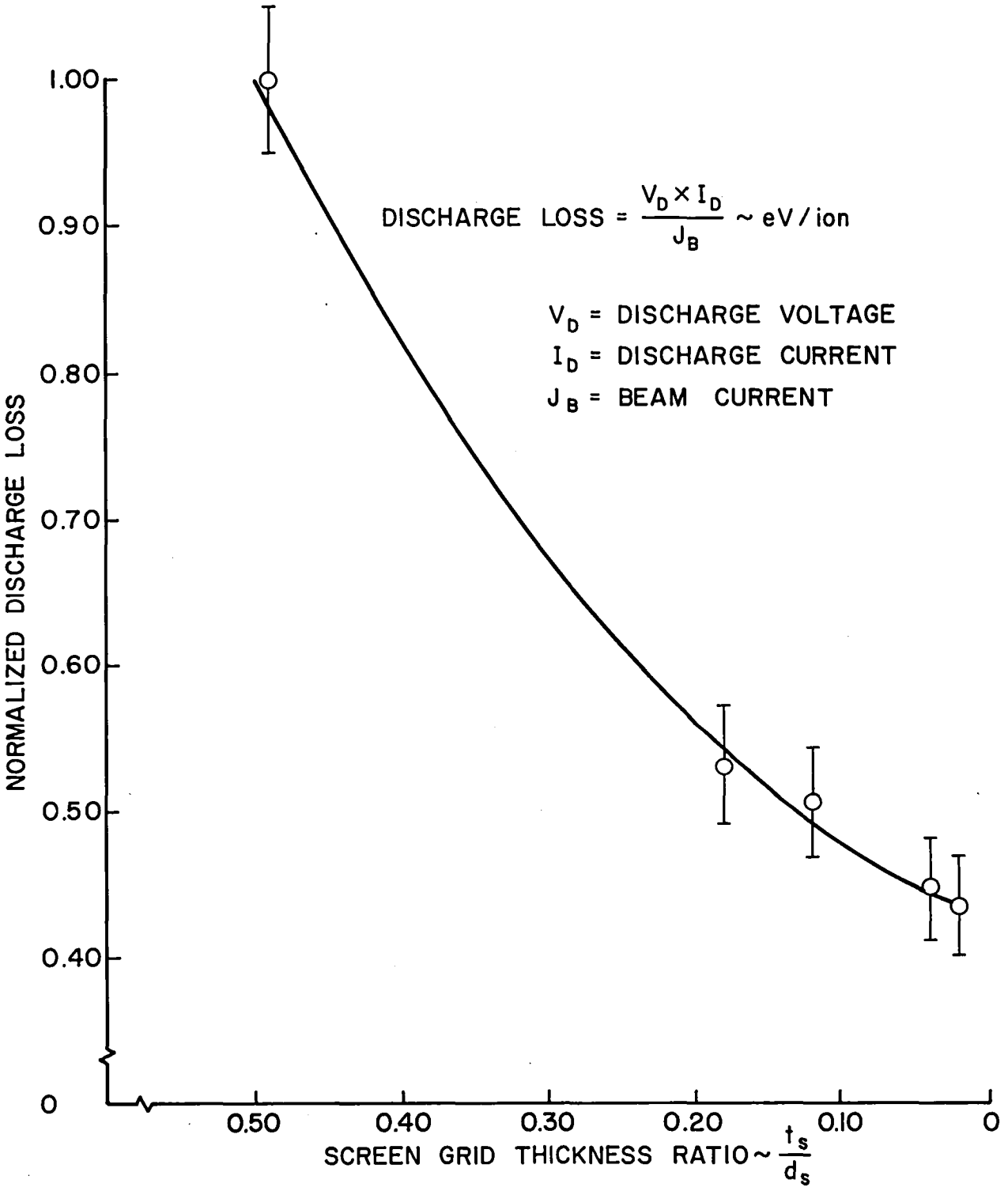

Figure 3. Effect of Screen Grid Thickness on Discharge Losses

screen grid erosion as the screen grid thickness is reduced. Indeed, it appears that an effort to thicken the screen grid to give longer erosion life may accelerate the erosion effect. Of course there are definite, but perhaps not insurmountable problems in fabricating screen grids of the thicknesses suggested in Figs. 1 and 3. Also, without some sort of comparative erosion life test being undertaken the conclusions presented here are somewhat conjectural.

Screen Hole Shaping

Numerous workers[2-5] have reported conflicting results as to the effect shaping the screen grid hole has on beam current and ion beam divergence. In order to clarify the beneficial or detrimental effects of screen grid hole shaping the screen hole plasma sheath of some shaped screen holes were examined experimentally. It was found that chamfering the upstream hole face (with a 41° chamfer) had only a very slight effect on the screen hole plasma sheath potential contours. Similarly, no change from the unchamfered screen grid geometry was observed in the discharge loss level and maximum obtainable beam current. This null result supports earlier evidence by Kerslake and Pawlik[2] that screen grid hole chamfering has little merit.

Some workers[4,5] have reported computer solutions and experimental results which indicate that counter boring the downstream screen hole face leads to significant screen hole sheath shape changes with lower divergence angles and increased beam current. Such a modification was made to the tapered screen grid discussed previously. Figure 4 compares screen hole sheath profiles for this chamfered and counter bored screen grid to those of a conventional cylindrical screen hole geometry. Only slight differences in the sheath profiles are observed. At the sheath adjacent to the screen

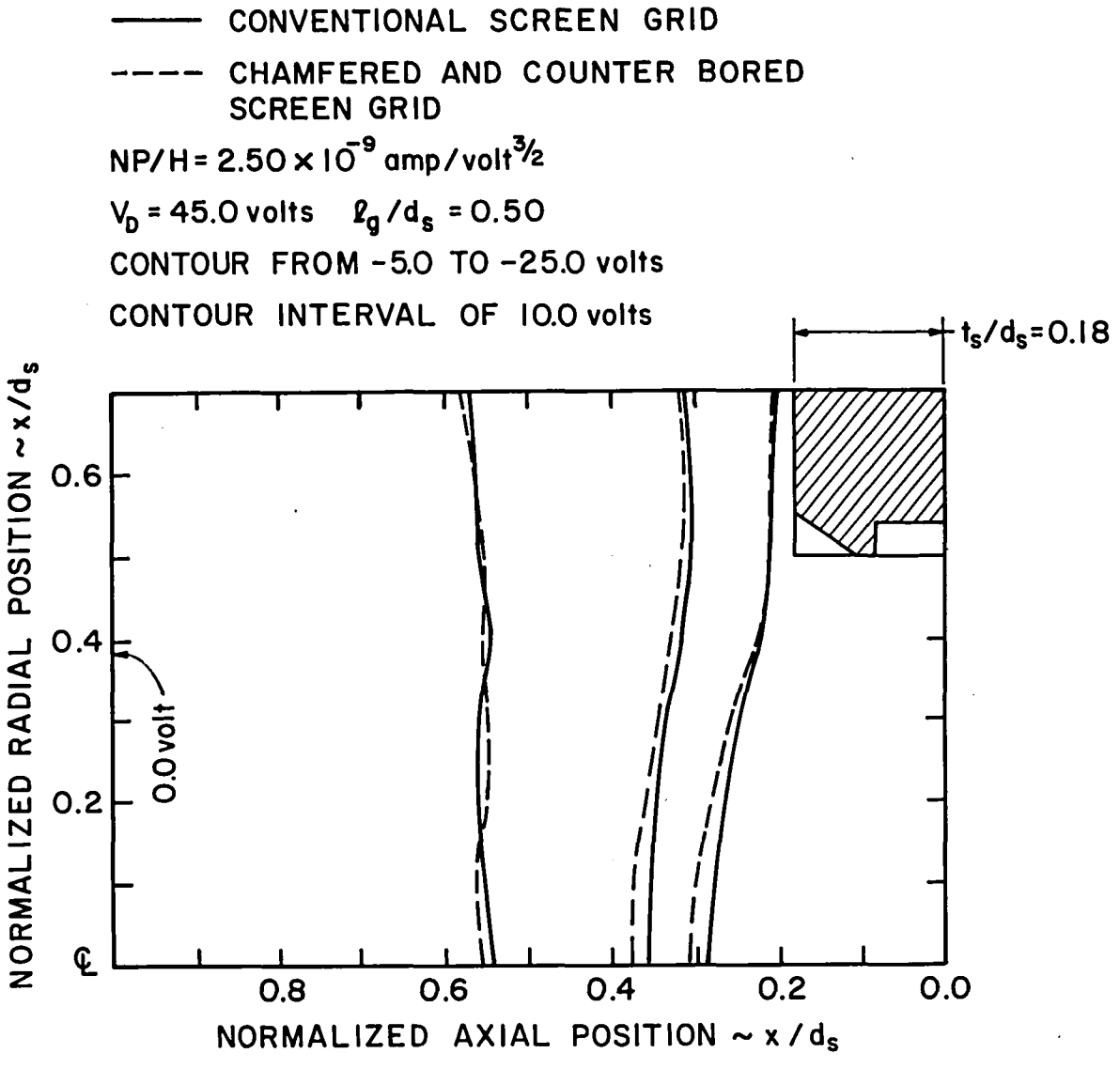

Figure 4. Effect of Screen Grid Shape on Sheath

grid webbing the potential contours are amost coincident. Towards the screen hole center more differences are apparent and the sheath boundary for the chamfered and counter bored screen hole is displaced upstream slightly relative to the boundary of the cylindrical screen hole. This trend agrees qualitatively with the previously mentioned computer solution prediction although it is much less pronounced than these solutions predict. One would expect that by counter boring the screen hole in the manner shown in Fig. 4 the average screen hole diameter has been enlarged slightly. Such a hole enlargement must slightly decrease the positive potential that the screen grid webbing can impress at the screen hole center. Consequently, what shielding effect the screen grid could interpose between the discharge plasma and negative accelerator grid will have been reduced. As a result, the plasma electrons would see a stronger retarding electric field as they approach the central portion of the screen hole. This stronger retarding field prevents the plasma electrons from penetrating through the ion acceleration region to a depth possible with the cylindrical hole geometry. The net effect is that the central portion of the sheath boundary is moved upstream slightly, as shown in Fig. 4.

Perhaps the discrepancy between computer solutions and experimental results is because all attempts to model the screen hole sheath theorectically have the sheath positioned within the screen hole for the beam current or normalized perveance per hole of Fig. 4. With the sheath inside the screen hole it is apparent that screen hole shape changes might have a significant effect on the ensuing ion trajectory calculations. However, as has been mentioned previously, the screen hole plasma sheath is within the screen hole for large screen grid thickness values only. Normally the screen grid thickness is kept to a minimum because of the improved ion source plasma efficiency.

Chamfering and counter boring the screen grid gave a slight decrease in discharge loss (<3%) and a slight decrease in the maximum obtainable beam current (<3%), compared to similar parameters observed with the cylindrical hole geometry. No beam divergence data were obtained as a function of screen hole geometry. Also, direct accelerator grid impingement currents could not be measured accurately because of the relatively high facility background pressure ($\sim 2 \times 10^{-4}$ Torr). However, the slight screen hole sheath shape and position changes apparent in Fig. 4 suggest beam divergence and direct ion impingement variations would be small as the screen hole shape was altered.

It is noteworthy that all of the experiments described herein were conducted at a constant accel-to-screen hole diameter ratio of 0.64. The effect of variation in this parameter has not been investigated but this work suggests that the effects of such variations are probably significant.

Space Charge Neutralization

Langmuir[6] has discussed the possibility of increasing the space charge limited electron current between two electrodes by injecting ions into the electron space charge and thereby partially neutralizing its detrimental effect on electron emission. It was thought that perhaps the opposite tack might be pursued whereby the ion space charge in the screen hole plasma sheath could be partially neutralized by injecting low energy electrons into this sheath.

Figure 5 illustrates the manner in which electrons were injected into the screen hole plasma sheath. Briefly, a circular filament was placed between the discharge chamber plasma and the accelerator grid. Although

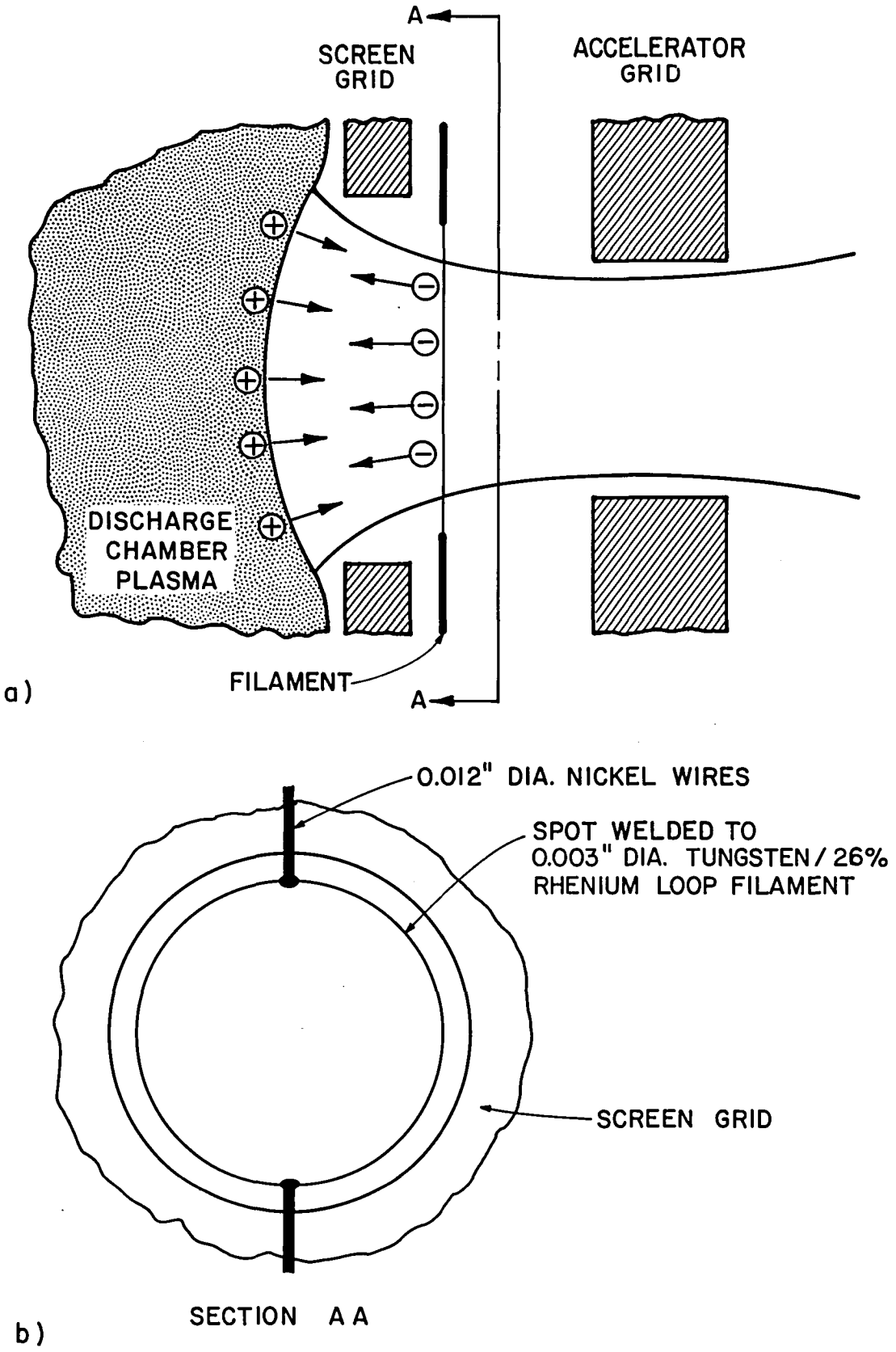

Figure 5. Electron Injection Test Configuration

Fig. 5(a) shows the filament slightly downstream of the screen grid, it was also positioned at varying distances inside the screen hole and inside the screen hole plasma sheath. The filament was biased relative to the anode supply (although the screen grid was also used as a reference) and its bias potential could be varied. Direct current was provided to the filament loop via the heavier nickel support wires; ensuring that only the filament loop immersed in the ion beamlet was heated to incandescence. Only the central hole of the large seven hole array was modified in this manner; the surrounding holes were masked off at the screen grid.

Unfortunately all efforts to increase the beam current by neutralizing the ion space charge using the electron injection method depicted in Fig. 5 failed. By correct filament biasing, substantial filament electron currents could be drawn through the screen hole sheath. However, it appeared that even with the filament immersed in the screen hole plasma sheath and using a bias barely sufficient to drive off electrons, the filament electrons were going too fast to establish a sufficiently large negative charge density to neutralize the ion space charge to any measurable extent. A simple analysis assuming the filament electrons were at thermal energies only suggested that their velocity would still exceed the local ion velocity by three orders of magnitude. This effect was realized before undertaking the experiment. In hindsight, the tremendous disparity in velocity between the filament electrons and ions is still the basic problem. No judicious choice of biasing potential or filament emission level seems capable of circumventing this problem with the geometry shown in Fig. 5. Other schemes of space charge neutralization are however still conceivable.

HOLLOW CATHODE STUDIES

Dan Siegfried

A paper[7] presented at a recent electric propulsion specialist conference and included in Appendix B of this report describes much of the work accomplished on the subject topic over the past year. This paper describes experimental work conducted on a quartz tube hollow cathode which demonstrated the effects of cathode emission current level, propellant flow rate, cathode orifice diameter and internal cathode pressure on cathode insert temperature profiles and the distribution of emission current in the cathode. The downstream end of the insert is identified as the dominant emission site. Internal cathode pressure is identified as a very important parameter which influences the cathode temperature and emission profiles. Data presented in this paper support the field-enhanced thermionic mechanism of electron emission. Additional research conducted during the past year but not included in Ref. 7 are discussed in the following paragraphs.

Effect of Magnetic Field on Hollow Cathode Operation

During the test program for the 8 cm thruster it was observed that the keeper voltage of the main cathode for this thruster was slightly higher than expected. The magnetic field configuration in the cathode/baffle region of this thruster was known to be substantially different than that of earlier thrusters and it was suggested that the interaction of the magnetic field with the cathode discharge could be the cause of this higher voltage. In order to investigate the effect of this magnetic field/cathode interaction, a mercury hollow cathode was operated in a

diode arrangement in the presence of a variety of magnetic field configurations and strengths. Langmuir probes were used to measure the plasma properties of the cathode discharge both upstream and downstream of the cathode orifice plate at each operating condition.

Apparatus and Procedure

The test configuration used to examine the effects of the magnetic field in the vicinity of the cathode on cathode performance is shown in Fig. 6. The cathode used in these tests was a standard 6.35 mm diameter tantalum body cathode with a thoriated tungsten orifice plate having a 0.76 mm diameter orifice. The insert used in the cathode was fabricated using rolled tantalum foil coated with chemical R-500.* The anode was a cylinder made of perforated stainless steel and having its axis congruent with the cathode axis. The enclosed keeper had an orifice diameter of 2.5 mm and was separated from the orifice plate by a 3 mm long quartz spacer. Two coils (19 mm ID x 30 mm OD), each with 15 turns of #18 wire and each with its axis congruent with the cathode axis, were used to produce the magnetic field. The coils were mounted as shown in Fig. 6 so that they could be moved along the cathode axis; and they were connected to separate power supplies so the fields they produce could be controlled independently. These coils were sized to produce magnetic fields in the range of 50-100 gauss when operated at currents of up to 10 A. Langmuir probes were mounted both upstream and downstream of the orifice plate.

---

* J. R. Baker Chemical Co., Phillipsburg, New Jersey.

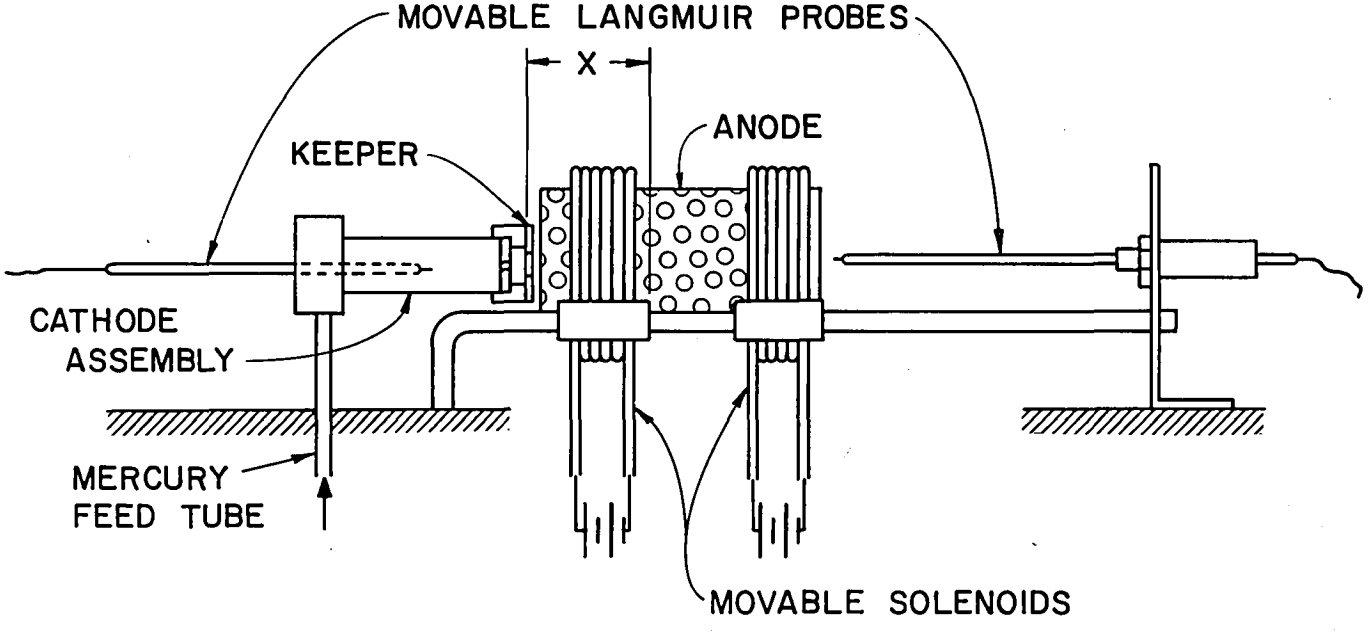

Figure 6. Test Configuration for Magnetic Field Study

In order to get a qualitative feel for the effects of the magnetic field, the cathode was operated over a wide range of conditions and magnetic field configurations. The magnetic field was found to have very significant effects on the operation of the cathode in this diode test configuration. Turning on the solenoids during cathode operation significantly increased the luminous intensity of the discharge downstream of the keeper and changed its pattern in a manner that depended on the magnetic field shape and location. Discharge current, mode of operation, flow rate, and anode shape and location were all found to be interrelated with the magnetic field strength and configuration in determining the character of the cathode operation. This large number of variables, particularly as it was complicated by the effect of anode configuration, made it difficult to characterize the effect of the magnetic field or to define a specific experiment. The present interest in decreasing the keeper voltage in the 8 cm (SIT) thruster suggested, however, that the effect of the magnetic field on keeper voltage would be of greatest interest. The procedure for this experiment was therefore limited to the case where the discharge current, keeper current, mass flow rate, and anode configuration were held constant while the magnetic field shape, strength, and location were changed. A discharge current of 3.0 A, a keeper current of 0.3 A, and a flow rate of $\sim$100 mA were chosen as the test conditions; and the test was conducted using the cylindrical anode shown in Fig. 6. The above operating conditions are typical for this size cathode when used in the 15 cm SERT II thruster where the field strength in the cathode region is on the order of a few tens of gauss. These operating conditions and the anode configuration that was used for these tests were not meant to model a specific thruster configuration but were chosen as a reference condition

typical of thruster conditions to allow a qualitative determination of the effect of magnetic fields on cathode operation. Although a number of solenoid coil spacings were investigated, the greatest effect was seen with the coils spaced as close as the test apparatus would allow. All of the data will therefore be presented for this minimum spacing between coils of ∿7.5 mm. The position of the coils will be identified using the dimension X (Fig. 6) which is, under this constraint, the distance from the keeper to the midpoint of the coils.

Results

The effect of magnetic field in the vicinity of the cathode on keeper voltage is examined in Fig. 7. Two magnetic field configurations are considered; 1) the cusped field case where currents through the coils were in opposite directions and 2) the axial field case where these currents were in the same direction. The currents through each coil were held constant at 10 A for all tests. Figure 7 shows that moving the cusp axially resulted in two conditions of minimum keeper voltage (when the cusp was at the keeper and when it was ∿20 mm downstream of the keeper). For the axial field case (same current polarity) the only minimum occurs near the 20 mm location.

In order to gain additional insight into the cause of these minima in the keeper voltage, plasma properties were measured at points 8 mm upstream and 15 mm downstream of the orifice plate under operating conditions corresponding to the minima in Fig. 7. The conditions for the case where there was no magnetic field present were observed to be as shown in Fig. 8. The conditions for the cathode operating with the null region of the cusped magnetic field (midpoint of the coils) located at the keeper are shown for

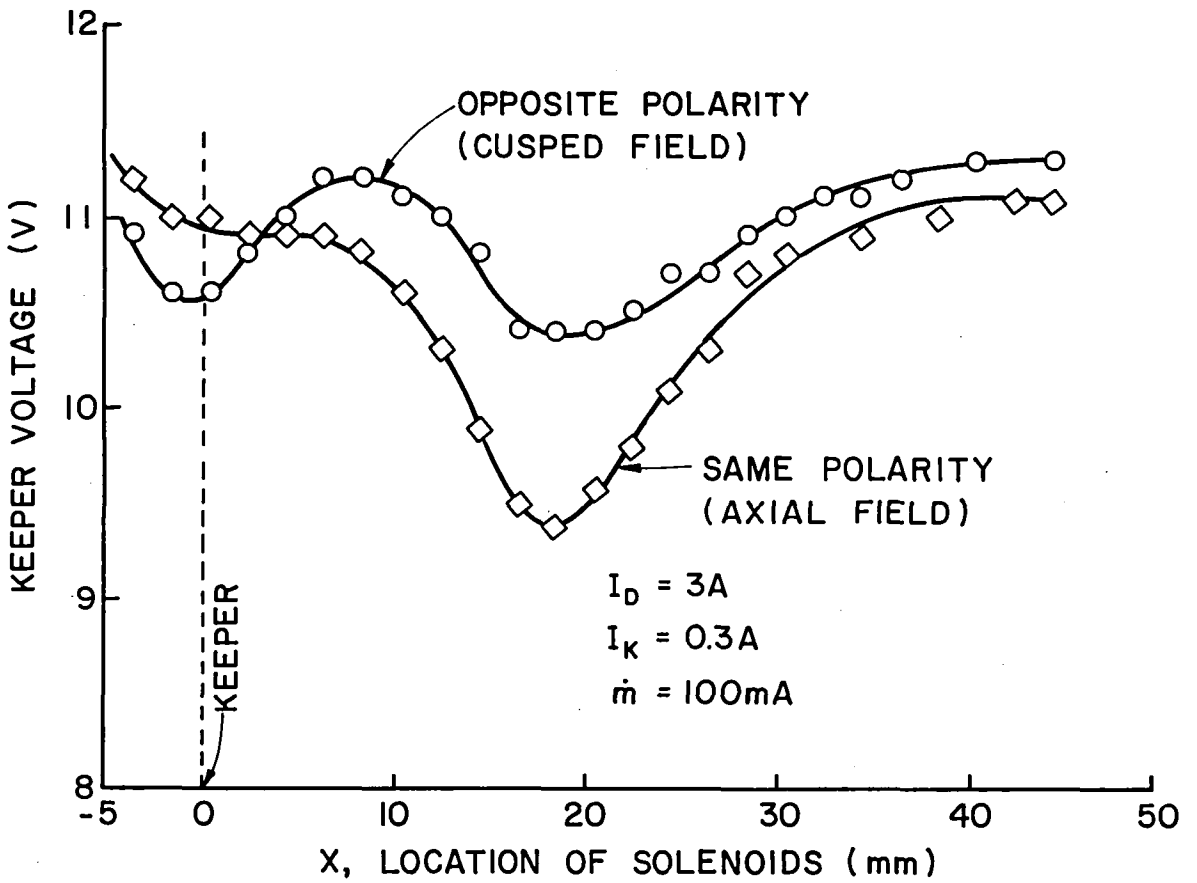

Figure 7. Keeper Voltage Variation with Solenoid Location

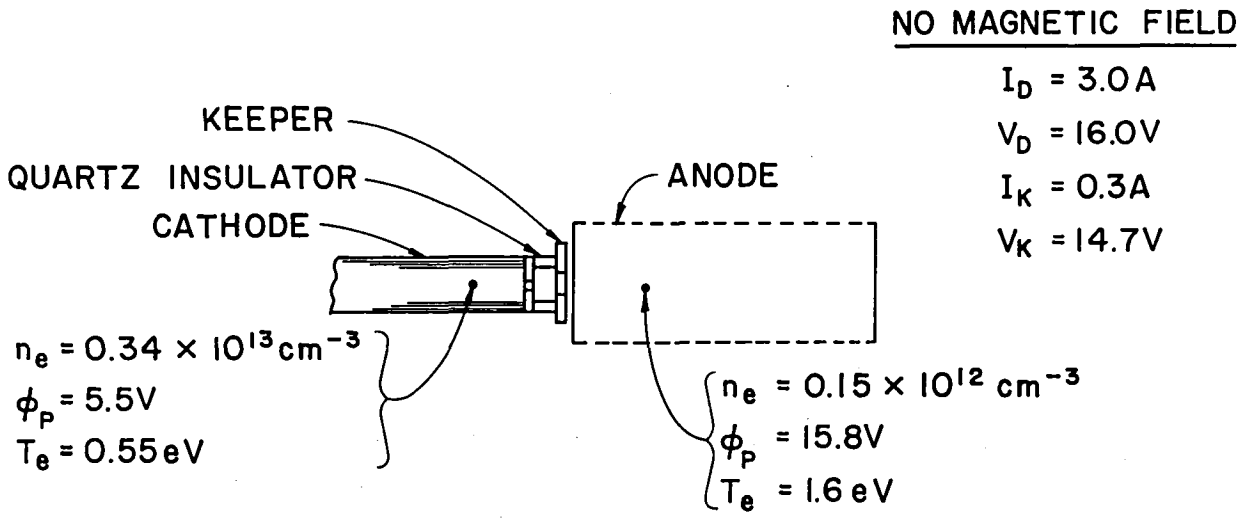

Figure 8. Test Configuration - No Magnetic Field

comparison in Fig. 9. The shape of the magnetic field lines and the field intensity at a few points are also indicated on the iron filings map below the figure. Both the iron filings map and the figure are shown full scale. The conditions associated with the cathode operating at the minimum keeper voltage for the axial magnetic field are shown in Fig. 10.

When the magnetic field cusp was located at the point associated with the second minima of Fig. 7 (i.e., cusped field with the cusp ∿20 mm downstream of keeper), it was found that switching off the solenoid furthest downstream did not affect the keeper voltage. The plasma and magnetic field conditions associated with this configuration are shown in Fig. 11. The presence of the downstream solenoid had little effect on the magnetic field shape or magnitude in the keeper region for this configuration (Fig. 11) and this is probably the reason that switching it off had no effect on the results. In fact, a comparison of the magnetic fields in Fig. 10 and Fig. 11 shows that the field shape in the keeper region is essentially the same in both cases with only the field strength differing. This suggests that the cusped field shape is important only when the null region is centered at the keeper.

As shown in the various cases of Figs. 8 through 11 the plasma properties at a point ∿8 mm upstream of the cathode orifice were not changed significantly by the magnetic field, so it has been concluded that these fields have little effect on the internal cathode discharge. On the other hand, the discharge downstream of the orifice was significantly affected by the presence of magnetic fields. The most notable effect was an order of magnitude increase in the plasma density when the magnetic field was applied. This agrees with the visual observation that the luminous intensity of the discharge in that region increased when the magnetic field was applied.

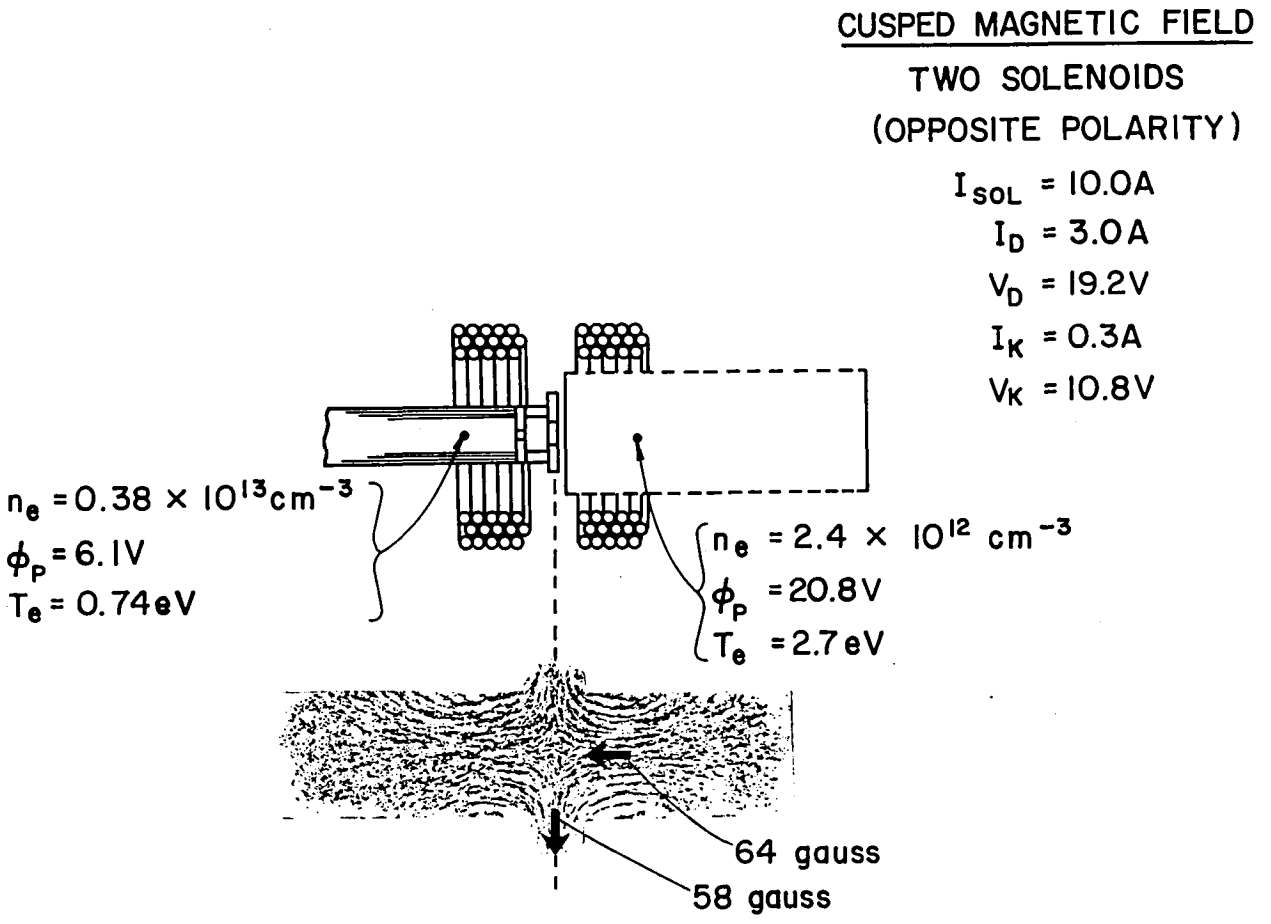

Figure 9. Cusped Magnetic Field Test Configuration

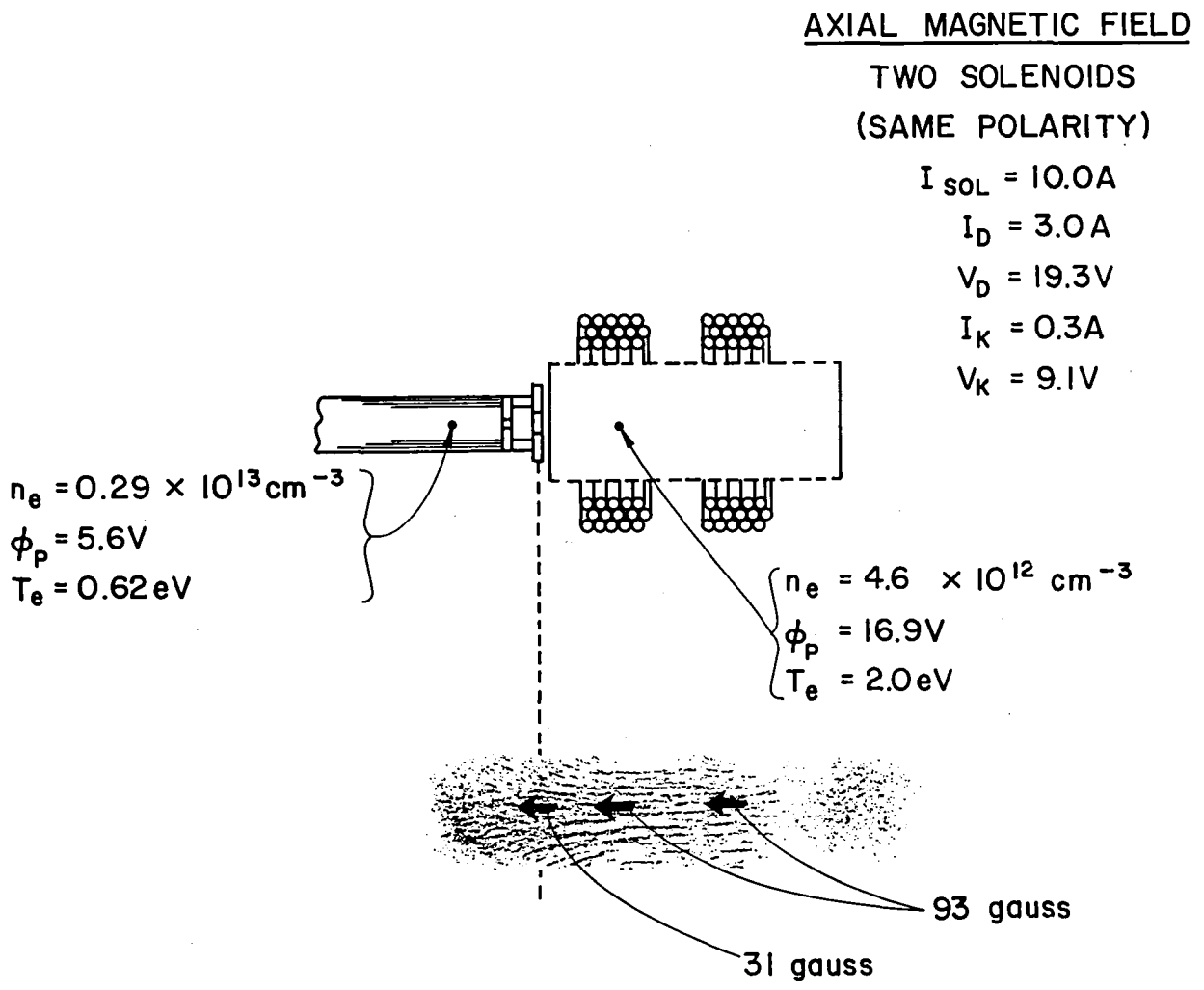

Figure 10. Axial Field Test Configuration

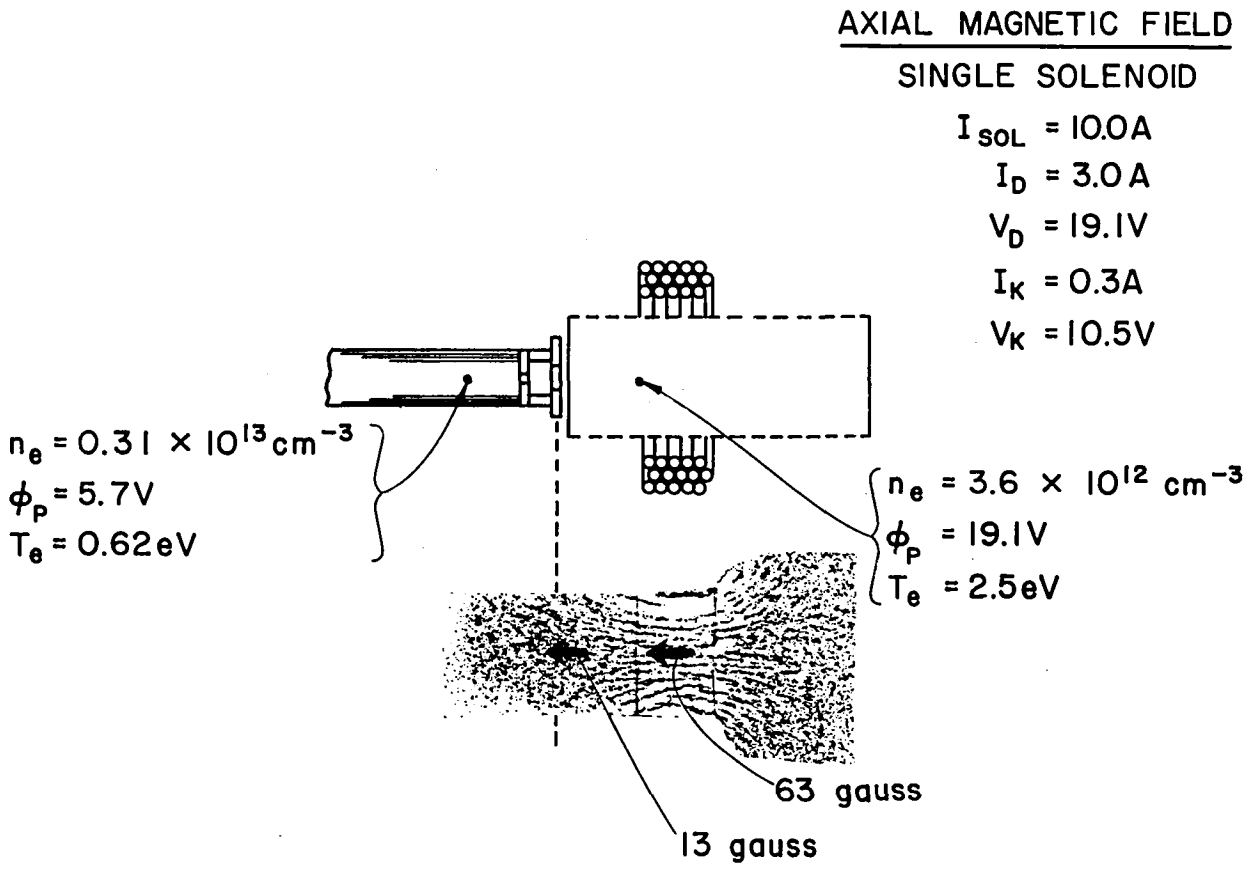

Figure 11. Single Solenoid Test Configuration

Figure 12 shows the effect of magnetic field strength on keeper voltage for the case of the cusped field centered at the keeper and for the case of like-polarity solenoids located 19 mm downstream of the keeper. In both cases the keeper voltage is seen to decrease linearly with increases in magnetic field strength over the 0 to 10 A current range of the magnet power supplies.

Note that the results shown in Fig. 12 indicate that the keeper voltage was ∿11.2 v when there was no magnetic field present compared to a keeper voltage of 14.7 v shown in Fig. 8 for the same operating conditions with no magnetic field present. The reason for this ∿3.5 v difference in keeper voltage was traced to the presence of an insulating coating on the keeper when the data of Fig. 8 were collected. This will be discussed in more detail later.

Discussion of Results

As shown in Fig. 7 the presence of a magnetic field in the range of 50-100 gauss can result in a keeper voltage reduction of 0.75 to 2.0 volts, if the field is properly positioned with respect to the keeper electrode. Figures 8 through 11 provide some insight into the mechanism causing this reduction in keeper voltage. Since the presence of the magnetic field seems to have negligible effect on the internal cathode discharge, it probably acts to reduce keeper voltage mainly by providing better access for electrons to the keeper. This is most obvious in the case presented in Fig. 9. In this case the electrons leaving the cathode orifice can travel along many field lines which intersect the keeper. The electron gyro radius for 2 eV Maxwellian electrons in a magnetic field of 50-100 gauss is ∿0.5 to 1.0 mm. The cathode electrons would, therefore, be expected

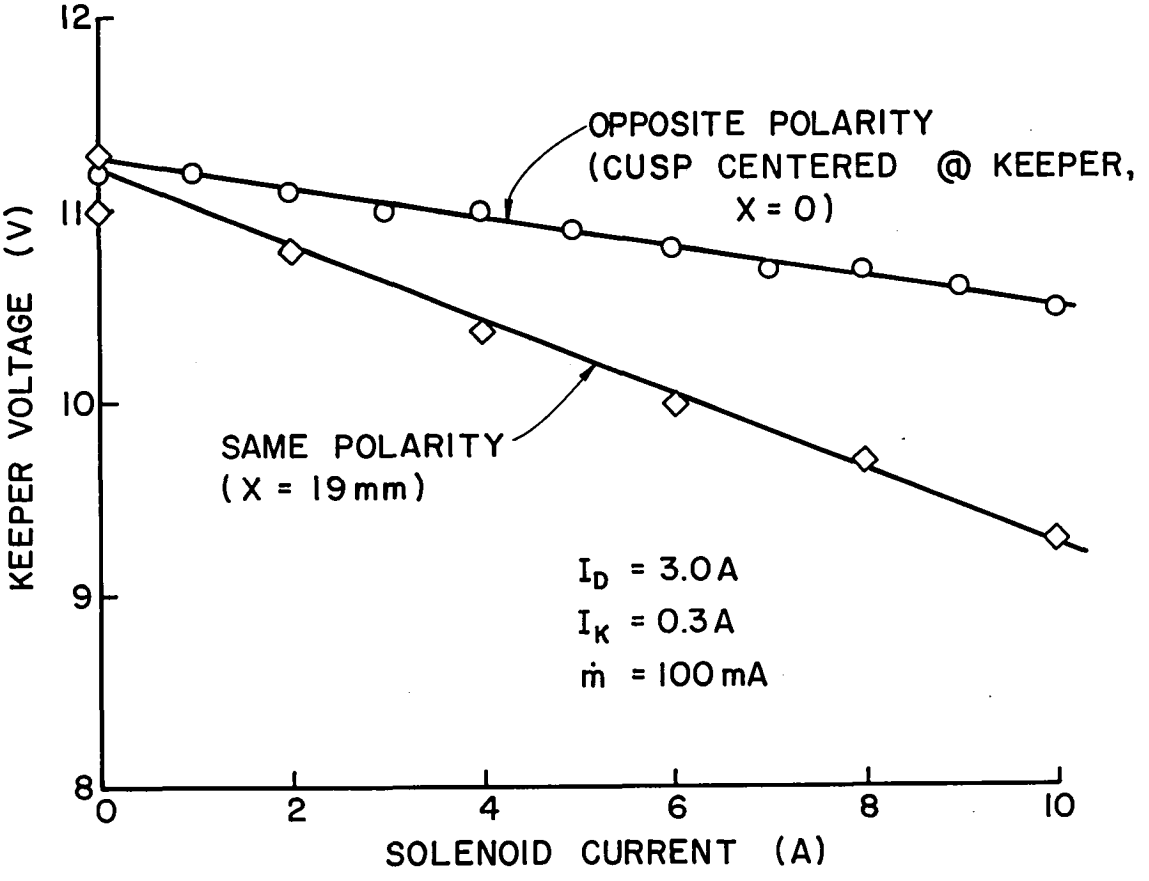

Figure 12. Effect of Solenoid Current on Keeper Voltage

to follow the field lines reasonably closely over the few millimeters distance between the orifice and the keeper. In the cases represented by Figs. 10 and 11, the reason for the lower keeper voltage is not as clear since magnetic field lines intersecting the keeper do not generally pass through the cathode orifice. However, a similar mechanism is probably operating here as well. The presence of the magnetic field traps electrons on the field lines, and therefore, increases their residence time in the region along the cathode axis downstream of the keeper. This apparently increases the number of ionization reactions taking place in that region. This is indicated by both the increased plasma density and the increased plasma luminosity in that region. The field lines from this region of increased ionization activity do intersect the keeper electrode and so electrons producted in such reactions would have direct access to the keeper by traveling upstream along magnetic field lines. This effect would also be present in Fig. 9 to some degree.

As indicated in the results presented in Figs. 8 to 11, the application of the magnetic field resulted in an increase in discharge voltage of $\sim$3 volts. This is probably due to the fact that the field lines on the axis of the cathode in all three cases (Fig. 9, 10, and 11) are parallel to the anode surface. The electrons exiting the cathode orifice must, therefore, diffuse across magnetic field lines to reach the anode, and as a result their access to the anode is impeded when the magnetic field is present.

The cathode was also operated with anodes of various sizes, shapes, surface areas and locations. As might be expected the discharge voltage was found to be highly dependent on the anode configuration as well as magnetic field strength and configuration in the region adjoining the anode. The results of these other configurations were not of sufficient interest

to present in detail, except to note that when the anode was constructed such that field lines aided electron access to the anode the discharge voltage was decreased. Conversely when, as above, the magnetic field lines impeded access to the anode the discharge voltage was increased. The keeper voltage on the other hand was found to be rather insensitive to anode configuration.

The data for Fig. 7 and Fig. 12 were not collected during the same operating period as those for Figs. 8 to 11. As noted earlier, the keeper voltage when no magnetic field was present differed by ∿3.5 volts between these two experiments. An investigation into the reason for this difference led to the conclusion that the probable cause of the ∿3.5 volt difference in keeper voltage in the absence of a magnetic field was an insulating coating on the upstream surface and orifice of the keeper electrode during collection of the data presented in Figs. 8 through 11. This coating, while it influenced the voltage observed when no magnetic field was present did not appear to have a substantial affect on the level of the keeper voltage when the magnetic field was present. For example, Figure 7 shows that the minimum keeper voltage in the presence of the cusped magnetic field was ∿10.5 v which is similar to that indicated in Fig. 9 and Fig. 11 where the insulating coating was present on the upstream face of the keeper. This suggests that much of the keeper current is conducted to the upstream side of the keeper when no magnetic field is present. When the field is applied, however, the current appears to flow to the downstream side of the keeper. That this is occurring is supported by two test results. First, when the field is applied, the plasma density adjacent to the downstream side of the keeper increases by an order of magnitude and electrons from this region have access to the downstream side of the keeper by traveling along magnetic

field lines as previously discussed. Second, the application of a thin insulating ceramic coating to the upstream face of the keeper was found to cause an increase in the keeper voltage for the no magnetic field case and no change in the keeper voltage for the case where the magnetic field was present. This also suggests that high keeper voltages may in some cases be caused by sputtering of material onto the upstream face of the keeper. This occurrence would probably be more likely in enclosed keeper configurations.

Conclusions

When magnetic fields on the order of 100 gauss are present in the keeper region of the hollow cathode, the keeper voltage can be reduced by up to 2.0 volts if the field is properly oriented with respect to the keeper. This keeper voltage reduction is apparently due to the combined effect of increased plasma density and of providing direct access of electrons to the keeper along magnetic field lines. The reduction in keeper voltage is proportional to the strength of the magnetic field. Plasma properties within the hollow cathode do not appear to be affected by the presence of the magnetic field. However, the plasma density downstream of the keeper increases by about an order of magnitude when the magnetic fields are turned on. Based on results obtained with and without an insulating coating on the upstream side of the keeper it is concluded that much of the keeper current is collected at the upstream side of the keeper when no magnetic field is present. The presence of the magnetic field configurations used in these tests appeared to cause the keeper current to flow to the downstream side of the keeper. These results also suggest high keeper voltages may be due to insulating materials sputter coated on the upstream face of the keeper.

ION BEAM PLASMA INVESTIGATION

Introduction

The recent return of the SERT II spacecraft to continuous sunlight conditions has led to increased testing activity on its two mercury, electron bombardment ion thrusters. Kerslake and Domitz[8] have reported that not only has Thruster #2 been operated normally, but Thruster #1, which has a grid short, has been operated without high voltage and in this condition has served as a neutralizer for Thruster #2. They report that neutralization using the #1 thruster results in a lower coupling voltage than that observed when the Thruster #2 neutralizer is being used. This exceptional performance of the Thruster #1 discharge plasma as a neutralizer is surprising when it is first considered for two reasons. First, the thruster is about 1 meter away from the ion beam to be neutralized and second the potential difference between the discharge plasma and the beam plasma is such that electrons should be retarded and even prevented from leaving the discharge to reach the beam plasma and effect neutralization. In order to determine the character of the plasma emanating from Thruster #1 with its grids shorted and at spacecraft potential and to determine the mechanism of neutralizing electron flow from the thruster the experiments described next were performed. A further experiment wherein the grids were biased to extract electrons was conducted to investigate the usefulness of a discharge plasma such as this as a super-neutralizer as suggested by Kerslake and Domitz.[8]

Apparatus and Procedure

The beam plasma tests were conducted in a 1.2 m by 5 m vacuum test facility using a SERT II thruster[9] as the source of discharge plasma. The

actual test setup is shown in Figure 13. As suggested by this figure the downstream plasma could communicate with the 1.2 m diameter liquid nitrogen cooled cylindrical liner and a radiation cooled target located 3 m downstream of the source. The liner was held at ground potential during the tests, but the target potential could be maintained at various values to simulate the range of beam potential variations observed during the space tests.

The ion source used for the tests (a standard SERT II unit[9]) was modified to allow independent control and measurement of the main and cathode flow rates. The only additional modification made to it concerned the neutralizer which had been moved from its initial location near the accel grid to a point 5 cm downstream of this grid and 5 cm outside of the edge of the beam. The axis of the neutralizer cathode/keeper assembly was also oriented parallel to the thruster axis rather than inclined relative to it as in the original design. For the test results reported here the cathode and main flow rates totalled about 180 mA eq. with some adjustment in the relative distribution being used to achieve the discharge voltage condition desired. The grids were kept shorted to ground except during one test when they were biased to facilitate electron extraction from the source. When the neutralizer was operated the mercury flow rate to it was about 30 mA and the neutralizer keeper current was maintained at 0.2 A. The facility pressure was maintained near 8×10^{-6} torr during the testing.

Plasma properties downstream of the source were measured using a movable Langmuir which could be swept from the beam centerline either through the neutralizer axis or opposite it out to a radius of 30 cm (measured from the thruster axis). This probe could also be moved axially from a plane within 5 cm of the accelerator grid to one about 30 cm downstream

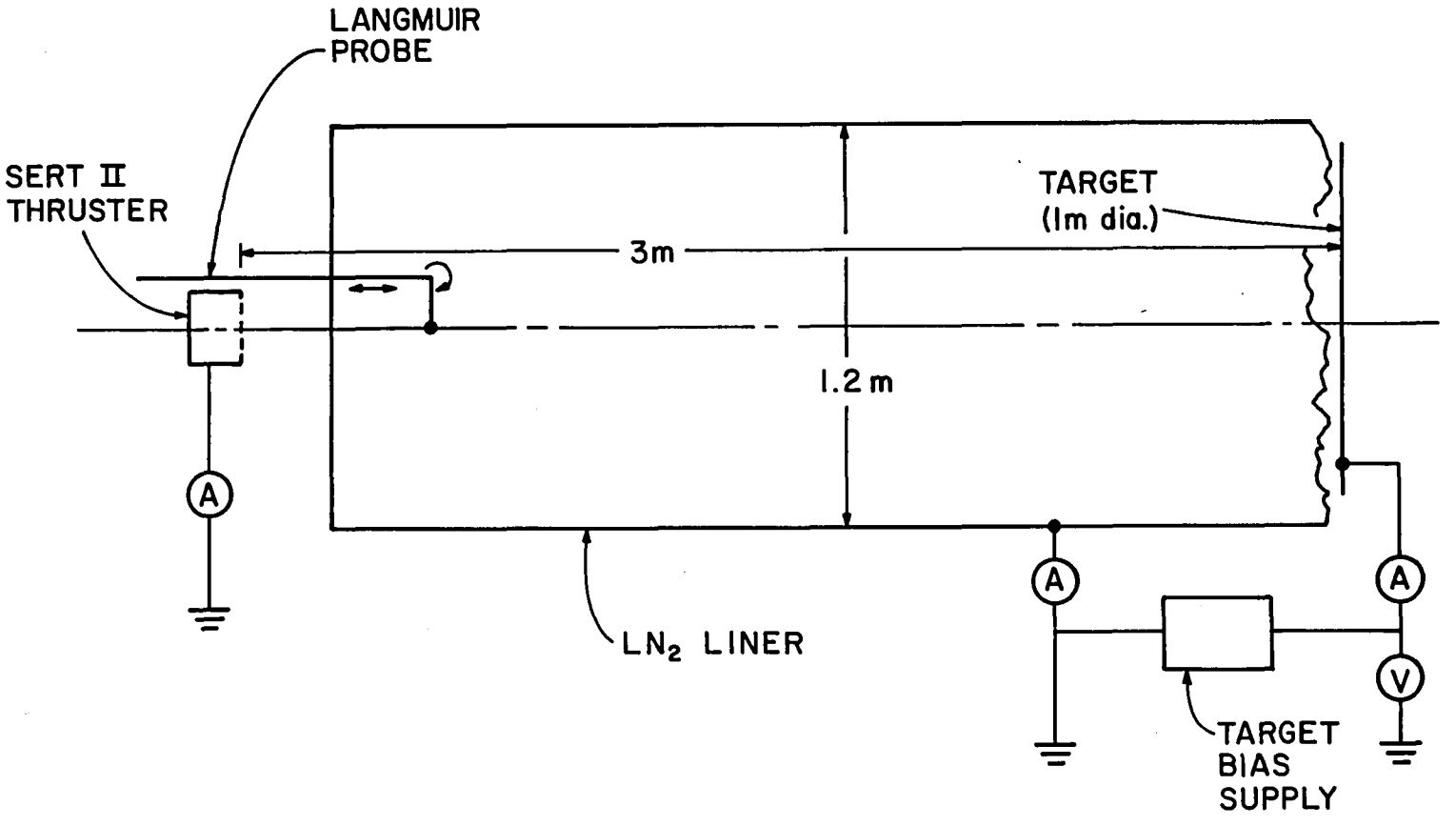

Figure 13. Beam Plasma Test Configuration

of it. The probe was fabricated using a spherical platinum sensor 2.2 mm in diameter supported from the end of a quartz tube. Analysis of current/voltage traces obtained from the probe was accomplished using a thick sheath approach. This analysis assumes exponential current variation with voltage in the retarding region of the probe trace and linear variation in the accelerating region. The procedure is described in detail in Appendix A. Plasma conditions within the discharge chamber were also measured on occasion using a conventional cylindrical Langmuir probe. The resultant traces were analyzed using a thin sheath probe analysis procedure.[10]

In order to assure that currents flowing to and from the thruster, neutralizer, tank, and target were reasonable these currents were measured where possible. Figure 14 is a schematic of the test configuration showing the various currents involved. The arrows on the figure show the direction of net positive current flow -- a net electron current would correspond to electron flow in the opposite direction. All of the currents shown in the figure were measured directly in the tests except the tank current (I_{tank}) which was determined by requiring zero net current flow to the beam plasma.

The conduct of tests concerning the beam plasma was accomplished by establishing discharge chamber and neutralizer operating conditions and allowing the system to stabilize for a few hours before collecting data. Langmuir probe data were collected using an x-y plotter to record probe current/voltage traces typically at four radial locations within the thruster (5 mm upstream of the screen grid) and at six or more radial locations at each of three axial locations downstream of the accelerator grid. Target bias could then be changed and data collection would be repeated. If discharge or neutralizer operating conditions were altered they were allowed to stabilize before the collection of additional data.

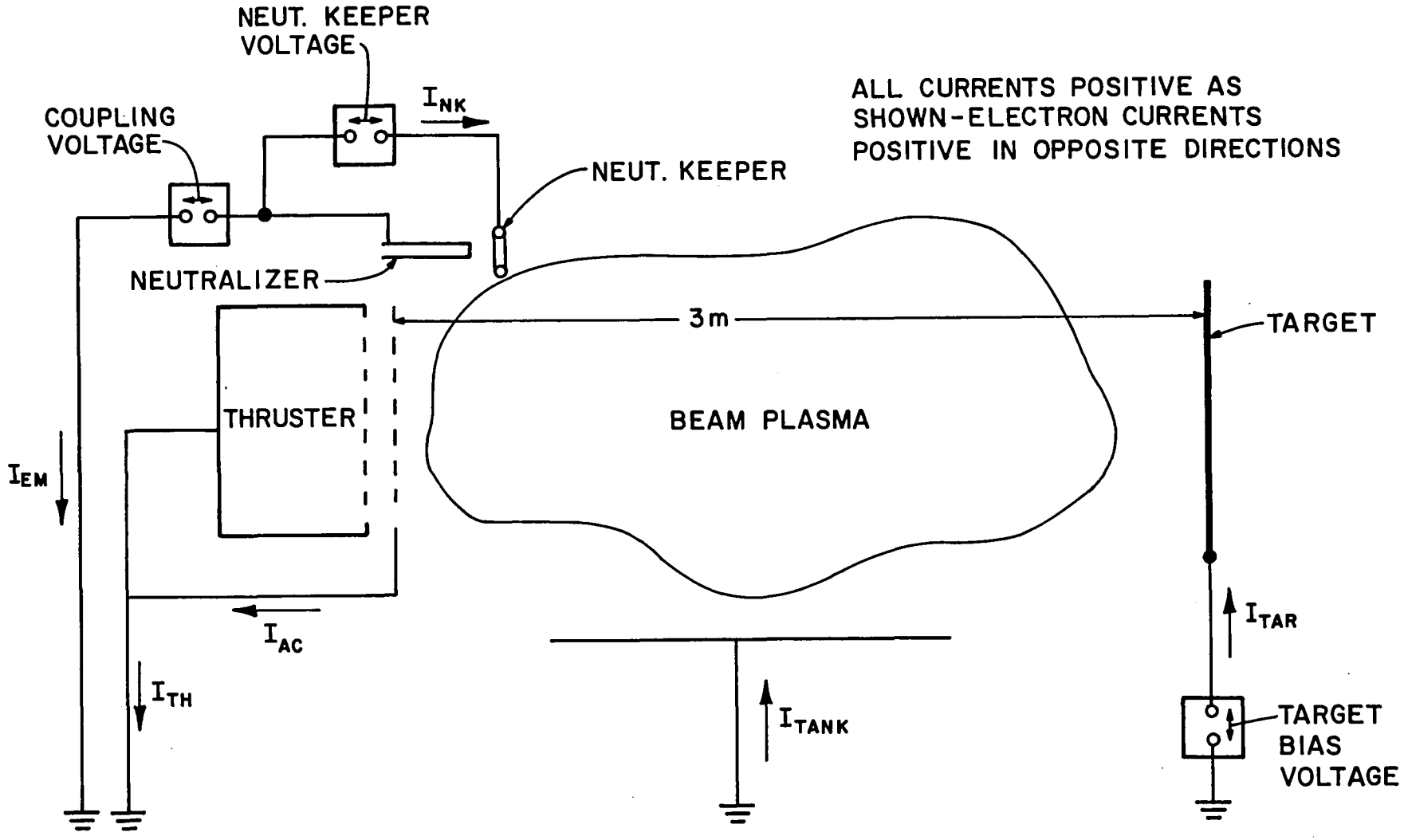

Figure 14. Current Definition Diagram

Results

Downstream Plasma Properties

The thruster was operated at discharge conditions close to those at which Thruster #1 (with the short between its grids) is operating in space and the beam plasma was probed. Figure 15 shows these plasma properties measured along the extension of the thruster centerline as a function of axial position downstream of the grids at a discharge current (I_D) and voltage (V_D) of 2.0 A and 38.4 V respectively and a main keeper voltage (V_K) of 10.6 V. The parameter in the figures is the target bias voltage above tank ground and values of 40 V, 20 V, and -0.1 V (floating) were established during the tests. Probe measurements within the discharge chamber showed the plasma potential was ∿37 V as suggested in the upper graph. The mean discharge chamber plasma had a Maxwellian electron temperature and density of about 6 eV and 1.5×10^{11} cm^{-3} and a primary electron energy and density of about 23 eV and 1×10^{10} cm^{-3}. The data of Figure 15 were obtained with the neutralizer off, but results obtained later with it on suggested that its operation did not alter these results significantly.

Several observations can be made regarding Figure 15. First, the downstream thruster potential tends to lie about 10 V above the target potential and the temperature and density profiles do not appear to be affected significantly by target bias. Second, the axial variations in plasma potential and electron temperature are probably not significant to within the accuracy of the measurements. The electron density does however decrease rapidly with axial position probably because of expansion of the plasma as suggested by Kerslake.[8] During the course of the collection of the data shown in Figure 15, the current collected by the target was measured. No net electron current was drawn when the target was floating

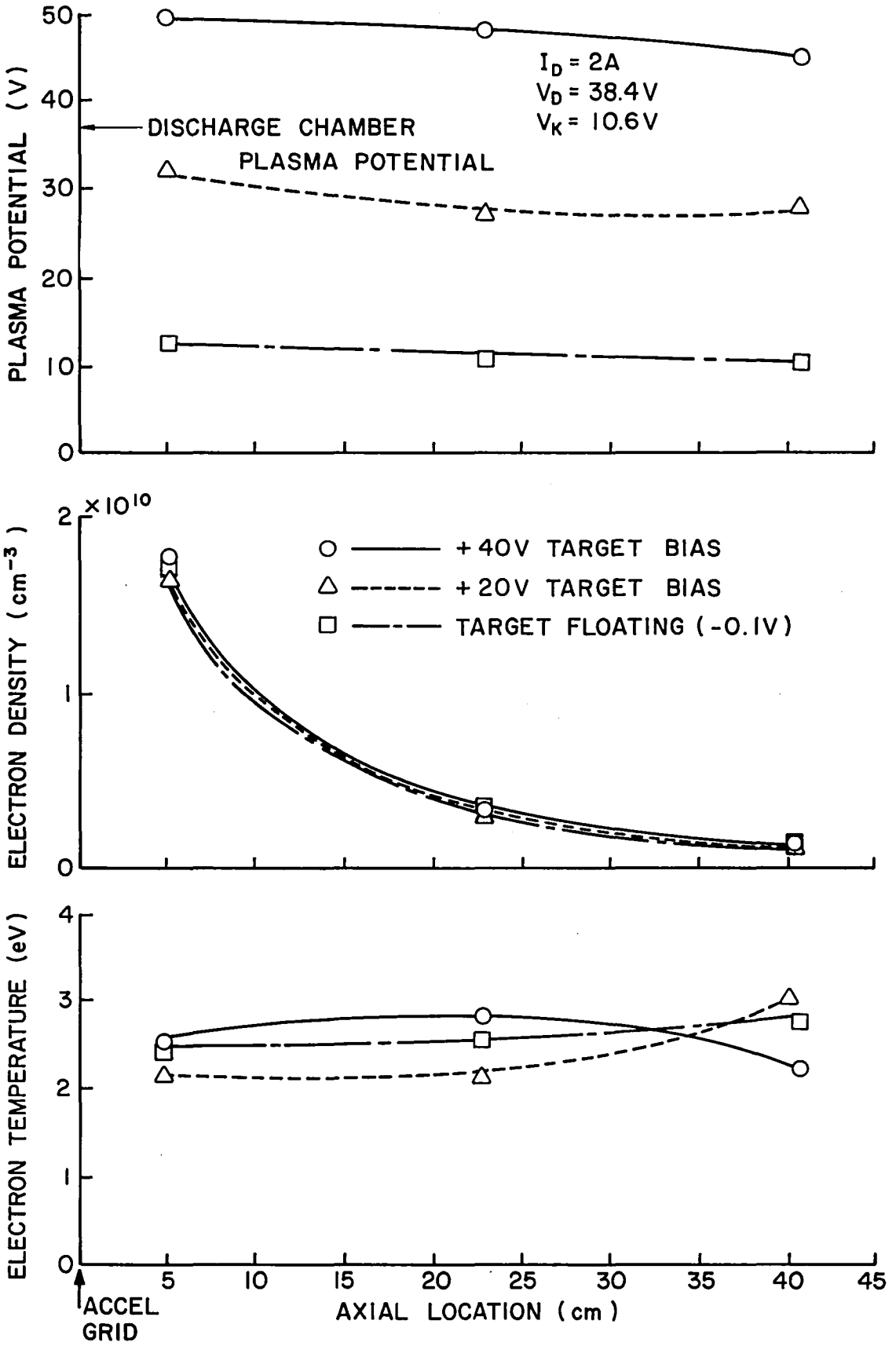

Figure 15. Centerline Plasma Properties Downstream of SERT II Thruster (High Voltage Off)

of course, but a current of 32 mA was drawn at a target bias potential of 20 V and 54 mA was drawn when the target was biased to 40 V. An ion current -- determined by the Bohm condition at the screen grid -- of the order of a few tens of milliamperes should be drawn out of the thruster so the actual electron current to the target could be higher than the net electron current by this amount.

The radial variation in the plasma properties of the thruster efflux with a floating target is illustrated by the data of Figure 16. These data were measured 20 cm downstream of the thruster with the neutralizer operating at a potential 7 V below ground potential and skewing of the data is considered to be a result of neutralizer operation. Comparison of Figure 16 data with those of Figure 15 suggests that the plasma potential and electron temperature data are in agreement but electron densities of Figure 16 are somewhat lower than those of Figure 15. The reason for this is not apparent, but the data for these two plots were obtained at different times and the discharge voltage was about 2 volts lower when the data of Figure 16 were obtained than it had been when the Figure 15 data were collected. This discharge voltage did seem to influence the thruster efflux and it is believed that the variation in the discharge voltage caused the observed difference. The data of Figure 16 suggest that the plasma efflux from a source operated with its grids at ground potential tends to spread quite rapidly. This is suggested by the fact that the centerline plasma density decays rapidly (Figure 15) and that the beam diameter has increased from about 15 cm at the grids to 40 to 50 cm in the data of Figure 16, taken $\sim$20 cm further downstream. Comparing the radial spread of these data 20 cm downstream of the grids data with those of Thruster #2 operating in space (with high voltage applied)[8] it appears that beam plasma is more highly

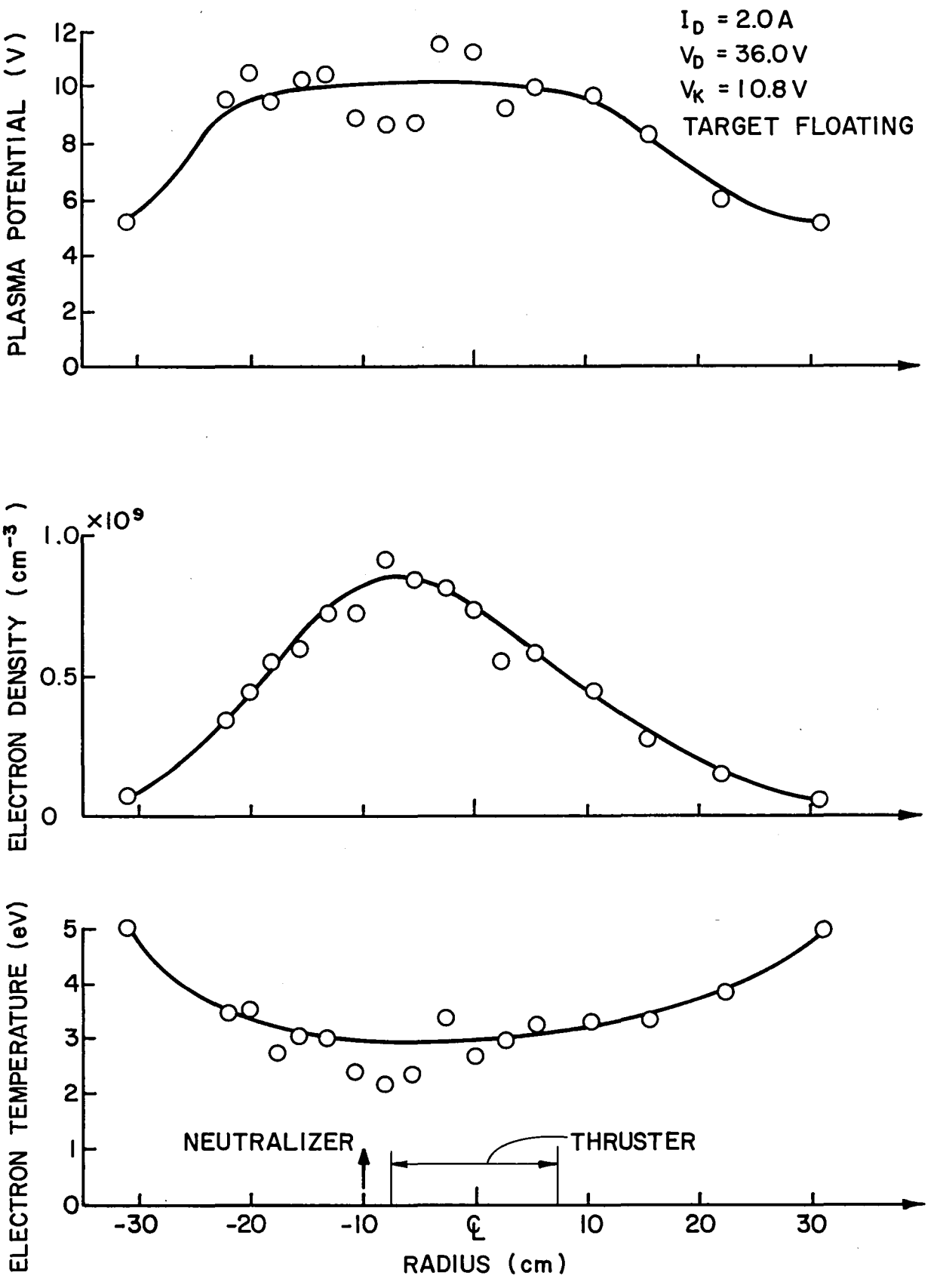

Figure 16. Plasma Property Profiles 20 cm Downstream of SERT II Thruster (High Voltage Off)

columnated when the high voltage is on.

Effects of Neutralizer Operation

It was considered desirable to account for the various currents going to and from the neutralizer and the thruster operating without high voltage to assure that all of these currents were reasonable and to facilitate an examination of the effects of neutralizer bias potential (coupling voltage) on these currents. This latter effect was considered important because the coupling voltage had been varied in space tests.

Figures 17 and 18 show the effect of variations in neutralizer bias on the currents defined in Figure 14. They suggest that a negative neutralizer bias results in increased neutralizer emission and that most of this emission goes to the vacuum tank. This would presumably correspond to increased emission to the space plasma in space tests. Net electron emission from the thruster is not affected greatly by this negative bias. Positive neutralizer bias results in an increased emission from the thruster which is collected by the neutralizer. The parameter on the curves is the target bias which was varied from floating potential (near ground) to 20 V and 35 V. These variations in target potential do not seem to alter the qualitative description given above. Figure 19 shows the variation in neutralizer keeper potential measured with respect to ground as coupling voltage is varied. It is interesting to note that the neutralizer keeper becomes the most positive surface in the test facility at -18 V, -12 V and -6 V coupling voltages for the floating, 20 V and 35 V target potentials respectively. Significant electron currents are not drawn from the thruster to the neutralizer, however, until the coupling voltage reaches about 5 V. Review of Figures 17 to 19 has suggested the following observations:

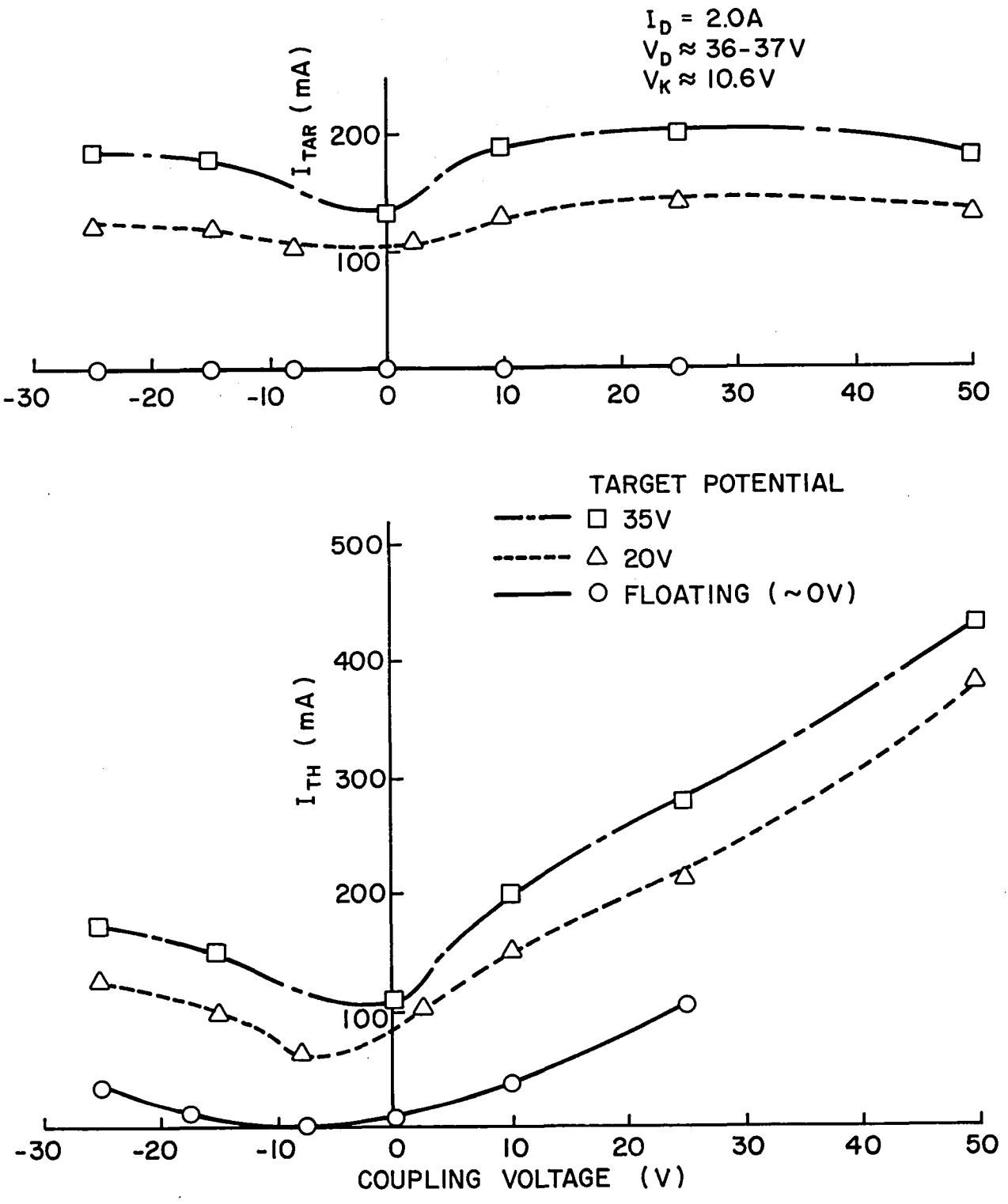

Figure 17. Effect of Neutralizer Bias on Current Distribution

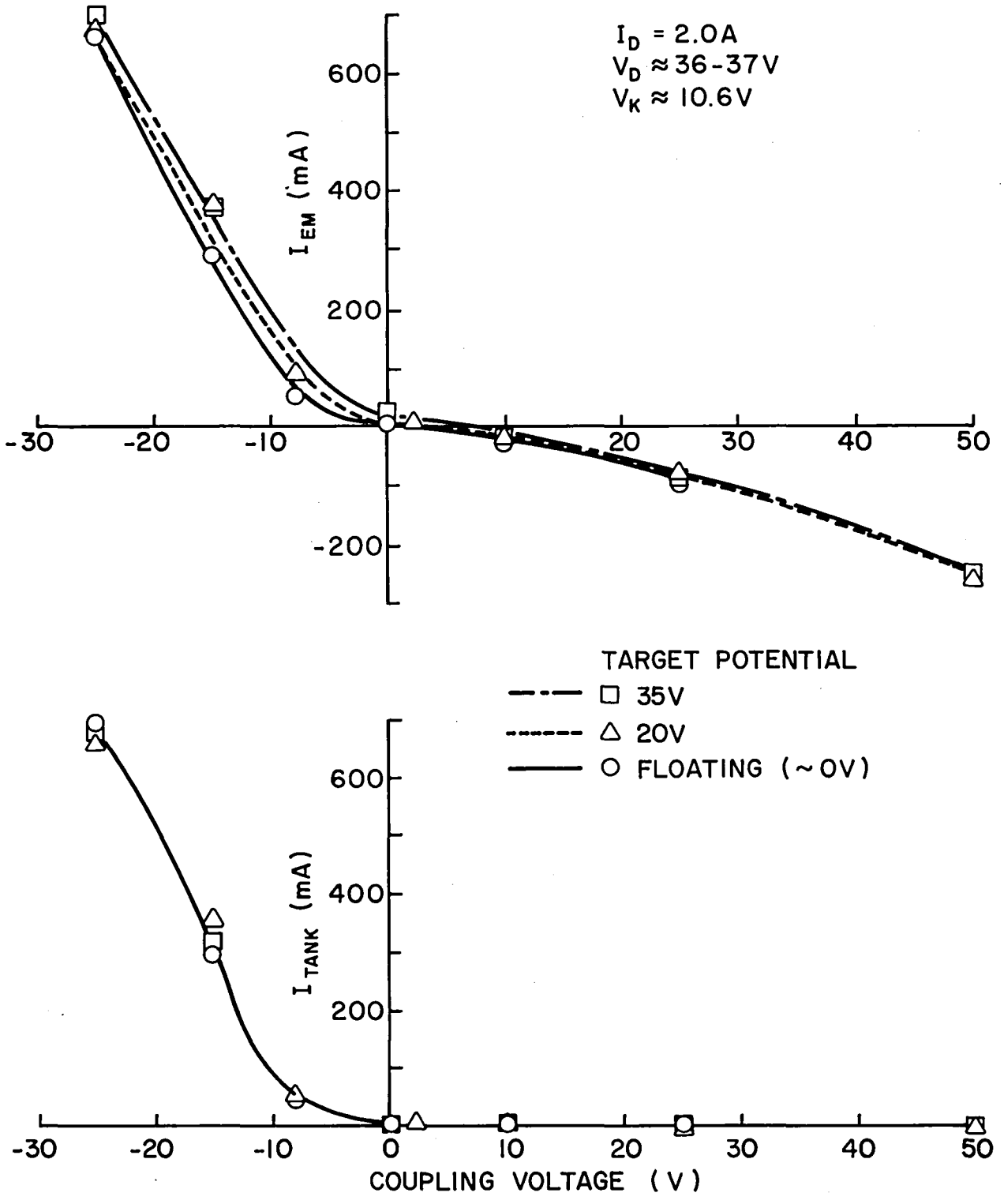

Figure 18. Effect of Neutralizer Bias on Current Distribution

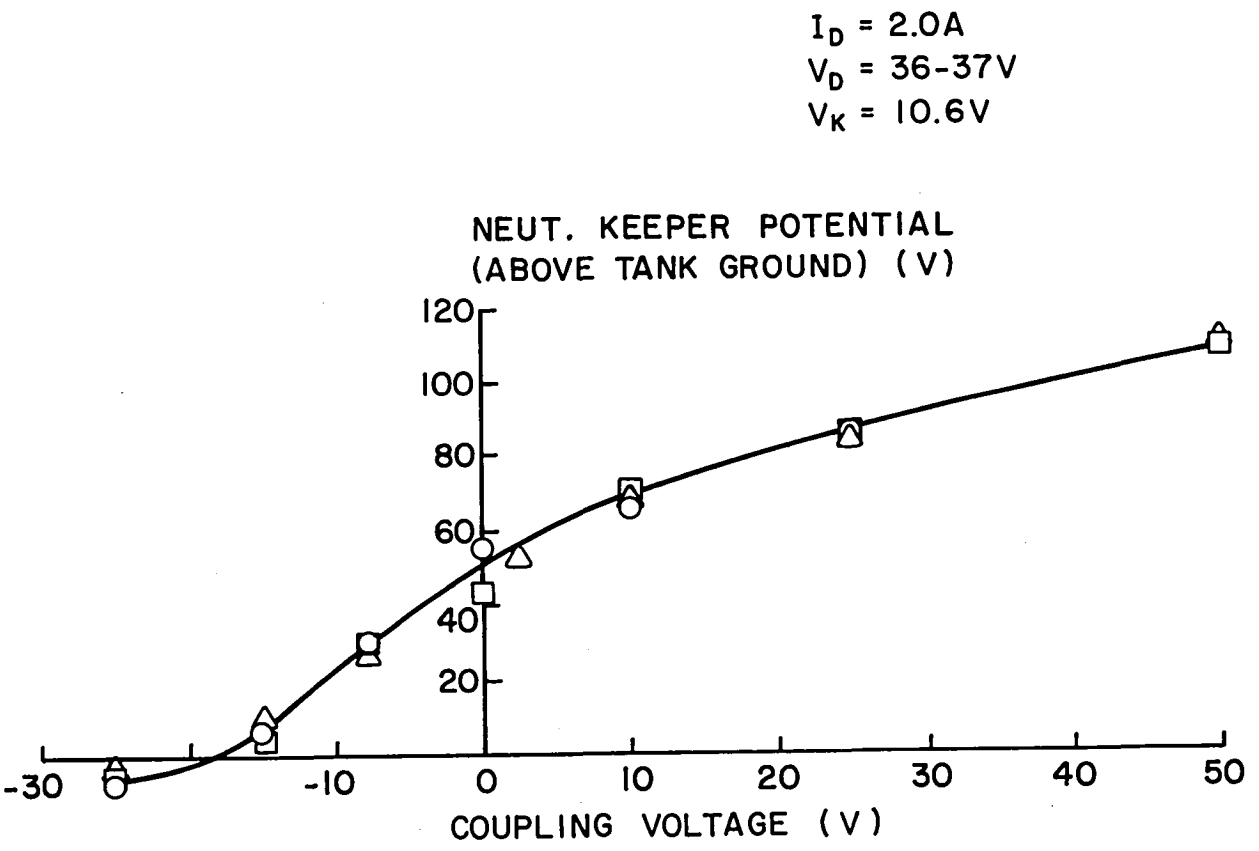

Figure 19. Effect of Neutralizer Bias on Neutralizer Keeper Potential

- Neutralizer emission is not affected significantly by target bias,
- The target seems to collect most of the thruster emission (even when the neutralizer keeper is as much as 50 V positive of the target), and
- When the neutralizer is biased negative most of its emission goes to the vacuum tank ground.

Operation of An Ion Source as a Neutralizer

Initially one might conclude after considering the adverse potential difference from the discharge plasma to the beam plasma of a source operating with its grids at ground potential that electrons would not escape through the grids. This would make the device useless as a neutralizer, but space tests have revealed that such a source works well in this application.[8] The question of how electrons can escape from a discharge plasma at ∿40 V into a beam plasma at about ∿20 V as observed in space begs for an answer. In order to answer this question a series of tests were run in which thruster discharge voltage was changed by adjusting the discharge current or propellant flow rates. The data of Figure 20 were obtained, for example, by varying the discharge current at a constant flow rate condition. They suggest that an increase in the discharge-keeper voltage difference results in an increase in the electron current from the thruster and that this voltage difference must rise above a threshold near 26 volts before net electron loss occurs. Since this discharge-keeper voltage difference determines the primary electron energy[11] it was postulated that net electron current was given off by the thruster when the primary electron energy was sufficient to overcome the potential difference between the discharge chamber and beam plasmas. Figure 21 shows the plasma conditions for one typical operating condition where the net

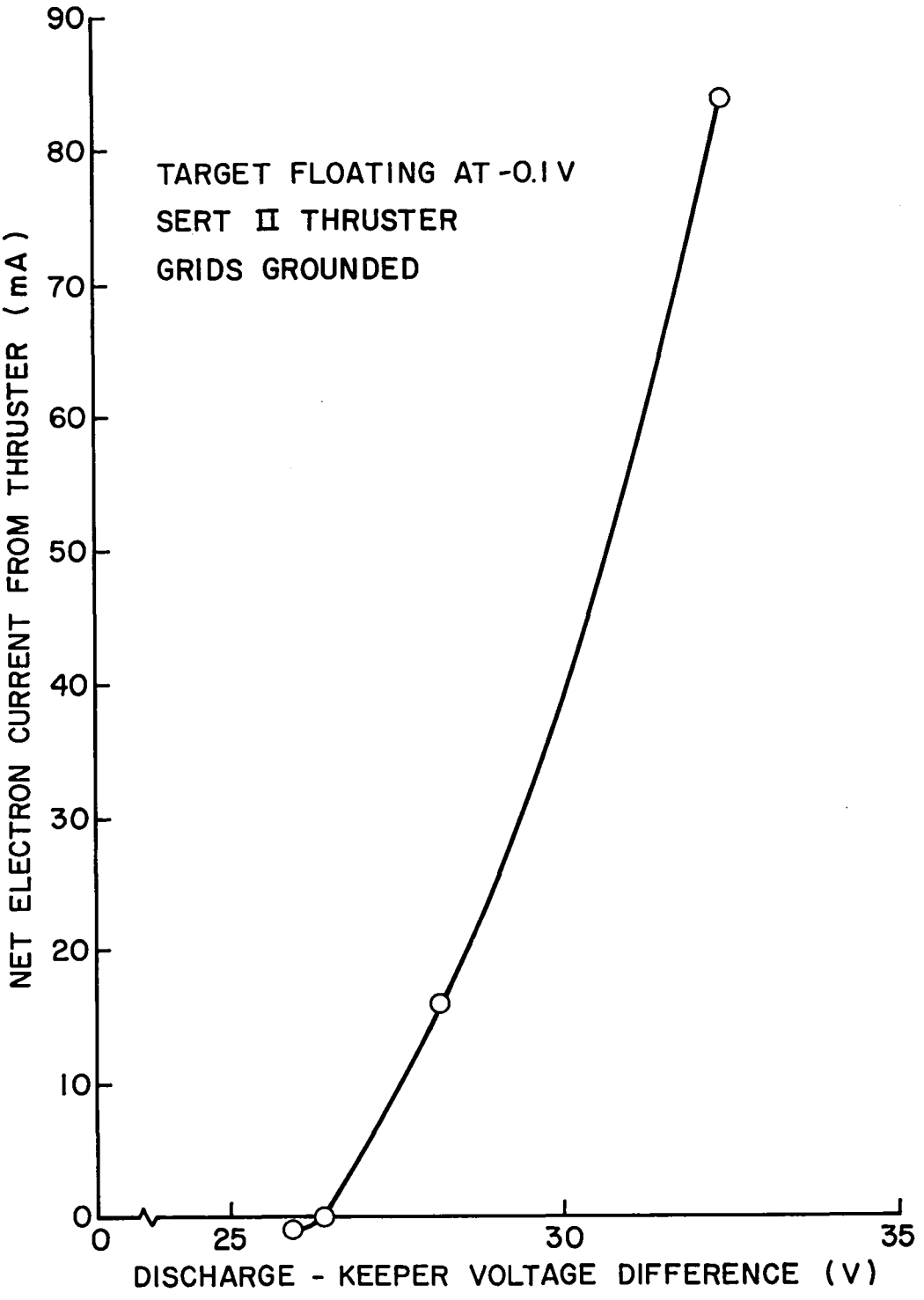

Figure 20. Effect of Discharge - Keeper Voltage Difference on Net Electron Loss Rate

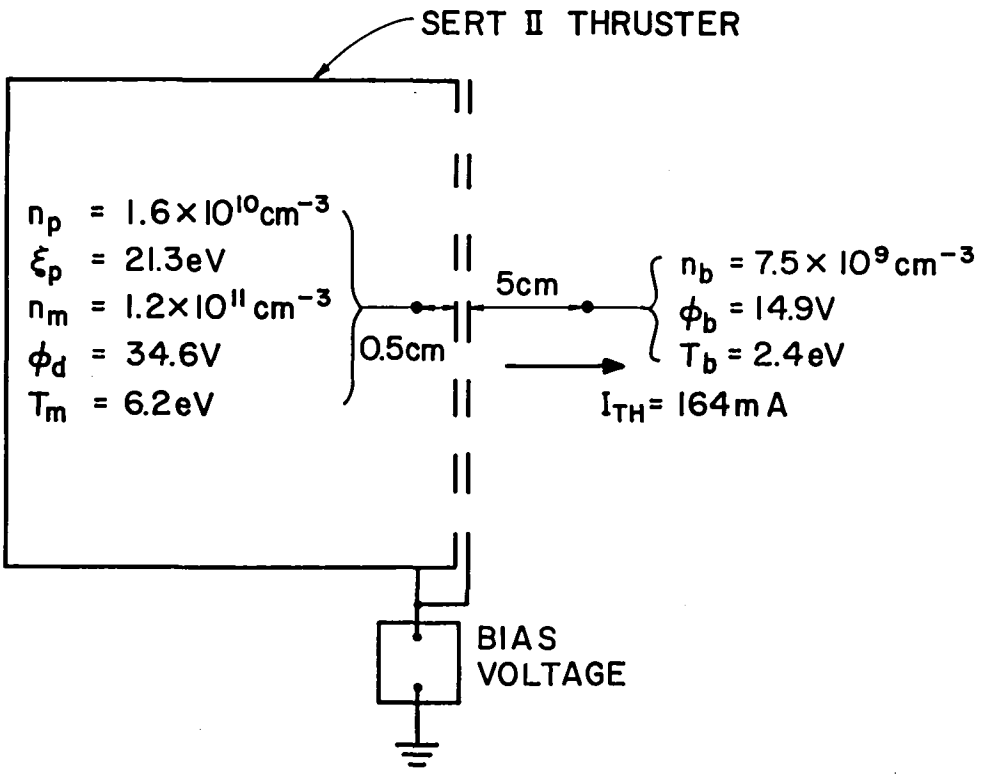

DISCHARGE CURRENT	= 1.94A
DISCHARGE VOLTAGE	= 37.4 V
KEEPER VOLTAGE	= 10.2 V
KEEPER CURRENT	= 0.3A
MAIN MASS FLOW RATE	= 75mA
CATHODE MASS FLOW RATE	= 91 mA

Figure 21. Typical Operating Condition

electron emission current from the thruster (I_{TH}) is 164 mA. If the proposed model were to be valid the primary electron energy (ε_p = 21.3 eV) would have to be greater than the discharge chamber-beam potential difference ($\phi_d - \phi_b$ = 19.7 V) for this case where emission is occurring. One can see that in this case the condition is indeed satisfied. It is also noteworthy that the electron density in the beam ($n_b = 7.5 \times 10^9$ cm^{-3}) is of the same magnitude as the discharge chamber primary electron density ($n_p = 16 \times 10^9$ cm^{-3}) while the Maxwellian electron density is much greater ($n_m = 120 \times 10^9$ cm^{-3}). Since electron drift velocities in the two regions should be of the same order, this too suggests it is primary electrons that find their way into the beam plasma while discharge chamber Maxwellian electrons having a temperature of several eV tend to remain in the chamber. It is important to note at this point that the uncertainty in primary electron energy and plasma potential measurements is greater than the escaping electron energy ($\varepsilon_p - [\phi_d - \phi_b]$) being computed here. One can therefore do no better than to show that this energy is near zero at low electron emission levels and substantially higher at high emission levels. Table I contains plasma property data for a number of operating conditions including the one corresponding to Figure 21. In the first five cases given the emission is relatively low (near the threshold) and the escaping electron energy ($\varepsilon_p - [\phi_d - \phi_b]$) is small. In the last two cases the thruster was biased negative. This caused a large electron emission current and a correspondingly high escaping electron energy. In this case it is likely that substantial numbers of Maxwellian electrons can also overcome the potential difference and contribute to the net electron current.

TABLE I

SERT II PLASMA PROPERTIES

Thruster Bias Voltage (V)	Electron Emission Cur. from Thruster I_{TH} (A)	Probing Location	Max. Elec. Temp T (eV)	Max. Elec. Density n (cm^{-3})	Energy ξ_p (eV)	Density n_p (cm^{-3})	Plasma Potential ϕ (V)	Escaping Electron Energy (eV)
0	0.164	Beam Chmbr	2.4 6.2	1.6×10^{10} 1.2×10^{11}	-- 21.3	-- 7.5×10^{9}	14.9 34.6	+1.6
0	0	Beam Chmbr	2.2 5.2	5.0×10^{9} 1.4×10^{11}	-- 20.8	-- 6.6×10^{9}	12.3 33.6	-0.5
0	0.016	Beam Chmbr	1.5 6.9	1.0×10^{10} 1.4×10^{11}	-- 27.1	-- 1.7×10^{10}	9.4 37.6	-1.1
0	0.84	Beam Chmbr	1.8 6.9	1.4×10^{10} 1.2×10^{11}	-- 28.0	-- 2.6×10^{10}	9.4 36.3	+1.1
0	0	Beam Chmbr	2.9 5.4	8.7×10^{9} 1.5×10^{11}	-- 20.3	-- 3.6×10^{9}	14.4 33.7	+1.6
-20	1.8	Beam Chmbr	2.2 7.0	8.8×10^{9} 1.5×10^{11}	-- 27.6	-- 3.1×10^{9}	11.3 19.4	+19.5
-20	1.8	Beam Chmbr	6.2 6.6	6.0×10^{9} 1.5×10^{11}	-- 27.2	-- 5.0×10^{9}	17.4 19.0	+25.6

The effect of negative thruster bias (including both grids) on the electron emission current is considered further in Figure 22. Relatively small thruster bias voltages are seen to enable one to draw electron currents of the order of a few amperes. Discharge conditions were observed to change suddenly when the bias voltage was in the -20 to -25 V range between two distinct modes of operation as this figure suggests. The high currents achieved here suggest that super-neutralizer operation as proposed by Kerslake and Domitz would probably be most effective if the grids were biased in this way.

Conclusions

When the discharge chamber of an ion thruster is operated with its grids at ground potential both ions and electrons escape from it. The electrons escaping seem to be mostly primary electrons which are the electrons having a sufficiently high kinetic energy to overcome the adverse potential difference between the discharge and beam plasmas. If the thruster is biased negatively so both primary and Maxwellian electrons can overcome the potential hill between the discharge and beam plasmas the electron current drawn from the thruster increases substantially.

Tests conducted with the thruster at ground potential suggest that when the neutralizer is on, it can draw some electron current from the thruster, provided it is maintained at a potential significantly above thruster potential. The electron current drawn to the target from the discharge chamber does not seem to be altered significantly because of changes in neutralizer potential, and the neutralizer emission doesn't seem to contribute to the net electron current drawn by the target at any neutralizer potential.

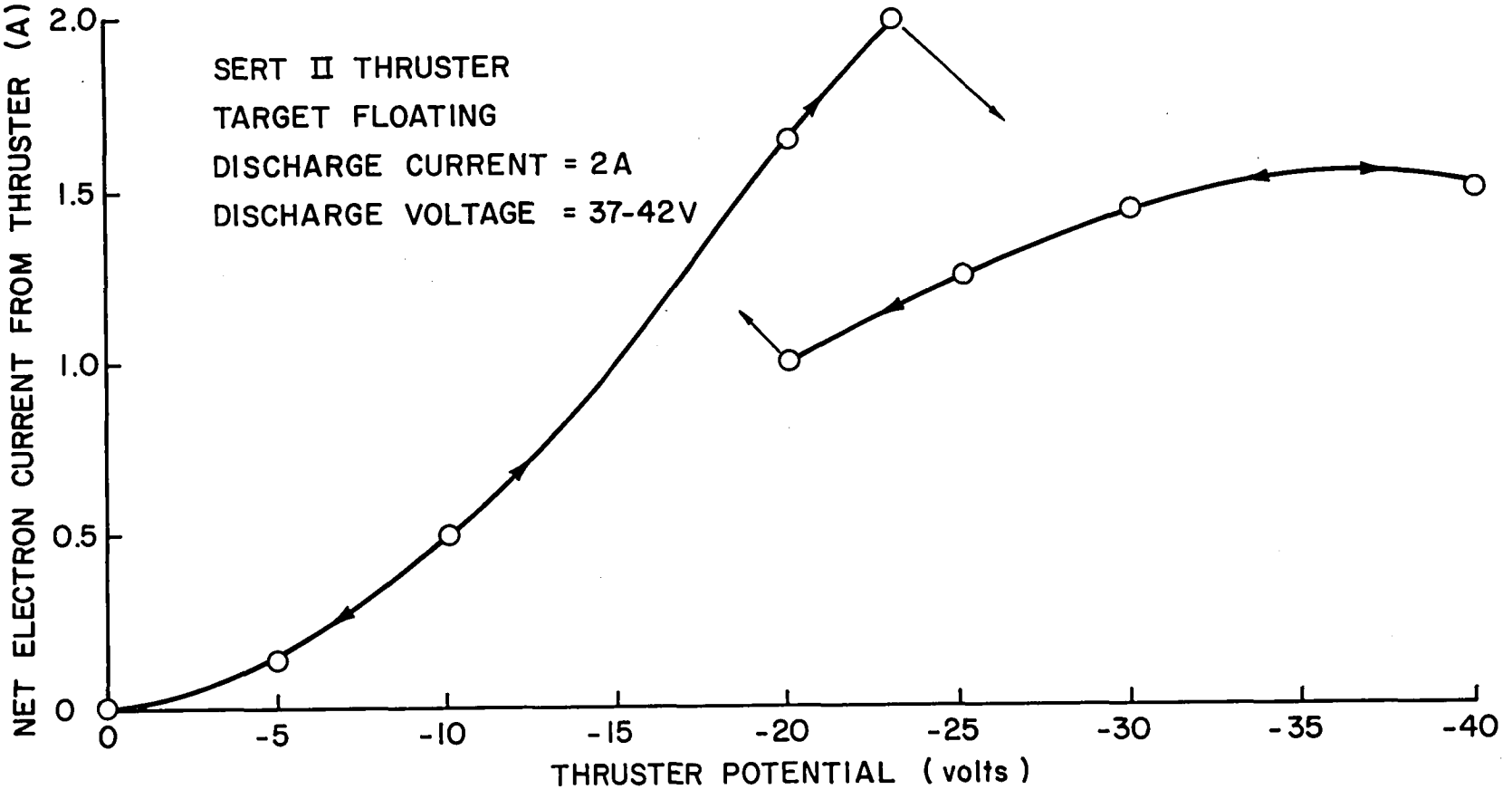

Figure 22. Effect of Grid Bias on Electron Emission

BAFFLE APERTURE DESIGN STUDY

John Brophy

Introduction

The use of a hollow cathode in place of an oxide cathode to increase thruster operating lifetime requires, among other things, the addition of a baffle to restrict the flow of electrons from the hollow cathode. This separates the plasma into two distinct regions,[12,13,14] -- the cathode region and the main discharge region. The cathode region is defined as the one containing the plasma that is outside of the hollow cathode but inside the cathode pole piece/baffle assembly. Proper thruster operation depends on the creation of primary electrons with sufficient energy to ionize the neutral propellant atoms, yet not so great that they produce a large number of doubly charged ions. For example, a hollow cathode, mercury ion thruster would typically operate with primary electrons having an energy in the 20 to 30 eV range. The creation of these primary electrons is accomplished by accelerating the electrons from the cathode region plasma into the main discharge region through a potential difference occurring in the proximity of the baffle aperture.[14] Since the primary electrons constitute an important aspect of electron bombardment thruster operation it is desirable to understand the processes on going in the baffle aperture region. In the past the design and optimization of the cathode pole piece/baffle assembly has been accomplished by physically performing a number of parametric variations.[12,13,15,16] This procedure is both time consuming and expensive, therefore it is desirable to minimize the number of variations required. The objective of this study has been to develop a theoretical model relating the baffle aperture area to the magnetic field strength and plasma

properties in this region, with the result that this model could be used as an aid in thruster design. Extensive Langmuir probing was undertaken to test the validity of the model. Much of the work accomplished under this task has been reported in Reference (11) which is included in Appendix B. What follows is an extension of that work reflecting somewhat different assumptions in the model.

Apparatus and Procedure

All experiments pertaining to this study were carried out on a 14 cm dia. radial field thruster. The thruster was equipped with the pole piece assembly shown schematically in Figure 23. For these tests the cathode pole piece outer diameter was held constant at 3.18 cm and the wall and baffle plate thicknesses were both 0.32 cm. The magnetic baffle assembly of Figure 23 provided separate control over the magnetic field strength in the aperture through the use of a 12 turn magnetic baffle solenoid. The magnetic coupling rods shown were made of soft iron and were of sufficient cross section to assure that the magnetic flux through the rods was well below the saturation point at the maximum solenoid current. Control of the magnetic field strength in the main discharge region was accomplished through the use of 8 radially oriented electromagnets. Since the cathode pole piece was part of the main thruster's magnetic circuit, increasing the current through the radial magnets increased the magnetic field strength in the aperture region as well as the main discharge region. However, changing the field strength in the aperature by using the baffle solenoid did not significantly change the magnetic field in the main discharge region. Magnetic flux densities in the center of the aperture ranging from 9×10^{-4} to 120×10^{-4} tesla could be established using either the baffle or the radial magnets.

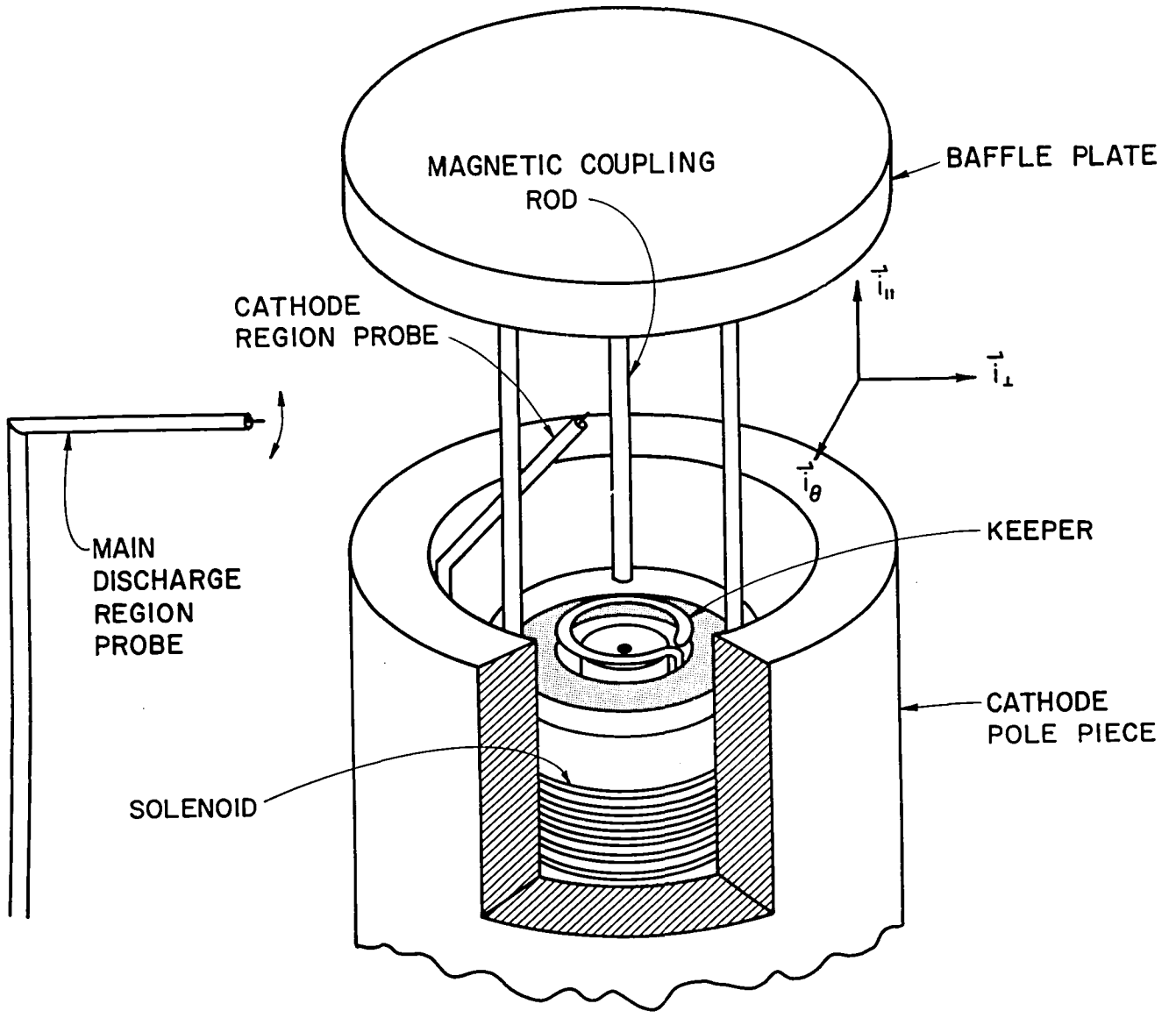

Figure 23. Cathode Pole Piece/Baffle Assembly

The pole piece/baffle geometry of Fig. 23 was chosen for this study because it tends to concentrate the magnetic field lines in the aperture region. A plot of the magnetic flux density as a function of the radial position measured from the thruster centerline through the aperture is given in Fig. 24 for various values of radial electromagnet current (I_R) and baffle electromagnet current (I_{BAF}). These magnetic field profiles were taken through the midpoint of the gap and they do show that the magnetic field is quite peaked in the aperture region.

Two cylindrical Langmuir probes were used to measure the plasma properties on each side of the aperture. The cathode region probe was a 0.076 cm diameter tantalum wire 0.076 cm long supported from a quartz tube insulator. It was positioned at a radial distance approximately equal to the keeper radius at the axial midpoint of the aperture gap. Because the plasma properties in the cathode region are fairly uniform the positioning of the cathode probe was not critical, but it was placed fairly near the centerline to assure that it was not in the region of plasma heating. The main discharge region probe was a 0.076 cm diameter tantalum wire 0.123 cm long again supported from a quartz tube insulator. The positioning of both probes can be seen in Figure 23. The main discharge region probe could also be swept radially through the aperture and several measurements of plasma properties as a function of the radial distance through the aperture were made. The probe traces were analyzed using a computer program developed by Beattie.[10]

Extensive plasma property measurements were made using the cathode region and main discharge region probes over a wide range of operating conditions. Three different baffle aperture areas were probed. A summary of the values of the important variables for each test is listed in Table II.

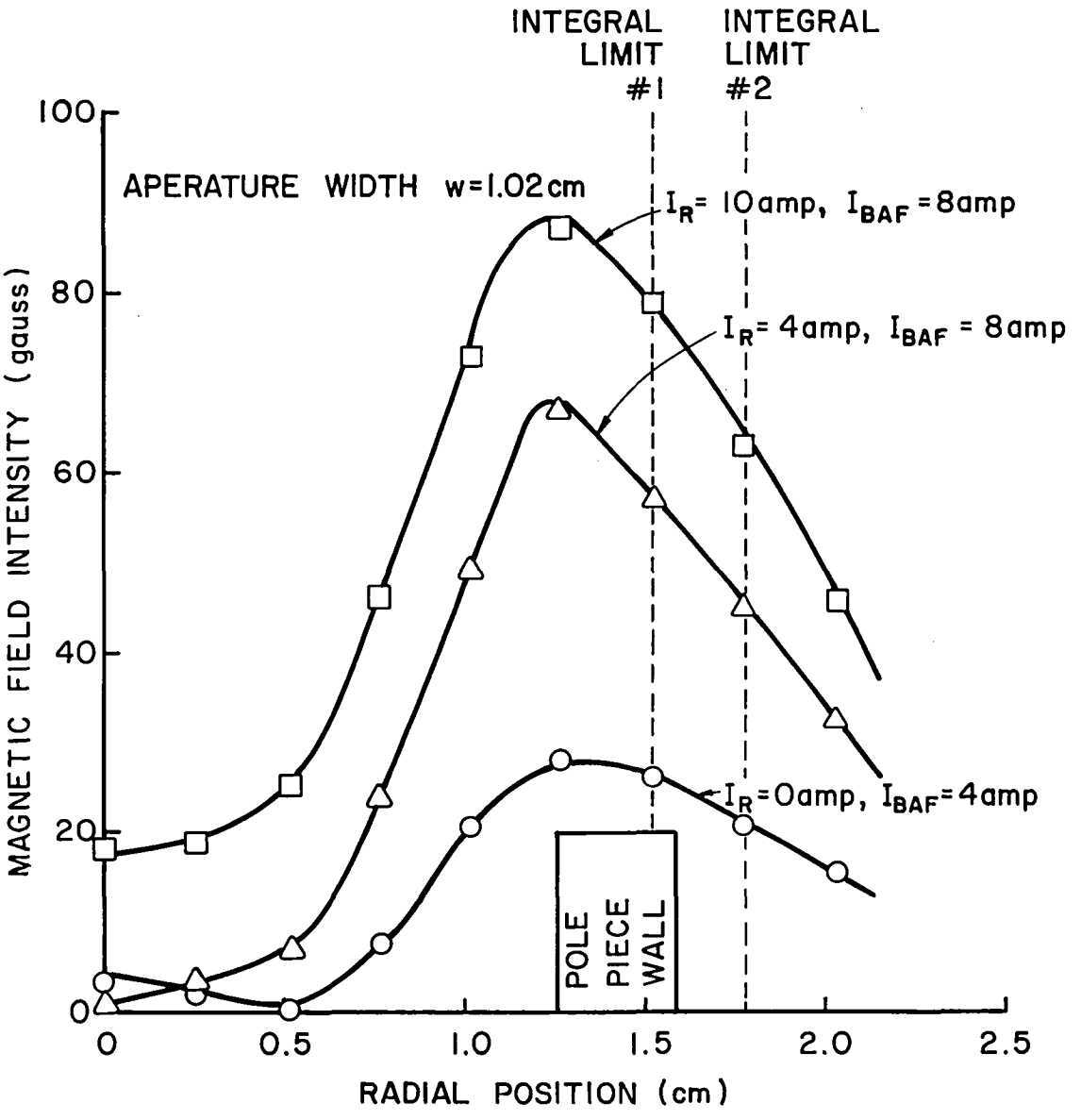

Figure 24. Magnetic Flux Density Through Aperture

Table II

Test Conditions

Test No.	Aperture Area [m^2]	Gap Spacing w[cm]	Main Flow Rate [mAeq]	Cathode Flow Rate [mAeq]	Arc Cur. [A]	Range of Peak Mag. Flux Density in Gap [10^{-4} tesla]
1	5.71×10^{-4}	0.64	650	165	4.50	9-111
2	6.85×10^{-4}	0.76	500	100	3.50	15-107
3	9.14×10^{-4}	1.02	500	100	3.50	13-88
4	9.14×10^{-4}	1.02	400	80	3.50	13-100

The screen and accelerator grid voltages were held at +1000 V and -500 V respectively for all tests. Before each test the aperture area was set by adjusting the gap spacing. During the data collection the arc current, cathode flow rate and main flow rate were maintained approximately constant while the magnetic field strength in the aperture was varied by changing the currents through the radial and baffle electromagnets, this in turn caused the discharge voltage to change. At each field strength setting two Langmuir probe traces were taken, one with the cathode region probe and the other with the main discharge region probe. The parameters describing the operating condition (arc current, arc voltage, beam current and keeper voltage) were also recorded.

Theory and Analysis

In a properly designed thruster two fields exist in the aperture region which influence the electron diffusion process there. Oriented across the aperture is a magnetic field and normal to it through the aperture is a steady electric field. The following paragraph gives a qualitative model proposed for the process of electron diffusion through the aperture.

The electrons which eventually form the discharge current are initially thermal electrons in the cathode regions with a relatively low temperature ($\sim$2 eV). They diffuse across the magnetic field lines under the influence of a potential gradient, a density gradient and a temperature gradient. The electrons are accelerated by the electric field, and they diffuse across the magnetic field lines by having collisions that change the position of their guiding centers.[17] The electrons lose little energy in these collisions since they are primarily elastic collisions where the fractional energy lost is of the order of the ratio of the electron mass to the mass of a neutral particle.[18] It might also be that some type of plasma turbulence facilitates this electron transport. The electrons continue to diffuse across magnetic field lines and gain energy from the electric field until they reach an energy at which inelastic collisions also become important. At this point several things can happen. Some of the electrons might undergo additional elastic collisions and escape from the aperture carrying with them the full amount of the energy gained from the electric field, i.e., these electrons leave as the so called primary electrons. Other electrons might undergo inelastic collisions and lose a significant portion of the energy just gained and leave the aperture region as thermal electrons.* This dumping of energy through inelastic collisions in the aperture region could explain qualitatively why the plasma glows noticeably brighter in the baffle aperture region than it does in the rest of the discharge chamber. Thus it appears possible that the discharge current through the aperture consists of both primary and Maxwellian electrons.

---

* Still other electrons might escape with their energy intact through the interaction of some type of plasma turbulence so they may also become primaries.

To derive a relationship between the baffle aperture area and the magnetic field and plasma properties in this region one can best start with the momentum equation[19]

$$m\frac{d\vec{v}}{dt} = -\frac{\vec{\nabla}P}{n} + e(\vec{E} + \vec{v} \times \vec{B}) - \nu_c m\vec{v} . \tag{1}$$

In this equation m and e are the electron mass and charge respectively, n is the electron number density, P is the electron pressure, $\vec{E}$ and $\vec{B}$ are the electric and magnetic field vectors respectively, ν_c is the average electron collision frequency and $\vec{v}$ is the average electron drift velocity. For the case where the average drift velocity is small compared to the electron thermal velocity and for steady state conditions Eqn. (1) can be written

$$ne\vec{\nabla}V - \vec{\nabla}P + \vec{j} \times \vec{B} - \frac{\nu_c m}{e}\vec{j} = 0. \tag{2}$$

Where the electron current $\vec{j} = ne\vec{v}$ and plasma potential gradient $\vec{\nabla}V = -\vec{E}$, have been defined and incorporated into Eqn (2). Now if a coordinate system that has its axes everywhere parallel or perpendicular to the magnetic field is defined, Eqn (2) can be written in component form as,

$$\text{Normal to } \vec{B} \text{ (radial)}: \quad en\nabla_\perp V - \nabla_\perp P - j_\theta B - \frac{m\nu_c}{e} j_\perp = 0 \tag{3a}$$

$$\text{Parallel to } \vec{B}: \quad en\nabla V_{\parallel} - \nabla_{\parallel} P - \frac{m\nu_c}{e} j_{\parallel} = 0 \tag{3b}$$

$$\text{Azimuthal}: \quad en\nabla_\theta V - \nabla_\theta P + j_\perp B - \frac{m\nu_c}{e} j_\theta = 0 \tag{3c}$$

Where the subscripts $\perp$, $\parallel$ and θ refer to the normal, parallel and azimuthal directions with respect to the magnetic field vector. For the experimental configuration here, these directions are defined in Figure 23.

Assuming there are no potential* or pressure gradients in the azimuthal direction Eqn. (3b) becomes,

$$j_{\parallel} = 0 \ . \tag{4}$$

Therefore, there is no net current flow parallel to the magnetic field. Equations (3a & b) can be solved simultaneously for the components of the current in azimuthal and normal directions to give,

$$j_{\theta} = - \frac{Be}{m\nu_c} j_{\perp} \ , \tag{5}$$

$$j_{\perp} = \frac{\frac{\nu_c e}{m} [ne\nabla_{\perp} V - \nabla_{\perp} P]}{\nu_c^2 + \omega_B^2} \ . \tag{6}$$

The quanity $\omega_B = \frac{eB}{m}$ is the electron cyclotron frequency. These equations are essentially the same as those given by Wells.[14] It can be seen from Eqn. (5) that if there is a current across the magnetic field lines from the main to cathode discharge region ($j_{\perp}$) then there must also be a current in the azimuthal direction (j_{θ}).

Equation (6) can be written in terms of the classical coefficient for electron diffusion across magnetic field lines D_C as,

$$j_{\perp} = D_C \left[\frac{ne^2}{kT} \nabla_{\perp} V - \frac{e}{kt} \nabla_{\perp} P\right] \tag{7}$$

where,

$$D_C = \frac{kT}{m} \left[\frac{\nu_c}{\nu_c^2 + \omega_B^2}\right] \ . \tag{8}$$

---

* Plasma oscillations leading to potential gradients in the azimuthal direction have been proposed as a mechanism for Bohm diffusion. However, we shall assume here that there are no steady state potential gradients, while maintaining that Bohm diffusion is still possible.

Now assuming the electron velocity distribution is Maxwellian, the electron pressure is related to the number density and temperature by,

$$P = n\,kT \tag{9}$$

so that Eqn. (7) becomes,

$$j_\perp = D_C\left[\frac{ne^2}{kT}\nabla_\perp V - e\nabla_\perp n - \frac{en}{T}\nabla_\perp T\right] . \tag{10}$$

Finally, making the notation change $\nabla_\perp \rightarrow \frac{d}{dr}$ Eqn.(10) can be written,

$$j_\perp = D_C\left[\frac{ne^2}{kT}\frac{dV}{dr} - e\frac{dn}{dr} - \frac{en}{T}\frac{dT}{dr}\right]. \tag{11}$$

The diffusion coefficient that appears in Eqn. (11) is that obtained from classical diffusion theory and is defined in Eqn. (8). For magnetic field strengths such that

$$\frac{\omega_B}{\nu_C} >> 1 \tag{12}$$

which is typical of the aperture region, the classical diffusion coefficient becomes,

$$D_C = \frac{kT\,m\nu_c}{e^2B^2} . \tag{13}$$

However, it has been found that a diffusion coefficient proportional to B^{-1} correlates better with experimental results obtained in ion thrusters.[20] This diffusion coefficient, first proposed by Bohm,[21] may be written as,

$$D_B = \frac{kT}{16eB} . \tag{14}$$

At this point in the analysis it was necessary to determine what form of the diffusion coefficient should be used. (i.e. whether Bohm or classical diffusion applies through the baffle aperture.) An attempt was made to determine experimentally an average value for the diffusion coefficient

through the aperture. To do this Eqn. (10) was solved for the electron diffusion coefficient across magnetic field lines to give,

$$D_{\perp} = j\left[\frac{ne^2}{kT}\frac{dV}{dr} - e\frac{dn}{dr} - \frac{en}{T}\frac{dT}{dr}\right]^{-1} . \qquad (15)$$

The diffusion coefficient appropriate to the experimental apparatus can be determined from Eqn. (15) provided the derivatives on the right hand side of this equation can be determined experimentally. The information required as input to this equation was obtained for a few cases by measuring the plasma properties at several radial positions through the aperture with a Langmuir probe. An example of the results obtained by doing this are given in Fig. 25 where the plasma potential is plotted as a function of radial position. This type of extensive data collection provides good approximations to the derivatives required by Eqn. (15). However, the amount of work required to implement this procedure over a wide variety of test conditions is prohibitive. The derivatives were therefore approximated as the change in the property through the aperture divided by the distance over which the change occurred, that is, the derivative dV/dr was approximated by $\Delta V/\Delta r$, etc. A typical example of the approximation of the potential gradient is shown in Fig. 25 as the dashed line. The approximation is seen to be fairly good and is typical of the results obtained for other test conditions. At very low magnetic flux densities (less than $\sim 20 \times 10^{-4}$ tesla) in the aperture this method tends to overestimate in the value of the derivative and this artificially lowers the calculated diffusion coefficient slightly. This is not a serious problem however since the magnetic field in the aperture of a normally operating thruster is generally well above this value. The advantage of this procedure is that it enables the experimenter to obtain satisfactory results with only two Langmuir probe measurements at each

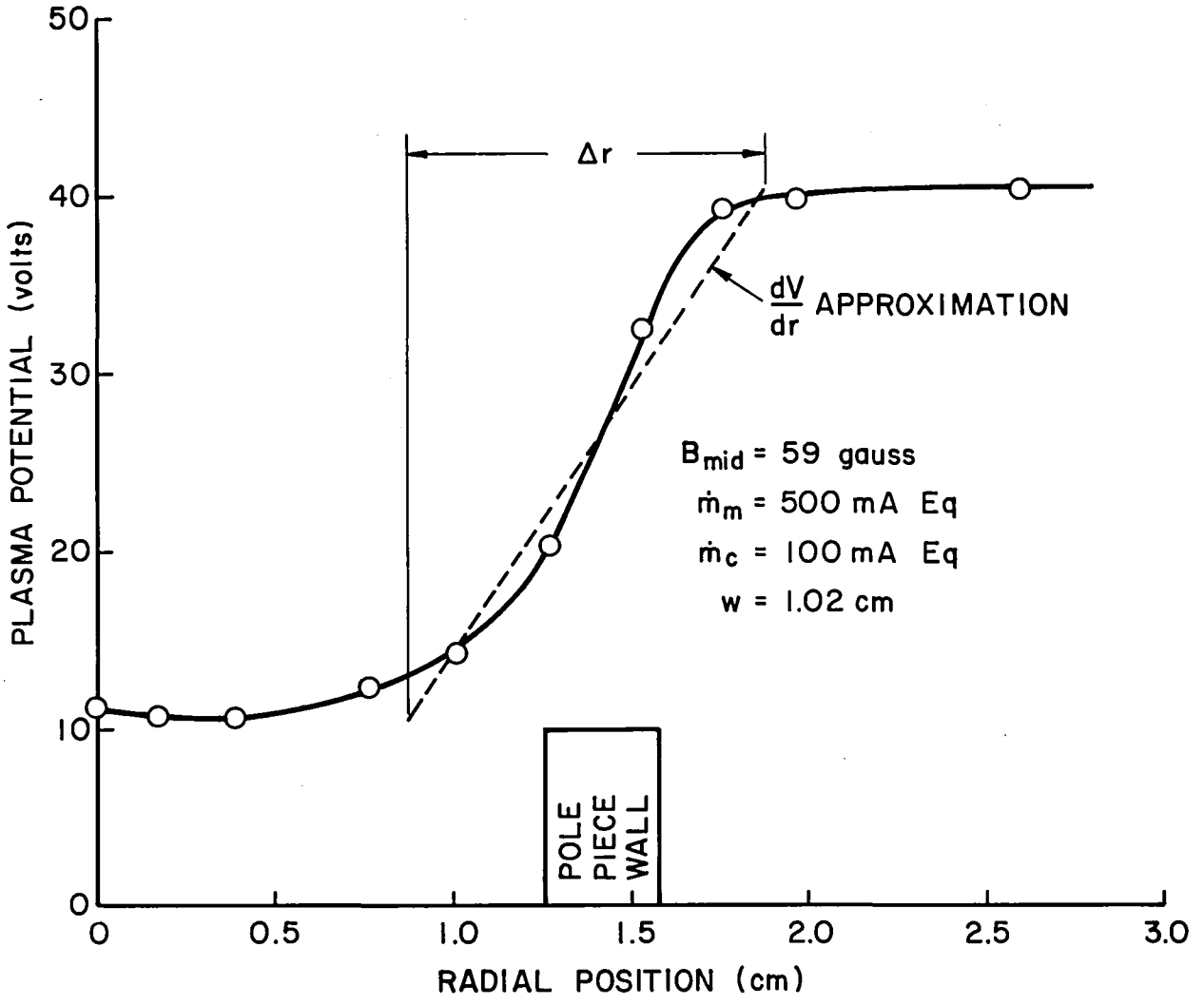

Figure 25. Typical Plasma Potential Profile Through Aperture

operating condition. With these approximations Eqn. (15) takes the form,

$$D_{\perp} = j\left[\frac{ne^2}{kT}\frac{\Delta V}{\Delta r} - e\frac{\Delta n}{\Delta r} - \frac{en}{T}\frac{\Delta T}{\Delta r}\right]^{-1} \tag{16}$$

where the distance Δr is taken to be equal to the aperture gap size w. The gap size is the distance from the downstream end of the cathode pole piece to the baffle plate (Fig. 23). It was assumed that the length of significant magnetic flux density through which the electrons had to diffuse to escape into the main discharge region was approximately the same as the distance over which the changes in plasma properties occurred. Further, it was assumed that this length of significant magnetic flux density was equal to the gap size. This led finally to the condition that the quantities Δr in Eqn. (16) are approximately equal to the gap size w*.

It must now be decided what values for the density (n) and temperature (T) should be used in Eqn. (15) since both of these quantities change as one passes through the aperture. Two different methods of assigning these parameters were investigated.

The first method assigns average values to the density and temperature through the aperture. These averages were defined according to the following equations,

$$n_{avg} = \frac{n_c + n_m}{2} \tag{17}$$

$$T_{avg} = \frac{T_c + \frac{1}{10}\left(9T_m + \frac{e}{k}\varepsilon_p\right)}{2} \tag{18}$$

where the subscripts "c" and "m" refer to the cathode and main discharge regions respectively and ε_p is the primary electron energy in eV. The

* This assumes that the potential, density and temperature changes all occur over the same size distance. However this isn't necessarily the case and a better calculation of the diffusion coefficient could be made if the distance over which each property change occurred was known.

average temperature was defined in the manner described by Eqn. (18) in an attempt to account for the presence of primary electrons at the main discharge side of the aperture.

The second method is based on an assumption suggested by Kaufman and Robinson.[22] The assumption is essentially that in traversing through the aperture from the cathode region to the main discharge region the density change occurs first while the potential and temperature are constant and then the potential and temperature changes occur while the density is constant.

Depending on which method is used Eqn. (16) becomes,

$$\text{Method 1:}\quad D_{\perp} = j\left[\frac{e^2 n_{avg}}{kT_{avg}}\frac{\Delta V}{\Delta r} - e\frac{\Delta n}{\Delta r} - \frac{en_{avg}}{T_{avg}}\frac{\Delta T}{\Delta r}\right]^{-1} \tag{19}$$

$$\text{Method 2:}\quad D_{\perp} = j\left[\frac{e^2 n_m}{k\,T_c}\frac{\Delta V}{\Delta r} - e\frac{\Delta n}{\Delta r} - \frac{en_m}{T_c}\frac{\Delta T}{\Delta r}\right]^{-1} \tag{20}$$

By utilizing the experimental data obtained in tests conducted with the test appartus described previously it should now be possible to determine diffusion coefficients from Eqns. (17) and (18) which are appropriate to the two methods which have been described. Diffusion coefficients evaluated in this way will be given later, but it is necessary to note now that the experimentally determined coefficients are better described by a Bohm model of the form

$$D_B = \frac{kT}{16eB\alpha}\ . \tag{21}$$

The coefficient α and the temperature T appearing in this expression will take on different values for the two methods, but the theoretical development continues in basically the same way.

Substituting Eqn. (21) for the diffusion coefficient in Eqn. (11) yields,

$$j = \frac{kT}{\alpha 16eB}\left[\frac{ne^2}{kT}\frac{dV}{dr} - e\frac{dn}{dr} - \frac{en}{T}\frac{dT}{dr}\right] \tag{22}$$

which can be rearranged to obtain

$$\alpha 16jBdr = endV - kT\,dn - kndT\ . \tag{23}$$

Integrating Eqn. (23) over the diffusion depth as suggested by Kaufman and Robinson[22] yields,

$$16\alpha \int jBdr = e\int ndV - k\int Tdn - k\int ndT\ . \tag{24}$$

Assuming now that there is negilible electron production in the aperture region so that the current is constant, the current density can be written as,

$$j(r) = \frac{I}{A(r)} \tag{25}$$

where A(r) is the area as determined by the magnetic field line at a distance r from the origin from which the electrons find immediate access to the main discharge region. For the particular pole piece geometry being considered experimentally here, the area A(r) is essentially constant through the aperture region so that Eqns. (24) and (25) combine to give,

$$A = \frac{16\ \alpha\ I \int Bdr}{e\int ndV - k\int Tdn - k\int ndT}\ . \tag{26}$$

In this equation "A" represents the area which the electrons can flow through just as they reach the critical field line which takes them into the main discharge region. For the geometry studied experimentally here it also corresponds to the physical area of the aperture. Equation (26) then is the desired theoretical relationship between the aperture area and the magnetic field strength and plasma properties through the gap. In order to calculate the aperture area from Eqn. (26) the integrals in the

denominator on the right hand side of the equation must be evaluated. This can be done using either of the two methods discussed previously.

Results and Discussion

It was considered important in this study to determine the diffusion coefficient that seemed to describe the electron flow through the baffle most accurately. This was done by computing the diffusion coefficient from Eqns. (19 and 20) using experimentally determined plasma property data. The results obtained using Eqn. (20) (Method 2) to determine the diffusion coefficient are given in Figure 26 where this coefficient is plotted against the magnetic flux density in the aperture. In this case it is apparent that the experimental diffusion coefficient agrees with Bohm theory (Eqn. 21) without the need for any correction factor ($\alpha = 1$). The diffusion coefficient determined from Eqn. (20) agreed with Eqn. (21) for $\alpha = 1$ to within an average of about 30%. For Method 1 the correction factor (α) was determined by dividing the Bohm diffusion coefficient (Eqn. 21) by Eqn. (19) for all of the test results. This ratio determines then for each case what correction factor is needed to make the Bohm diffusion coefficient agree with Eqn. (19). This correction factor is plotted against the magnetic field strength at the center of the aperture in Fig. 27, where the average and standard deviation are indicated by the solid and dashed lines respectively. This figure shows that the coefficient takes on a constant value of 2.6 to with $\pm$ 35% over all test conditions. Regardless of the method used in the work the predictions of the classical diffusion theory were at least an order of magnitude too low. Therefore it appears that either Method 1 or 2 could be used to model the electron diffusion through the aperture, although Method 2 would seem preferable on the grounds that it doesn't require the correction factor used in Method 1.

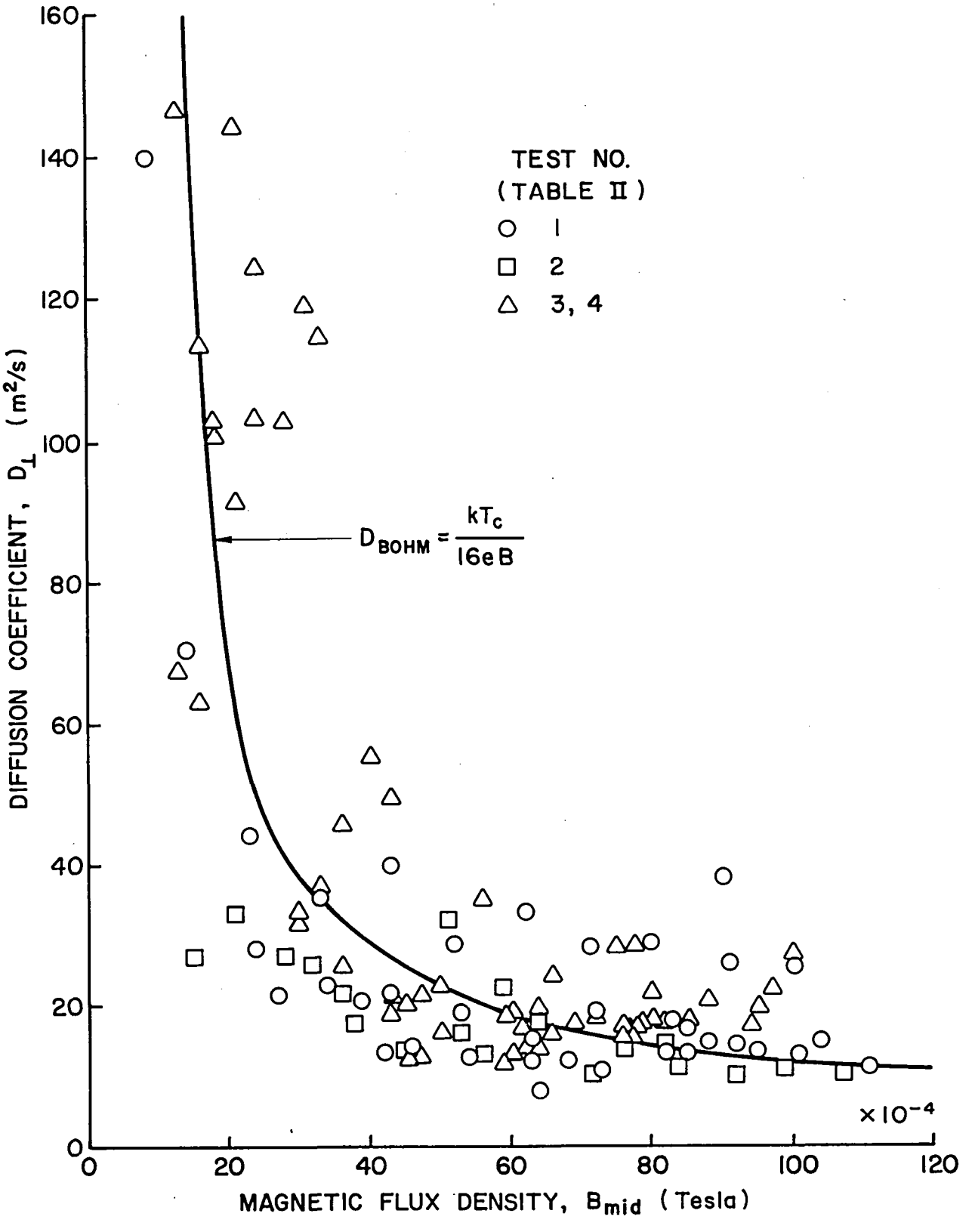

Figure 26. Diffusion Coefficient Computed Using Method 2

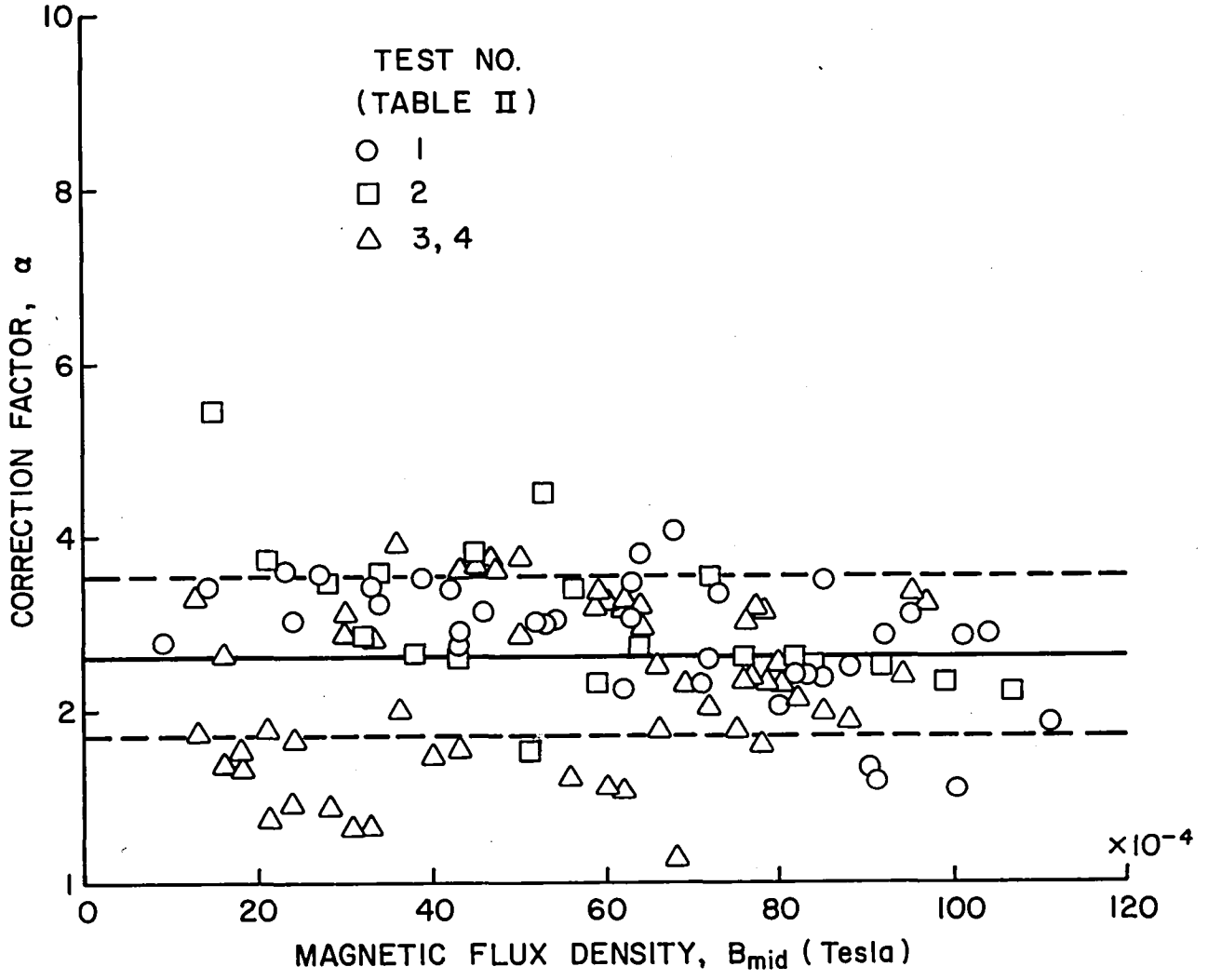

Figure 27. Correction Factor for Method 1

It is noteworthy to point out here that the dominant reasons why the factor of 2.6 is needed in Method 1 while it is not in Method 2 is that Method 2 employs the cathode electron temperature in the Bohm diffusion expression (Eqn. 21) while Method 1 employs the average temperature and the mean value of the ratio of these two temperatures is about 2.6.

Aperture Area Determined Using Method 1

As described previously, this method assigns average values to the plasma properties through the aperture. It also requires the use of the correction factor α so that the aperture area is given by,

$$A = \frac{16\ \alpha\ I \int Bdr}{e \int ndV - k \int Tdn - k \int ndT} \quad . \tag{28}$$

The use of average quantities allows the integrals in the denominator of Eqn. (28) to be approximated as,

$$\begin{aligned} \int ndV &\simeq n_{avg}\ \Delta V \\ \int Tdn &\simeq T_{avg}\ \Delta n \\ \int ndT &\simeq n_{avg}\ \Delta T \end{aligned} \tag{29}$$

where n_{avg} and T_{avg} are defined in Eqns. (17) and (18) respectively. Therefore we can write Eqn. (28) as,

$$A = \frac{16\ \alpha\ I \int Bdr}{en_{avg}\ \Delta V - kT_{avg}\Delta n\ - kn_{avg}\Delta T} \quad . \tag{30}$$

Finally for the geometry of the pole piece used in this study it was possible to make the following approximation for the integral of the magnetic field through the aperture,

$$\int Bdr = B_{mid}\Delta r \tag{31}$$

where B_{mid} is the magnetic flux density at the midpoint of the aperture

and Δr is the aperture gap w. To determine the validity of this approximation both the integral and the approximation were evaluated for several experimental cases. The results are shown for $\int B dr$ plotted against $B_{mid}\Delta r$ in Fig. 28. In evaluating the integral, the integration is assumed to take place over the distance from the centerline of the cathode to the critical magnetic field line. There is some difficulty however in knowing exactly the location of the critical magnetic field line. For this reason the magnetic field integrals were evaluated up to the two different limits shown in Fig. 24 which were observed from iron filings maps to bracket the range of uncertainty. The results of these calculations (Figure 28) suggest that the approximation of Eqn. (31) is sufficiently accurate for this work. Certainly it is accurate to within the uncertainty for determining the location of the critical magnetic field line. With this approximation then Eqn. (28) can be written as,

$$A = \frac{16\ \alpha\ I\ B_{mid}\Delta r}{en_{avg}\Delta V - kT_{avg}\Delta n - kn_{avg}\Delta T} \quad . \tag{32}$$

In an effort to make Eqn. (32) easier to apply for someone designing a thruster it was noticed that to a first approximation the ratio $en_{avg}\Delta V / kT_{avg}\Delta n$ was constant. This constancy is discussed in some detail in Reference 11. Its average value was very close to 4 and was constant to within $\pm 46\%$. Therefore one can use the approximation,

$$kT_{avg}\Delta n \simeq \frac{1}{4}\, en_{avg}\Delta V \quad . \tag{33}$$

The data also show that the temperature gradient term ($kn_{avg}\Delta T$) contributes a negligible effect in Eqn. (32) so it can be rewritten

$$A \simeq \frac{16\,\alpha\ I\ B_{mid}\Delta r}{\frac{5}{4}\, en_{avg}\Delta V} \quad . \tag{34}$$

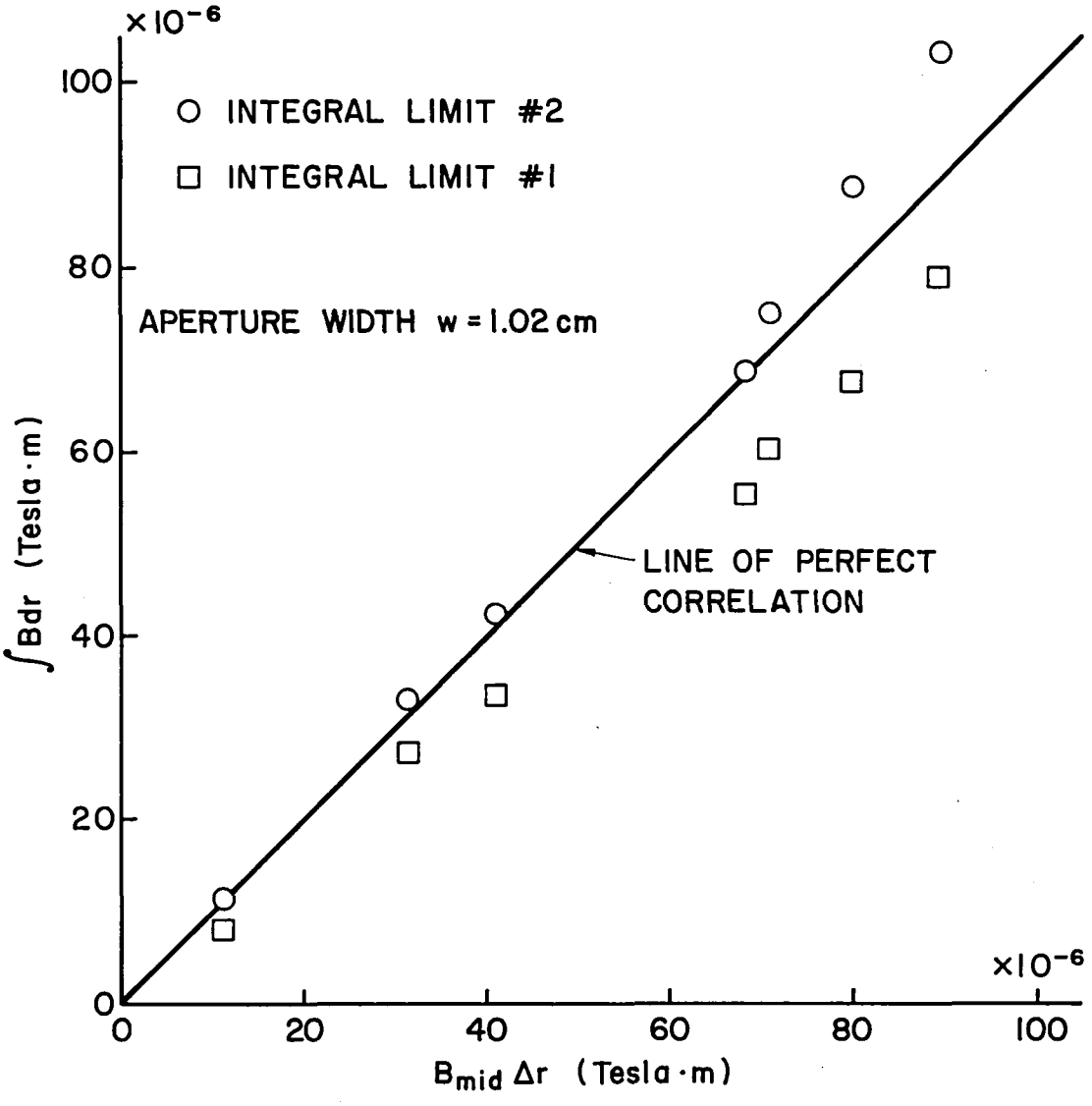

Figure 28. Comparison of Measured and Approximate Magnetic Field Integals

To test Eqn. (34) experimentally the plasma properties on both sides of the aperture were measured for a wide variety of magnetic field strengths in the gap for three different aperture configurations described in Table II. The results of these tests are given in Reference (11) were the aperture area calculated from Eqn. (34) is plotted against the magnetic flux density at the center of the gap. These results are summarized in Fig. 29 where the mean values and standard deviations of the areas calculated using Eqn. (34) are plotted against the measured aperture areas. The mean calculated values are observed to be relatively close to the actual areas although standard deviations of as high as 45% are observed in some of the data.

Aperture Area Determined Using Method 2.

This method makes use of the assumption[22] that in going through the aperture the density change occurs first while the potential and temperature are constant and then the potential and temperature change while the density is constant. Experimental measurement of plasma properties through the aperture, of which Fig. 30 is an example, suggest that this is probably an acceptable assumption although the physical basis for this behavior is not apparent. Ideally the density change should occur at lesser radii for the assumption to be completely valid. Using this assumption the integrals in the denominator of Eqn. (27) can be approximated to give,

$$A = \frac{16\ I \int B dr}{e n_m \Delta V - k T_c \Delta n - k n_m \Delta T} . \qquad (35)$$

Now if the approximation of Eqn. (31) is used Eqn. (35) becomes,

$$A = \frac{16\ I\ B_{mid} \Delta r}{e n_m \Delta V - k T_c \Delta n - k n_m \Delta T} . \qquad (36)$$

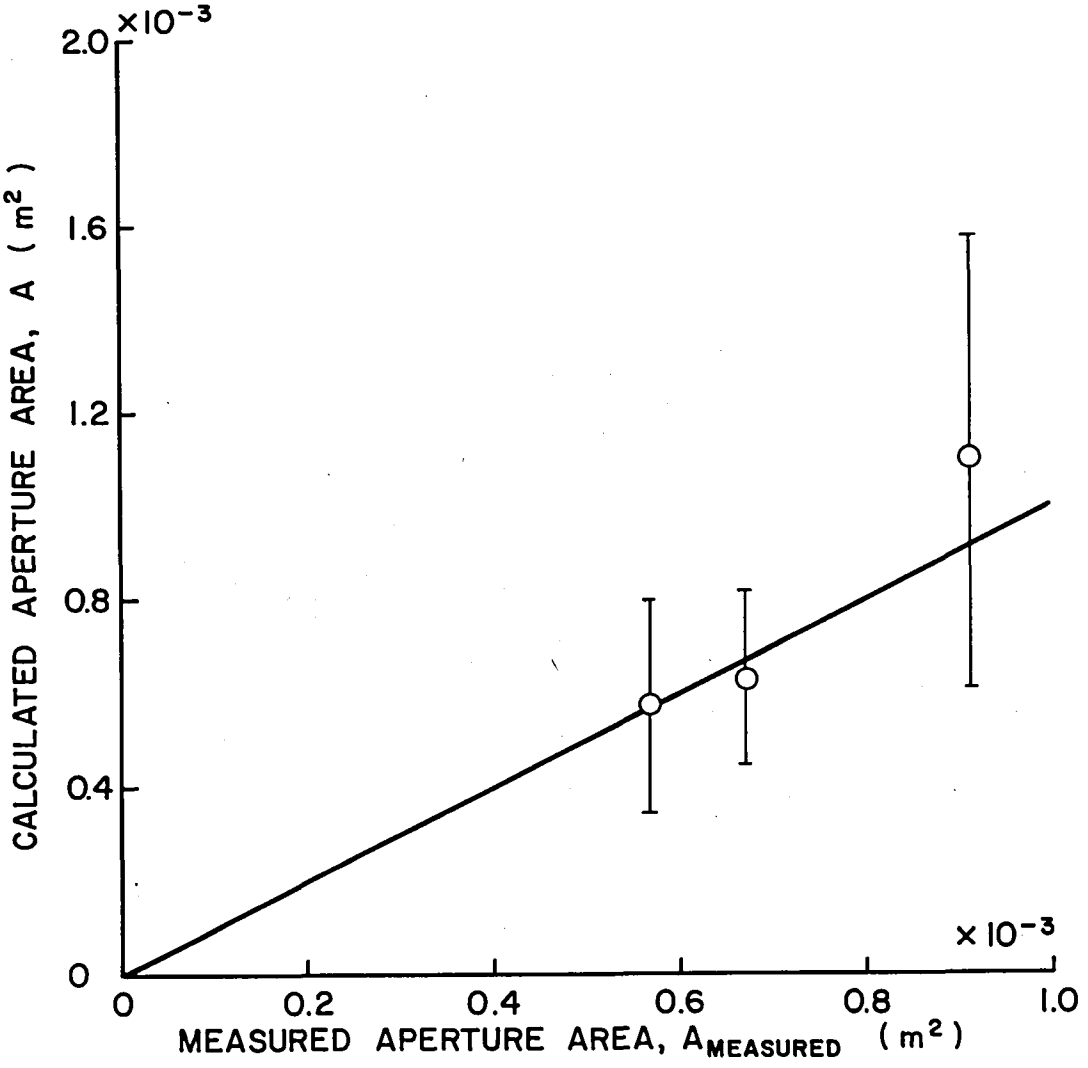

Figure 29. Comparison of Calculated and Measured Aperture Areas (Method 1)

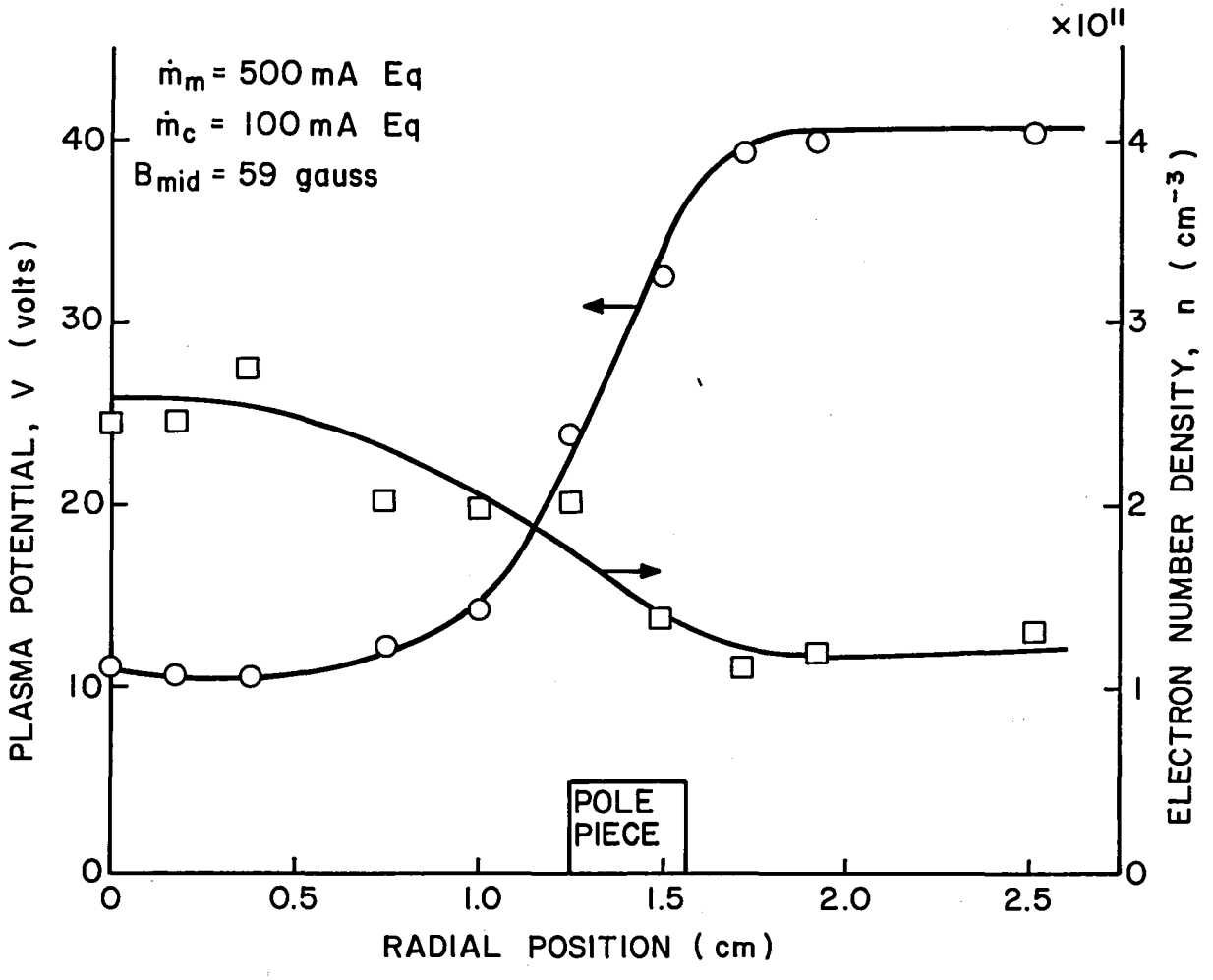

Figure 30. Potential and Density Variations Through the Aperture

The data collected in the tests of Table II has been used in this equation to determine the calculated aperture area. The mean values of these calculated areas along with standard deviations obtained from several tens of tests at the various test conditions of Table II is plotted against measured aperture area in Fig. 31. The circular symbols correspond to the results obtained using Eqn. (36) as written. The difference in temperatures, ΔT, required as input to the equation was taken as the difference in Maxwellian temperature across the aperture in this case. The square symbols correspond to the results obtained neglecting the temperature gradient term. Clearly the temperature gradient term, defined in this manner, exhibits a small effect. The correlation obtained between the calculated and measured values using Method 2 is about as good as that obtained with Method 1.

Equation (35) can also be used to solve for the value of the magnetic field integral required to effect operation at a specified aperture area given the plasma properties on either side of the gap, the current flow through the aperture and its area. To facilitate calculation of this quantity Eqn. (35) was solved for the integral to yield,

$$\int Bdr = \frac{en_m\Delta V - kT_c\Delta n - kn_m\Delta T}{16\ (I/A)} \quad . \tag{37}$$

The magnetic field integral calculated from Eqn. (37) is plotted against the measured integral determined using $B_{mid}\Delta r$, in Fig. 32. The dashed line represents a linear least squares curve fit of the data and the line of perfect correlation is indicated by the solid line. Again the agreement between calculated and measured values as indicated by the proximity of these two lines is quite good. Figure 32 does show however that there is considerable scatter in the actual data about the mean values represented by the lines.

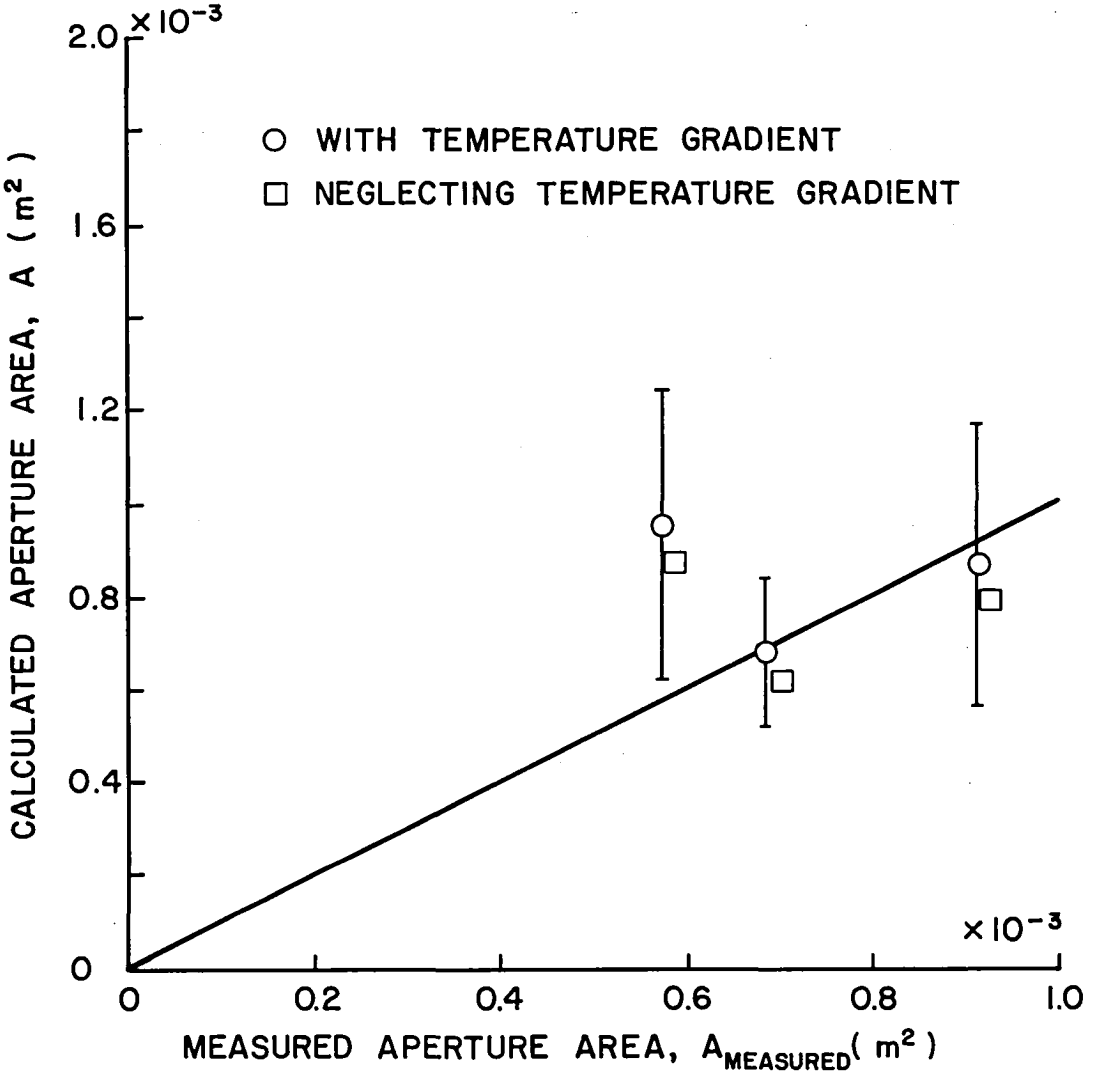

Figure 31. Comparison of Calculated and Measured Aperture Areas (Method 2)

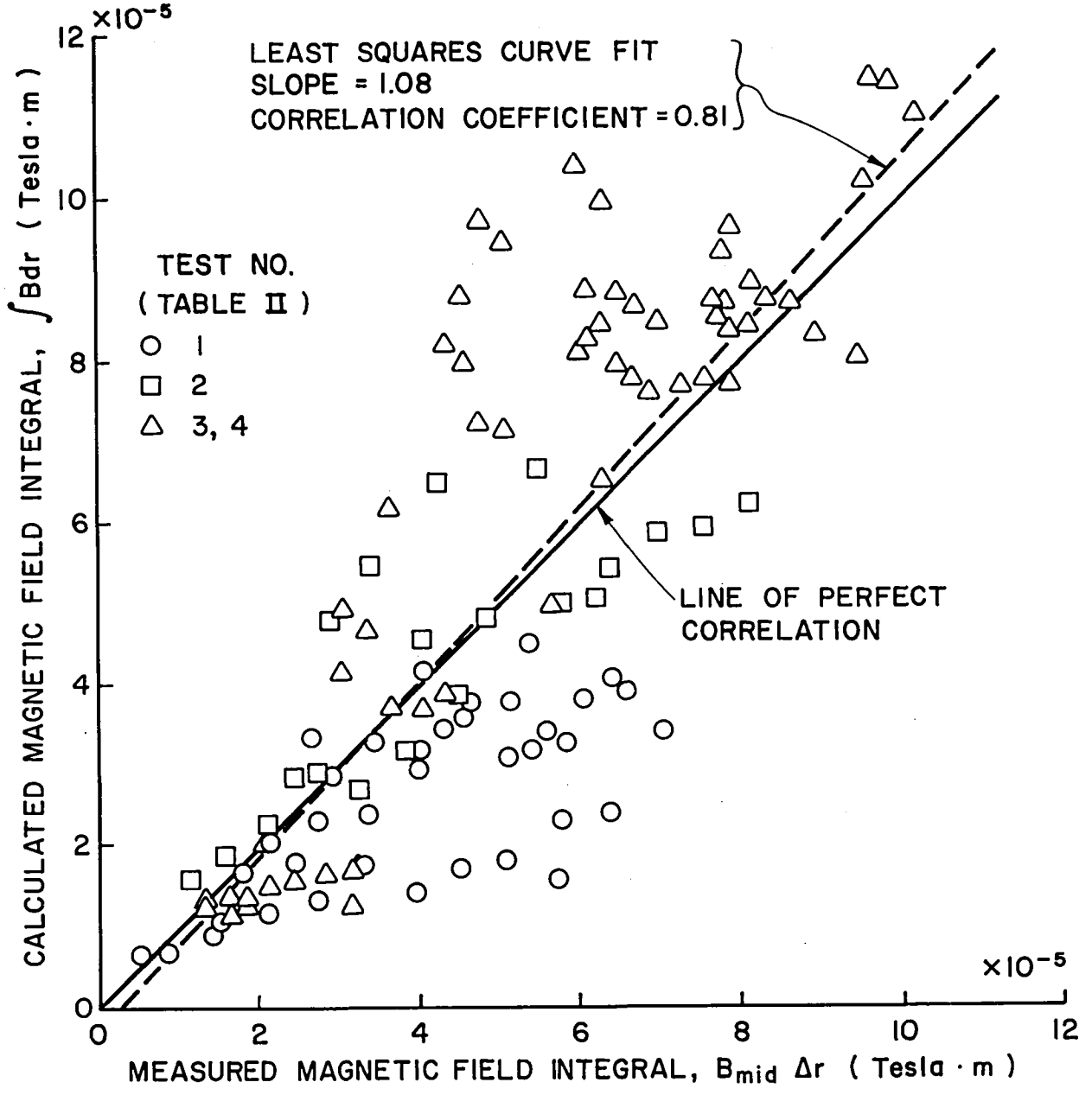

Figure 32. Comparison of Measured and Calculated Magnetic Field Integrals

Conclusions

1. The diffusion of electrons through the aperture region can be described by some form of the Bohm diffusion coefficient. The form of the diffusion coefficient which agrees with experimental results depends on how the values for the plasma parameters in the aperture are assigned. If average values are used, then a correction factor of 2.6 must be applied to the Bohm diffusion coefficient to make it agree with the experimental results. However, if the assumptions of Method 2 are made then the Bohm diffusion theory agrees with the experiments without the need for a correction factor.
2. Classical theory underestimates the diffusion coefficient by at least an order of magnitude.
3. Given the magnetic field and plasma properties in the aperture region as inputs to the theory, calculated aperture areas agreed with measured values to within an accuracy of about $\pm$45% for both methods.
4. It is also possible to calculate the magnetic field integral through the aperture required to effect operation at a given current level for a given aperture area and specified plasma properties.

REFERENCES

1. Aston, G. and P. Wilbur, "The Screen Hole Plasma Sheath of an Ion Accelerator System," AIAA Paper 79-2114, Nov. 1979.

2. Kerslake, W. R. and Pawlik, E. V., "Additional Studies of Screen and Accelerator Grids for Electron-Bombardment Ion Thrusters," NASA TN-D-1411, Aug. 1963.

3. Hyman, J. Jr., Eckhardt, W. O., Knechtli, R. C. and Buckey, C. R., "Formation of Ion Beams from Plasma Sources: Part I," AIAA Journal, Vol. 2, No. 10, Oct. 1964, pp. 1739-1748.

4. Coupland, J. R., Green, T. S., Hammond, D. P. and Riviere, A. C., "A Study of Ion Beam Intensity and Divergence Obtained from a Single Aperture Three Electrode Extraction System," Rev. Sci. Instrum., Vol. 44, No. 9, Sept. 1973, pp. 1258-1270.

5. Grisham, L. R., Tsai, C. C., Whealton, J. H. and Stirling, W. L., "Effect of Emission Aperture Shape upon Ion Optics," Rev. Sci. Instrum., Vol. 48, No. 8, Aug. 1977, pp. 1037-1041.

6. Langmuir, I., "The Interaction of Electron and Positive Ion Space Charges in Cathode Sheaths," Phys. Rev., Vol. 33, June 1929, pp. 954-990.

7. Siegried, D. S. and P. J. Wilbur, "Studies on an Experimental Quartz Tube Hollow Cathode," AIAA Paper No. 79-2056, Nov. 1979.

8. Kerslake, W. R. and S. Domitz, "Neutralization Tests on the SERT II Spacecraft," AIAA Paper No. 79-2064, Nov. 1979.

9. Kerslake, W. R., et al., "SERT II: Mission, Thruster Performance, and In-Flight Thrust Measurement," J. Spacecraft and Rockets, V. 8, No. 3, March 1971, pp. 213-224.

10. Beattie, J. R., "Numerical Procedure for Analyzing Langmuir Probe Data," AIAA Journal, V. 13, No. 7, July 1975, pp. 950-952.

11. Brophy, J. R. and P. J. Wilbur, "Electron Diffusion through the Baffle Aperture of a Hollow Cathode Thruster," AIAA Paper No. 79-2060 Nov. 1979.

12. Poeschel, R. L., Ward, J. W. and Knauer, W., "Study and Optimization of 15-cm Kaufman Thruster Discharges," AIAA Paper No. 69-257, March 3-5, 1969.

13. Palumbo, G., et al., "Effect of Geometry and Field Inside the Pole Piece in an Electron Bombardment Thruster, "AIAA Paper No. 70-1082, Aug. 31 - Sept. 2, 1970.

14. Wells, A. A., "Current Flow Across a Plasma 'Double Layer' in Hollow Cathode Ion Thruster," AIAA Paper No. 72-418, April 17-19, 1972.

15. King, H. J., Poeschel, R. L. and Ward, J. W., "A 30-cm Low-Specific Impulse, Hollow Cathode Mercury Thruster," AIAA Paper No. 69-300, March 3-5, 1969.

16. Bechtel, R. T., "Performance and Control of a 30-cm Dia. Low-Impulse Kaufman Thruster," AIAA Paper No. 69-238, March 3-5, 1969.

17. McDaniel, E. W., Collision Phenomena in Ionized Gases, Wiley and Sons, Inc., New York, 1964, Ch. 4.

18. Massey, H. W. W. and Burhop, F. H. S., Electronic and Ionic Impact Phenomena, Oxford University Press, London, 1956.

19. Uman, M. A., Introduction to Plasma Physics, McGraw-Hill, 1964, p. 168.

20. Longhurst, G. R., "The Diffusion and Collection of Electrons in Ion Thrusters," in "Mercury Ion Thruster Research - 1977" ed. P. J. Wilbur, NASA CR-135317, Dec. 1977.

21. Bohm, D., et al., "The Use of Probes for Plasma Exploration in Strong Magnetic Fields," Characteristics of Electrical Discharges in Magnetic Fields, Chap. 2, ed. A. Guthrie and R. K. Wakerling, McGraw-Hill, New York, 1949.

22. Kaufman, H. R. and Robinson, R. S., "Plasma Processes in Inert Gas Thrusters," AIAA Paper No. 79-2055, Oct. 30 - Nov. 1, 1979.

APPENDIX A

SPHERICAL PROBE TRACE ANALYSIS

Graeme Aston

Plasma conditions inside the ion source used for the screen hole sheath study and the region downstream of the SERT II thruster with high voltage off are such that the Debye length at typical operation conditions is approximately 0.5 mm or greater. This fairly large Debye length necessitates the use of a thick sheath Langmuir probe analysis. For both studies spherical probes are used. A typical spherical probe trace obtained in these studies is shown in Figure A-1. This probe trace may be analyzed in the following way.

In the electron retarding region the electron current to the probe is given by

$$\text{Ln } I = AV + B \ . \tag{A-1}$$

While in the saturation region the electron current for a thick sheath spherical probe is described by

$$I = CV + D \ . \tag{A-2}$$

Substituting Eqn. A-2 into Eqn. A-1 and rearranging gives

$$I = \left(D - \frac{CB}{A}\right) + \frac{C}{A} \text{Ln } I. \tag{A-3}$$

Here, A is the inverse of the electron temperature (eV) which may be obtained from the slope of a plot of the retarding region of the trace on semilog graph paper. Also, C is the slope of the saturation region of the original probe trace, which is linear and is a measure of the conductance of the plasma. Both B and D may be obtained once A and C are known by solving Eqns. (A-1) and (A-2) at any current-voltage point in each

region of the original probe trace. Having found the constants A, B, C and D the transcendental Eqn. (A-3) may be solved iteratively to obtain the electron saturation current I_{sat} and either Eqn. (A-1) or (A-2) may be used to give the plasma potential V_p. These results may be used to determine the electron density n_e, by using the following equations.

In the retarding region

$$n_e = 2.969 \times 10^{12} \frac{I_{sat}}{a^2\sqrt{T_e}} \ m^{-3} \qquad \text{(A-4)}$$

In the saturation region

$$n_e = 2.969 \times 10^{12} \cdot C \cdot \frac{\sqrt{T_e}}{a^2} \ m^{-3} \ . \qquad \text{(A-5)}$$

Here, T_e is the Maxwellian electron temperature in eV, while a is the probe radius in meters. The values of electron density computed from Eqns. (A-4) and (A-5) agree to within 20% in data analyzed to date.

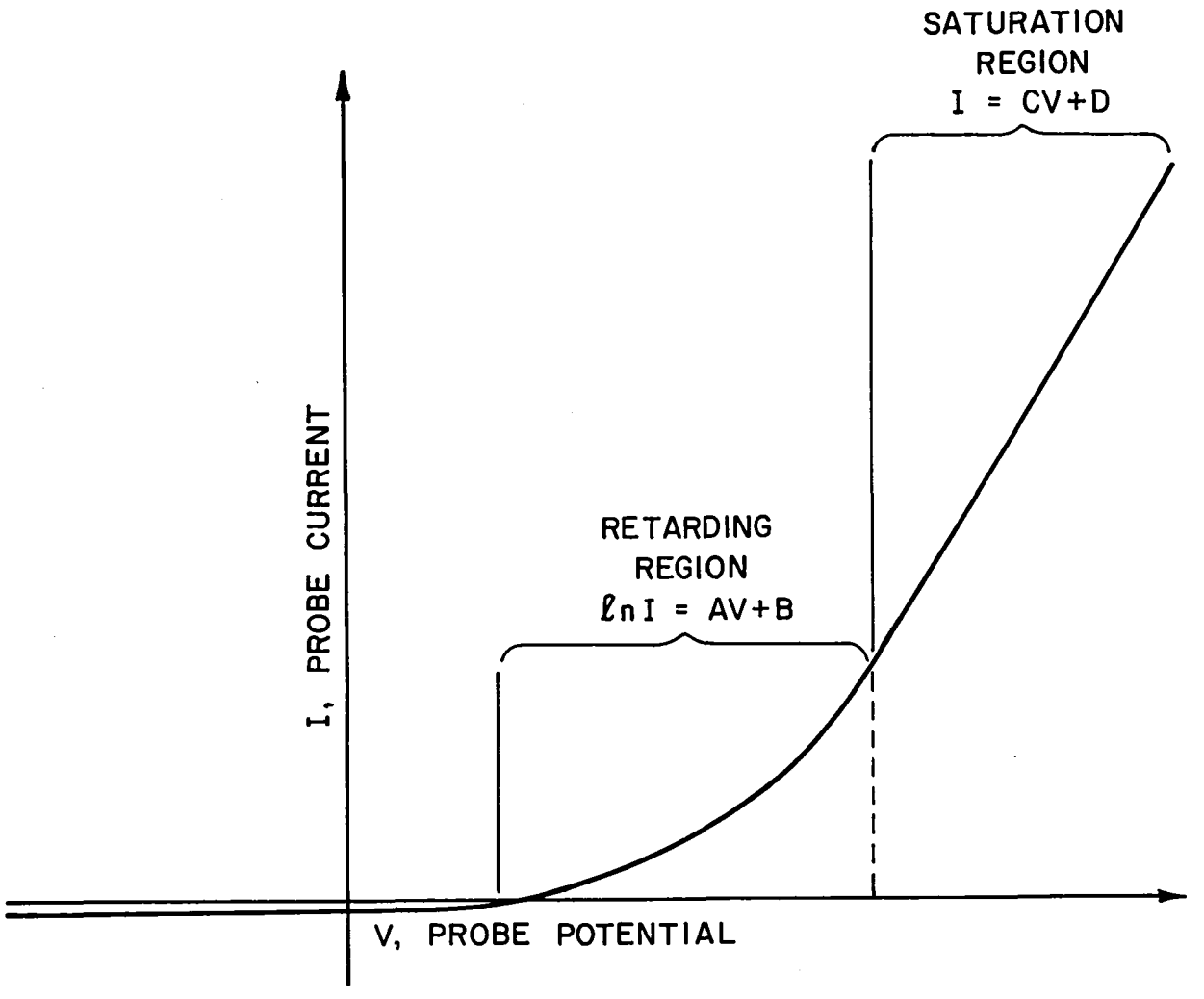

Figure A-1. Typical Thick Sheath Spherical Probe Trace

APPENDIX B

Results obtained during the past year under the subject grant which were reported at the

Princeton/AIAA/DGLR 14th
International Electric
Propulsion Conference.

Paper 79-2054 - Plasma Property and Performance Prediction for Mercury Ion Thrusters

Paper 79-2056 - Studies on an Experimental Quartz Tube Hollow Cathode

Paper 79-2060 - Electron Diffusion through the Baffle Aperture of a Hollow Cathode Thruster

Paper 79-2062 - A Model for Nitrogen Chemisorption in Ion Thrusters

Paper 79-2114 - The Screen Hole Plasma Sheath of an Ion Accelerator System

SPONSORED BY:
PRINCETON UNIVERSITY CONFERENCE
AMERICAN INSTITUTE OF AERONAUTICS AND ASTRONAUTICS (AIAA)
DEUTSCHE GESELLSCHAFT FUR LUFT-UND RAUMFAHRT (DGLR)

79-2054
Plasma Property and Performance Prediction for Mercury Ion Thrusters

G. R. Longhurst and P. J. Wilbur, Colorado State University, Fort Collins, Colo.

PRINCETON/AIAA/DGLR 14th INTERNATIONAL ELECTRIC PROPULSION CONFERENCE

Oct. 30-Nov. 1, 1979/Princeton, N.J.

PLASMA PROPERTY AND PERFORMANCE PREDICTION FOR MERCURY ION THRUSTERS*

Glen R. Longhurst** and Paul J. Wilbur†
Colorado State University
Fort Collins, Colorado 80523

Abstract

The discharge chambers of mercury ion thrusters are modelled so the principal effects and processes which govern discharge plasma properties and thruster performance are described. The conservation relations for mass, charge and energy when applied to the Maxwellian electron population in the ion production region yield equations which may be made one-dimensional by the proper choice of coordinates. Solutions to these equations with the appropriate boundary conditions give electron density and temperature profiles which agree reasonably well with measurements. It is then possible to estimate plasma properties from thruster design data and those operating parameters which are directly controllable. By varying the operating parameter inputs to the computer code written to solve these equations, performance curves are obtained which agree quite well with measurements.

Nomenclature

A	Surface area (m^2)
B	Magnetic flux density (T)
D	Electron diffusivity (m^2/s)
d	Diameter (m)
E	Electron kinetic energy (j)
e	Electron charge (1.6×10^{-19} coul)
$F_{z'}$	Divergence drift force in z' direction (N)
f	Maxwellian electron velocity distribution function
g	Maxwellian electron energy distribution function
I	Electric current (A)
K	Electron thermal conductivity (w/m)
k	Boltzmann's constant (1.38×10^{-23} J/°k)
L	Axial length of discharge chamber (m)
M	Particle Mass (kg)
N	Number of particles in control volume
n	Particle number density (m^{-3})
P	Reaction rate factor for primary electrons (m^3/s)
p	Pressure (Pa)
Q	Reaction rate factor for Maxwellian electrons (m^3/s)
q	Ion charge (coul.)
R	Radius (m)
r	Radial location in cylindrical geometry (m)
r'	Radial location in magnetic field geometry (m)
T	Temperature (°k)
t	Time (s)
V	Potential (V)
V	Volume of ion production region (m^3)
v	Velocity (m/s)
W	Electron kinetic energy per Maxwellian electron (J)
z	Axial location in cylindrical geometry (m)
z'	Axial location along magnetic field line (m)
Γ	Particle flux $(m^2s)^{-1}$
η	Propellant utilization fraction
θ	Azimuthal location in either coordinate system (radian)
θ_a	Angle between magnetic field and anode (radian)
μ	First adiabatic invariant (J/T)
ν	Effective electron collision frequency $(s)^{-1}$
ν_i	Ionization frequency per Maxwellian electron $(s)^{-1}$
ρ_D	Discharge loss in ion production region (ev/ion)
σ	Reaction cross section (m^2)
τ	Primary electron thermalization rate per Maxwellian electron $(s)^{-1}$
τ_e	Effective period between electron collisions (s)
ϕ	Grid open area fraction
ω	cyclotron frequency (radian/s)

Subscripts

a	Anode or virtual anode
ag	Accelerator grid
b	Upstream end or baffle region
B	Bohm
c	Cathode or cathode region
cv	Control volume
e	Electron
i	Ion
j	Index pertaining to state before a collision
k	Keeper
L	Larmor
m	Maxwellian electron
n	Pertaining to neutral propellant
p	Primary electron
s	Plasma sheath
sg	Screen grid
x	pertaining to electron collection
α	Atom
β	Beam
ϕ	Plasma
+	Single ion
++	Double ion
$\perp$	Perpendicular to magnetic field
0	Reference location
1	Neutral ground state mercury
2	6^3P_0 metastable state mercury
3	6^3P_2 metastable state mercury
4	$6^2S_{\frac{1}{2}}$ singly ionized state mercury
5	5^1S_0 doubly ionized state mercury
6	Lumped state mercury

Superscripts

i	Index pertaining to state after a collision
*	Averaged over control volume

* Work performed under NASA Grant NGR-06-002-112.

** Research Assistant, Dept. of Mechanical Engineering, presently at EG&G Idaho, Idaho Falls, Idaho.

† Professor, Dept. of Mechanical Engineering, Member AIAA.

Introduction

The investigation of ion thruster performance and the phenomena and conditions governing it has been ongoing for many years. Perhaps the most significant insights to this problem were given by Knauer, et al.[1] and by Masek.[2] Subsequent models to calculate thruster performance have relied to a large extent on estimates or measurements of one or more plasma properties. The need for a relatively simple, tractable model which can provide plasma property and thruster performance data from only those parameters controlled directly by the thruster designer or operator has motivated this investigation.

What follows is an analysis of the discharge in terms of the processes which appear to govern it. These processes are evident mainly through their effects on plasma properties. Because of uncertainties attendant in reducing Langmuir probe data from which these properties are determined, it is appropriate to neglect many minor effects in the analysis and concentrate on the first order effects. Before applying the conservation laws to obtain the predictive equations, the factors contributing to these effects will be discussed.

Ion Production Region

It has been observed[3,4,5] that virtually all of the ionization in the discharge chamber is done within the region bounded by the surface of revolution of the innermost magnetic field line to intersect the anode. That region is therefore called the ion production region. It is shown schematically in Fig. 1. The magnetic surface forming the lateral boundary of the ion production region is called the virtual anode because electrons diffusing across the magnetic field of the ion production region are collected with high probability very soon after they become bound to guiding centers on or outside that surface. The field lines labelled "critical field lines" in Fig. 1 are those whose surfaces of revolution define that region of the discharge to which the primary electrons coming from the cathode have direct access without the need of collisions or drifts.

The ion production region is the control volume for energy, mass and charge balances. Before performing those balances, however, consider the macroscopic nature of particle behaviors in this region. Propellant atoms enter either through the cathode chamber or by diffusion across the virtual anode. Because atom densities are low and their mean free paths are large, they are assumed to be nearly uniformly distributed and to have a Maxwellian velocity distribution function at the temperature of the thruster walls. Propellant atoms leave the ion production region either by being converted to ions or by drifting out through the grids. Atoms which are excited by electron bombardment to other than ionic or metastable states are assumed to de-excite immediately by photon emission to the neutral ground state. Metastable and ground ionic state atoms are assumed to either travel across the discharge chamber to the thruster surfaces, where they de-excite to ground state neutral atoms, or to the grid apertures where they are lost. It is believed[6] that only the 6^1S_0 ground state neutral,

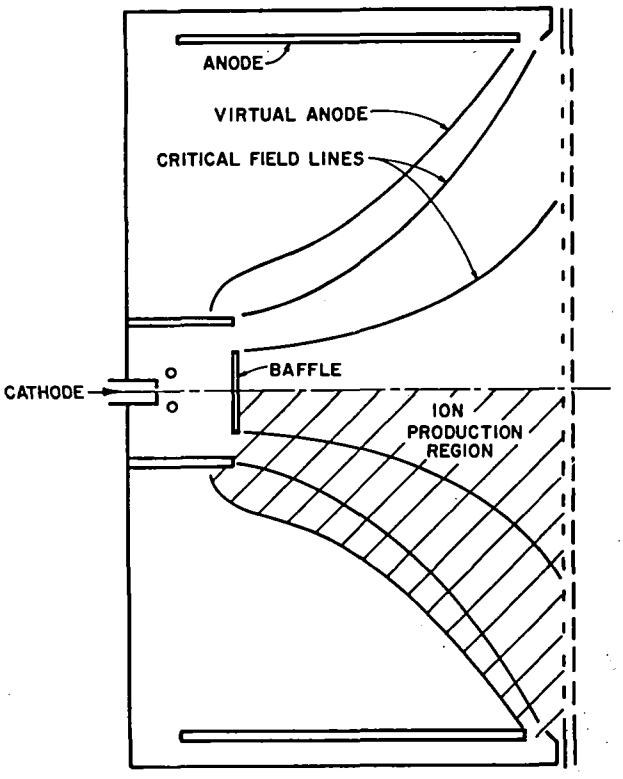

Figure 1. Typical Ion Thruster Magnetic Field Configuration.

6^3P_0 and 6^3P_2 metastable, $6^2S_{1/2}$ single ion 5^1S_0 double ion atomic states will exist in any significant densities in a mercury plasma discharge. The transitions between the states considered in this analysis are illustrated schematically by lines in Fig. 2. Lines extending to the walls and back to the 6^1S_0 state symbolize de-excitation reactions occurring at the walls.

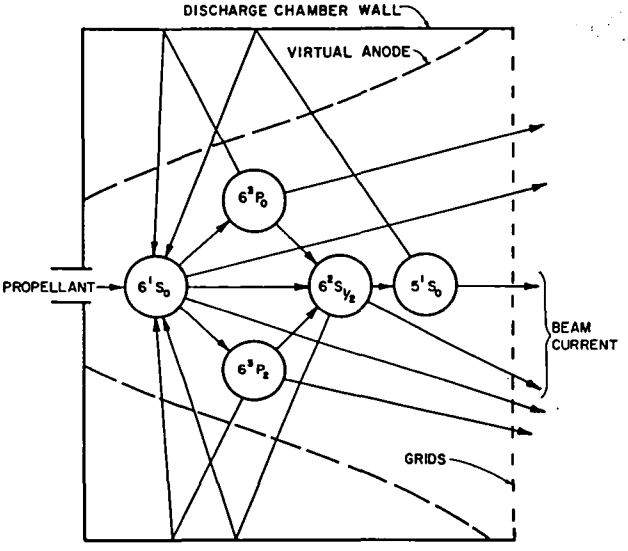

Figure 2. Schematic of important mass flows and atomic transitions in mercury ion thrusters.

Primary electrons enter the ion production region from the cathode or cathode chamber plasma at an energy corresponding to the difference between main discharge plasma potential and either cathode potential or cathode plasma potential depending on the design. In the latter case where a cathode chamber is used, the cathode plasma is assumed to be near keeper potential. Provided the region defined by the critical field lines in Fig. 1 lies wholly within the ion production region, the entire cathode or primary electron current may be assumed to enter the ion production region. It is further assumed that all the primary electrons equilibrate with the Maxwellian electrons before leaving the ion production region. The slowing or thermalization of primary electrons constitutes one distributed source of Maxwellian electrons. The other source, also distributed spatially, is derived from the ionization being done. As a result of the plasma being substantially positive in potential with respect to most thruster surfaces except the anode, very few electrons leave the ion production region except by diffusing across the virtual anode surface. They are then collected quickly from a fairly thin plasma layer near this surface. Collection over a thin anode segment is suggested by anode melting patterns and current measurements to segmented anodes on Beatties' cusped field thruster.[5] Reader[7] also found that anode length did not significantly alter performance provided the location of the anode-virtual anode intersection was not altered, again suggesting the localized collection of electrons. It is assumed that all the electrons collected by the anode are Maxwellian.

Plasma Properties

A survey of plasma property data from the discharge chambers of a number of different thruster configurations[1,4,5,8,9] suggests certain generalizations regarding plasma properties. These are illustrated by the SERT II plasma property data of Fig. 3 taken by Peters.[4] Perhaps most significant is that Maxwellian electron temperature has been found[10] to be nearly constant along magnetic field lines within the ion production region. The correlation between magnetic field lines and lines of constant Maxwellian electron temperature (obtained by linear interpolation of published data) is shown in Fig. 4 for the SERT II and Axial Field thrusters.[1] This correlation is important because

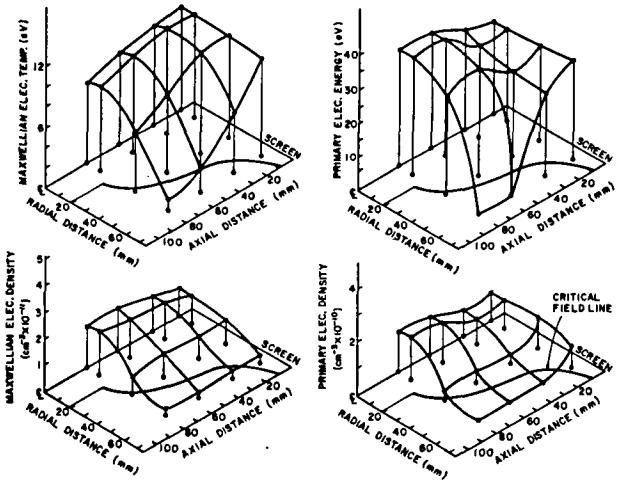

Figure 3. Plasma property profiles for the SERT II Thruster.

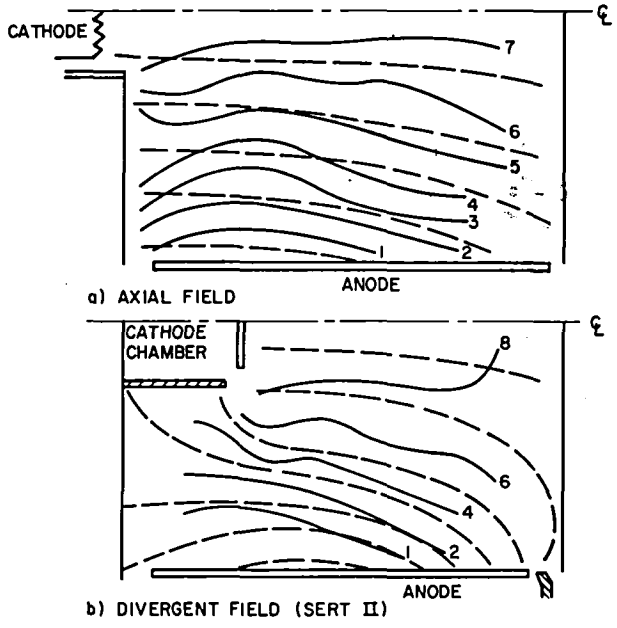

Figure 4. Correlation of Maxwellian electron temperature contours with magnetic field lines-of-force.

it assures that electrons have relatively unrestricted motion along field lines. This allows the one-dimensionalization of the transport equations. Also of interest are the observed absence of primary electrons outside the ion production region and the uniformity of primary electron energy within that region. This is significant because it indicates that primary electrons are able to move outside the region bounded by the critical field line surfaces (Fig. 1) without losing energy to collisions. The details of the scattering are not understood presently. Next, it is noted that to a first approximation, the primary and Maxwellian electron density profiles are nearly the same shape. Considering the difficulty associated with obtaining primary electron data from probe traces, it appears justifiable to assume that the ratio of primary-to-Maxwellian electron densities is a spatial constant. This assumption greatly simplifies calculations. Finally, it is observed that Maxwellian electron density, and therefore total charged particle density, is very low outside the ion production region. This appears to be a result of the combined effects of ion acceleration to the Bohm velocity at or near the virtual anode surface[3] and the rapid collection of electrons outside the ion production region. It appears to be the latter process which brings about the former. Having made these generalizations and

assumptions regarding plasma properties and the processes ongoing in the thruster, the control volume of the ion production region will now be quantitatively analyzed. Units will be SI unless stated otherwise.

Mass and Charge Conservation

If electric fields within the ion production region are ignored, the diffusion of the electrons within that control volume is given by

$$\vec{\Gamma}_e = - D \cdot \nabla n_e \qquad (1)$$

where $\vec{\Gamma}_e$ is a vector electron flux, and D is a tensor describing the diffusivity of electrons which have density n_e. This equation may be reduced to one-dimensional form. It was noted previously that electrons appear to have relatively unrestricted motion along magnetic field lines and that because of plasma sheath effects there is virtually no net transport of electrons in the direction of those field lines within the ion production region except at the virtual anode surface. Now let the local coordinate system r', θ, z' be defined such that at every location in the ion production region the unit vector z' is tangent to the local magnetic field, θ is the azimuthal unit vector in a plane perpendicular to the thruster axis and r' is away from the thruster axis and mutually perpendicular to θ and z'. This is represented in Fig. 5. The assumption of no net

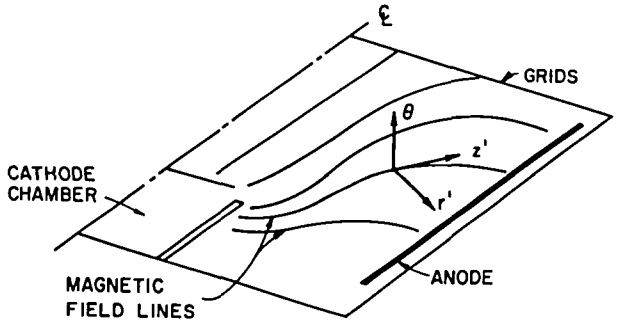

Figure 5. Definition of local unit vectors r', θ and z'.

electron motion along field lines together with the assumed absence of azimuthal gradients due to symmetry, implies that the only diffusion is in the r' direction. Eq. (1) thus becomes for Maxwellian electrons

$$\Gamma_{\perp m} = - D_\perp \nabla_\perp n_m \qquad (2)$$

where the subscript ⊥ signifies the fact that the flux and gradient are in the r'direction, and the diffusivity in this same direction $D_\perp$ is a scalar.

The classical diffusivity of Maxwellian electons of charge e, mass M_e and temperature T_m, diffusing across a magnetic field of flux density B as a result of collisions which occur with frequency ν is [11]

$$D_\perp = \frac{k\, T_m\, M_e\, \nu}{e^2\, B^2} \qquad (3)$$

where k is the Boltzmann constant. It has been found[12,13,14], however, that a better model for diffusion in bombardment ion thrusters is the Bohm model given by

$$D_B = \frac{k\, T_m}{16\, eB} \cdot \qquad (4)$$

Eq. (4) was determined empirically rather than derived and fits most experimental data within a factor of two or three.[15] It will be used here as calculated from the local magnetic flux density B and the Maxwellian electron temperature averaged over the ion production region volume, T_m^*. Using this single temperature is arbitrary, but because of the approximate way in which Eq. (4) models the electron diffusion and also because of the simplification it affords, it is deemed acceptable.

It is noted at this point that if the effective collision frequency per electron ν in Eq. (3) is taken to be one sixteenth the electron cyclotron frequency ω_e where

$$\omega_e = \frac{e\, B}{M_e} \qquad (5)$$

then Eqs. (3) and (4) become identical. Use will be made of this observation later.

The mass continuity relation for the Maxwellian electrons requires that

$$\nabla \cdot \vec{\Gamma}_m = n_m (\nu_i + \tau) \qquad (6)$$

where the right hand side of Eq. (6) represents the rate per unit volume at which Maxwellian electrons are added to the population. The first term in parentheses ν_i is the rate per Maxwellian electron at which electrons are added due to the ionization process in any region of the control volume. The rate per Maxwellian electron at which primary electrons are thermalized is τ. The quantity ν_i is given by

$$\nu_i = \sum_{j=1}^{4} n_j \left[\frac{n_p}{n_m} P_j^i (E_p) + Q_j^i (T_m) \right] \qquad (7)$$

where the summation implied is over the number of atomic states which are present in the control volume and which may be ionized. It is assumed that 6^1S_0, 6^3P_0, 6^3P_2 and $6^2S_{\frac{1}{2}}$ are the only such states and that each gives up a single Maxwellian electron in the ionization reaction. Those reactions are characterized by the ionization rate factors $P_j^i(E_p)$ and $Q_j^i(T_m)$ for collisions with primary and Maxwellian electrons, respectively, which are given by

$$P_j^i(E_p) = \sigma_j^i(E_p) \sqrt{\frac{2\, E_p}{M_e}} \qquad (8)$$

and

$$Q_j^i(T_m) = \int_0^\infty g(E,T_m)\, P_j^i(E)\, dE. \qquad (9)$$

The ionization cross sections $\sigma_j^i(E)$ used in evaluating Eq. (8) are those of Rockwood[16] for ground state neutral atoms and of Peters[4] for ionizations involving other states. The function $g(E,T_m)$ in Eq. (9) is the Maxwellian energy distribution function

$$g(E,T_m) = \frac{2}{\sqrt{\pi}} \frac{E^{\frac{1}{2}}}{(k\,T_m)^{3/2}} \exp(-\frac{E}{k\,T_m}) \quad . \qquad (10)$$

Returning to Eq. (7), one notes that n_j is the number density of the atoms of state j while n_p and n_m are the primary electron and Maxwellian electron number densities, respectively. The atom densities n_j will be discussed further later. Since the ratio of primary electrons to Maxwellian electrons is assumed constant the local value of the ratio is equal to the ratio of the average densities.

$$\frac{n_p}{n_m} = \frac{n_p^*}{n_m^*} \qquad (11)$$

The asterisks denote average over the control volume. It was found unsatisfactory to calculate n_p^* from known boundary conditions and cross sections. Instead a correlation of experimental data, shown in Fig. 6 and represented by the equation

$$n_p^* = 2.75 \times 10^{15} (I_a^{0.15} V_a^{0.75} - 12), \qquad (12)$$

is used to calculate n_p^*. In this equation I_a and V_a are respectively the discharge current and the discharge potential, both of which are assumed controllable.

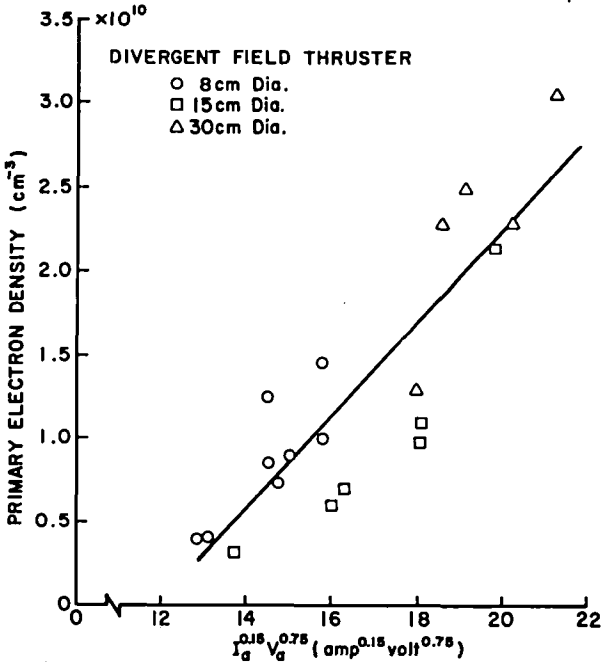

Figure 6. Average primary electron density correlation.

Primary electrons are thermalized as they are released into the discharge chamber at the rate τ (Eq. (6)) which is given by

$$\tau = \frac{I_c}{e\, n_m^*\, \forall} \qquad (13)$$

where I_c is the cathode electron current, and $\forall$ represents the volume of the ion production region. Because the electron current to the anode, I_a, must include an electron for each ion leaving in the beam current (I_β) as well as one for each electron entering from the cathode,

$$I_c = I_a - I_\beta. \qquad (14)$$

The net flux of Maxwellian electrons in the ion production region is in the r' direction. This means that the basic equations describing electron diffusion (Eqs. 1 and 6) can be combined and simplified into a one-dimensional expression in terms of the independent variable r'. Unfortunately the differential equation for electron diffusion in this direction is very complex because of the structure of the magnetic field surfaces. In order to obtain a tractable diffusion equation and thereby facilitate calculation of the electron density contour it will be assumed that the process of diffusion in the r' direction can be described in an approximate way by representing the complex surface everywhere normal to the field lines and having a total extent in the r' direction from centerline to virtual anode of radius R, as a circular plane normal to the axis with radius also equal to R. Then in this plane the solution for the Maxwellian electron density n_m at the radial distance r/R will be taken to approximate the solution on the real surface at the location r'/R. For the approximating planar region Eqs. (1) and (6) combine to give

$$\frac{\partial^2 n_m}{\partial \xi^2} + \frac{1}{\xi}\frac{\partial}{\partial \xi} n_m + \left(\frac{\nu_i + \tau}{D_B}\right) R^2 = 0 \qquad (15)$$

in terms of the reduced coordinate $\xi \equiv r/R$. This equation is solved easily subject to the boundary condition $n_m = n_{mo}$ at $\xi = 0$ to give

$$n_m = n_{m_o} J_o\left(\sqrt{\frac{\nu_i + \tau}{D_B}}\; R\, \xi\right) \qquad (16)$$

where J_o represents the zeroth order Bessel Function. Then, also, the solution on the real surface normal to the field lines is given by

$$n_m = n_{m_o} J_o\left(\sqrt{\frac{\nu_i + \tau}{D_B}}\; R\, \xi'\right) \qquad (17)$$

or

$$n_m = n_{m_o} J_o\left(\sqrt{\frac{\nu_i + \tau}{D_B}}\; r'\right) \qquad (18)$$

Figure 7 shows a discharge chamber magnetic field geometry with orthogonals to the magnetic field lines drawn in. Typical distances from the thruster axis to the virtual anode along surfaces perpendicular to magnetic field lines as they have been estimated for this analysis are drawn in as dotted lines in the figure (R_o at the baffle location and R at the grids).

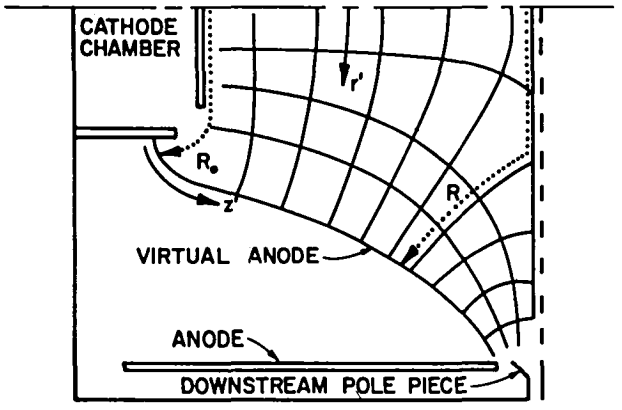

Figure 7. Curvilinear geometry of a divergent magnetic field.

Eq. (18) approximates the variation of Maxwellian electron density on a surface everywhere normal to the field lines in the ion production region in the absence of electric fields. Because the primary-to-Maxwellian density ratio (n_p/n_m) is assumed constant, Eq. (18) also describes the total electron density profile. By the quasi-neutrality condition for plasmas the total ion density must also have this profile.

The longitudinal variation in electron density will now be examined. Even though there is no net flux of Maxwellian electrons in the z' direction, density gradients may exist along magnetic field lines due to body forces. Consistent with previous assumptions and the fact that ion energies are typically only one percent or so of electron energies except at ion production region boundaries, electric fields in the z' direction are ignored.

The data points of Figure 8 show the variation of electron density along the axes of several thrusters. Typically this density is observed to drop off as one proceeds either upstream or downstream from the point where z'/L = 0.3. The decrease in density occurring upstream and downstream of this point is due at least in part to the divergence of the field lines and the associated change in the cross sectional area of the ion production region. Since the surface area-magnetic flux density product is essentially constant over a surface everywhere normal to the field lines in the ion production region, one might expect the plasma density to vary directly with the magnetic flux density.[10]

$$\frac{n_m}{n_{m_0}} \simeq \frac{B}{B_0} \qquad (19)$$

Some correction to this expression is needed however to reflect the effects of forces such as those due to magnetic field divergence.[17] An empirical modification to the direct proportionality of Eq. (19) that seems to facilitate better matching of the experimental data is

$$\frac{n_m}{n_{m_0}} = \frac{B}{B_0} \exp\left(1 - \frac{B}{B_0}\right) . \qquad (20)$$

The solid lines shown in Figure 8 were obtained using Eq. (20) with the reference magnetic flux density B_0 defined as the average value of flux density evaluated over the surface everywhere normal to the field lines at z'/L = 0.3. At this axial location the centerline and reference Maxwellian electron density n_{m_0}, takes on its maximum value. As the proximately of the solid lines and data

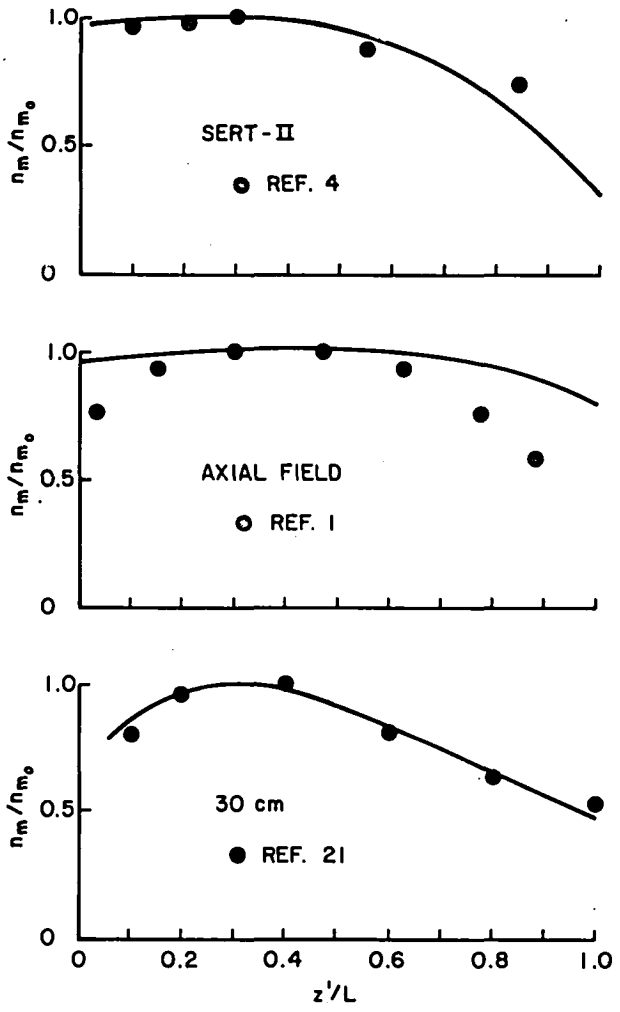

Figure 8. Relative Maxwellian electron density as a function of normalized thruster length measured from the upstream end of several thrusters along the thruster axis. Lines are plots of Eq. (20) evaluated with B_0 at z'/L=0.3.

points in Figure 8 suggest, incorporation of the exponential term of Eq. (20) yields a good match with experimental data particularly in the cases of the SERT II and 30 cm dia. thrusters.

Eq's. (18) and (20) may be combined to give a two-dimensional Maxwellian electron density profile within the ion production region:

$$n_m(r',z') = n_{m_0} \frac{B(z')}{B_0} \exp\left(1 - \frac{B(z')}{B_0}\right) J_0\left(\sqrt{\frac{\nu_i + \tau}{D_B(z')}}\, r'\right) . \quad (21)$$

The evaluation of the reference density n_{m_0} leads to the final area of consideration under the topic of conservation of mass and charge. For the discussion which follows it may be helpful to refer to Fig. 2.

It is apparent from the quasi-neultrality requirement of a plasma that the total electron density must equal the ion density. That density will be such that the production and loss rates of ions are equal. To calculate the loss rate of ions from the ion production region it is assumed that sufficiently few three body collisions (required for recombination in the control volume) occur that the only ion loss mechanism is recombination at the thruster walls or loss to the beam. Ions have been found[2,3] to leave the ion production region at the Bohm velocity[18] which is given by

$$v_B = \left[\frac{q\, kT_m}{M_i e}\left(1 + \frac{n_p}{n_m}\right)\right]^{\frac{1}{2}} . \quad (22)$$

Here q is the ion charge and M_i is its mass. For single ions q is replaced by e. The single ion loss rate may be calculated by integrating over the surface of the ion production region,

$$\left(\frac{dN_+}{dt}\right)_{loss} = \iint_{A_{cv}} n_+ \, v_B \, dA . \quad (23)$$

For doubly charged ions v_B is $\sqrt{2}$ times that for single ions, hence

$$\left(\frac{dN_{++}}{dt}\right)_{loss} = \frac{\sqrt{2}\, n_{++}}{n_+}\left(\frac{d\, N_+}{dt}\right)_{loss} . \quad (24)$$

Recalling that ion density profiles are assumed to follow electron density profiles and that the ratio n_p/n_m is taken to be constant, Eq. (23) may also be written

$$\left(\frac{d\, N_+}{dt}\right)_{loss} = \left(1 + \frac{n_p}{n_m}\right)\left(\frac{n_+}{n_+ + n_{++}}\right) \iint_{A_{cv}} n_m \, v_B \, dA. \quad (25)$$

The production rate for single ions is the sum of the production rates from the 6^1S_0, 6^3P_0 and 6^3P_2 state atoms respectively

$$\left(\frac{d\, N_+}{dt}\right)_{gain} = \iiint_{\forall} \sum_{j=1}^{3} \left[n_m \, Q_j^+(T_m) + n_p \, P_j^+(E_p)\right] n_j \, d\forall . \quad (26)$$

For convenience in calculations, it is found sufficiently accurate to evaluate this as

$$\left(\frac{d\, N_+}{dt}\right)_{gain} = \forall\, n_m^* \sum_{j=1}^{3} \left[Q_j^+(T_m^*) + \frac{n_p}{n_m} P_j^+(E_p)\right] n_j \quad (27)$$

where the * denotes volume averaged properties. Double ions are produced primarily from single atoms and their production rate is given by

$$\left(\frac{d\, N_{++}}{dt}\right)_{gain} = \forall\, n_m^* \, n_+ \left[Q_+^{++}(T_m^*) + \frac{n_p}{n_m} P_+^{++}(E_p)\right] . \quad (28)$$

Before evaluating n_+ and n_{++}, the densities of the ground and excited state neutral atoms must be found. For the metastable states, 6^3P_0 and 6^3P_2, it is assumed that production occurs solely from ground state neutral atoms and that loss occurs only at the boundaries, as with ions, because of their relatively long lifetimes. Specifically the production and loss of the j^{th} excited state (where j=2,3) is described satisfactorily by assuming atom state densities are spatial constants. When these rates are equated one obtains

$$\forall\, n_m^* \, n_1 \left[Q_1^j(T_m^*) + \frac{n_p}{n_m} P_1^j(E_p)\right] = A_{cv} \frac{n_j \, v_a}{4} + \forall\, n_m^* \, n_j \left[Q_j^4(T_m^*) + \frac{n_p}{n_m} P_j^4(E_p)\right] . \quad (29)$$

The left side of this equation approximates the rate of formation of j^{th} state atoms. The first term on the right is the rate of loss across the area of the ion production region (A_{cv}) where v_α is the thermal velocity of the atoms given by

$$v_\alpha = \sqrt{\frac{8\, kT_\alpha}{\pi m_\alpha}} . \quad (30)$$

The atom temperature T_α is assumed equal to the thruster wall temperature which is assumed known. The second term on the left of Eq. (29) is the rate at which j^{th} state atoms are converted to single ions and thus lost.

One more equation is needed to form a deterministic set for the computation of atomic specie densities. It is the equation for the conservation of neutral ground state atoms. Neutral ground state atoms enter from the propellant feed system. They are converted to the 6^3P_0 and 6^3P_2 metastable state atoms and to single ions. As previously stated, it is assumed that all other sub-ionic excited states decay immediately leaving atoms in their ground state. The recombination of ions and metastable atoms at the walls constitutes an additional source of ground state neutral atoms. Another loss mechanism is escape of neutral atoms through the grids. Considering these effects the conservation of neutral ground state atoms may be written as

$$\forall\, n_m^* \, n_1 \sum_{j=2}^{4} \left[Q_1^j(T_m^*) + \frac{n_p}{n_m} P_1^j(E_p)\right] + A_{sg}\phi \frac{n_1 \, v_\alpha}{4} = \frac{I_n}{e} + (A_{cv} - A_{sg}\phi) \sum_{j=2}^{3} \frac{n_j \, v_\alpha}{4} + (n_4 + \sqrt{2}\, n_5) \iint_{(A_{cv} - A_{sg})} v_B \, dA . \quad (31)$$

The left side is the neutral ground state atom loss rate in which the first term approximates collisional excitations. The states referred to by the index j as it varies from 1 to 5 are respectively 6^1S_0 neutral ground state, 6^3P_0 and 6^3P_2 metastable states, $6^2S_{\frac{1}{2}}$ single ion and 5^1S_0 double ion states. The second term on the left is the rate at which state 1 atoms leave through the grids which have total area A_{sg} and effective open area fraction to neutrals ϕ. Since virtually none of the atoms go directly through both grids without scattering off at least one surface, it is appropriate to consider the flow restrictions associated with the open area fractions of each grid, ϕ_{sg} for the screen and ϕ_{ag} for the accelerator grid, as series resistances such that

$$\phi = \frac{\phi_{sg}\,\phi_{ag}}{\phi_{sg} + \phi_{ag}} \quad . \tag{32}$$

The right side of Eq. (31) is the rate at which state 1 atoms are added to the control volume. I_n/e is the propellant mass flow expressed in equivalent amperes divided by the electronic charge. The second right hand term is the rate at which excited state atoms go to the walls, de-ecite, and return to the ion production region. The final term in Eq. (31) is the rate at which the two ionic state atoms reach the walls, recombine, and come back as state 1 atoms.

Now equating the production and loss rates of single ions, Eq's. (23) and (27), and double ions, Eq's. (24) and (28), and considering also Eq's. (29) (two equations for two species) and (31); one obtains five equations which are linear in and can be solved for the five atomic state densities. An additional equation derived from the quasi-neutrality condition enables one to solve for the total electron density as well.

$$n_p^* + n_m^* = n_4 + 2\,n_5 \tag{33}$$

Thus if the electron temperature T_m^* and the primary electron energy E_p are known, the atomic and ionic specie densities may be calculated (recall that the volume-averaged primary electron density n_p^* is obtained using Eq. (12) and that the ratio n_{pr}/n_{mx} is assumed equal to n_p^*/n_m^* so the Maxwellian electron density is known as well). Obtaining Maxwellian electron temperature and primary electron energy will be discussed next.

Energy Conservation

Having neglected electric fields within the ion production region, the conservation of energy deals with accounting for electron kinetic energy and inelastic collisional energy transfers. Ionic and atomic kinetic energies are not important except as previously discussed in connection with loss rates.

The only energy input to the control volume is the kinetic energy carried by the primary electrons which come from the cathode. This energy is gained as these electrons are accelerated across the sheath into the ion production region. The cathode sheath potential is the difference between the plasma potential V_ϕ in the ion production region and the potential of the plasma near the cathode. For hollow cathode thrusters the cathode plasma is near keeper potential V_k. Additionally, the electrons in the cathode chamber have a Maxwellian temperature of typically from 1 to 3 eV[19] before they cross the cathode plasma sheath. Taking kT_c as this thermal energy, the primary electron energy E_p may then be found from

$$E_p = V_\phi - V_k + kT_c \tag{34}$$

and the energy flow to the ion production region from

$$\dot{E}_{in} = \frac{I_c}{e} E_p \tag{35}$$

where I_c is the net cathode emission current which is assumed specified.

The plasma potential V_ϕ is usually within a few volts of anode potential V_a. Fair results may be obtained by assuming it is exactly at anode potential, but some improvement is obtained by calculating V_ϕ. This is difficult to do exactly, but an approximation can be made by recalling that nearly all of the electron current collected by the anode comes from a very thin layer near the virtual anode surface. Thickness of that layer is about equal to the mean free path for collisional diffusion across the magnetic field, which is about equal to the average Larmor radius.[20] Using the symbol T_{ma} to represent the Maxwellian electron temperature at the virtual anode this becomes

$$\langle R_L \rangle = \frac{M_e}{eB}\left[\frac{8\,k\bar{T}_{ma}}{\pi M_e}\right]^{\frac{1}{2}} \quad . \tag{36}$$

The plasma potential is established such that for the electron density near the anode - virtual anode intersection n_{mx} only enough electrons can cross the anode plasma sheath to supply the anode current I_a. For an electron collection area A_x (assumed less than the anode area) given by

$$A_x = \frac{\pi d_a \langle R_L \rangle}{\sin\theta_a} \quad , \tag{37}$$

where d_a is the anode diameter and θ_a is the angle the magnetic field makes with the anode surface as shown in Fig. 9. The equation describing electron collection is obtained by integrating the differential flux:

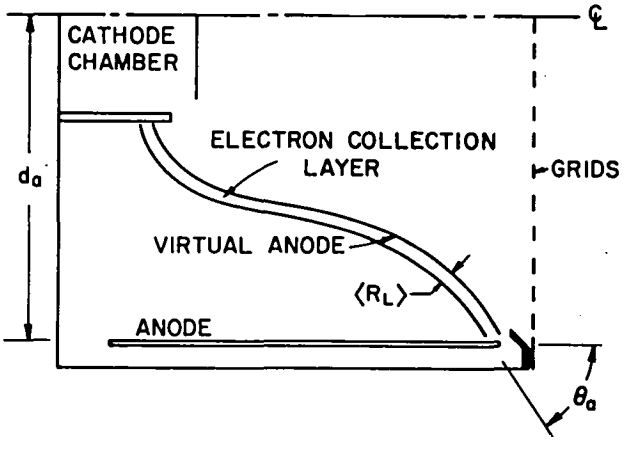

Figure 9. Electron Collection Geometry.

$$\frac{I_a}{en_{ma}A_x} = \int_{\sqrt{\frac{2eV_{sa}}{M_e}}}^{\infty} v\,F(v)dv = \left[\frac{kT_a}{2\pi M_e}\right]^{\frac{1}{2}} \exp\left\{\frac{-e\,V_{sa}}{kT_a}\right\}. \quad (38)$$

This may be solved explicity for the anode sheath potential V_{s_a}:

$$V_{s_a} = V_\phi - V_a = \frac{kT_a}{e}\,\ell n\left[\frac{A_x\,e\,n_{ma}}{I_a}\left(\frac{kT_a}{2\pi M_e}\right)^{\frac{1}{2}}\right]. \quad (39)$$

Table 1 gives a comparison of values of V_{s_a} so computed along with values $(V_\phi - V_a)$ observed in tests for several thrusters. Data for the axial field and SERT II thrusters are from Knauer, et al.[1] The SIT-8 data were taken at Colorado State University, and the 30 cm data are from Hughes Research Laboratories.[21] The agreement is seen to be good. Plasma potential V_ϕ may then be found by summing V_{s_a} with the known anode potential V_a to calculate the primary electron energy from Eq. (34).

Having thus found the rate at which energy is supplied to the ion production region $\dot{E}_{in}$, attention is now given to energy losses from this region. The kinetic energy of the primary electrons goes either to heating the Maxwellian electrons or to inelastic collisions with atoms or ions. The mass difference between electrons and atoms precludes significant atom or ion heating by the electrons.

The inelastic collisional energy lost by the primary electrons is approximately given by

$$\dot{E}_{\forall_p} = \iiint_{\forall} n_p \sum_{i=2}^{6} \sum_{j=1}^{4} n_j^* P_j^i(E_p)\,E_j^i\,d\forall\,. \quad (40)$$

Here the index i denotes the excited states considered as possible outcomes from the collisions, and j refers to the state of the atoms before the collisions. Thus n_j^* is the volume averaged density of j^{th} state atoms (6^1S_0, 6^3P_0, 6^3P_2, $6^2S_{\frac{1}{2}}$), P_j^i is the cross section - velocity product (rate factor) for transitions from j^{th} to i^{th} states, and E_j^i is the characteristic energy of the j-i transition. It is noted that in addition to the two metastable and two ionic states (i=2 through 5) considered as possible products of the collisional process, ground state (j=1) neutral atoms are also assumed to be available for excitation to what Rockwood[16] calls the "lumped state" (i=6) which is a collection of all other sub-ionic excited states and for which he gives an effective cross section function with its characteristic energy.

Some of the energy transferred to the Maxwellian electrons eventually leaves the control volume in the form of ions or as de-excitation photons resulting from collisions of Maxwellian electrons with atoms. That energy loss rate is

$$\dot{E}_{\forall_m} = \iiint_{\forall_{cv}} n_m \sum_{i=2}^{6} \sum_{j=1}^{4} n_j^*\,Q_j^i(T_{mx}^*)\,E_j^i\,d\forall \quad (41)$$

where $Q_j^i(T_m^*)$ is a rate factor for Maxwellian electrons and is related to $P_j^i(E)$ through Eq. (9).

The only other significant energy loss from the Maxwellian electrons in the ion production region is that carried across the boundaries of the control volume. The dominant loss at the boundary is the convective loss at the virtual anode. Its magnitude can be calculated from

$$\dot{E}_a = A_x \int_{-\infty}^{\infty}\int_{-\infty}^{\infty}\int_{v_{min}}^{\infty} n_{m_x} \frac{M_e}{2}\,(v_{r'}^2+v_\theta^2+v_{z'}^2)\,v_{r'}\,f(v_{r'})\,f(v_\theta)\,f(v_{z'})\,dv_{r'}dv_\theta\,dv_{z'} \quad (42)$$

where v_{min} the velocity required to overcome the sheath potential is $\sqrt{\frac{2eV_{sa}}{M_e}}$ for $V_{s_a} > 0$ and zero otherwise. Eq. (42) reduces to

$$\dot{E}_a = \frac{I_a}{e}\,(2\,kT_{m_a} + eV_{s_a}) \quad (43)$$

Table I

Comparison of Calculated Anode Sheath Potential with Measured Values for Several Thrusters

Thruster	Axial Field	SERT-II	SIT-8	30 cm
T_a (eV)	4.6	5	11.6	2.3
B (T)	.0019	.0015	.0044	.0018
θ_a (deg)	26	75	55	76
d_a (m)	.15	.15	.088	.296
I_a (A)	1.03	1.7	0.72	10.0
$n_m(m^{-3}x10^{-16})$	0.8	2.0	2.0	4.3
V_{s_a} (V)	1.69	1.30	6.33	-1.4
$V_\phi - V_a$ (V)	1.5	1.5	7	-2

for an assumed isotropic Maxwellian distribution of velocities with the temperature of the Maxwellian electrons at the virtual anode surface T_{m_a}.

One surface other than the virtual anode surface over which significant Maxwellian electron energy is lost is that at the upstream end of the ion production region where the magnetic field lines intersect the structure. There a few of the electrons in the tail of the Maxwellian distribution have sufficient energies to cross the sheath and carry their energies from the ion production region. Applying Eq. (42) to this baffle region by noting that the potential to be overcome in this case is V_ϕ rather than V_{s_a} and that one must integrate for V_{s_a} in Eq. (42) gives the flux density for this energy flow. Then for upstream area A_b the energy loss rate $\dot{E}_b$ becomes

$$\dot{E}_b = \iint_{A_b} n_{m_b} \left(\frac{kT_m}{2\pi M_e}\right)^{1/2} \exp\left(\frac{-eV_\phi}{kT_m}\right) (2kT_m + eV_\phi)\, dA. \quad (44)$$

This energy loss rate from the tail of the Maxwellian distribution is small, typically 5 to 15 percent of the energy loss rate to the virtual anode for the cases studied. Electron energy losses across the downstream end of the ion production region are even less important because of the lower densities at that end and the small fraction of the area there which is at cathode potential. The accelerating grid potential is assumed to reflect nearly all electrons over most of the screen grid area.

For steady state operation the power into the electron population must be balanced by the power loss from it; that is

$$\dot{E}_{in} = \dot{E}_{V_p} + \dot{E}_{V_m} + \dot{E}_a + \dot{E}_b \,. \quad (45)$$

For a given input power, the temperature of the Maxwellian electrons will adjust itself to satisfy this balance. Before Eq. (45) can be evaluated, however, the electron temperature profile must be found.

Because the magnetic field restricts significant electron motion in the direction perpendicular to the magnetic field (r') while there is no such restriction along the field, any gradient in temperature will be in the r' direction. That this is the case is evident in Fig. 4. Furthermore, the energy transport mechanism across the magnetic field is expected to be principally conduction for which the accepted[22] expression for conductivity is

$$K_\perp = 4.7 \frac{n_m\, kT_m}{M_e\, \omega_e^2\, \tau_e} \,. \quad (46)$$

Here ω_e is the electron cyclotron frequency given by Eq. (5), and τ_e is the effective electron momentum transfer collision period. For this case where Bohm diffusion was assumed to apply it was found that this period was effectively $16/\omega_e$. Making use of this relation and Eq. (4) it is seen that for conductivity to be consistent with diffusivity Eq. (46) may be rewritten as

$$K_\perp = 4.7\, n_m\, D_B \,. \quad (47)$$

Using the same effective electron collision period τ_e makes the electron thermal conductivity parallel to the magnetic field approximately 175 times the value perpendicular to the field $K_\perp$.[22]

The kinetic power to and from the Maxwellian electrons in the ion production region constitute a distributed source of heat. The net power addition per Maxwellian electron in the ion production region may be defined as

$$\dot{W} = \frac{1}{n_m^* \forall_{cv}} (\dot{E}_{in} - \dot{E}_{V_p} - \dot{E}_{V_m} - \dot{E}_b) \,. \quad (48)$$

In the steady state this power must be removed by conduction across the field lines as rapidly as it is supplied. The conduction equation for one-dimensional temperature gradients which describes this condition is:

$$\nabla^2 (K_\perp T_m) = - \dot{W} n_m \,. \quad (49)$$

Note from Eq's. (40) and (41) that the energy loss rate terms in Eq. (48) are locally proportional to the Maxwellian electron density n_m or the primary electron density which has a similar profile. The upstream energy loss rate E_b is proportional to n_b, the electron density on the upstream surface of the thruster, however, the effectively infinite conductivity parallel to the magnetic field suggests that treating it as also everywhere proportional to n_m will be acceptable. Now substituting Eq. (47) into Eq. (49) and applying the same arguments, assumptions and limitations considered in density profile calculations regarding the cylindrical coordinate system approximation, Eq. (49) may be rewritten as

$$\frac{1}{r'} \frac{d}{dr'} \left(r' n_m \frac{dT_m}{dr'} \right) = - \frac{\dot{W} n_m}{4.7 D_B} \,. \quad (50)$$

Then using Eq. (18) and performing the indicated differentiation this becomes

$$\frac{d^2T_m}{dr'^2} + \frac{dT_m}{dr'} \left[\frac{1}{r'} - \frac{Y J_1(Yr')}{J_0(Yr')} \right] + \frac{\dot{W}}{4.7 D_B} = 0 \quad (51)$$

where

$$Y = \sqrt{\frac{\nu_i + \tau}{D_B}} \,. \quad (52)$$

Eq. (51) is not amenable to analytic solution, but for $Yr' < 2.4$ gives a numerical solution similar to the parabola

$$T_m(r') = T_{m_0} - \frac{1}{4} \left[\frac{\dot{W}}{4.7 D_B} \right] r'^2 \quad (53)$$

where T_{m_0} is the value of Maxwellian electron temperture alone the thruster axis. Recalling that the diffusion coefficient varies inversely with magnetic flux density (Eq. 4) and that the magnetic flux density-surface area product is essentially constant over surfaces everywhere normal to field lines in the ion production region one can show that the parameter $r'^2 D_B$ is approximately constant along field lines. Eq. (53) therefore suggests that electron temperature $T_m(r')$ is also constant along field lines, in general agreement with the results given in Figure 4.

To perform the energy balance of Eq. (45), the

average temperature T_m^* given by

$$T_m^* = \frac{1}{\forall_{cv}} \iiint_{\forall_{cv}} T_m \, d\forall \tag{54}$$

and the virtual anode temperature $T_{m_a} = T_m(r'=R)$ are needed. Using these relations, and the boundary condition that

$$\dot{E}_a = n_m^* \forall \dot{W} , \tag{55}$$

the temperature T_{m_0} may be uniquely determined. Hence the complete one-dimensional temperature profile can be found.

Thruster Performance

The equations presented to this point are almost sufficient to calculate the plasma density and electron temperature profiles from design and operational data. These data include the volume and the various bounding areas of the ion production region, the function $B/B_0(z')$ which describes the magnetic field divergence, the values for B_0, A_{sg}, ϕ_{ag} and ϕ_{sg}, the functions $P_j^1(E_p)$ and $Q_j^1(T_m^*)$, keeper and anode potentials V_k and V_a, cathode emission current I_c, propellant mass flow rate I_n, and the thruster wall temperature, T_a. The remaining quantity required for the analysis is the beam current I_β. It is found by integrating the Bohm flux density over the open area of the screen grid. If the screen grid has area A_{sg} and open area fraction ϕ_{sg} this is

$$I_\beta = \iint_{A_s} e \, \phi_{sg} \left[n_+(r',z') + 2\sqrt{2} \, n_{++}(r',z') \right] v_B(r') \, dA . \tag{56}$$

where v_B is the local Bohm velocity (Eq. 22) based on the electron temperature at the location r'.

Once the beam current has been calculated the discharge loss ρ_D (eV/ion) and the propellant utilization η can be found. The equation used here for calculating ρ_D,

$$\rho_B = \frac{I_a V_a}{I_\beta} , \tag{57}$$

neglects keeper power since keeper current is small and was not calculated nor assumed known. Heater powers are also neglected. Utilization is easily calculated from

$$\eta = \frac{I_\beta}{I_n} . \tag{58}$$

Since double ions have been considered here, the results can be compared directly with experimental data, and utilizations may exceed unity slightly.

Calculations

Analytical solution of the system of equations described is quite tedious, especially when trying to obtain plasma properties and peformance from operating and design data. The inverse problem of finding, say, the discharge current or cathode emission required to sustain a given set of plasma properties is much easier. To solve the former problem a computer code has been written which converges to the required plasma properties using a two-step iterative procedure. First, because the equations connected with density profile calculation are far less sensitive to temperature errors than temperature equations are to density errors, Maxwellian electron temperature is guessed, and a consistent solution for the various densities is obtained. The energy balance is then performed leading to a better estimate of T_m. The process then repeats until both sets are simultaneously satisfied to a specified accuracy. Two percent has been used successfully, requiring often only a few (~2-5) iterations on the Maxwellian temperature. By varying I_c and the discharge voltage V_a about nominal values while holding the other parameters constant, it is possible to generate performance curves (ρ_D vs η) similar to those measured on operating thrusters.

As an example of the comparison between calculated and measured values, Figs. 10 and 11 compare

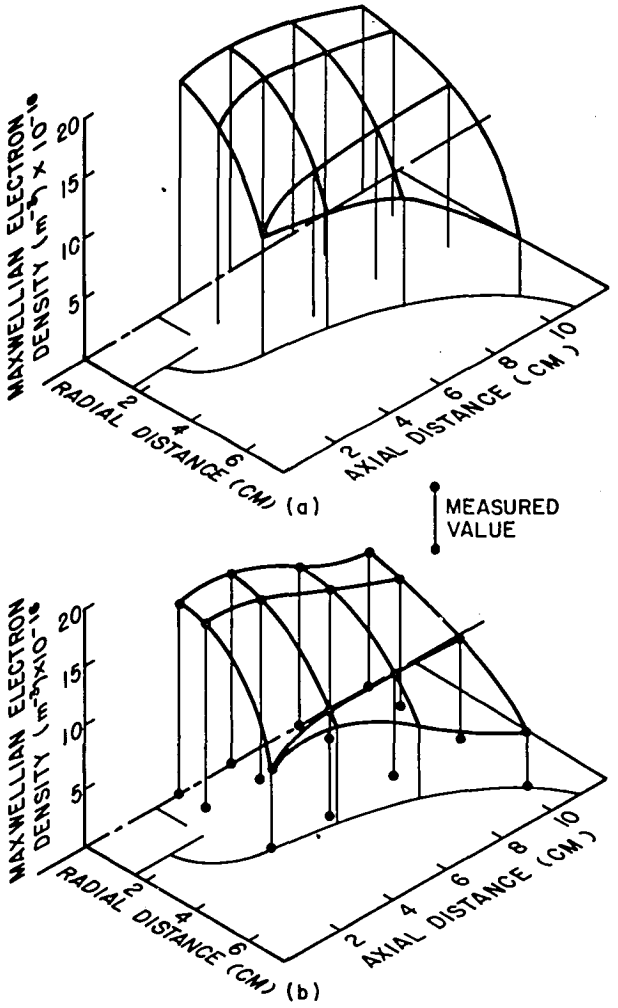

Figure 10. Comparison of (a) calculated with (b) measured Maxwellian electron density for the SERT II thruster operating at 1.7 A, 37.2 V and .307 Aeq propellant mass flow rate.

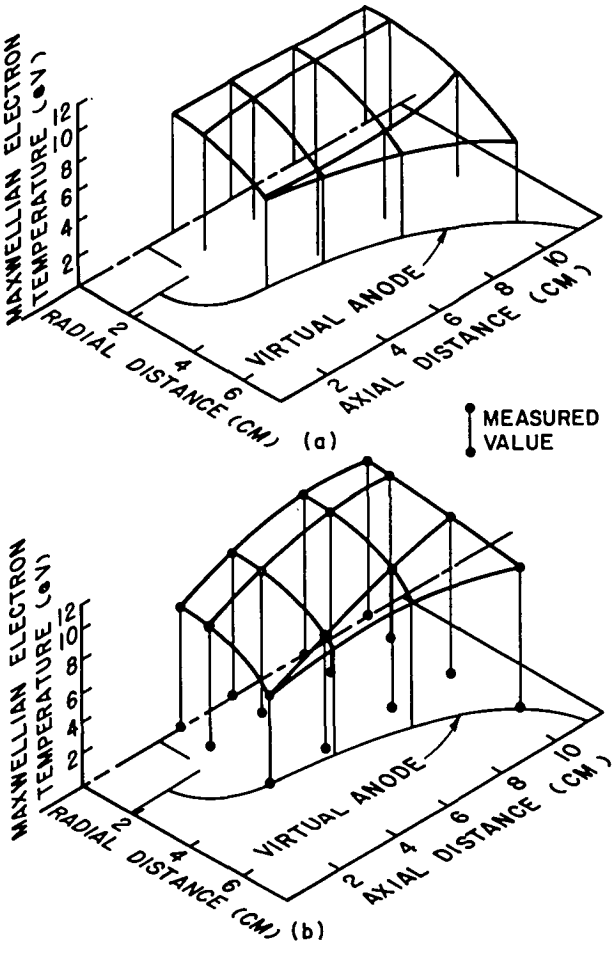

Figure 11. Comparison of (a) calculated with (b) measured Maxwellian electron temperature for the SERT II thruster operating at 1.7 A, 32.7 V and .307 Aeq propellant mass flow rate.

Peters'[4] SERT II measurements with the computed profiles of n_m and T_m for the same operating conditions. Table II lists other calculated values and the corresponding measurements (in parenthesis) for several thrusters. Fig. 12 shows calculated and measured performance curves for those same thrusters. Data are from Knauer et al[1] (axial field), Peters[4] (SERT II) and Rawlin[23] (30 cm).

Considering the gross approximations which have been made, the agreement seen in Table II is fairly good except for Maxwellian electron properties in the 30 cm thruster case considered. The poorer agreement in this case is believed to be the result of the very strong magnetic field divergence in that thruster which apparently exceeds the applicability of the cylindrical geometry assumption in the equations which model the transport processes. The r' variation of B in that thruster is also substantial. These variances not withstanding, the calculated performance curves of Fig. 12 agree well with the measured ones.

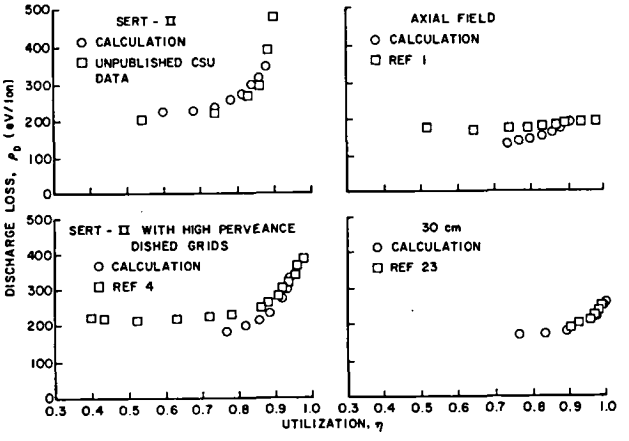

Figure 12. Comparison of calculated performance with measurement for several thrusters.

Table II

Comparison of Calculated with Observed (in parentheses) Parameter Values for Several Thrusters

Thruster	SERT-II	SERT-II HPD Grids	Axial Field	30 cm
I_β (A)	.240 (.258)	.640 (.654)	.267 (.268)	2.1 (2.0)
T_{m_0} (eV)	7.29 (9)	7.7 (9)	5.77 (7)	2.0 (2.5)
T_m^* (eV)	6.4 (6)	6.7 (7.1)	4.8 (5)	1.6 (2.5)
n_m^* ($m^{-3}x10^{-16}$)	8.8 (8)	17.3 (23)	8.3 (9)	63 (19)

Conclusions

The processes which appear to control the discharge of a mercury ion thruster have been related to plasma properties and thruster performance. A computer code which solves that set of equations gives results that agree reasonably well with measurements. Based on the success of that model the following conclusions are drawn:

1. The region of prime importance to ion thruster operation is the ion production region. Virtually all important processes occur within or at the surfaces of that control volume.

2. The innermost field line to intersect the anode has a surface of revolution which is in effect a virtual anode. Electrons which diffuse across this surface are collected from a layer approximately one average electron Larmor radius thick. Electron collection from that layer appears to govern plasma potential relative to anode potential.

3. Electrons diffuse across the magnetic field of the ion production region essentially according to the Bohm diffusion model. They appear to be virtually unrestricted in their motion along the magnetic field lines.

4. The plasma density in the ion production region is determined by equating the production and loss rates of ions. Production is principally by electron - atom collisions for single ions and electron-ion collisions for double ions. Ions are lost as a result of migration at the local Bohm velocity across the boundaries of the ion production region. Density profiles for charged particles are governed by cross-field diffusion of electrons and by the divergence drift force for divergent field thrusters.

5. Maxwellian electron temperature is that required to satisfy a basic energy balance which involves kinetic energy supplied by the primary electrons and lost to inelastic collisions and by convection across the boundaries of the control volume. Transport of this energy across the magnetic field appears to be described adequately by a classical conductive process wherein the effective collision frequency is one sixteenth the electron cyclotron frequency. The temperature profiles across the magnetic field are governed by this conduction process. Maxwellian electron temperatures are nearly constant along magnetic field lines.

6. It is possible to approximate plasma property and performance data using only controllable parameters and thruster configuration data. Performance curves generated using the model agree with measured curves.

Acknowledgement

The authors are indebted to Drs. A. V. Phelps of the Joint Institute for Laboratory Astrophysics, Boulder, Colorado, and H. R. Kaufman and C. E. Mitchell of Colorado State University for their helpful discussions and suggestions.

References

1. Knauer, W., Poeschel, R. L., King, H. J., and Ward, J. W., "Discharge Chamber Studies for Mercury Bombardment Ion Thrusters," NASA CR-72440, September 1968.

2. Masek, T. D., "Plasma Properties and Performance of Mercury Ion Thrusters," AIAA Paper No. 69-256 (1969).

3. Kaufman, H. R., "Ion Thruster Propellant Utilization," Ph.D. Dissertation, Colorado State University, 1971.

4. Peters, R. R., "Double Ion Production in Mercury Ion Thrusters," NASA CR-135019, April 1976.

5. Beattie, J. R., "Cusped Magnetic Field Mercury Ion Thruster," NASA CR 135047, July 1976.

6. Phelps, A., Joint Institute for Laboratory Astrophysics, Boulder, Colorado. Private communication.

7. Reader, P. D., "Investigation of a 10 cm Diameter Electron Bombardment Ion Rocket," NASA TN D-1163, 1962.

8. Isaacson, G. C., "Multipole Gas Thruster Design," NASA CR-135101, June 1977.

9. Longhurst, G. R. and Wilbur, P. J., "Multipole Mercury Ion Thruster," AIAA Paper No. 78-682 (1978).

10. Longhurst, G. R., "Prediction of Plasma Properties in Mercury Ion Thrusters," NASA CR-159448, December 1978.

11. Krall, N. A., and Trivelpiece, A. W., Principles of Plasma Physics, McGraw-Hill, New York, 1973, Chapter 6.

12. Kaufman, H. R., "Electron Diffusion in a Turbulent Plasma," NASA TN D-1324, June 1962.

13. Isaacson, G. C., "Multipole Gas Thruster Design," NASA CR-135101, June 1977.

14. Krall and Trivelpiece, loc. cit., p. 21.

15. Bohm, D., "The Use of Probes for Plasma Exploration in Strong Magnetic Fields," in The Characteristics of Electrical Discharges in Magnetic Fields, eds. A. Guthrie and R. K. Wakerling, McGraw-Hill, New York, 1949, p. 65.

16. Rockwood, S. D., "Elastic and Inelastic Cross Sections for Electron-Hg Scattering from Hg Transport Data," Phy. Rev. A., Vol. 8, No. 5, November 1973, pp. 2348-2358.

17. Krall and Trivelpiece, loc. cit. p. 622.

18. Bohm, D., "Minimum Ionic Kinetic Energy for a Stable Sheath," in Guthrie and Wakerling, op. cit., pp. 77-86.

19. Wells, A. A., "Current Flow Across a Plasma 'Double Layer' in a Hollow Cathode Ion Thruster," AIAA Paper No. 72-418, AIAA 9th Electric Propulsion Conference, Bethesda, Maryland, April 17-19, 1972.

20. Chen, F. F., Introduction to Plasma Physics, Plenum, New York, 1974, p. 150.

21. Hughes Research Laboratories, "High Power and 2.5 kW Advanced Technology Ion Thruster," Contract NAS 3-19703, Monthly Report No. 2, 1 July 1975 to 1 Aug. 1975, NASA Lewis Research Center, Cleveland, Ohio.

22. Book, D. L., 1978 Revised NRL Plasma Formulary, Plasma Physics Division, Naval Research Laboratory, Washington D. C., p. 31.

23. Rawlin, V. K., "Performance Comparison of 30 cm Ion Thrusters with Dished Grids," AIAA Paper 73-1053, AIAA 10th Electric Propulsion Conference, Lake Tahoe, Nevada, 31 Oct. to 2 Nov. 1973.

SPONSORED BY:
PRINCETON UNIVERSITY CONFERENCE
AMERICAN INSTITUTE OF AERONAUTICS AND ASTRONAUTICS (AIAA)
DEUTSCHE GESELLSCHAFT FUR LUFT-UND RAUMFAHRT (DGLR)

79-2056

Studies on an Experimental Quartz Tube Hollow Cathode

D. Siegfried and P. J. Wilbur,
Colorado State University, Fort Collins, Colo.

PRINCETON/AIAA/DGLR 14th
INTERNATIONAL ELECTRIC
PROPULSION CONFERENCE

Oct. 30-Nov. 1, 1979/Princeton, N.J.

STUDIES ON AN EXPERIMENTAL QUARTZ TUBE HOLLOW CATHODE*

Daniel E. Siegfried and Paul J. Wilbur
Colorado State University
Fort Collins, Colorado

Abstract

An experimental investigation is described in which a special quartz tube, hollow cathode was operated in a test fixture which allowed the simultaneous measurement of internal cathode pressure, insert temperature profiles, and the emission currents from various cathode components as a function of discharge current and propellant (mercury) mass flow rate for a number of different cathode orifice diameters. The experimental set up included the capability of rapid, in vacuo variation of the internal cathode pressure and the orifice diameter. These capabilities were considered necessary to eliminate insert surface condition changes which could occur with time or exposure to air. The results include an empirical correlation of the internal pressure, mass flow rate, and orifice diameter with the cathode emission current; as well as, the effects of each of these parameters on the insert temperature profile and the emission current distribution. The results show that the insert temperature profile is essentially independent of orifice diameter but depends strongly on internal cathode pressure and emission current. It is shown that for normal cathode operation $\sim$ 87% of the emission current is from the insert while only $\sim$ 10% comes from the orifice plate. By using a special segmented insert, the emission region of the insert is shown to be localized on the last few millimeters at the downstream end of the insert. The product of internal cathode pressure and insert diameter is shown to be important in determining the emission location and the minimum keeper voltage. The simultaneous measurement of local insert temperature and emission current allow the calculation of the average effective work function for various segments of the insert. The results support earlier work indicating that field-enhanced, thermionic emission is the most probable candidate for the emission mechanism for this type of hollow cathode. The results are discussed as they apply to the design of hollow cathodes for thrusters.

Introduction

The orificed mercury hollow cathodes used in electron bombardment thrusters are critical components in the thruster design from both a lifetime and a performance viewpoint. One long term goal of hollow cathode research, both by the present authors and other researchers in the field, has been the thorough understanding of the physical phenomena involved in hollow cathode operation leading ultimately to the development of an analytical model to predict cathode performance. This goal has proven elusive. A number of models of various kinds of hollow cathodes have been proposed. These models have shed light on various aspects of cathode physics but have not proved wholly satisfactory, or capable of providing a fully self-consistent explanation of cathode operation. Ferreira and Delcroix[1] recently proposed a theoretical model for tubular (non-orificed) hollow cathodes which correlates well with experimental data but requires the knowledge of the emitting surface temperature profile as input. Using this profile as input is generally unsatisfactory, however, both because the profile is usually not known and because the results are extremely sensitive to these temperatures. Bessling,[2] Krishnan,[3] and Siegfried[4] have all presented models which correlated various aspects of cathode operation with experimental data and led to a better understanding of certain hollow cathode phenomena. This is all to suggest that the search for physical understanding and analytical rigor continues; and that, both the practical matter of designing hollow cathodes for thrusters and the ultimate goal of developing a fully self-consistent model to predict cathode performance are dependent on gaining additional experimental evidence about hollow cathode operation.

The objective of this study has been to determine precisely where the emmission takes place in the hollow cathode and what operating parameters are important in determining hollow cathode operating characteristics. This experimental investigation relies heavily on the use of a special quartz tube, hollow cathode mounted in a test fixture which allows the simultaneous measurement of internal pressure, insert temperature profiles, and the emission currents from various cathode components as a function of discharge current and propellant mass flow rate for a number of different cathode orifice diameters. The results of these measurements will be presented and discussed as they pertain to an understanding of the basic cathode phenomena and to the design of hollow cathodes for thrusters.

Apparatus and Procedure

Cathode

In order to isolate the insert electrically and to provide for direct visual observation of the insert, a special cathode was constructed using a quartz body tube in the manner suggested by Fig. 1.

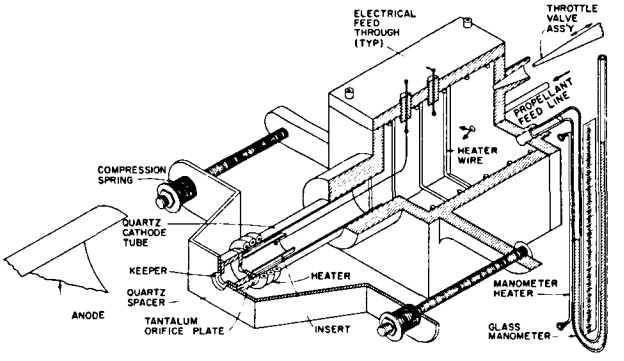

Fig. 1 Hollow cathode test configuration.

* Work performed under NASA Grant NGR-06-002-112.

The cathode consisted of a quartz tube 6.3 mm OD x 4.0 mm ID covered on the downstream end with an orifice place. The end of the quartz tube and the back of the orifice plate were both ground flate to facilitate a good seal between them. The plate was held tight against the tube by a tensioning device which also acted as the keeper electrode. This electrode had an orifice diameter of 3.6 mm and was separated from the orifice plate by a 2.5 mm thick quartz spacer as shown in Fig. 1. Although preliminary testing was conducted using the orifice plate shown in the figure, most of the data presented in this paper were collected using the orifice plate/valve assembly shown in Fig. 2.

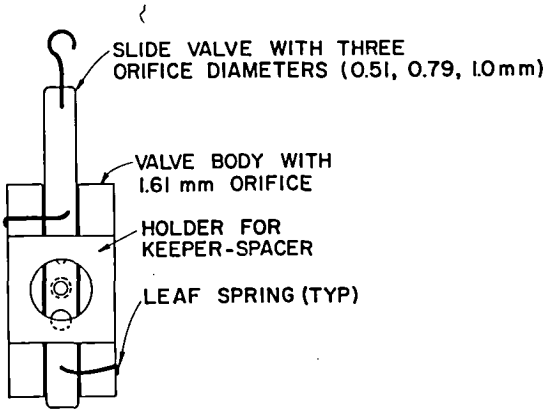

Fig. 2 View of downstream side of orifice plate/valve assembly.

This assembly consisted of a tantalum body ground flat on both sides having an orifice diameter of 1.6 mm drilled through it together with a sliding orifice plate. This tantalum orifice slide, also ground smooth and flat, had three orifices with diameters of 0.51, 0.79, and 1.0 mm drilled through it. A pair of leaf springs held the slide in contact with the downstream side of the body. By moving the slide to match different slide orifices with the body hole, one could change the cathode orifice diameter quickly without the necessity of opening the bell jar and exposing the insert to the atmosphere. During cathode operation the orifice diameter was changed incrementally by turning off the discharge and moving the slide to change from one diameter orifice to another. It was also possible, by moving the slide through a short distance, to change the orifice area continuously without having to shut off the discharge. For some tests this latter mode of operation was preferred.

The quartz tube was covered on the outside by a wire heater wrapped in a serpentine pattern, which was in turn covered on both its interior and exterior surfaces by a tantalum foil radiation shield. The heater covered $\sim$ 75% of the perimeter of the quartz tubing allowing a longitudinal gap along one side of the cathode through which the insert could be viewed. The insert, which was 3.9 mm in diameter, was constructed of 0.025 mm tantalum foil coated with chemical R-500.* It was placed in the quartz body in such a way that it presented a single layer thickness in the viewing direction. Its construction will be discussed in greater detail later. The cathode assembly was mounted in the support structure shown in Fig. 1. The anode was a cylinder 6 cm in diameter and 8 cm long, made from perforated metal sheet. The stainless steel support structure shown in Fig. 1 included a plenum chamber with removable covers on both the top and the upstream end. The inside of the chamber was fitted with a wire heater to prevent mercury condensation. The top cover was fitted with five electrical feedthroughs which could be used to make electrical connections to the inside of the cathode such as the one to the insert shown in Fig. 1. The rear plate contained a tapered hole which was used as a throttle valve seat and another straight hole which accepted the pressure tap of a U-tube monometer. The needle of the throttle valve was made of a piece of tapered quartz tubing which could be moved axially to vent a portion of the mercury propellant into the bell jar. This allowed rapid adjustment of the pressure in the plenum chamber without requiring an adjustment of the mercury vaporizer heater.

Most of the cathode current data in this paper will be presented as total emission current, I_E, which is the sum of the keeper current, I_K, and the anode current, I_D. It was found that, for a given emission current the keeper current, I_K had a negligible effect on the insert temperatures and the internal pressure (over the range of interest for thruster application). For all tests the keeper current was therefore held constant at 0.3 A. The bell jar pressure was in the 10^{-3} to 10^{-4} torr range for the tests.

Insert Construction

Earlier testing showed that insert temperatures were very dependent on operating history and exposure to the atmosphere. This was found to be particularly important with a single layer, foil insert which did not contain a significant amount of R-500 to be released once the original surface was depleted or contaiminated. Since the surface work function of the insert is critically important in determining insert temperatures as well as keeper and discharge voltages, considerable care was taken in the fabrication and conditioning of the inserts. Inserts were constructed of 0.025 mm tantalum foil 15 mm long and $\sim$1.75 times the perimeter of the 3.9 mm diameter mandrel around which they were wrapped. The flat foil was first cleaned with chlorothene and then with acetone. The three quarter turn section which would be two layers thick in the final insert was coated with R-500. This was done to provide a reservoir of R-500 thereby extending the useful lifetime of the insert. The foil was then wrapped around the mandrel and both free edges were spot welded. The inside diameter of the insert and the upstream side of the orifice plate were then coated with R-500. The insert was assemblied in the cathode with the one quater circumference section, which was a single layer thick, positioned where it could be viewed directly. The downstream edge of the insert was positioned $\sim$ 0.5 mm from the orifice plate. The insert was conditioned by allowing the cathode assembly to warm up overnite with the cathode tube heater operating at $\sim$ 850°C and the mounting structure heaters at operating temperature. The cathode was started and allowed to operate at 2 to 3 A emission current until the insert temperatures had stabilized. This required 4 to 5 hours of operation. On initial startup it was found

* J. R. Baker Chemical Co., Phillipsburg, New Jersey.

that the insert would operate cold (no visible radiation) or would have a small hot region along or near the downstream edge. During the break in period the temperature profile would change to what was considered the normal operating condition for this insert, a condition that will be shown later in the results. Between operating periods the cathode was maintained in a vacuum environment with the mechanical pump. If the bell jar was opened it was kept open for as short a period as possible. After the initial break in, the cathode warmup time was a few hours and the cathode was generally allowed to run for an additional couple of hours before data were collected. These precautions were sufficient to insure that insert temperatures at a given operating condition could be reproduced to within ± 25°C during different runs and within ± 10°C or less during a single run.

Segmented Insert

A special, segmented insert was constructed in order to determine more precisely where the emission takes place on the insert and to correlate this with the insert surface temperature at that location. An insert was first constructed in the manner described previously, and then it was cut into four 2 mm long sections and one 7 mm long section. Each section was connected with a lead wire to a separate feedthrough on the top cover of the cathode mounting structure. A sketch of this segmented insert is shown in Fig. 3. The segments were separated by ∿ 0.3 mm, and the emission current for each segment was monitored separately. The conditioning procedure and precautions mentioned above in regard to the continuous insert were also followed with this segmented one.

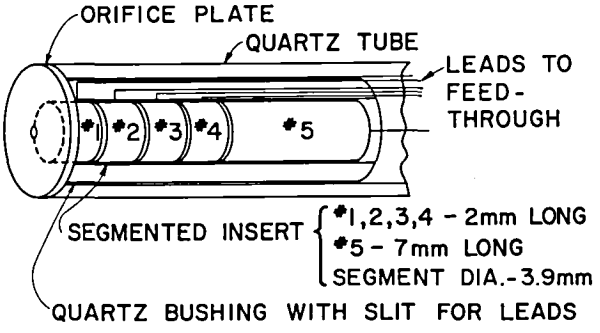

Fig. 3 Detail of segmented insert.

Pressure Measurements

The stagnation pressure in the plenum chamber supporting the quartz cathode was sensed by a U-tube manometer (Fig. 1) filled with Dow Corning 705 diffusion pump fluid. This fluid has a vapor point at 0.5 torr of 245°C compared to 108°C for mercury. The heater on the high pressure side of the manometer maintained that column at a temperature which prevented mercury condensation without causing the diffusion pump fluid to boil. The manometer was contained completely within the bell jar and thus provided direct measurement of the pressure difference between the bell jar and the plenum chamber. The manometer had a pressure range of 24 cm of fluid which was equivalent to 18.2 torr.

The fluid levels in the manometer could easily be read to within ± .5 mm, which for the low specific gravity indicating fluid was equivalent to 0.038 torr. Because of this the precision of the pressure data is considered to be very good. However, the heater on the high pressure column of the manometer causes that column to be at a higher temperature than the low pressure column. This significantly affects the fluid density of the high pressure column. The results presented in this report are corrected for this effect. The uncertainty associated with this correction is estimated to be 0.25 torr although errors as high as 1 torr are considered possible. Unfortunately the greatest absolute error occurs at low pressures when the two column heights are nearly equal resulting in what could be substantial relative error at these pressures.

Throttle Valve

In order to determine whether the throttle valve could be used to adjust the internal pressure and, therefore, the flow rate through the cathode orifice rapidly and without adverse experimental effects, the following experiment was conducted. The cathode was operated at a constant emission current for four different flow rates into the plenum chamber. In each case the internal cathode pressure was maintained at a constant value by adjusting the throttle valve. This test was performed on three occasions and included operation with two different orifice diameters and operation at two different emission currents. In all cases, it was found that, for a constant emission current and constant internal pressure, the insert temperatures remained essentially constant regardless of the flow rate into the plenum chamber. The total mass flow into the plenum chamber does affect the bell jar pressure however and, as expected, changes in total flow rate were found to have a small effect on the discharge and the keeper voltages.

Temperature Measurements

In all of the tests which will be described in this paper, insert surface temperatures were measured using a micro-optical pyrometer. This method of temperature measurement is influenced by both the emissivity of the radiating surface and the transmissivity of the quartz tube and glass bell jar. These effects were accounted for by calibrating the pyrometer against a platinum/platinum-rhodium thermocouple. The calibration was carried out for a sample of the tantalum foil used in making the inserts. The material sample was spot welded to a section of swaged heater wire and the thermocouple was attached to the surface of the sample. This sample/heater assembly was then inserted into a quartz tube and the whole apparatus was placed in the bell jar. The surface temperature of the sample was then measured at various heater powers using both the thermocouple and the micro-optical pyrometer. All of the results contained in this report were corrected based on the calibration curves resulting from these tests.

Experimental Procedure

The purposes of the experiments which will be reported in this paper were to determine the effects of internal pressure, orifice diameter, and emission current on the temperature and emission distribution

of the insert. This was done by operating the cathode over a range of emission currents while using the throttle valve to adjust the internal pressure and the orifice plate slide to set the orifice diameter. The details of the individual experiments will be discussed in the next section along with the results which were obtained.

Results

Pressure - Mass Flow Rate

The stagnation pressure in the plenum chamber immediately upstream of the cathode was measured with the manometer for emission currents of 0, 0.3, 0.5, 0.7, 1.3, 2.3, and 3.3 amps, orifice diameters of 0.51, 0.79, and 1.00 mm, and for mass flow rates ranging from 90 to 450 mA. The throttle valve was closed during these tests. Fig. 4 shows the pressure in torr plotted as a function of mass flow, $\dot{m}$, divided by the orifice diameter squared, d_0^2, in mA/mm^2 as determined in these tests. The data for the case where there is no discharge present follows closely a single curve for all three orifice diameters.

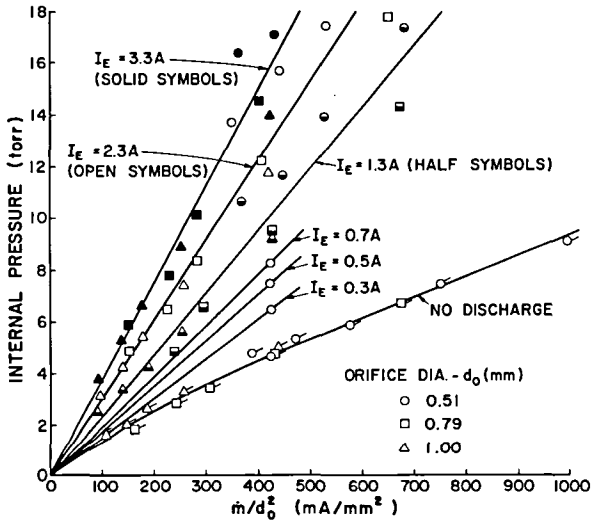

Fig. 4 Internal pressure correlation of mercury hollow cathode.

The fact that the data for this no discharge case is not linear with respect to flow rate is not surprising since pressures in the range from 0.5 torr to 18 torr correspond to flow conditions in the regime for transition from free molecular to continuum flow for all three of the orifice diameters. However, the curve can be characterized by two slopes: one at the origin and one for the straight portion of the curve at higher flow rates. The data for the cases where there is an emission current are fitted with straight lines through the origin. These straight lines fit the data sets reasonably well except for the data at higher pressures particularly for the smallest orifice diameter of 0.51 mm, which shows considerable scatter. Fig. 5 plots the slope of the straight lines in Fig. 4 as a function of emission current. For the no discharge condition Fig. 5 shows both the slope at the origin, 0.014 torr mm^2/mA, and that for the straight section, 0.008 torr mm^2/mA. Although it is a purely empirical presentation of the data, Fig. 5 should

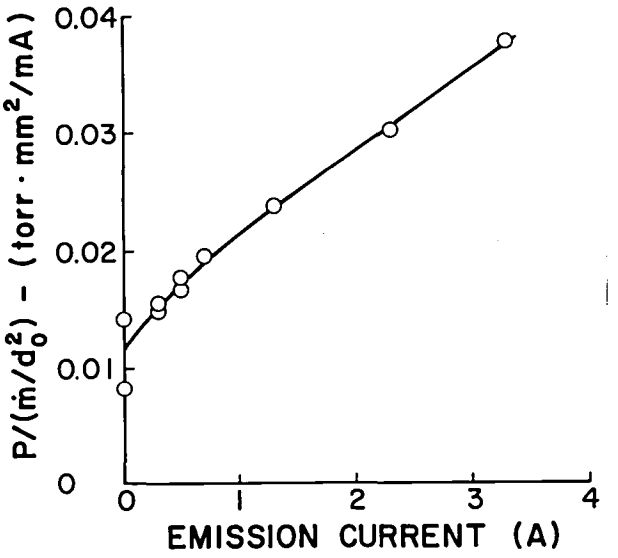

Fig. 5 Effect of emission current on pressure correlation coefficient.

provide sufficient information to yield a reasonable estimate of the stagnation pressure upstream of the insert in a mercury hollow cathode over a wide range of emission current, flow rate, and orifice diameter conditions. It is noteworthy that both the theory of free molecular flow and the theory of continuum, choked flow predict that the pressure-mass flow relation takes the functional form

$$P \propto \sqrt{T/m}\,\frac{\dot{m}}{d_0^2} \qquad (1)$$

where T is the gas stagnation temperature at the orifice and m is the atomic weight of the gas. This simply represents a straight line through the origin of slope $C\sqrt{T/m}$ where C is a constant of proportionality which is different for the two cases (free molecular and continuum). The gas temperature for the no discharge case was estimated on the basis of the plenum and cathode wall temperatures to be $\sim$ 425°C. However, in the presence of the internal discharge the single temperature cannot adequately describe the kinetic energy of the multi-component gas. The situation is also complicated by the fact that the stagnation pressure decreases and the stagnation temperature increases as one approaches the orifice because of the heating effect of the discharge. Presumably it is because of these effects that the ratio $(Pd_0^2/\dot{m})$ increases with emission current.

The internal cathode pressure has been found in all of the tests to be a very important parameter in determining cathode operating conditions. It is believed that the orifice diameter and the mass flow rate are important in determining internal cathode processes primarily to the extent that they determine the internal pressure. For this reason, all of the data presented in this paper will use the pressure as a parameter rather than mass flow rate. Mass flow rate through the cathode orifice at a given condition can, however, be easily estimated from the results shown in Fig. 5.

Insert Temperature Profiles

The effect of changes in orifice area on insert temperatures was investigated by operating the

cathode at a constant emission current of 3.3 A and a constant internal pressure of 3.3 torr while varying the orifice area. This was done by establishing the above pressure and discharge conditions using the 1.0 mm diameter orifice ($\sim$ 0.79 mm^2) and recording insert temperatures. The orifice slide was then moved to close the orifice partially to what was estimated on the basis of the pressure increase to be an area of $\sim$ 0.40 mm^2. The throttle valve was then opened to maintain the pressure at 3.3 torr and the insert temperatures were again recorded. This procedure was repeated for an orifice area of $\sim$ 0.21 mm^2. The results of this experiment are shown in Fig. 6. Both the magnitudes of the insert temperatures and the insert temperature profile are seen to be relatively insensitive to the almost four-fold change in orifice area as long as the emission current and pressure are held constant.

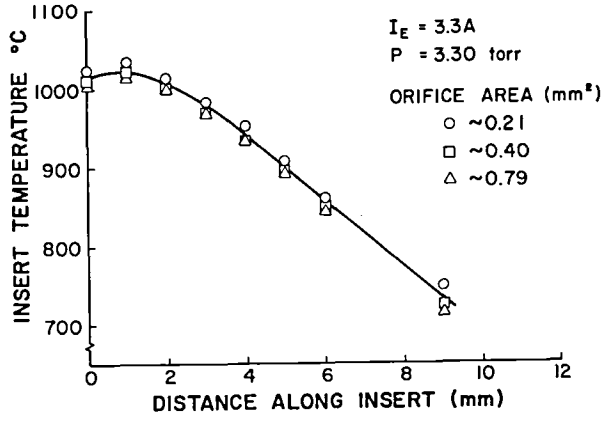

Fig. 6 Effect of orifice area on insert temperature profile.

This experiment was also conducted for emission currents of 2.3 and 4.3 A on two different occasions. In each of these tests there was a slight tendency for the insert temperature to increase as the orifice area was decreased. However, in all of these tests the results were similar to those shown in Fig. 4. The maximum increase in insert temperature observed during the tests was $\sim$ 35°C, although in most instances it was considerably less than this. It was interesting to note during the tests that, although reductions in orifice diameter at constant internal pressure did not cause a substantial increase in insert temperature, they did result in a substantial increase in orifice plate temperature.

The next parameter to be varied was the internal pressure. The cathode was operated at a constant emission current of 3.3 A with the 0.79 mm orifice while the internal pressure was varied from 0.90 torr to 12.7 torr. The pressure was adjusted using the throttle valve. Fig. 7 shows that the internal pressure changes cause significant change in the insert temperatures. For example, the maximum insert temperature decreased by $\sim$ 125°C as the pressure was increased from 0.9 torr to 12.7 torr.

Finally, the effect of emission current on the insert temperature profile was determined by operating the cathode with the 0.79 mm orifice at a constant pressure of 6.3 torr while varying the emission current from 1.3 to 4.3 A. As shown in

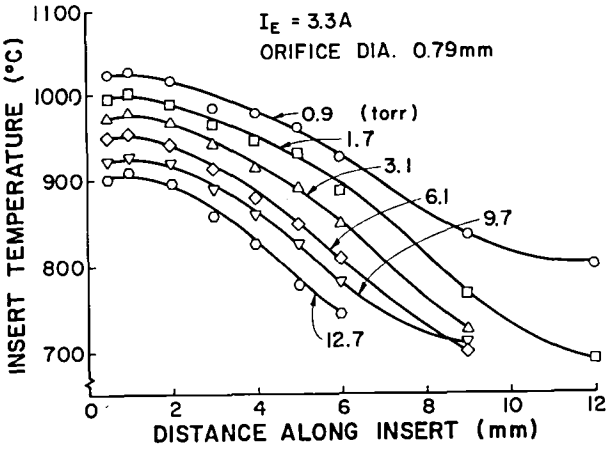

Fig. 7 Effect of internal cathode pressure on insert temperature profile.

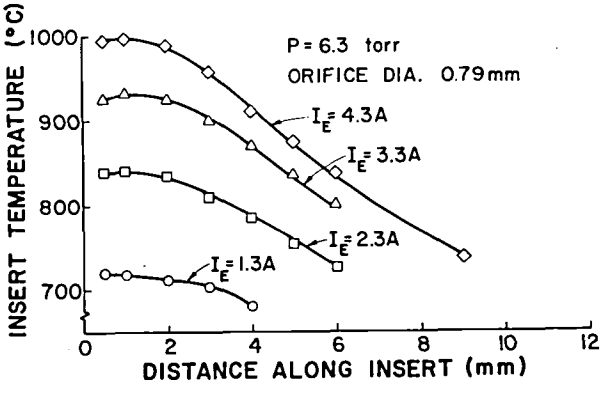

Fig. 8 Effect of total emission current on insert temperature profile.

Fig. 8, the temperature profiles remain similar as the emission current is increased while the maximum temperature increases from 720°C at 1.3 A to 1000°C at 4.3 A.

Emission Current Distribution

Insert and orifice plate emission currents were measured separately in all of the tests described above. It was found that the insert contributed approximately 85% of the total emission current while the orifice plate contributed $\sim$ 10%. The remainder of the current can presumably be accounted for as ion current to the internal surfaces of the cathode mounting structure and to other surfaces at ground potential in the facility. The relative fractions of the current from the insert, orifice plate, and structure for a given operating condition were found to be constant and very repeatable. There were, however, definite trends in the percentage of insert and orifice plate emission current which could be identified with changes in discharge current, pressure, and orifice diameter. Over the wide range of these parameters, the fraction of emission current from the orifice plate ranged from 3 to 12% and the fraction of the emission current coming from the insert ranged from 80 to 90%.

The importance of the insert in the emission process was also demonstrated through a test in which the insert was isolated by disconnecting it from the circuit during cathode operation. This caused an immediate extinction of the discharge. However, disconnecting the orifice plate from the circuit showed little effect on the discharge outside of a slight (less than one volt) increase in discharge voltage. When the orifice plate was disconnected, it was found to float at 3 or 4 volts above ground potential. The fact that the orifice plate can be floated with respect to ground without significantly affecting cathode operation is considered important. By operating with the floating orifice plate one would expect to reduce orifice erosion because operation in such a condition would result in a marked decrease of the impact energy of the impinging ions.

It was considered desirable to investigate further the effect of the above parameters on the emission current distribution between the insert and orifice plate and to determine more accurately the emission current profile for the insert. In order to do this an experiment was set up using the same experimental configuration used for the insert temperature measurements but incorporating the segmented insert described earlier and shown in Fig. 3. It was hoped that the ability to measure insert temperatures and emission currents simultaneously would shed additional light on the location and type of emission process taking place in the cathode.

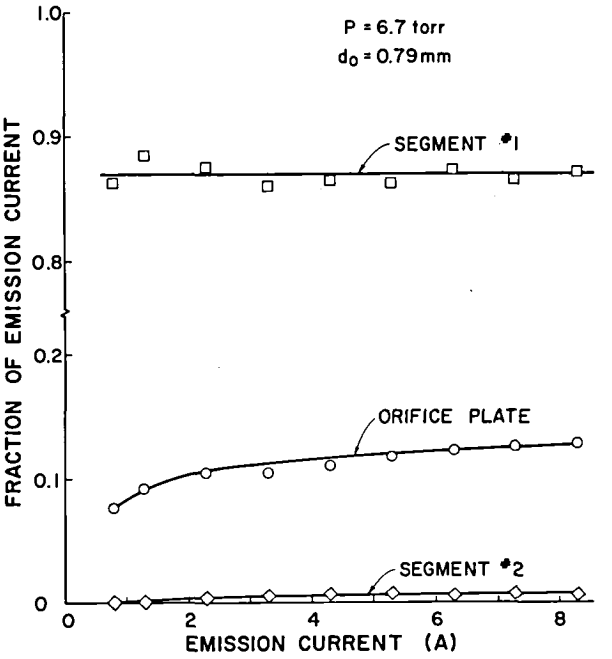

Fig. 9 Emission current distribution in a mercury hollow cathode.

The experiments conducted with the segmented insert were carried out in a manner similar to those described for the temperature measurements of the continuous insert. The pressure was controlled using the throttle valve and the orifice diameter was selected by moving the orifice valve slide. Temperatures and emission currents were measured for each insert segment and for the orifice plate assembly. The temperature was measured at the center of each of the short insert segments (Fig. 3). The temperature of these short segments was found to be reasonably uniform (typically a gradient of $\sim$ 10°C along the segment was observed). The #1 segment was an exception and was found to have a local hot region during most of the testing. This region, which initially had a temperature as much as 65°C hotter than the rest of the segment, eventually dropped in temperature to the same value as the rest of the segment. The temperature at the center of each segment was considered to represent a reasonable value of the average segment temperature and is the one which will be presented in the results and used in later calculations of average surface work function.

Figure 9 shows that at a pressure of 6.7 torr and an orifice diameter of 0.79 mm most of the emission comes from segment #1 of the insert. It is also seen that the emission fraction of 0.87 for this segment is essentially independent of total emission current. The emission fraction of the orifice plate increases rather rapidly at low total emission currents changing from 0.075 at 0.8 A to 0.11 at 2.3 A. However, at emission currents over 2.3 A, the orifice plate fraction is seen to increase by only 0.004 per amp of emission current. Figure 9 shows that segment #2 of the insert contributes less than 1% of the total emission current. The results of Fig. 9 are felt to be significant because they indicate that at this moderate pressure the emission region is localized to the downstream end of the insert including at most the 2 mm of the insert closest to the orifice plate, and it probably covers only a small fraction of that region.

The effect of pressure on the emission current distribution is shown in Fig. 10 for the cathode operating at an emission current of 7.3 A with the 0.79 mm orifice. Figure 10 shows that at pressures over 4 or 5 torr the emission current is distributed in essentially the same way as indicated in Fig. 9. However, as the pressure is reduced below $\sim$ 4 torr, the emission current coming from the orifice plate and the first segment is seen to decrease; and the second segment is seen to become active in the emission process. At still lower pressures segment #3 and then #4 begin to make a small contribution to the emission current.

Qualitative results obtained in the early stages of this investigation suggested that the work function and the pressure are both important in determining the area of the insert over which the emission takes place. Figure 11 shows temperature profiles for a cathode operating with an insert which was believed to have a surface work function which was somewhat higher than usual due to depletion or contamination. At the high cathode pressures the emission region, as indicated by the shape of the temperature profile, was at the tip of the insert. As the pressure was decreased the temperature profile changed shape becoming flat over a longer portion of the downstream end of the insert, suggesting that the emission region was covering a greater area of the insert. This is the same sort of result seen in Fig. 10 where more of the segments began to emit as the pressure was decreased. Situations were observed with inserts that appeared to

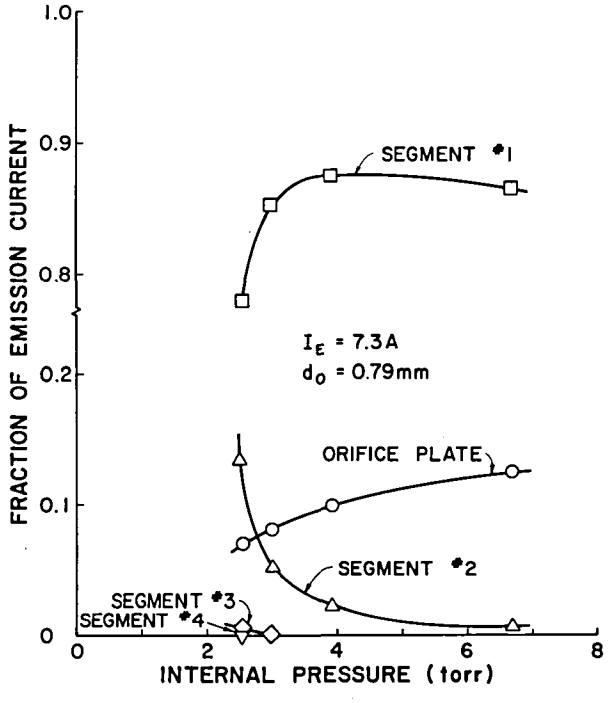

Fig. 10 Effect of internal pressure on emission current distribution.

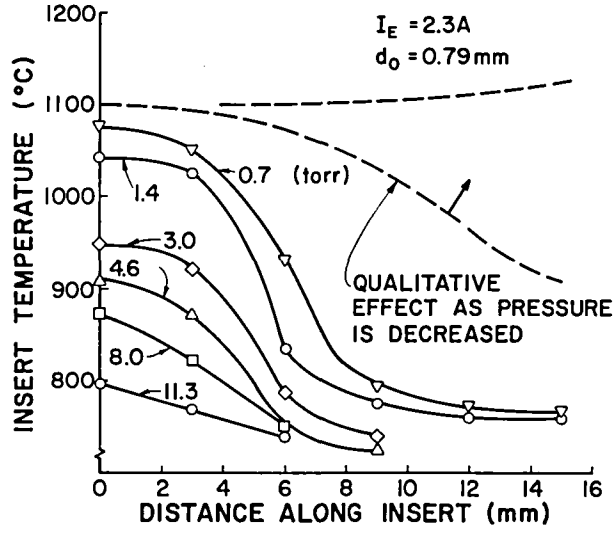

Fig. 11 Effect of internal pressure on insert temperature profile for depleted or contaminated insert.

be almost completely depleted of R-500 in which the insert temperature profile changed qualitatively in the manner indicated by the dashed lines of Fig. 11 as the pressure was decreased to very low values. This suggests that, if the insert work function is low enough or if the pressure is sufficiently high, the emission will take place near the downstream end of the insert, but that as the pressure decreases and/or the work function increases the emission region will tend to move upstream covering more of the surface area of the insert.

The orifice diameter was also found to affect the fractions of the emission current coming from the insert and the orifice plate. Figure 12* shows that as the orifice diameter is increased while internal cathode pressure is held constant the fraction of the emission current from the insert segment #1 increases and that from the orifice plate and segment #2 decreases.

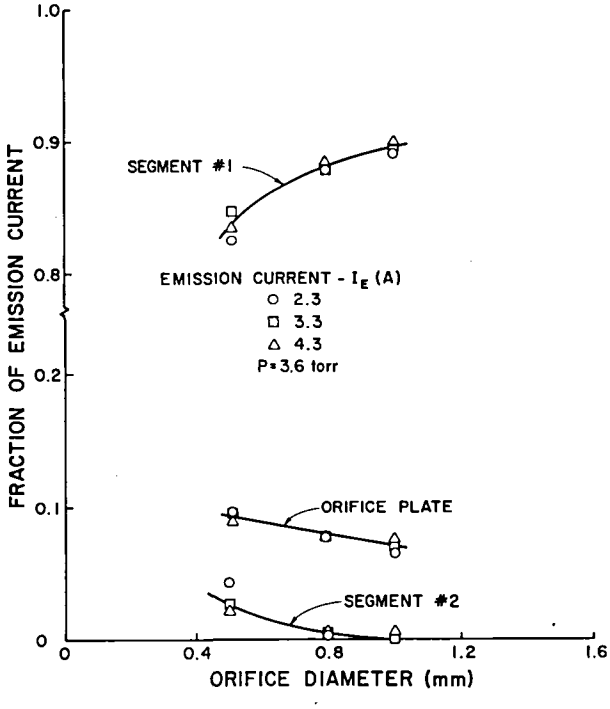

Fig. 12* Effect of orifice diameter on emission current distribution.

Figure 12 also shows that the effect due to orifice diameter is rather insensitive to emission current, at least over the range of 2.3 to 4.3 amps.

Discussion of Results

Insert

The results presented in the previous section suggest a number of important features of orificed, hollow cathode operation which may be useful in cathode design. It was seen that the insert is responsible for most of the emission and that under normal operating conditions the emission is localized to the downstream end of the insert. This suggests that insert design might be improved by providing a surface specifically designed for emission. The low work function material would then be replenished by a separate dispenser or reservoir designed to supply the material directly

* Figure 12 was incorrect as it appeared in the original publication of this paper. The figure and associated text have been corrected in this printing.

and specifically to the emission surface. One means of accomplishing this would be to use an impregnated, sintered tungsten insert which is sealed on all outer surfaces except the last few millimeters on the downstream end of the inside diameter. This would force all of the R-500 to evolve through the emission surface.

Orifice Plate

The results showed that the important operating parameters affecting the insert temperatures were the surface work function, the internal pressure, and the total emission current. The insert temperatures, were on the other hand, found to be rather insensitive to the orifice diameter. This suggests that the main functions of the orifice are to restrict the propellant flow in order to maintain a high neutral density inside the cathode and to provide a current path to the downstream discharge. The effect of the orifice plate as an emissive surface was seen to be minimal. It was also suggested that one way of reducing orifice plate erosion would be to allow the orifice plate to float with respect to ground in order to reduce the incident energy of the impinging ions.

It should be noted here that the orifice diameter does affect the keeper and the discharge voltage as well as the orifice plate temperature. Figure 13 shows the effect of orifice diameter on keeper voltage, discharge voltage, and orifice plate temperature for the experimental quartz tube cathode operating at an emission current of 3.3 A and an internal pressure of 3.2 torr. The temperatures shown in the figure were measured on an outer edge of the orifice plate/valve assembly. The results of Fig. 13 agree with evidence presented by Crawford[5] which showed that a plasma sac forms on the cathode side of a constriction in a plasma discharge. This sac was found to be bounded by a double sheath which accelerates electrons across the sheath to sufficiently high energies so that they can produce a dense plasma with a high ionization fraction within the constriction. Crawford measured the potential drop across such a constriction sheath in a mercury discharge tube. He found the increase in plasma potential across the sheath to be on the order of 10 volts and to be dependent on the ratio of the diameter of the discharge tube on the cathode side of the constriction to the diameter of the constriction. In hollow cathodes the orifice provides a discharge constriction which would be expected to produce the type of double sheath found by Crawford. The diameter dependence of the potential drop across such a constriction sheath at the hollow cathode orifice is considered to be the probable basis for the voltage-orifice diameter effect seen in Fig. 13.

Insert Diameter and Internal Cathode Pressure

One parameter which was not varied in this study, which is almost certainly of importance in the internal cathode process, is the insert diameter. Krishnan[3] working with large diameter (non-orified) argon hollow cathodes suggested that the parameter λ/d, the ratio of the energy exchange mean free path to the cathode diameter, determines the length of the cathode region over which the discharge establishes itself. He presented evidence to indicate that the optimum operating condition was one at which λ/d was approximately unity and that this condition resulted in the site of the

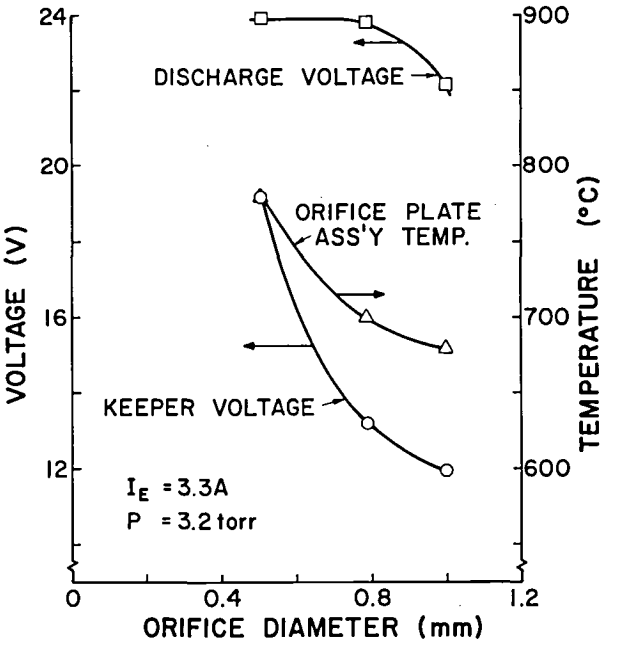

Fig. 13 Effect of orifice diameter on discharge voltage, keeper voltage, and orifice plate-valve assembly temperature.

maximum emission current density locating itself approximately one diameter upstream of the cathode exit. Lidsky[6] and Delcroix[7] both found experimentally that one criterion for the emission location was that the local pressure-diameter product be equal to $\sim$ 1 torr-cm. Although the insert diameter was not varied in the present investigation, there was evidence that the insert diameter and specifically that the pressure-insert diameter product is of importance. This was demonstrated during some preliminary tests of the quartz tube cathode equipped with a thoriated tungsten orifice plate having an orifice diameter of 0.51 mm with a 1.5 mm diameter counterbore on the upstream side of the orifice channel. The orifice plate disc was 6 mm in diameter and 0.9 mm thick. While operating the cathode with this stepped orifice plate it was found that the fraction of emission current from the orifice plate increased with increases in internal cathode pressure in a manner similar to that shown in Fig. 10. However, as the mass flow rate was increased beyond a fairly well defined transition point the orifice plate would begin to emit up to 99% of the emission current and the insert emission would effectively cease. For an emission current of a few amperes the transition occurred at a mass flow rate of about 70 mA which was estimated to correspond to an internal pressure of $\sim$ 8 torr. When the transition occurred and the orifice began to emit, the temperature at the downstream end of the insert would drop from 1030°C to less than 840°C while the outside edge of the orifice plate increased in temperature from $\sim$ 900°C to $\sim$ 1130°C. This transition was very consistent and repeatable, but was seen only with this orifice plate and only when the orifice plate was installed with the counterbore on the upstream side. This suggests that the upstream counterbore region was beginning to operate as in insert at high pressures where the

counterbore diameter-pressure product was nearer the desired operating point than the insert diameter-pressure product. It was expected that a similar transition would be seen with the orifice plate/valve assembly shown in Fig. 2, since it had a 1.6 mm diameter bore immediately upstream of the smaller orifice on the slide. However, no transition was seen under any operating conditions with the orifice plate/valve assembly. It is believed that the reason no transition occurred in this case was because the greater mass and surface area of the orifice plate/valve assembly acted to cool the orifice region below a temperature at which it could emit.

In order to test this hypothesis regarding the orifice temperature, an orifice plate was fabricated from a tantalum disc ∿ 10 mm in diameter and 1.0 mm thick. This orifice plate had a 0.51 mm orifice with a 1.8 mm diameter counterbore that was ∿0.75 mm deep. The orifice counterbore was coated with R-500. Operation with this orifice plate showed that a transition between emission from the insert to emission from the orifice plate could occur at internal cathode pressures above ∿ 7 torr. However, a transition would actually occur above this pressure only if the emission current was increased above ∿ 5.0 A. An emission current of 5.0 A was sufficient to heat the orifice plate so that it began to glow red. Once the emission switched to the orifice plate, the emission current could be decreased to a few amperes, and the emission would continue to come from the orifice plate until the pressure was decreased beflow ∿ 7 torr. This orifice plate had a thermal mass and surface area intermediate between the thoriated tungsten orifice plate and the orifice plate/valve assembly. The above results, therefore, support the earlier suggestion that since the thermal properties of the orifice plate affect the surface temperature in the orifice region, they can be a determining factor on whether or not the emission region can establish itself on the orifice counterbore. Additional support of this was found by covering the wall of the orifice plate counterbore with a few layers of 0.025 mm tantalum foil. The foil, since it presented an emission surface which was not in very good thermal contact with the orifice plate, would presumably be able to maintain a temperature which would be sufficient for emission. This appeared to be the case because operation with the foil in place allowed a repeatable transition of the emission location to occur at a pressure of 2 - 3 torr when operating at an emission current of 3.3 A. It should be noted that evidence of a similar transition phenomenon with a stepped orifice plate was previously reported by Fearn.[8] Fearn suggested that the shifting of the emission region would also account for the transition from the high-voltage plume to the low-voltage spot mode of operation. In the present investigation, it was found that the so called plume-to-spot mode transition occurred with all of the emission current coming from the orifice plate which indicates that it is not a result of the shift in emission location.

The above tests indicate that both the pressure and the emission surface diameter are important parameters in determining the location at which the emission process takes place. Further, testing is needed to better quantify this effect; specifically, it would be desirable to remove the effects associated with the thermal properties of the orifice plate by conducting the test with an insert having either a multiple or a continuously varying (such as in a conical section) cross-section but with uniform thermal properties. It is interesting to note, however, that the pressure diameter-product estimated from the tests with the stepped orifice plate are similar to those reported by a number of other researchers. At the pressure condition where the emission transferred to the orifice plate, the product of the upstream stagnation pressure and the counterbore diameter was ∿ 1.25 torr-cm in the case of both the thoriated tungsten orifice plate and the tantalum orifice plate. For the case of the tantalum orifice plate having the tantalum foil insert in the counterbore, the pressure-diameter product was ∿ 0.5 torr-cm. Lidsky[6] determined, based on experiments with a tubular hollow cathode operating with a number of gases (H_2, He, A, N_2), that the emission region locates itself at a point where the local pressure-diameter product is ∿ 1 torr-cm. Delcroix[7] found for similar cathodes that the pressure-diameter product criteria was in the range of 0.2 to 1.6 torr-cm over a very wide range of mass flow rates. It should be stressed that the pressure-diameter criteria referred to above are based on the local pressure which may be considerably lower than the upstream stagnation pressure. However, it is believed to be significant that the results for the orificed hollow cathode of the present investigation are in approximate agreement with those referenced above for tubular, non-orificed cathodes.

Discharge Voltages

One goal in the design of hollow cathodes for thrusters has been to provide a cathode which will operate at a minimum discharge voltage for a given emission current. Here again a pressure-characteristic dimension product appears important. Martin and Rowe[9] found that for a low-voltage arc operating with noble gases between plane, parallel electrodes that a pressure-electrode spacing product of ∿ 3 torr-cm resulted in a minimum discharge voltage. This agrees qualitatively with the results discussed above concerning emission location which is presumed to be determined ultimately by the criterion of operation at some minimum energy condition. It also has implications for designing cathodes to minimize the keeper voltage. It is easy to imagine with the orificed, hollow cathode that a number of characteristic dimensions are of importance in minimizing the voltage. The insert diameter is important because the plasma potential adjacent to the insert surface is dependent on the volume plasma processes taking place within the boundary of the insert. As discussed previously, the orifice diameter affects the potential drop across the orifice region; and, finally, the keeper-orifice plate separation distance would be expected to have some effect on the potential drop across the region between the orifice plate and the keeper electrode. In each case the pressure of interest would be the local pressure in the region of the characteristic dimension. If all of these variables are, in fact, important in determining the keeper voltage, then a rather complex experiment would be required to establish the importance of the various effects. This was not done; however, the effect on keeper voltage of varying the internal cathode pressure was investigated.

Figure 14 shows the keeper voltage normalized by the minimum keeper voltage plotted against the internal pressure for the experimental cathode operating with the 0.79 mm diameter orifice and

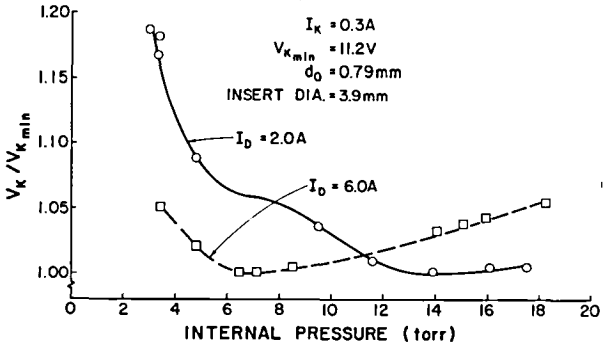

Fig. 14 Effect of internal cathode pressure on normalized keeper voltage.

3.9 mm diameter insert at a keeper current of 0.3 A and discharge currents of 2.0 and 6.0 A. Figure 14 shows that there is a definite minimum in keeper voltage for the 6.0 A condition at a pressure of ∿ 7 torr. The 2.0 A discharge condition shows a keeper voltage minimum at ∿ 14 torr. The 2.0 A curve in Fig. 14 shows an anomoly in the form of an inflection point at ∿ 7 torr. Data obtained with other orifice diameters showed similar but more definite inflection points and in some cases a second minimum. The data of Fig. 14 were all collected at approximately the same bell jar background pressure (i.e. total mas flow rate was held constant and the internal cathode pressure was set by adjusting the throttle valve). Operation at other total mass flow rates showed, however, that background bell jar pressure has a significant effect on the keeper voltage and the keeper voltage minimum. Though not shown in the figure, the discharge voltage was also found to go through one or more minima as the internal pressure was varied, and all of the comments above also hold for it. However, the discharge voltage is characterized by the plume-to-spot mode transition which is felt to be highly dependent on downstream conditions[4] and tends to over shadow the other effects. All of this suggests that a more carefully controlled experiment is warranted and that there probably is not a single keeper voltage minimum determined exclusively by the internal cathode pressure. In fact, this is in qualitative agreement with the earlier discussion which suggested that there are probably a number of pressure-characteristic dimension products that are important and that, depending on their relative importance, each product could result in a separate voltage minimum as the internal cathode pressure is varied. The data of Fig. 14 is presented, therefore, only as a representative case to illustrate the existence of the keeper voltage minimum and to suggest that the pressure-insert diameter product is probably one of the important parameters. It is interesting that the minimum condition found at ∿ 7 torr represents a pressure-insert diameter product of 2.7 torr-cm which is in good agreement with the results of Martin and Rowe[9] discussed earlier.

Insert Temperatures

Insert temperatures are of crucial importance in hollow cathode design because they affect both the performance of the cathode and the depletion rate of the low work function material that it contains. The results presented earlier are useful in that they show the shape of the temperature profile of the insert and indicate its sensitivity to such parameters as internal pressure and emission current. However, the magnitude of the insert temperature is highly dependent on insert design and the thermal configuration of the cathode itself. The thermal configuration of the experimental quartz tube cathode is obviously very different from that of a standard thruster hollow cathode because the quartz tube has a very low thermal conductivity and is more transparent to thermal radiation than a metallic one. An earlier experimental investigation[10] used a quartz tube cathode with a 1.9 mm diameter insert to simulate the cathode used in the 8 cm thruster. In this study insert temperature profiles were measured for a multiple layer rolled foil insert and a sintered tungsten insert under a variety of operating conditions. It was found that for each insert the maximum insert temperature varied approximately linearly with the discharge current and could be characterized by the slope of the maximum insert temperature verses discharge current line. It was also found that this slope was independent of the level of cathode heater power. For the multiple layer, tantalum foil insert used in those tests, the constant was 315°C/A and for the sintered tungsten insert the constant was found to be 137°C/A. The difference in the two constants was attributed to the different thermal properties of the two types of inserts. In the investigation discussed above,[10] it was suggested that the energy input to the insert was effected by ion bombardment of the internal surface of the insert and the major energy loss was in the form of thermal radiation between the outer surface of the insert and the cathode body. Based on these assumptions, a parameter was defined which was common to both the experimental quartz cathode and the actual cathode used in the 8 cm thruster. The details of this, which have been presented previously,[10] will not be repeated here except to note that once the insert constant is known it should be feasible to define a parameter which bridges the gap between the experimental quartz cathode and the cathode which is being modelled.

In the case of the present investigation, Fig. 15 shows the variation of maximum insert temperature as a function of emission current for the cathode operating at a pressure near 6.5 torr with the 0.79 mm orifice. Although the data does not fit a straight line over the full range of emission current, there is a straight line portion of the curve over most of the range which can be characterized by a slope of ∿ 73°C/A. The data of Fig. 15 indicated by the square symbols were obtained using the segmented insert. The temperatures represented by these data were from the center of segment #1 and are believed to be a good estimate of the bulk average temperature of that insert segment. It is interesting to note that the data in Fig. 15 for both the continuous and segmented insert fall very close together. This suggests that segmenting the insert did not alter its thermal and emission characteristics. Considering the usual cathode sensitivity to variations in insert conditions this condition is considered at least in part fortuitous. However, this result does tend to support the suggestion that the energy is transported primarily by radiation in the radial direction for this relatively thin (∿ 1.75 layer of 0.025 mm foil) insert, rather than by conduction in the axial direction.

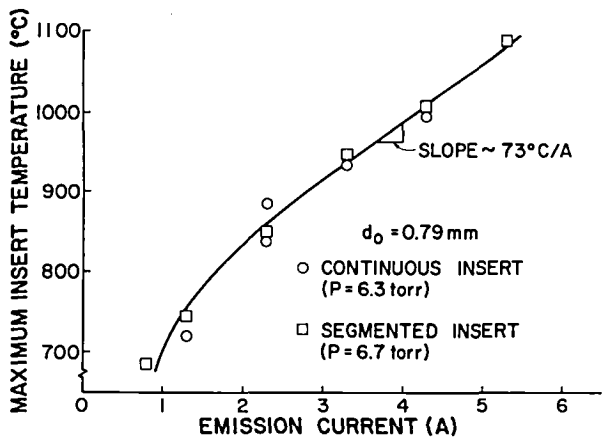

Fig. 15 Effect of total emission current on maximum insert temperature.

The effect of internal pressure on the maximum insert temperature can be presented in a manner similar to that described above where the effect of emission current was considered. Figure 16 shows the maximum insert temperature as a function of internal pressure for the cathode with a 0.79 mm orifice operating at an emission current of 3.3 A.

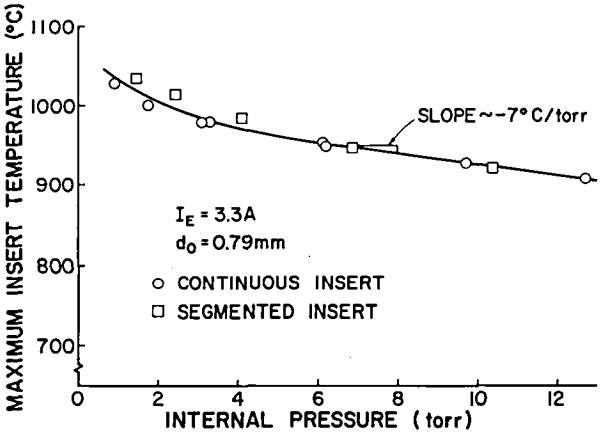

Fig. 16 Effect of internal cathode pressure on maximum insert temperature.

Again the data from both the continuous insert and the segmented insert follow the same curve. Over a wide range of pressures a straight line provides a good fit to the data. In this case the slope of the insert temperature verses internal pressure line is - 7°C/torr.

The Emission Mechanism

Evidence provided from a number of experimental investigations[1, 2, 4] has suggested that the emission mechanism for this type of hollow cathode is that of field-enhanced, thermionic emission. This experimental investigation has suggested a physical location for the emission site at the downstream end of the insert. With the test apparatus used for this work, it has been possible to measure both the insert surface temperature and the current to a segment of the insert at a given location. For the first time this allows a reasonably accurate estimate of the effective work function for the emission surface of the hollow cathode. For field-enhanced, thermionic emission the current density can be calculated using the Schottky equation

$$j = A_o T_s^2 \exp\left[-\frac{e\bar{\phi}_e}{kT_s}\right] \qquad (2)$$

where A_o = 120 A/cm^{2}K, T_s is the local insert surface temperature in °K, $\bar{\phi}_e$ is the effective work function of the emitting surface in volts, e is the electronic charge in coulombs, and k is Boltzmann's constant. The effective work function is defined by the expression

$$\bar{\phi}_e \equiv \phi_s - \sqrt{eE/4\pi\epsilon_o} \quad . \qquad (3)$$

Here ϕ_s is the surface work function associated with the material, E is the electric field adjacent to the emitting surface in volts per meter, and ϵ_o is the permittivity of free space in farads per meter. Eq. 3 shows that the effect of a strong electric field adjacent to the emission surface is to reduce the effective work function of the surface, that is it acts to pull more electrons from the surface than would be expected from the thermionic model for the prevailing temperature. Since the temperature, the surface area, and the current are known for each segment, Eq. 3 can be used to calculate the average effective work function for each segment. It should be recognized this assumes that all of the measured current from each segment is due to electron emission; and therefore it ignores the fact that a portion of the apparent emission current is actually due to a positive ion current to the segment. The effect of the ion current should, however, be small. The average effective work function has been calculated based on this assumption for the first two segments of the segmented insert. Figure 17* shows this effective work function plotted against internal pressure for the cathode operating at 3.3 A with the 0.79 mm orifice. Figure 17 shows that the average effective work function for the emitting surfaces is in the range of 1.7 to 2.0 volts. Material work functions with values this low are reasonable for tantalum surfaces coated with R-500, so the emission could be due to thermionic emission alone. However, Fig. 17 also shows that the average effective work function of segment #1 decreases as the internal pressure is increased and this suggests it is affected by the electric field. The probable mechanism for this can be seen by noting that as the internal pressure is increased the neutral density and, therefore, the plasma density both increase. An increase in the plasma density would effect a decrease of the sheath thickness and lead to larger electric fields at the insert surface. As indicated by Eq. 3, an increase in the electric field strength would decrease the effective work function. Such a decrease in the effective work function resulting from increases in internal pressure are also in agreement with the results of Fig. 16. As the cathode pressure is increased, the maximum insert temperature can decrease by 7°C/torr for a given emission current because of increased electric field strength which acts to enhance the electron emission.

11 * Figure 17 was incorrect as it appeared in the original publication. The figure and associated text have been corrected in this printing.

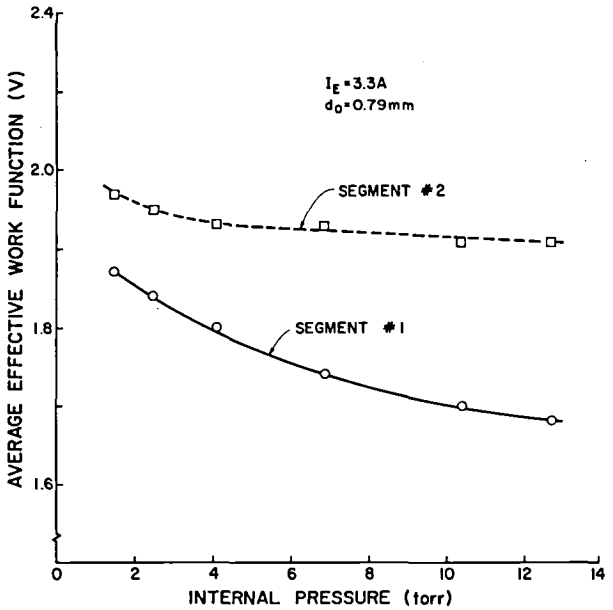

Fig. 17 Effect of internal pressure on average effective work function.

The electric field strength at the surface of the cathode can be estimated on the basis of Child's law considerations as

$$E = -\frac{dV}{dx} = -\frac{4}{3}\frac{V_c}{\lambda_D} \qquad (4)$$

where V_c is the cathode drop at the sheath and λ_D is the thickness of the sheath. The sheath thickness is assumed to be one Debye length and can be calculated as

$$\lambda_D = \sqrt{\frac{\varepsilon_o k T_e}{n_e e^2}} \qquad (5)$$

where T_e and n_e are the electron temperature (°K) and density (m^{-3}) at the location where the field is to be calculated. In an earlier experimental investigation,[4] Langmuir probes were used to measure the plasma properties a few millimeters upstream of the orifice plate of a mercury hollow cathode operating at an emission current of 2.3 A. Using the results of that experiment together with Eqs. 4 and 5 to calculate the electric field adjacent to the downstream end of the insert, the field at the insert surface is estimated to be 4.8×10^7 V/m. Based on Eq. 3 this would be equivalent to a decrease in the surface work function of 0.26 volts over the case where there was no field. This effect is of the right order of magnitude to explain the results of Fig. 17. If it is assumed that by doubling the pressure the plasma density is also doubled, then Eqs. 4 and 5 show that the electric field would be expected to increase by a factor of $(2)^{\frac{1}{2}}$ and the factor $(e\,E/4\pi\varepsilon_o)^{\frac{1}{2}}$ would, therefore, increase by $(2)^{\frac{1}{4}}$. So for the sixfold increase in pressure shown in Fig. 17, it is easy to imagine that the effect of the electric field on the work function would increase from 0.26 to $(0.26)(6)^{\frac{1}{4}}$ or 0.41 v.

It is interesting to compare this result with that shown in Fig. 17 for segment #1. For example, assume that at the 2 torr condition the effect of the electric field on the average effective work function was 0.26 volts. Then according to Eq. 3 ($\phi_s = \overline{\phi}_e + 0.26$), the surface work function at that condition would be $\phi_s \simeq 2.13$ v, since $\overline{\phi}_e$ is equal to ~ 1.87 volts. Assuming that the sixfold increase in pressure from 2 to 12 torr results in an effective work function reduction of 0.41 v due to the electric field as suggested above, then the average effective work function at the 12 torr condition would be expected to be 1.72 volts ($\overline{\phi}_e \simeq 2.13$-041). This is in good agreement with the value shown in Fig. 17 for segment #1 at a pressure of 12 torr. The results of Fig. 17 for segment #2 are also in qualitative agreement with the theory of field-enhanced, thermionic emission. Both the plasma and the plasma density are known[1, 4] to fall off rapidly with distance upstream of the emission region. This drop off would result in a marked decrease in the electric field as one moves upstream along the insert, and this would in turn result in a higher average effective work function for the segments of the insert upstream of the first segment. This sort of effect is indicated by the results of Fig. 17 for segment #2. The results discussed above are felt to provide significant additional evidence that field-enhanced, thermionic emission is the primary emission mechanism in orificed, mercury hollow cathodes.

Conclusions

In the normal operating condition, 80 to 90% of the emission current from a mercury hollow cathode comes from the insert. The hollow cathode will operate in a normal manner with electron emission from the insert alone. The main functions of the orifice appear to be as a flow restriction to maintain a high neutral density inside the cathode and as a current path to the downstream discharge. However, the orifice diameter does affect the keeper voltage, the discharge voltage, and the orifice plate temperature, all of which decrease as the orifice diameter is increased.

The insert emission region is localized on the last few millimeters at the downstream end of the hollow, cylindrical insert. The emission region tends to extend upstream along the insert as the internal cathode pressure is reduced or the surface work function is increased. Field-enhanced, thermionic emission can account for the total emission current. The surface work function of the insert is estimated to be ~ 2.13 volts; and the effect of the electric field acts to substantially reduce this by a few tenths of a volt. Increases in internal cathode pressure cause the electric field adjacent to the insert surface to increase and, thereby, cause a decrease in the average effective work function of the emission surface.

The insert temperatures are essentially independent of the orifice diameter, but highly dependent on surface work function, internal cathode pressure, and emission current. Insert temperatures tend to vary linearly with internal cathode pressure and emission current over a wide range of conditions. The insert can be characterized by the coefficients describing these varations. In

the case of the insert used in these tests, the effect of emission current can be characterized by a coefficient of 73°C/A and the effect of internal cathode pressure by - 7°C/torr. These insert coefficients from the experimental quartz cathode can probably be applied to model the insert temperature of an actual thruster cathode by the careful selection of a parameter which bridges the gap between the thermal properties of the experimental quartz cathode and the cathode being modelled.

The internal cathode pressure and the insert diameter are important parameters affecting the location of the emission region and the keeper voltage of the hollow cathode. The emission tends to occur at a point where the local pressure-emission surface diameter product achieves an optimum value. The results of this investigation are in general agreement with those of other researchers who have suggested that this optimum value is $\sim$ 1 torr-centimeter. The keeper voltage passes through at least a single minimum as the internal pressure is increased from a very small value. An internal pressure-insert diameter product of a few torr-centimeters is estimated to be a criterion for the realization of a minimum keeper voltage.

References

1. Ferreira, C.M. and Delcroix, J.L., "Theory of the Hollow Cathode Arc," Journal of Applied Physics, Vol. 49, No. 4, April 1978, pp. 2380-2395.

2. Bessling, H., "Theorie de Hochtemperatur-Hohlkathode, ein Modell fur den Kathodenmechanismus," DFVLR Report DLR-FB 76-50, Stuttgart, West Germany, 1976.

3. Krishnan, M., Jahn R. G., von Jaskowsky, W. F., and Clark, K. E., "Physical Processes in Hollow Cathodes," AIAA Journal, V. 15, No. 9, Sept. 1977, pp. 1217-1223.

4. Siegfried, D. E. and Wilbur, P. J., "An Investigation of Mercury Hollow Cathode Phenomena," AIAA Paper No. 78-705, April 25-27, 1978.

5. Crawford, F. W. and Freestone, I. L., "The Double Sheath at a Discharge Constriction," Proceedings of the 6th International Conference of Ionization Phenomena in Gases, Paris, July 1963.

6. Lidsky, L. M.; Rothleder, S. D.; Rose, D. J.; Yoshikawa, S.; Michelson, C. and Macken, Jr., R. J., "Highly Ionized Hollow Cathode Discharge," Journal of Applied Physics, Vol. 33, No. 8, August 1962.

7. Delcroix, J. L. and Trindade, A. R., "Hollow Cathode Arcs," Advances in Electronics and and Electron Physics, Vol. 35, ed. L. Marton, Academic Press, New York, 1974, p. 158.

8. Fearn, D. G. and Philip, C. M., "An Investigation of Physical Processes in a Hollow Cathode Discharge," AIAA Paper No. 72-416, April 17-19, 1972.

9. Martin, R. J. and Rowe, J. E., "Experimental Investigation of the Low-Voltage Arc in Noble Gases," Journal of Applied Physics, Vol. 39, No. 9, August 1968, pp. 4289-4298.

10. Siegfried, D., "Hollow Cathode Studies," appears in "Mercury Ion Thruster Research - 1978," NASA CR-159485, December 1978, pp. 7-37.

SPONSORED BY:
PRINCETON UNIVERSITY CONFERENCE
AMERICAN INSTITUTE OF AERONAUTICS AND ASTRONAUTICS (AIAA)
DEUTSCHE GESELLSCHAFT FUR LUFT-UND RAUMFAHRT (DGLR)

79-2060
Electron Diffusion Through the Baffle Aperture of a Hollow Cathode Thruster

J. R. Brophy and P. J. Wilbur, Colorado State University, Fort Collins, Colo.

PRINCETON/AIAA/DGLR 14th INTERNATIONAL ELECTRIC PROPULSION CONFERENCE

Oct. 30-Nov. 1, 1979/Princeton, N.J.

ELECTRON DIFFUSION THROUGH THE BAFFLE APERTURE OF A HOLLOW CATHODE THRUSTER*

John R. Brophy** and Paul J. Wilbur†
Colorado State University
Fort Collins, Colorado

Abstract

A mathematical model relating the baffle aperture area of a hollow cathode thruster to the magnetic flux density and plasma properties in the aperture region is developed. The results of the developments considering both Classical and Bohm diffusion theories, is presented. The diffusion coefficient determined experimentally from Langmuir probe trace data indicates that the Bohm diffusion theory can be used to predict the diffusion coefficient in the aperture region provided a constant correction factor equal to 2.6 is used. The classical theory typically underestimated the diffusion coefficients by an order of magnitude. A number of assumptions were made to simplify the baffle aperture model so that it could be used as an aid in thruster design. Extensive Langmuir probing was undertaken to verify the validity of the simplified model. The results show that the model can be used to calculate the aperture area required to effect discharge operation at a specified discharge voltage and arc current. The dominate force driving the electrons through the baffle aperture was seen to be the force due to the electric potential gradient. This force being approximately four times the force due to the electron density gradient. The results also show that the value of the electric potential difference through the aperture can be approximated by the difference between the arc voltage and the keeper voltage, and that this difference is equal to the primary electron energy in eV.

Nomenclature

A_{Baf}	Baffle aperture open area
$(A_{Baf})_{Bohm}$	Calculated aperture area using Bohm model.
$(A_{Baf})_{Classical}$	Calculated aperture area using Classical model.
B	Magnetic flux density
D	Electron diffusivity tensor
$D_\perp$	Coefficient for electron diffusion across magnetic field lines
D_{Bohm}	Bohm electron diffusion coefficient
$D_{Classical}$	Classical electron diffusion coefficient
e	Electronic charge
I	Current through the baffle aperture
I_{Beam}	Beam current
I_{Arc}	Arc current
I_R	Radial electromagnet current
I_{Baf}	Baffle electromagnet current
J	Current density through the baffle aperture
k	Boltzmann's constant
m_e	Electron mass
n	Electron number density
n_{Avg}	Average electron density in the aperture
n_i	Ion number density
n_n	Neutral number density
Q_n	Electron-neutral collision cross section
T	Electron temperature
T_{Avg}	Average electron temperature through the aperture
V_{Keeper}	Keeper voltage
V	Plasma potential
V_{Arc}	Arc voltage
$\bar{v}$	Average electron velocity
w	Baffle aperture gap
α	Correction factor for Bohm diffusion
Γ	Electron flux vector
$\Gamma_\perp$	Electron flux across magnetic field lines
Λ	Non-dimensionalized plasma shielding distance
μ	Electron mobility tensor
$\mu_\perp$	Electron mobility across magnetic field lines
ν_c	Electron momentum exchange collision frequency
ν_{ei}	Electron-ion momentum exchange collision frequency
ν_{en}	Electron-neutral momentum exchange collision frequency
ω_B	Electron cyclotron frequency

* Work performed under NASA Grant NGR-06-002-112

** Research Assistant, Department of Mechanical Engineering.

† Professor, Department of Mechanical Engineering, Member AIAA.

Introduction

The use of a hollow cathode in place of an oxide cathode to increase thruster operating lifetimes requires among other things the addition of a baffle to restrict the flow of electrons from the hollow cathode. This separates the plasma into two distinct regions;[1,6,9] 1) the plasma outside the hollow cathode but inside the cathode pole piece/baffle assembly, which will be called the cathode region plasma, and 2) the plasma in the main discharge region. It is well known that for proper thruster operation the discharge voltage must lie within a relatively narrow range. For example a hollow cathode mercury ion thruster would typically operate in the 30 to 40 volt range. The creation of primary electrons is accomplished by accelerating the electrons from the cathode region plasma into the main discharge region through a potential sheath of approximately this magnitude occurring in the proximity of the baffle aperture.[9] The aperture impedence, which might be defined as the ratio of the potential rise across this sheath to the current through the aperture, is primarily a function of three variables;[1,2,4,5,9] 1) the physical dimensions of the aperture, 2) the strength and shape of the magnetic field across the aperture and 3) the neutral density (the ion density is also important but to a lesser extent).

In the past the design and optimization of the cathode pole piece/baffle assembly has been done by physically performing a number of parametric variations.[1,2,3,6] This procedure is both time consuming and expensive; therefore, it is desirable to minimize the number of variations required. The objective of this study has been to develop a theoretical model, relating the aperture impedence to the variables listed above, with the result that this model could be used as an aid in thruster design. Extensive Langmuir probing was undertaken to verify the validity of the model and demonstrate its capability.

Theory and Analysis

Cathode Region Plasma

The cathode region plasma has properties similar to the plasma created when a hollow cathode is operated in a diode configuration in the spot mode.[1] Throughout most of the cathode region (except in the vicinity of the aperture) the plasma potential is approximately constant and the Maxwellian electron temperature is about 1 or 2 eV.[1,7,11] According to wells[9] the current initially flows from the cathode in a 30° diverging plume and is driven by the density gradients caused by the plasma flow from the hollow cathode. The plasma conductivity near the cathode is classical. At distances nearing the baffle the axial component of current becomes substantially reduced. Through the baffle aperture the plasma potential and electron energy rise sharply to approximately their main discharge region values. It is in this region that plasma heating occurs and primary electrons are created.

Electron Diffusion

In a properly designed thruster two fields exist in the aperture region which influence the electron diffusion process there. Oriented across the aperture is a magnetic field and normal to it through the aperture is a steady electric field. The electrons must diffuse across the magnetic field lines to form the discharge current. Due to the low thermal energy of the Maxwellian electrons orginating from the cathode region plasma the initial penetration of the electrons into the region of significant magnetic flux density will be on the average small (this can be approximated from the analysis given by Robinson[12]). Under the influence of the crossed electric and magnetic fields the electron motion may be separated into three parts. One is the helical motion about the magnetic field lines or guiding centers, the second is the drift in the E x B direction, and the third is the net motion of the guilding centers across the magnetic field lines due to momentum exchange collisions. It is this third motion, that of the diffusion of electrons across the field lines that results in the discharge current. Throughout the following analysis the effect of the non-Maxwellian electron energy distribution in the baffle aperture will be neglected. The diffusion process through the aperture may be modeled as suggested by Kaufman and Robinson[13] as

$$\Gamma = n\mu\vec{\nabla}V - D\vec{\nabla}n \qquad (1)$$

where Γ represents the electron flux vector, D and μ are tensors which describe the diffusivity and mobility of the electrons respectively, V is the plasma potential and n is the electron number density. In order to describe the pole piece geometry shown in Figure 1 a cylindrical coordinate system was used. The magnetic field through the aperture will be approximately parallel to the axis of symmetry of the pole piece. This line of symmetry will be taken as the Z-axis. The electric field is normal to this and directed through the aperture in the radial direction. Since the direction of current flow through the aperture is normal to the magnetic field lines,[9] Equation (1) may be written in one dimension as,

$$\Gamma_\perp = n\mu_\perp \frac{dV}{dr} - D_\perp \frac{dn}{dr} \quad . \qquad (2)$$

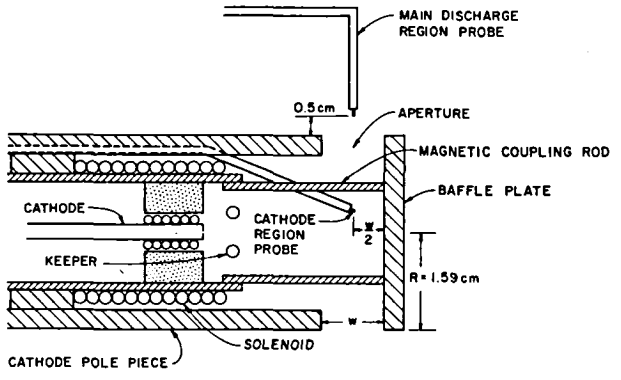

Fig. 1 Cathode pole piece/magnetic baffle assembly.

The electron flux $\Gamma_\perp$ is related to the current density

J by,

$$\Gamma_{\perp} = \frac{J}{e} \quad . \tag{3}$$

Assuming the Einstein relation,

$$\mu = \frac{e}{kT} D \tag{4}$$

to be valid we can combine Eqs. (2), (3) and (4) to obtain

$$J = D_{\perp} \left[\frac{e\,n}{kT} \frac{dV}{dr} - e \frac{dn}{dr} \right] \quad . \tag{5}$$

This equation relates the current density through the aperture to the coefficient for diffusion normal to the magnetic field lines and the plasma parameters in this region. The classical diffusion coefficient for Maxwellian electrons[14] is given by

$$D_{Classical} = \frac{kT}{M_e} \left[\frac{\nu_c}{\nu_c^2 + \omega_B^2} \right] \tag{6}$$

where ν_c is the electron momentum exchange collison frequency and M_e is the electron mass. The electron cyclotron frequency ω_B is given by

$$\omega_B = \frac{eB}{M_e} \tag{7}$$

where B is the magnetic flux density. For the magnetic field strengths and densities in the aperture region it was found that,

$$\frac{\omega_B}{\nu_c} >> 1 \tag{8}$$

therefore we may neglect ν_c^2 relative to ω_B^2 in Equation (6) and write

$$D_{Classical} = \frac{kTM_e\nu_c}{e^2B^2} \tag{9}$$

which yields the familiar result that the classical diffusion coefficient varies as B^{-2}. However it has been found that a diffusion coefficient proportional to B^{-1} gives better results in an ion thruster.[15] This diffusion coefficient first proposed by Bohm[16] may be written as,

$$D_{Bohm} = \frac{kT}{16eB} \quad . \tag{10}$$

Since this expression is uncertain to a factor of 2 or 3 it will be written as,

$$D_{Bohm} = \frac{kT}{\alpha 16eB} \tag{11}$$

where α is a constant correction factor. In order to decide whether Classical or Bohm diffusion is applicable in the baffle aperture region Equation (5) can be solved for the diffusion coefficient to yield,

$$D_{\perp} = J \left[\frac{e^2n}{kT} \frac{dV}{dr} - e \frac{dn}{dr} \right]^{-1} \quad . \tag{12}$$

Comparison of diffusion coefficients determined using measured plasma conditions with this equation and using the predictions of Equations (9) and (10) will enable the determination of the most appropriate diffusion model for the aperture region.

In order to apply Equation (12) it was found convenient to make a number of simplifications to facilitate calculation of many of the terms. For example the derivatives were approximated from the probe trace data as the slope of the line between the plasma potentials and densities in the cathode region and those in the main discharge region. Equation (12) can then be used in the form,

$$D_{\perp} = \frac{I}{A_{Baf}} \left[\frac{e^2 n_{Avg}}{kT_{Avg}} \frac{\Delta V}{\Delta r} - e \frac{\Delta n}{\Delta r} \right]^{-1} \tag{13}$$

Figure 2 shows the variation in plasma potential through the baffle aperture for a typical test case. The dashed line represents the approximation $\Delta V/\Delta r$ of the derivative dV/dr. The approximation is seen to be fairly good and is typical of the results obtained for other test conditions. At very low magnetic flux densities (less than $\sim 20 \times 10^{-4}$ tesla) in the aperture this method tends to overestimate the value of the derivative and this artificially lowers the calculated diffusion coefficient slightly. This is not a serious problem however since the magnetic field in the aperture of a normally operating thruster is generally well above this value.

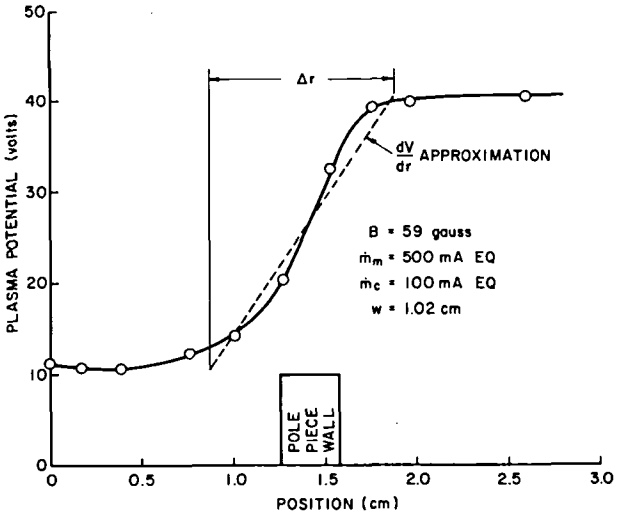

Fig. 2 Typical variation of plasma potential through the baffle aperture.

A similar type of approximation was made for the electron density variation. Plasma property profiles, like the one shown in Fig.2, were obtained by moving a Langmuir probe through the aperture region. This required a large number Langmuir probe traces while calculation of the gradients for Equation (13) required only that the differences in plasma properties measured on either side of the aperture be divided by the term Δr shown in Figure 2. Such an approximation enables the experimenter to obtain satisfactory results with only two Langmuir probe measurements at each operating condition. The quantity Δr represents physically the thickness of the plasma sheath in the aperture region through which the electrons are accelerated. It is the distance from the point where the magnetic flux density begins to rise dramatically in the cathode discharge region to the critical field line which carries the electrons into the

main discharge region. Figure 3 shows the magnetic flux density variation through a typical aperture.

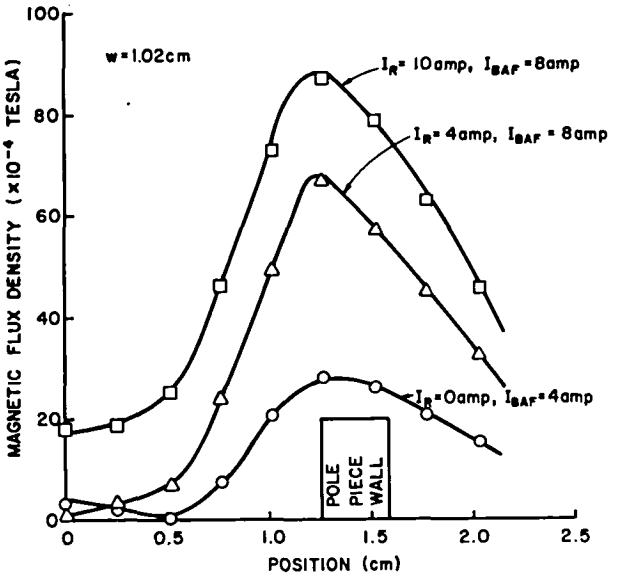

Fig. 3. Magnetic flux density variations through the baffle aperture.

The data, of which both Figures 2 and 3 are examples, suggested that this distance Δr could be approximated with reasonable accuracy as the aperture gap dimension w. This approximation was therefore used in the analysis of most of the data. The current through the baffle aperture, I, required in Equation (13) is simply the arc current minus the beam current,

$$I = I_{Arc} - I_{Beam} \quad . \tag{14}$$

The temperature through the aperture while not being constant was nevertheless approximated by an average temperature which attempts to account for the energy of the primary electrons, i.e.,

$$T_{Avg} = \frac{T_{Cathode} + \left(\frac{9\ T_{Main} + \frac{e}{k}\ E_p}{10}\right)}{2} \tag{15}$$

where $T_{Cathode}$ and T_{Main} are the Maxwellian electron temperatures in the cathode and main discharge regions respectively, and E_p is the primary electron energy. The electron density in the aperture was taken to be the average density measured by the two probes, n_{Avg}.

Baffle Aperture Model

An expression relating the aperture area to the magnetic flux density and plasma properties in the aperture will now be derived. The development can be based on either the Classical or Bohm diffusion models, and because both developments are similar only the one using the Bohm diffusion coefficient will be given here. Substituting the expression for Bohm diffusion into Equation (5) yields,

$$J = \frac{kT}{\alpha 16eB}\left[\frac{e^2 n}{kT}\frac{dV}{dr} - e\frac{dn}{dr}\right] \quad . \tag{16}$$

This expression can be rearranged to obtain

$$16\alpha\ JB\ dr = nedV - kT\ dn \quad . \tag{17}$$

Integration of this equation over the aperture potential sheath gives,

$$16\alpha \int JBdr = e\int ndV - k\int Tdn \quad . \tag{18}$$

To introduce the baffle aperture geometry it is assumed that the current density is constant over the sheath thickness, i.e.,

$$J = \frac{I}{A_{Baf}} \tag{19}$$

where I represents the current through the aperture and A_{Baf} is the open area of the aperture. Substituting Equation (19) into Equation (18) we have,

$$16\alpha \frac{I}{A_{Baf}} \int Bdr = e\int ndV - k\int Tdn \tag{20}$$

which can be solved for the baffle area to obtain,

$$(A_{Baf})_{Bohm} = \frac{(\frac{16\alpha}{e})I\int Bdr}{\int ndV - \frac{k}{e}\int Tdn} \tag{21}$$

where the subscript Bohm refers to the fact that Bohm diffusion was used in the derivation. If instead classical diffusion is used the result is

$$(A_{Baf})_{Classical} = \frac{(\frac{1}{\nu_c M_e})\ I\int B^2 dr}{\int ndV - \frac{k}{e}\int Tdn} \quad . \tag{22}$$

An interesting feature of Equation (21) is the appearance of the term $\int Bdr$ which has been used with some success in the modeling of primary electron containment for multipole thrusters.[12] Equation (22) differs from Equation (21) in that the integral $\int Bdr$ in Equation (21) has been replaced by $\int B^2 dr$ and the term $(16\alpha/e)$ was replaced by $(1/\nu_c M_e)$. In the derivation of Equation (22) the collision frequency was assumed constant over the region of interest.

The use of the classical diffusion coefficient requires the evaluation of the electron momentum exchange collision frequency. For diffusion through the aperture we need consider only electron-neutral and electron-ion elastic collisions. The electron-neutral collision frequency, ν_{en} was approximated using,[18]

$$\nu_{en} = n_n Q_n \bar{v} \tag{23}$$

where n_n is the number density of neutrals, which can be evaluated from the theory developed by Wilbur.[19] Q_n is the electron-neutral collision cross section, and $\bar{v}$ is the relative velocity of the colliding particles. The relative velocity is assumed equal to the average thermal velocity of the electrons given by

$$\bar{v} = \sqrt{\frac{8kT}{\pi M_e}} \quad . \tag{24}$$

The electron-ion collision frequency ν_{ei}, was evaluated from the expression given by Holt and Haskell,[18]

$$\nu_{ei} = \frac{0.83T^{3/2}}{n_i \ell n \Lambda} \tag{25}$$

where n_i is the ion number density and Λ is the non-dimensional plasma shielding distance which can be calculated from,[18]

$$\ell n \Lambda = \ell n \left[12.4 \times 10^3 \frac{T^{3/2}}{n_i^{1/2}}\right] \quad . \tag{26}$$

In order to calculate the baffle aperture area from Equations (21) or (22) several integrals must be evaluated. However most of the information necessary to evaluate these integrals would not be available to someone designing a thruster. In order to make these equations more useful the following simplifications were made. For the integrals $\int T dn$ and $\int n dV$ the average quantities T_{Avg} and n_{Avg} as defined previously were used so the temperature and density could be moved outside the integral to give,

$$\int T dn \approx T_{Avg} \, \Delta n \tag{27}$$

$$\int n dV \approx n_{Avg} \, \Delta V \quad . \tag{28}$$

It was also necessary to evaluate the integral of the magnetic flux density in Equations (21) and (22). For the fairly well confined magnetic field obtained with the pole piece geometry used in these tests the approximation

$$\int B dr \approx B \Delta r \tag{29}$$

was also made, where the B on the right hand side of this equation was the value of the magnetic flux density at the center of the aperture. However with other pole piece configurations it may be necessary to evaluate this integral. This could be accomplished by making magnetic flux density measurements through the aperture along a path perpendicular to the flux density vectors. Combining Equations (14), (27), (28) and (29) along with Equation (21) yields the simplified equation used to calculate the baffle area for the Bohm diffusion model,

$$(A_{Baf})_{Bohm} = \frac{16\alpha(I_{Arc} - I_{Beam})B\Delta r}{e \, n_{Avg} \, \Delta V - kT_{Avg} \, \Delta n} \quad . \tag{30}$$

The corresponding result for classical diffusion is

$$(A_{Baf})_{Classical} = \frac{\frac{e}{\nu_c M_e}(I_{Arc} - I_{Beam})B^2\Delta r}{e \, n_{Avg} \, \Delta V - kT_{Avg} \, \Delta n} \quad . \tag{31}$$

Apparatus

Magnetic Baffle

All experiments pertaining to this study were carried out on a 14 cm dia. radial field thruster. The thruster was equipped with the pole piece assembly shown schematically in Figure 1. For these tests the cathode pole piece outer diameter was held constant at 3.18 cm and the wall and baffle plate thicknesses were both 0.32 cm. The magnetic baffle assembly of Figure 1 provided separate control over the magnetic field strength in the aperture through the use of a 12 turn magnetic baffle solenoid. The magnetic coupling rods shown were made of soft iron and were of sufficient cross section to assure that the magnetic flux through the rods was well below the saturation point at the maximum solenoid current. Control of the magnetic field strength in the main discharge region was accomplished through the use of 8 radially oriented electromagnets. Since the cathode pole piece was part of the main thruster's magnetic circuit, increasing the current through the radial nagnets increased the magnetic field strength in the aperture region as well as the main discharge region. However changing the field strength in the aperture by using the baffle solenoid did not significantly change the magnetic field in the main discharge region. Magnetic flux densities in the center of the aperture ranging from 9×10^{-4} to 120×10^{-4} tesla could be established using either the baffle or the radial magnets. The pole piece/baffle geometry shown in Figure 1 was choosen for this study because it provided a magnetic field whose lines-of-force were nearly parallel to the Z-axis and concentrated mainly in the baffle aperture. This being the case, it would be expected that a plot of the magnetic field strength component in the Z-direction as a function of the radial position through the aperture would be rather peaked in the vicinity of the gap. Figure 3 is such a plot, where I_R is the radial electromagnet current and I_{Baf} is the baffle magnet current. These figures do show the magnetic field tends to be concentrated in the aperture Region. The measurements for Figure 3 were taken with the gap spacing, i.e., the distance from the downstream edge of the cathode pole piece to the upstream edge of the baffle plate (w in Figure 1), equal to 1.02 cm. This was the largest spacing used in the tests. Since the larger gap size resulted in greater spreading of the magnetic field, the curves in Figure 3 correspond to the case having the field lines spread over the greatest distance of any that were investigated. Since it was believed that the amount of this spread influences the thickness of the plasma sheath through the aperture, and since the approximations of the derivatives are better for small Δr it was considered desirable for this study to have the magnetic field spread out as little as possible.

Probes

Two cylindrical Langmuir probes were used to measure the plasma properties on each side of the aperture. The cathode region probe was a 0.076 cm diameter tantalum wire 0.076 cm long, and was positioned at a radial distance approximately equal to the keeper radius at the midpoint of the aperture gap. Because the plasma properties in the cathode region are fairly uniform the positioning of the cathode probe was not critical, thus it was placed fairly near the centerline to assure that it was not in the region of plasma heating. The main discharge region probe was a 0.076 cm diameter wire 0.123 cm long. The positioning of both probes can be seen in Figure 1. The main discharge region probe could also be swept radially through the aperture and several measurements of plasma properties as a function of the radial distance through the aperture

were made. The probe traces were analyzed using a computer program developed by Beattie.[17]

Data Collection

Extensive plasma property measurements were made using the cathode region and main discharge region probes over a wide range of operating conditions. Three different baffle aperture areas were probed. A summary of the values of the important variables for each test is listed in Table I.

Table I
Test Conditions

Test No.	Aperture Area [m^2]	Gap Spacing w[cm]	Main Flow Rate [mAEq]	Cathode Flow Rate [mA Eq]	Arc Cur. [Amp]	Range of Peak Mag. Flux Density in Gap [10^{-4} tesla]
1	5.71×10^{-4}	0.64	650	165	4.50	9-111
2	6.85×10^{-4}	0.76	500	100	3.50	15-107
3	9.14×10^{-4}	1.02	500	100	3.50	13-88
4	9.14×10^{-4}	1.02	400	80	3.50	13-100

The screen and accelerator grid voltages were held at +1000v and -500v respectively and the cathode pole piece diameter was 3.18 cm for all tests. Before each test the aperture area was set by adjusting the gap spacing. During the data collection the arc current, cathode flow rate and main flow rate were maintained approximately constant. The magnetic field field-strength in the aperture was varied by changing the currents through the radial and baffle electromagnets and this caused the discharge voltage to change. At each field strength setting two Langmuir probe traces were taken, one with the cathode region probe and the other with the main discharge region probe. The parameters describing the operating condition (arc current, arc voltage, beam current and keeper voltage) were also recorded.

Results and Discussion

It was of interest first to determine if Bohm or classical diffusion applies to the process of electron flow through the baffle aperture area. The diffusion coefficient was experimentally determined by using the Langmuir probe trace data obtained with the two probes in Equation (13).

$$D_{\perp} = \frac{I}{A_{Baf}} \left[\frac{e^2 n_{Avg}}{kT_{Avg}} \frac{\Delta V}{\Delta r} - e \frac{\Delta n}{\Delta r} \right]^{-1} .$$

As suggested previously evaluation of this equation was accomplished by setting the sheath thickness (Δr) equal to the aperture gap spacing (w) on the basis that this approximated the experimental situation adequately. This experimental diffusion coefficient along with the predictions from the Bohm and classical theories are shown in Figure 4. This figure contains only the points obtained under test number 1 in Table I. However the Bohm diffusion coefficient was seen to give good results in all cases when a constant correction factor of $\alpha = 2.6$ was used. Here Bohm diffusion seems to apply even

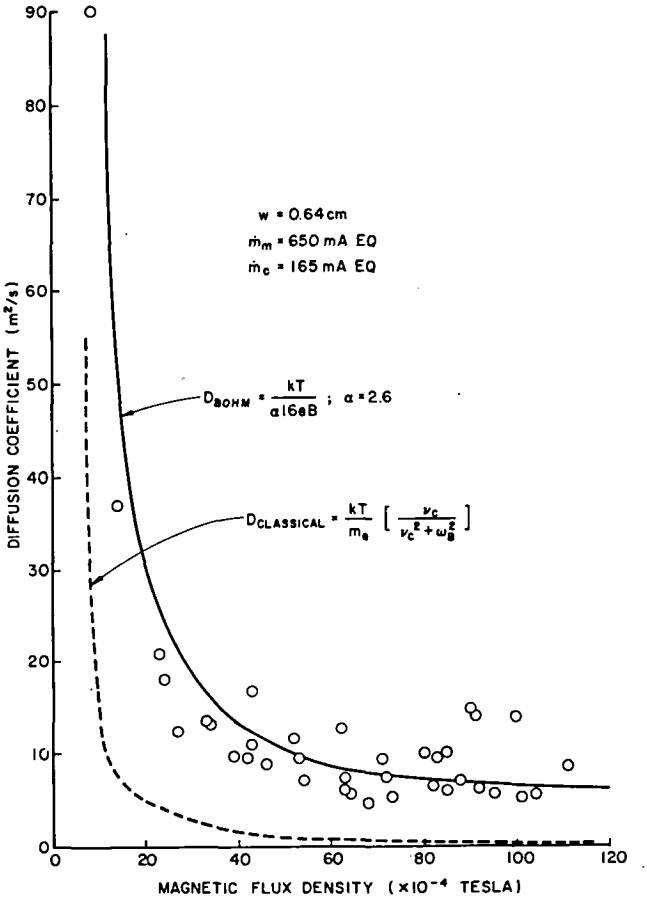

Fig. 4. Comparison of the experimentally determined diffusion coefficient with the Bohm and classical theories.

at low magnetic field strengths, but in some of the other sets of data not presented here a case could be argued for classical diffusion. In all sets of data at the higher magnetic field strengths the diffusion coefficient followed the Bohm theory more closely than the classical one. This observation is in agreement with the results of Wells.[9] The classically determined coefficient was typically an order of magnitude too small.

The aperture areas calculated from Equations (30) and (31) are plotted against the magnetic flux density in the aperture in Figures 5, 6 and 7. Ideally the calculated area should be independent of the flux density since in each case the area was held constant as the magnetic field strength was varied. For each of the three different areas tested the model using Bohm diffusion showed excellent agreement with the actual area. The solid lines in these figures represent the statistical average of the Bohm points only and the dashed lines represent the standard deviation. In all cases the classical theory failed badly. In some instances it was off by as much as two orders of magnitude and showed a strong dependence on the magnetic flux density. The

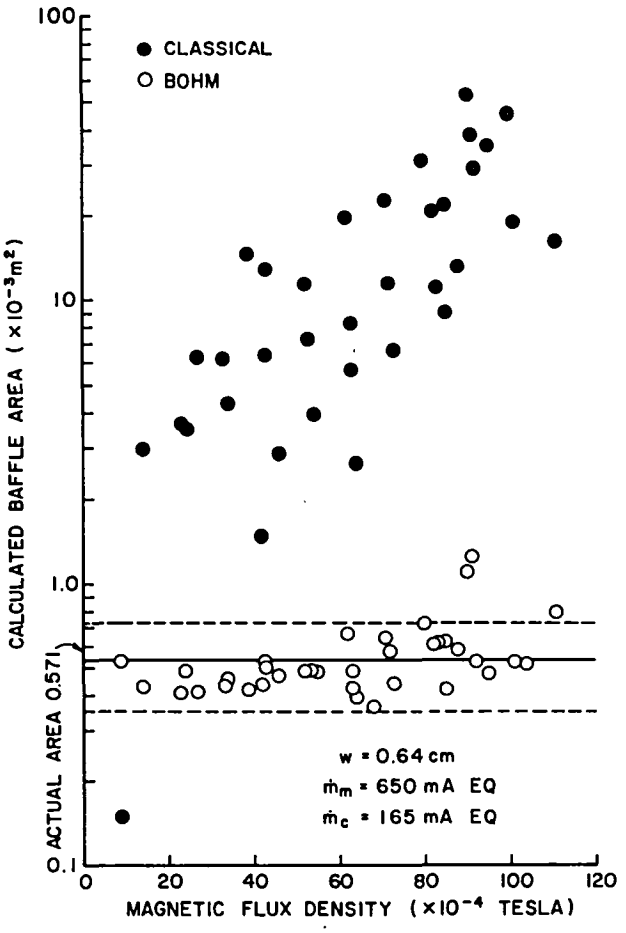

Fig. 5. Comparison of areas calculated with the Bohm and Classical theories for an actual area of $5.71 \times 10^{-4} m^2$.

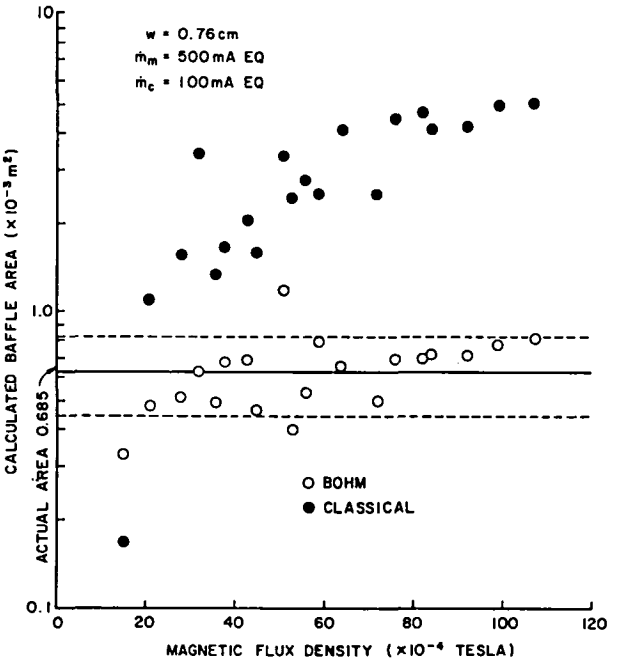

Fig. 6. Comparison of areas calculated with the Bohm and Classical theories for an actual area of $6.85 \times 10^{-4} m^2$.

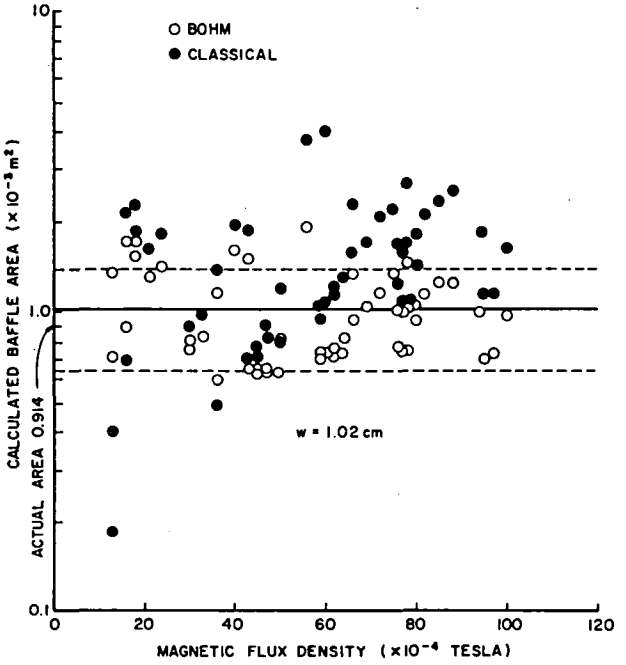

Fig. 7. Comparison of areas calculated with the Bohm and Classical theories for an actual area of $9.14 \times 10^{-4} m^2$.

explanation for this behavior can be traced back to Figure 4 and the failure of the classical diffusion coefficient to fit the experimental data. The end result of this effort can be seen in Figure 8 which shows the average calculated baffle area using the Bohm diffusion model plotted against the actual baffle area. The solid line represents the line of perfect correlation and the error bars indicate the standard deviation represented previously as the dashed lines in Figures 5, 6 and 7. The correlation is remarkably good considering the number of simplifications used.

Application

Finally a description of how to apply this model is in order. Equation (30)is rewritten here for convenience, with the subscript Bohm dropped and the line integral of the magnetic flux density through the aperture restored,

$$A_{Baf} = \frac{16\alpha(I_{Arc} - I_{Beam}) \int Bdr}{e\, n_{Avg}\, \Delta V - kT_{Avg}\, \Delta n} \quad . \qquad (32)$$

It is seen that in order to calculate the aperture area the user must determine a priori the value of each of the quantities on the right hand side of

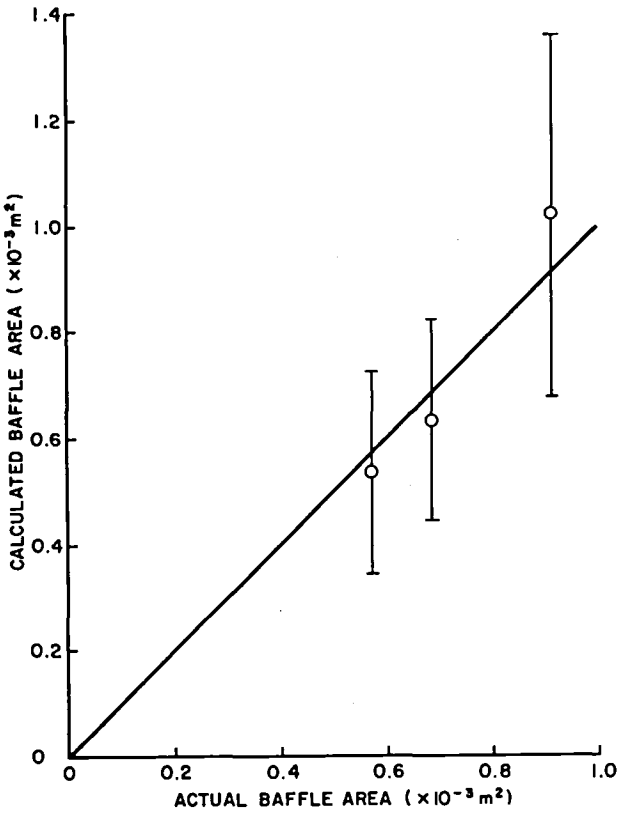

Fig. 8. Comparison of the calculated baffle area to the actual baffle area.

this equation. An important assumption which must be made now is that the value of the correction factor, $\alpha = 2.6$, which was used with success in this study, can be used for any thruster with any cathode pole piece geometry. Although this assumption has not been tested as yet it seems justifiable on the grounds that the mechanism of electron diffusion through the baffle aperture should be similar for other aperture configurations. The designer of a thruster will know in general from other considerations the values of the beam current, arc current, primary electron energy and the density at which the thruster should operate. The density of the main discharge region could be used as a first order approximation for the average plasma density in the aperture region (n_{Avg}). Further, the magnetic flux density and configuration of the lines-of-force in the aperture region will be under his control. Using a physical model of the magnetic circuit for the aperture region the magnetic field through the aperture can be mapped with a gaussmeter and the line integral of the flux density can be calculated.

Next it is appropriate to consider the relative magnitudes of the potential and density gradient driving terms in Equation (32). In particular it is desirable to determine if some simplification can be made here which would make the model more useful to a designer. This is necessary because the density gradient across the aperture would in general not be known before a thruster was built and tested. Fortunately it can be shown that the ratio of the voltage gradient term to the density gradient term is approximately a constant regardless of the prevailing magnetic flux density, flow rates, baffle aperture area or discharge current. The absolute value of this ratio written as,

$$\left|\frac{\text{voltage gradient term}}{\text{density gradient term}}\right| = \left|\frac{\frac{e^2 n}{kT}\frac{\Delta V}{\Delta r}}{e\frac{\Delta n}{\Delta r}}\right| = \left|\frac{en}{kT}\frac{\Delta V}{\Delta n}\right| \quad (33)$$

is plotted against the magnetic flux density in the aperture in Figure 9 for all test cases. The solid line represents the average value and the dashed lines represent the standard deviation. Considerable scatter is evident in the data. However to a first approximation the ratio is independent of the variables considered important in the baffle aperture model. This important result allows the term $kT\Delta n$ to be approximated by $-\frac{1}{4}en\Delta V$ for any combination of aperture area, magnetic flux density and flow rate investigated in these tests. No physical justification of this observation has been identified.

All that remains now is to determine the voltage difference across the aperture. It is this voltage difference through which the electrons are accelerated to become primary electrons. If the plasma potential in the cathode discharge region can be approximated by the keeper voltage, (V_{Keeper}) and the plasma potential in the main

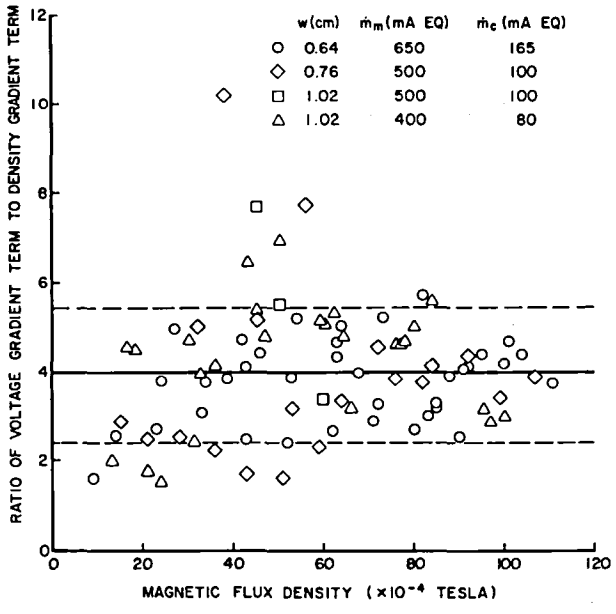

Fig. 9. Comparison of the voltage gradient term to the density gradient term.

discharge region by the arc voltage (V_{Arc}), then the voltage difference across the sheath could be determined using

$$\Delta V = V_{Arc} - V_{Keeper} \quad . \qquad (34)$$

If this is valid, then this difference should also be equal to the energy gained by the primary electrons after being accelerated through the aperture sheath. Figure 10 is a plot of the primary electron energy against the difference between the arc voltage and the keeper voltage, including data from all the test cases. The solid line represents the line obtained from a linear least squares curve fit and it has a correlation coefficient of r=0.92. The slope of the curve fit line is seen to be very close to one. The dashed line represents the line obtained if the primary electron energy was equal to this voltage difference. At any point along these lines the difference between them is about 2 eV which is approximately the temperature of the electrons in the cathode region plasma.

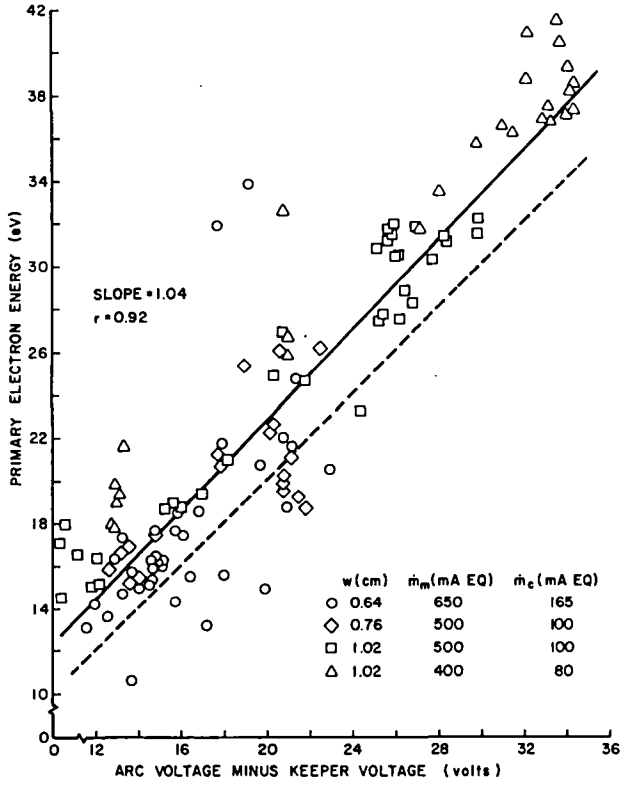

Fig. 10. Primary electron energy as a function of the difference between the arc and keeper voltages.

Therefore it appears that the voltage across the aperture sheath may be accurately approximated by the difference between the arc voltage and the keeper voltage. In reality the cathode region and main discharge region plasma potentials will differ from the keeper and arc voltages respectively by the keeper and anode sheath potentials. Apparently, however, the difference caused by these sheaths cancel.

Finally now we can write Equation (30) in the form in which it will be most useful

$$A_{Baf} = \frac{16\alpha(I_{Arc} - I_{Beam})B\Delta r}{\frac{5}{4} e\, n_{Avg} (V_{Arc} - V_{Keeper})} \quad . \qquad (34)$$

This is the form of the equation which was used to generate Figures 5-8.

Conclusions

The diffusion of electrons through the baffle aperture of a hollow cathode ion thruster closely follows the Bohm diffusion theory when a correction factor equal to 2.6 is used. Classical theory underestimates the diffusion coefficient by typically an order of magnitude. Applying the Bohm diffusion theory it is possible to calculate the aperture area required to effect discharge chamber operation at a specified discharge voltage and current. The areas calculated by this model using Langmuir probe trace data from an operating thruster agreed well with the actual baffle areas. The dominate physical force driving electrons through the aperture was identified as the electric potential gradient. The electron density gradient results in a force that is about one-fourth of the electric field force. The energy gained by the electrons (in eV) as they are accelerated across the baffle aperture sheath is approximately equal to the difference between the arc voltage and the keeper voltage. Therefore the value of the potential rise through the baffle aperture can be approximated using this difference.

References

1. Poeschel, R. L., Ward, J. W. and Knauer, W., "Study and Optimization of 15-cm Kaufman Thruster Discharges," AIAA Paper No. 69-257, March 3-5, 1969.

2. King, H. J., Poeschel, R. L. and Ward, J. W., "A 30-cm Low-Specific Impulse, Hollow-Cathode, Mercury Thruster," AIAA Paper No. 69-300, March 3-5, 1969.

3. Bechtel, R. T.,"Performance and Control of a 30-cm diam, Low-Impulse, Kaufman Thruster," AIAA Paper No. 69-238, March 3-5, 1969.

4. Poeschel, R. L. and Knauer, W., "A Variable Magnetic Baffle for Hollow Cathode Thrusters," AIAA Paper No. 70-175, Jan. 19-21, 1970.

5. Poeschel, R. L., "The Variable Magnetic Baffle as a Control Device for Kaufman Thrusters," AIAA Paper No. 72-488, April 17-19, 1972.

6. Palumbo, G., et al., "Effect of Geometry and Field Inside the Pole Piece in an Electron Bombardment Thruster," AIAA Paper No. 70-1088, Aug. 31- Sept. 2, 1970.

7. Longhurst, G. R., "Magnetic Baffle for 15 cm Multipole Mercury Thruster" in Appendix A of "15 cm Mercury Ion Thruster Research - 1976," ed. P. J. Wilbur, NASA CR-135116, December 1976.

8. Longhurst, G., "Prediction of Plasma Properties in Mercury Ion Thrusters," NASA CR-159448, December 1978.

10. Krall, N. A. and Trivelpiece, A. W., Principals of Plasma Physics, McGraw-Hill, Inc., New York, 1973. Ch. 6.

11. Wilbur, P. J., Isaacson, J., "Plasma Property Contours in a 15 cm Hollow Cathode Kaufman Thruster," Colorado State University report CER 72-73 PJW20, February 1973.

12. Robinson, R. S., "Electron Deflectron in a Spatially Varying Magnetic Induction," in "Inert Gas Thrusters," ed. H. R. Kaufman NASA CR-135100, July 1976.

13. Kaufman, H. and Robinson, R. S., "Plasma Properties in Inert Gas Thrusters," AIAA Paper No. 79-2055, October 29-31, 1979

14. Jahn, R. G., Physics of Electric Propulsion, McGraw-Hill, Inc., New York, 1968, Ch. 5.

15. Longhurst, G. R., "The diffusion and collection of Electrons in Ion Thrusters," in "Mercury Ion Thruster Research - 1977" ed. P. J. Wilbur, NASA CR-135317, December 1977.

16. Bohm, D., "The use of Probes for Plasma Exploration in Strong Magnetic Fields," in "The Characteristics of Electrical Discharges in Magnetic Fields," eds. A. Guthrie and R. K. Wakerling, McGraw-Hill, New York, 1949.

17. Beattie, J. R., "Numerical Procedure for Analyzing Langmuir Probe Data," AIAA Journal, Vol. 13, No. 7, July 1975, pp. 950-952.

18. Holt, E. H. and Haskell, R. E., Plasma Dynamics, The MacMillan Company, New York, 1965, Ch. 9.

19. Wilbur, P. J., "Neutral Balance Model for the Cathode Discharge Region," in "Experimental Investigation of a Throttlable 15 cm Hollow Cathode Ion Thruster," NASA CR-121038, December 1972.

20. McDaniel, E. W., Collision Phenomena in Ionized Gases, Wiley and Sons, Inc., New York, 1964, Ch. 4.

SPONSORED BY:
PRINCETON UNIVERSITY CONFERENCE
AMERICAN INSTITUTE OF AERONAUTICS AND ASTRONAUTICS (AIAA)
DEUTSCHE GESELLSCHAFT FUR LUFT-UND RAUMFAHRT (DGLR)

79-2062
A Model for Nitrogen Chemisorption in Ion Thrusters

P. J. Wilbur, Colorado State University, Fort Collins, Colo.

PRINCETON/AIAA/DGLR 14th INTERNATIONAL ELECTRIC PROPULSION CONFERENCE

Oct. 30-Nov. 1, 1979/Princeton, N.J.

A MODEL FOR NITROGEN CHEMISORPTION IN ION THRUSTERS*

Paul J. Wilbur†
Colorado State University
Fort Collins, Colorado

Abstract

A theoretical model describing the formation of nitrogen species subject to chemisorption on ion thruster discharge chamber surfaces is presented. Molecules, atoms, atomic ions and molecular ions are identified as the important species in the analysis. Current densities of the atomic and molecular ions predicted by the model are compared to current densities measured in the beam of a SERT II thruster. The predicted and measured values of these two current densities are shown to agree within about ± 100%. The mechanisms involved in the erosion of a surface subjected to simultaneous nitrogen chemisorption and sputter erosion by high energy ions are also discussed.

Nomenclature

A Area (m^2)

f Fraction of Surface Area

j Particle Current Density ($m^{-2}sec^{-1}$)

k Boltzmann Constant ($1.38 \times 10^{23} J/°k$)

m Mass of Molecular Nitrogen ($4.68 \times 10^{-26} kg$)

n Particle Density (m^{-3}).

p Pressure (nt/m^2)

P Primary Electron Rate Factor (m^3/sec)

Q Maxwellian Electron Rate Factor (m^3/sec)

S Sputtering Yield

T Temperature (°k)

v Velocity (m/sec)

V Volume (m^3)

$\dot{W}$ Sputtered Metal Removal Rate ($m^{-2}sec^{-1}$)

Z Rate Factor-Density Product for Primary plus Maxwellian Electrons-Eqn (15) $(sec)^{-1}$

ϕ Probability of Striking a Sputtering Site Affected by a Nitrogen Atom

Ψ Sticking Probability

Subscripts and Superscripts

a Accelerator Grid Open Area

c At cathode potential

e Effective Open Area of Grid Pair to Neutral Particles

H_g Sputter inducing mercury ions

m Maxwellian Electron

p Primary Electron or Primary Electron Region

s Screen Grid Open Area

w Discharge chamber Wall

0 In the Vacuum Tank

1 Atomic Nitrogen

2 Molecular Nitrogen

+ Atomic Nitrogen Ion

2+ Molecular Nitrogen Ion

' Sputtering Site Where the Effect of Nitrogen is Felt.

Introduction

When nitrogen is present in the discharge chamber of an ion thruster it is known to reduce the erosion rates of thruster components.[1] For ground based qualification tests of ion thrusters this phenomenon is undesirable because it results in greater component lifetime measurements than those that would be observed in the space environment where nitrogen is not present. On the other hand one can envision an operating mode wherein nitrogen might be carried on an electrically propelled spacecraft so it could be supplied to the discharge chamber during operation to extend the lifetime of critical thruster components. It is desirable to have a theoretical model describing the change in sputtering rates effected by the presence of nitrogen in the discharge chamber so one can compute the associated changes in component lifetimes that could be expected either in space or during a ground test. The purpose of this paper is to develop a portion of that model; namely that portion describing the arrival rate of reactive nitrogen species on the discharge chamber walls. Results predicted by the model will be compared with some experimental measurements. Further, the means by which results given by the model might be used to compute variations in sputtering rates caused by nitrogen impurities will be suggested. The amount of nitrogen, which would have to be carried on board a spacecraft to bring about a

* Work performed under NASA Grant NGR-06-002-112.

† Professor, Mechanical Engineering Department, Member AIAA.

substantial reduction in discharge chamber sputtering rates is estimated using the erosion rate data given by Rawlin and Mantenieks.[1] This analysis is contained in the Appendix.

Physical Processes

During ground based testing of ion thrusters nitrogen enters the discharge chamber as molecular nitrogen through the grids. Molecular nitrogen exhibits a low probability of being chemically adsorbed on thruster materials compared to other more reactive species so its rate of chemisorption will be neglected in this analysis.[2] Molecular nitrogen, which is present in the discharge chamber in the highest concentration of any nitrogen specie, is however subject to electron bombardment and the species resulting from these interactions generally do exhibit a high adsorption probability. The species produced include atomic nitrogen and atomic nitrogen ions both of which are highly reactive and exhibit a chemisorption probability near unity when they strike an unsaturated surface. As a surface becomes saturated with chemisorbed nitrogen however incident atoms and atomic ions would probably be held only for the time necessary to form molecular nitrogen which would be released back into the discharge chamber. Molecular nitrogen ions are also formed in the discharge chamber and they can also be chemisorbed into a metal surface if they can acquire a sufficiently high kinetic energy with which to impact a thruster surface.[3] In ion thrusters, molecular nitrogen ions acquire energies on the order of 30-40v as they pass from the bulk plasma to cathode potential surfaces and this is sufficient to facilitate their dissociation upon impact and subsequent chemisorption. In this energy range the sticking probability for molecular ions on molybdenum is for example about 50%. Molecular nitrogen ions striking anode surfaces will generally not stick and they will therefore come back off as neutral molecular nitrogen. Other species such as metastable nitrogen species would be expected to behave as molecular nitrogen so they will be neglected in this analysis.[4] Another process which can be important in some cases involves energetic electrons (>10eV) striking physically adsorbed molecular nitrogen.[4] This mechanism should not be important in thrusters because electrons striking the cathode potential surfaces which are of interest here do not have sufficient energy to effect dissociation.

Once nitrogen chemisorption has occurred, atomic nitrogen present in the metal apparently enhances the sputter resistance of the base metal in the surface. When the surface is impacted by an energetic ion and nitrogen is dislodged it appears to leave the surface in the atomic state.[4] This sputtering would of course be expected to occur from cathode potential surfaces where the energies of sputtering ions are substantial and it would not be expected from anode potential surfaces where the energies of sputtering ions are much lower.

The species which have been identified as important in the nitrogen chemisorption process are atoms, atomic ions and molecular ions. These species are considered in this analysis to be produced in the discharge chamber as a consequence of the following reactions:

$$N_2 + e \rightarrow N_2^+ + 2e \quad (1)$$

$$N_2 + e \rightarrow N + N^+ + 2e \quad (2)$$

$$N_2 + e \rightarrow 2N + e \quad (3)$$

$$N + e \rightarrow N^+ + 2e \quad (4)$$

The final reaction might be considered quite unlikely initially because the atomic nitrogen density would be expected to be substantially less than the molecular nitrogen density. The reaction is significant here however because of its comparatively high cross section. The electrons inducing the reactions given above will in this analysis be assumed to fit the two-group model (monoenergetic plus Maxwellian) generally applied to mercury ion thruster plasmas.

Theoretical Development

In order to calculate the current densities of the various species which are chemisorbed on the thruster walls it will be necessary to determine the density of nitrogen in the discharge chamber. For the case where a thruster being ground tested is considered, this is determined by a nitrogen balance equating inflow and outflow through the grids to and from the vacuum tank. Figure 1 is a schematic diagram of the vacuum tank and discharge chamber. In the vacuum chamber the nitrogen molecular density (n_o) can be related to the nitrogen partial pressure (p_o) and the tank wall temperature (T_o) through the perfect gas equation

$$n_o = \frac{p_o}{k\,T_o} , \quad (5)$$

where k is Boltzmann's constant. It has been assumed here that the molecules are in good thermal communication with the tank walls so they equilibrate at the tank wall temperature.

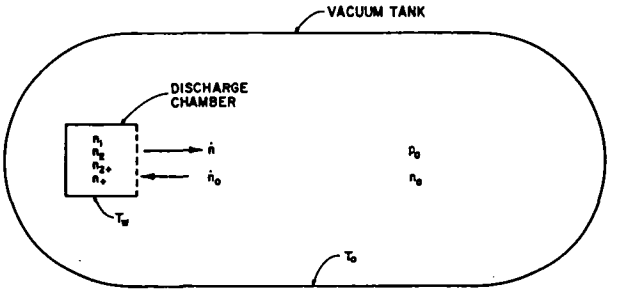

Figure 1. Nitrogen Flow Schematic

The flow rate of nitrogen atoms into the thruster ($\dot{n}_o$) is given by the equation for free molecular flow through a sharp-edged orifice,

$$\dot{n}_o = \frac{2n_o v_o A_a}{4} = \frac{n_o v_o A_a}{2} \quad (6)$$

where A_a is the open area of the accelerator grid

and v_o, the mean molecular velocity, is given by

$$v_o = \sqrt{\frac{8\ kT_o}{\pi\ m}} \quad . \tag{7}$$

The quantity m is the mass of a nitrogen molecule.

As a result of electron bombardment within the discharge chamber, nitrogen molecules (N_2) will be converted to molecular ions (N_2^+), atomic ions (N^+) and atoms (N) and these species will reach equilibrium densities n_2, n_{2+}, n_+ and n_1 respectively. The equivalent loss rate of nitrogen atoms ($\dot{n}$) from the discharge chamber as a result of migration of each of these species through the grids will then be given by

$$\dot{n} = 2\ j_2 A_e + 2\ j_{2+}\ A_s + j_+ A_s + j_1\ A_e \ , \tag{8}$$

The symbols j_2, j_{2+}, j_+ and j_1 represent respectively the particle current densities of nitrogen molecules, molecular ions, atomic ions and atoms toward the grids. The quantity A_s is the effective open area of the screen grid to ions and A_e is the effective open area of the screen and accelerator grid pair to neutral flow from the discharge chamber to the tank. This latter effective open area is determined by considering the effective resistance to flow for the two-grid system to be equal to the sum of the resistances of each separate grid and is given by

$$A_e = \frac{(A_s)\ (A_a)}{A_s + A_a} \quad . \tag{9}$$

The area given by this expression is being used because it seems to yield closer agreement with experimentally determined neutral loss rates through an accelerator system than the accelerator grid open area alone.[5,6]

The current densities of the various species in Eqn. (8) can be determined by considering each specie separately. The neutral molecules are assumed to be uniformly distributed throughout the discharge chamber and to have a Maxwellian velocity distribution corresponding to the thruster wall temperature (T_w). Hence the molecular current density (j_2) is

$$j_2 = \frac{n_2 v_2}{4} = \frac{n_2}{4}\sqrt{\frac{8\ kT_w}{\pi\ m}} \quad . \tag{10}$$

Molecular nitrogen ions are produced within the primary electron region of the thruster as a result of electron bombardment of molecular nitrogen by both primary and Maxwellian electrons. These ions are assumed to be lost uniformly at the same rate as they are produced by migration across the bounding surface area of this region (A_p). The current density of molecular ions (j_{2+}) is therefore given by the production rate divided by the surface area.

$$j_{2+} = \frac{V_p}{A_p}\, n_2\, (n_p\, P_2^{2+} + n_m Q_2^{2+}) \tag{11}$$

Inherent in the application of this equation is the assumption that the primary electrons at density n_p and the Maxwellian electrons at density n_m are distributed uniformly over the primary electron region of volume V_p. These densities as well as others used in this analysis are therefore volume-averaged values.

The rate constants for primary electrons (P_2^{2+}) and Maxwellian electrons (Q_2^{2+}) are defined as the relative velocity-cross section products based respectively on the primary electron energy and the Maxwellian electron temperature.[5] Values for these constants, pertaining to the production of molecular ions (2+) from molecular neutrals (2), have been computed using experimentally determined cross sections[7,8] and they are given in Figures 2 and 3. Tabular rate constant data are also given in the Appendix for this reaction and other reactions found to be important in this analysis.

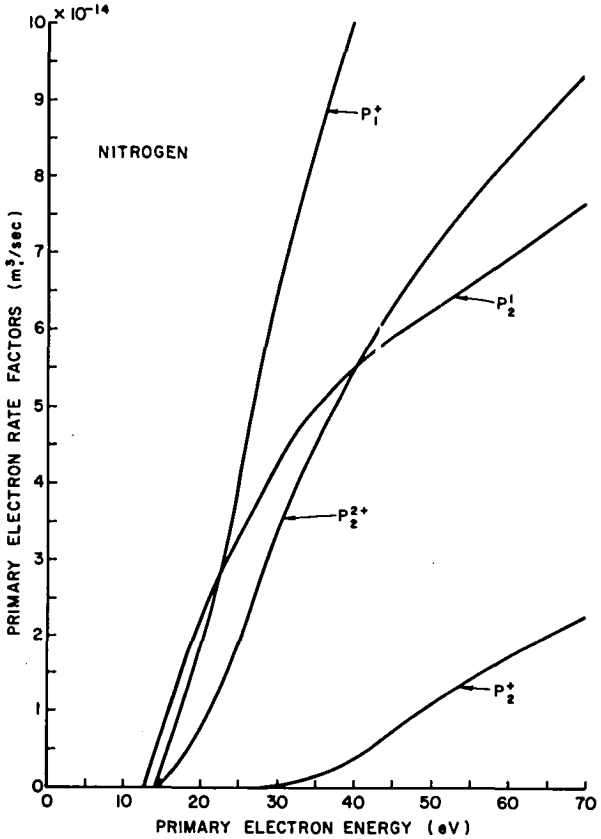

Figure 2. Primary Electron Rate Factors for Nitrogen

The current density of atomic ions which appears as the third term on the right side of Eqn. (8) is calculated in a way similar to that used for molecular ions. As suggested by Eqns. (2) and (4) however atomic ions can be produced from either atoms or molecules and the current density of this specie therefore becomes

$$j_+ = \frac{V_p}{A_p}\left[n_2(n_p P_2^+ + n_m\, Q_2^+) + n_1(n_p P_1^+ + n_m Q_1^+)\right] \quad . \tag{12}$$

The rate constants for production of atomic ions from molecules (P_2^+, Q_2^+) and from atoms (P_1^+, Q_1^+) have been determined using respectively the measured cross sections from Rapp, et al[8] and

Keiffer and Dunn,[9] and they are also given in Figures 2 and 3 and in the Appendix.

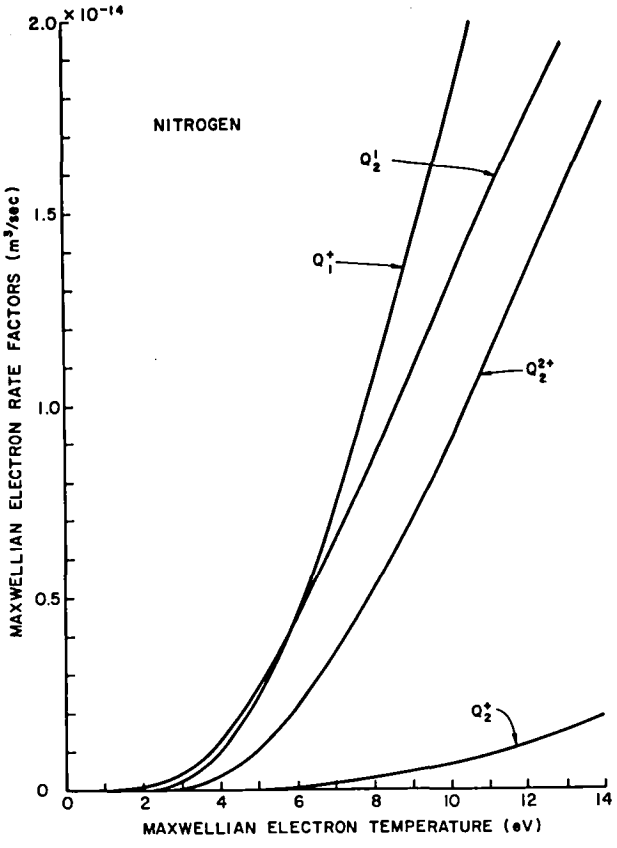

Figure 3. Maxwellian Electron Rate Factors for Nitrogen

The calculation of the current density of neutral nitrogen atoms is considerably more complex than those for the ionic species because each of the following phenomena must be considered in the formulation of the associated equation:

1) The production of atomic nitrogen in the primary electron region as a result of the reactions of Eqn. (2) and (3),

2) The loss of atomic nitrogen in the primary electron region as a result of the reaction of Eqn. (4), and

3) The release of atomic nitrogen from surfaces at cathode potential in sufficient numbers to assure no net accumulation of nitrogen once steady-state sputter desorption/chemi-adsorption conditions are achieved.

The third condition cited above reflects the fact that chemisorbed nitrogen tends to be sputtered off as atomic nitrogen.[4] This specie, which could have been derived originally from any of the atomic or ionic species subject to chemisorption, may end up being sputtered between several cathode potential surfaces. This results is an increase in the average atomic nitrogen current density going to any surface over that which would occur if nitrogen came back off of cathode potential surfaces in molecular form. It is important to note at this point that any of these species going to anode potential surfaces would be expected to return to the discharge chamber as molecular nitrogen. This occurs because anode surfaces are not subject to significant sputtering and they therefore tend to become saturated with nitrogen in the steady state condition. In order to simplify the analysis this model of nitrogen production will be decoupled from the sputtering model, and it will be assumed that the chemisorbed nitrogen coverage on cathode potential surfaces is small. This enables one to neglect cathode potential wall encounters in which a nitrogen atom or ion is rejected because the site it strikes is saturated. Considering the phenomena described above the equation for the current density of atomic nitrogen becomes

$$j_1 = \frac{V_p}{A_p}\left\{ n_2[n_p(P_2^+ + 2P_2^1) + n_m(Q_2^+ + 2Q_2^1)] - n_1[n_p P_1^+ + n_m Q_1^+]\right\} + j_1 f_{c1} + (j_+ + 2j_{2+}\Psi_{2+}) f_{c+} \quad . \tag{13}$$

The quantities f_{c1} and f_{c+} represent respectively the fractions of the discharge chamber surface area which appear to the neutral atoms and ions to be at cathode potential. These two factors differ because the grid system presents different open areas to neutral and ionized particles. The quantity Ψ_{2+} appearing in the last term is the probability that a molecular ion will be chemisorbed. This probability is dependent on both the energy of the average sputtering ion and the materials on which it is impacting. Molecular nitrogen ions, having energies characteristic of ion thruster sheaths which strike molybdenum have a sticking probability of about 50% for example.[3] Rearranging Eqn. (13) one obtains:

$$j_1 = \frac{\frac{V_p}{A_p}\left[n_2(Z_2^+ + 2Z_2^1) - n_1 Z_1^+\right] + (j_+ + 2\Psi_{2+}j_{2+}) f_{c+}}{(1 - f_{c_1})} \tag{14}$$

where the quantity Z, which has been used to simplify the expression, is defined by

$$Z_i^j = n_p P_i^j + n_m Q_i^j \quad . \tag{15}$$

In the steady state the flow rate of nitrogen atoms into the thruster ($\dot{n}_o$) would have to be equal to the nitrogen outflow rate ($\dot{n}$). Employing this condition and using Equations (5) through (8), (10) through (12) and (14) the following expression for the molecular nitrogen density in the discharge chamber is obtained:

$$n_2 = \frac{p_o}{\sqrt{2kT_o\pi m}}\left[\frac{A_e}{A_A}\sqrt{\frac{kT_w}{2\pi m}} + \frac{V_p}{A_p}\left\{ \frac{Z_2^+}{2}\left(\frac{A_s}{A_A} + \frac{A_e}{A_A}\left[\frac{f_{c+}+1}{1-f_{c1}}\right]\right) + \frac{n_1}{n_2}\left(\frac{Z_1^+}{2}\right)\left(\frac{A_s}{A_A} + \frac{A_e}{A_A}\left[\frac{f_{c+}-1}{1-f_{c1}}\right]\right) + \frac{Z_2^1}{1-f_{c1}}\left(\frac{A_e}{A_A}\right) + Z_2^{2+}\left(\frac{A_s}{A_A}\right) + \frac{A_e}{A_A}\left[\frac{f_{c+}}{1-f_{c1}}\right]\Psi_{2+}\right)\right\}\right]^{-1} \quad . \tag{16}$$

The first term in the square brackets generally tends to dominate this denominator term. This corresponds physically to the condition in which nitrogen is lost through the grids primarily in the form of neutral molecules. With the exception of the atomic-to-molecular nitrogen density ratio (n_1/n_2) Equation (16) is written in terms of quantities which can be evaluated. The quantities which would have to be known include the discharge plasma properties, the tank nitrogen partial pressure and the geometry and material specifications for the thruster. The atomic-to-molecular density ratio (n_1/n_2) can be obtained if one assumes that both of these species have a uniform Maxwellian distribution characterized by the discharge chamber wall temperature (T_w). Then the current density of atoms leaving the primary electron region where they are produced is given by:

$$j_1 = \frac{n}{4}\sqrt{\frac{8kT_w}{\pi(m/2)}} = n_1\sqrt{\frac{kT_w}{\pi m}} \qquad (17)$$

Combining Equations (11), (12), (14) and (17) one then obtains:

$$\frac{n_1}{n_2} = \frac{2\,Z_2^1 + (1+f_{c+})\,Z_2^+ + 2\Psi_{2+}\,f_{c+}\,Z_2^{2+}}{\frac{A_p}{V_p}(1-f_{c1})\sqrt{\frac{kT_w}{\pi m}} + (1+f_{c+})\,Z_1^+} \qquad (18)$$

The first term in the numerator and the first term in the denominator tend to dominate this expression. Physically this dominance means that neutral atoms are produced primarily by the reaction identified in Eqn. (3) and lost as a result of migration at thermal velocity to anode potential surfaces or through the grid apertures. It is probably desirable at this point to reiterate that atoms going to cathode potential surfaces are considered to be sputtered back off as atoms in the model and this physical condition is reflected in the $(1-f_{c1})$ term appearing in the denominator of Eqn. (18).

Eqns. (18), (16), (17), (11) and (12) now comprise a closed form solution for the particle densities of the nitrogen atoms and molecules and the current densities of molecular and atomic ions and neutral atoms in terms of plasma properties, known properties of nitrogen and geometrical properties of the discharge chamber. Current densities computed from these equations when multiplied by the chemisorption probability for each corresponding specie determine the rate of formation of sputter resistant sites on the base material. This information may now be applied to a sputtering theory to determine the effect of the nitrogen on the erosion rate of the base material.

Application of Nitrogen Arrival Rates in a Sputtering Theory

Rawlin and Mantenieks[1] observed what appeared to be a transition between two sputtering levels as the nitrogen partial pressure was increased from very low to very high levels. They suggested this transition was determined by the relative arrival rates of sputtering ions (mercury) and the contaminant particles which are being chemisorbed (nitrogen). Such a theory might be formalized by assuming that incident mercury ions arriving at a site would exhibit two distinct types of behavior depending on whether or not that site was influenced by a chemisorbed nitrogen atom. Similarly, incident nitrogen being chemisorbed would be expected to exhibit this same binary behavior. The wear rate of base metal per unit area would then be given by

$$\dot{W} = S\,j_{Hg}(1-\phi) + S'\,j_{Hg}\,\phi \qquad (19)$$

where S is the yield of base metal at a site where nitrogen doesn't influence the sputtering, S' is the yield at a site where the influence of the nitrogen is felt, ϕ is the probability of striking a site affected by nitrogen and j_{Hg} is the incident current density of the particles that effect sputtering. The nitrogen concentration would after a period of operation reach a steady value so the nitrogen chemisorption and sputter induced desorption rates would be equal. The equation describing this condition would be

$$(j_1 + j_+ + 2j_{2+}\,\Psi_{2+})(1-\phi) = j_{Hg}\,\phi\,S_1 \qquad (20)$$

where S_1 is the sputtering rate of nitrogen atoms from a site where nitrogen is present. Chemisorption probabilities of unity have been assumed for the nitrogen atoms and atomic ions in this equation. Combining Eqns. (19) and (20) to eliminate the probability factor ϕ one obtains the following expression for the base metal removal rate:

$$\dot{W} = j_{Hg}\,S\left\{\frac{\frac{S_1}{S'} + \frac{j_1 + j_+ + 2\Psi_{2+}\,j_{2+}}{S\,j_{Hg}}}{\frac{S_1}{S'} + \frac{j_1 + j_+ + 2\Psi_{2+}\,j_{2+}}{S'\,j_{Hg}}}\right\} \qquad (21)$$

In the limit of high nitrogen chemisorption this equation yields a base metal loss rate per unit area that is characteristic of a saturated surface ($j_{Hg}\,S'$) and for the opposite limit the rate is that for the virgin metal ($j_{Hg}\,S$). The limiting behavior is therefore consistent with the observations of Rawlin and Mantenieks.[1] The ratio (S_1/S') appearing in Eqn. (21) represents the average number of nitrogen atoms sputtered per base metal atom sputtered when a site influenced by nitrogen is bombarded. Equation (21), while it may not represent the sputtering processes involved in this problem with complete physical accuracy, does demonstrate how nitrogen currents to the surfaces of a thruster could be incorporated into a sputtering model.

Experimental Procedure

In an effort to verify the theoretical model of nitrogen specie production proposed in this paper, experiments were conducted in which the molecular and atomic ion currents coming from a SERT II thruster[10] were measured directly and also calculated using the model proposed herein. The SERT II thruster was equipped with a standard grid set (71% open area screen grid, 48% open area accelerator grid, 13.9 cm dia. beam) and was operated at 2kV and 3kV net and total accelerating voltages respectively.

Tests were conducted by operating the thruster on mercury for several hours until it was running stably and the vacuum tank pressure was in the 5 to 7 X 10^{-6} torr range. Nitrogen was then introduced into the tank at a location upstream of the thruster until stable thruster operation at the total tank pressure desired was established. The nitrogen was introduced into the tank in the manner mentioned to prevent direct access of the nitrogen through the thruster grids without at least one encounter with the tank wall. This facilitated equilibration of the molecular nitrogen and the tank wall temperatures. With the thruster operating stably its ion beam was probed using a collimating E x B momentum analyzer[11] to determine current density profiles for the pertinent ionized species (Hg^+, N_2^+, N^+) in the beam at probe pitch angles of 0°, 5°, 10° and 15°. These data were subsequently analyzed to determine the current density of each specie averaged across the beam. Immediately after the beam current density profiles had been obtained the discharge chamber was Langmuir probed at sixteen locations. Subsequent analysis of these Langmuir probe data using the technique developed by Beattie[12] yielded plasma property profiles for the discharge chamber. Plasma properties averaged over the primary electron volume were then determined so they could be used as input to the theoretical model described previously in this paper.

Figure 4 shows the E x B probe output measured as the plate voltage on the probe was varied to change the charge-to-mass ratio of the specie being sensed by the instrument. These data were obtained with the probe on centerline looking down the thruster axis. The figure shows the highest peak for singly-charged mercury with other, lower intensity peaks occurring at charge-to-mass ratios corresponding to doubly-ionized mercury, molecular nitrogen ions and atomic ions. Note that the upper curve is a thirty-fold amplification of the lower one. Figure 4 suggests that both molecular and atomic nitrogen ions are produced in significant numbers in the discharge chamber when nitrogen is present in the facility.

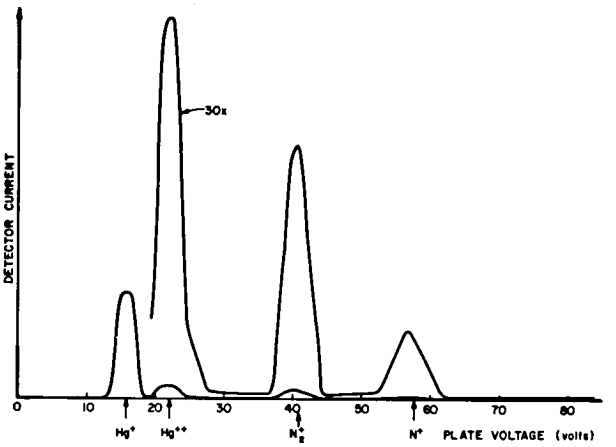

Figure 4. E x B Probe Signature in the Beam of a Nitrogen Contaminated Ion Thruster

Tests were conducted over a range of nitrogen partial pressures and thruster flow rates, discharge currents and voltages. The test conditions and results obtained in these tests are shown in Table I. The plasma properties given in this table are the volume-averaged values determined from Langmuir probe data which were used as input to the theoretical model. The calculated values of atomic and molecular ion current ratios were obtained by using these data to calculate nitrogen current densities from Eqn. (18), (16), (11) and (12), then multiplying the results by the beam cross sectional area and dividing by the measured beam current attributable to mercury ions.

The estimated temperatures and geometrical and chemisorption probability factors determined for the SERT II thruster and used as input to these equations are:

Table I

Test Conditions and Results

Test #	Nitrogen Partial Pressure (p_o) (torr)	Max. Elec. Temp. (eV)	Pri. Elec. Energy (eV)	Maxwellian Density n_m (m^-)	Primary Density n_p (m^-)	Atomic Ion Current Ratio meas. (%)	Atomic Ion Current Ratio calc. (%)	Molecular Ion Current Ratio meas. (%)	Molecular Ion Current Ratio calc. (%)
1	2.2×10^{-6}	6.5	21.6	2.0×10^{17}	8.0×10^{15}	0.99	0.81	2.07	1.47
2	1.2×10^{-5}	5.6	21.7	1.9×10^{17}	6.7×10^{15}	1.17	2.23	4.95	5.13
3	3.5×10^{-6}	7.5	28.2	8.5×10^{16}	1.0×10^{16}	0.68	1.03	4.86	2.10
4	3.0×10^{-6}	6.6	28.2	8.4×10^{16}	1.0×10^{16}	0.78	0.62	2.94	1.52
5	3.0×10^{-6}	5.7	25.7	8.8×10^{16}	1.1×10^{16}	0.67	0.48	3.42	1.27
6	1.3×10^{-5}	5.6	23.1	9.4×10^{15}	6.9×10^{15}	1.85	1.18	6.66	4.00
7	5.2×10^{-6}	6.5	28.4	1.4×10^{17}	1.6×10^{16}	1.53	1.69	4.96	2.89
8	1.5×10^{-5}	6.4	27.6	1.6×10^{17}	1.4×10^{16}	2.49	5.56	7.59	9.36
9	4.5×10^{-6}	8.7	29.9	1.2×10^{17}	1.4×10^{16}	1.76	2.81	5.70	3.68

- o Vacuum Tank Wall Temperature, $T_o \approx 77°k$
- o Discharge Chamber Wall Temperature, $T_w \approx 500°k$
- o Primary Electron Region Volume-to-Surface Area Ratio, $V_p/A_p = 1.45 \times 10^{-2}$ m
- o Screen-to-Accel Grid Open Area Ratio, $A_s/A_a = 1.5$
- o Effective Open Area-to-Accel Grid Open Area, $A_e/A_a = 0.60$
- o Fraction of Thruster Interior at Cathode Potential as seen by Neutrals, $f_{c1} = 0.36$
- o Fraction of Thruster Interior at Cathode Potential as seen by Ions, $f_{c+} = 0.28$
- o Sticking Probability for Molecular Nitrogen Ions, $\psi_{2+} = 0.5$ (this quantity is a function of ion energy and base material. Reference 3 suggests a value of 0.5 for molybdenum and discharge voltage of about 40v).

The measured current ratios in Table I were determined by taking the ratio of average nitrogen specie current density to average singly ionized mercury current density as determined from analysis of the E x B probe measurements. Figure 5 is a plot of the calculated molecular and atomic current ratios against the measured ones. The data show considerable scatter but suggest that the model for molecular and atomic nitrogen current density calculations is accurate to within about ± 100%. It is also noteworthy that the atomic ion data seem to be centered close to the line of perfect correlation. The majority of the molecular ion data on the other hand lie below this line and this suggests a possible systematic error in the model. The most probable sources of such an error are considered to be related to the values assumed for sticking coefficients and geometric factors. The accuracy of nitrogen partial pressure is also questionable because it was determined as the difference in pressures measured before and after the introduction of nitrogen rather than with a residual gas analyzer. Finally Langmuir probe trace analysis is always a source of possible error. Considering the crudeness of the model and the possible sources of experimental error the results appear to be satisfactory.

Although the atomic neutral current density given by Eqn. (17) could not be verified with the available instrumentation it is probably safe to assume that this equation would also be accurate to within about ± 100%. Examination of the magnitudes of the current densities of the various nitrogen species given by Eqns. (11), (12) and (17) for typical SERT II mercury thruster operating conditions suggests that it is the atomic neutral current density that has the greatest magnitude. The molecular and atomic ion current density were typically about one-fifth and one-tenth of the atomic neutral current density respectively.

Conclusion

A model describing the current densities of nitrogen species produced in the discharge chambers of ion thrusters has been developed. These species, which are identified as nitrogen atoms, atomic nitrogen ions and molecular nitrogen ions, tend to be chemisorbed on cathode potential thruster walls when they reach them. The model suggests that nitrogen atoms are produced primarily by electron induced dissociation of molecular nitrogen and lost as a result of atom migration to anode potential surfaces and through the grids. These atoms are the major contributer to the current density of species that are chemisorbed at cathode potential surfaces. The molecular and atomic current densities are about one-fifth and one-tenth respectively of the neutral atom current density. The current densities of nitrogen ions were measured in the beam of a SERT II thruster as a function of discharge chamber conditions and nitrogen partial pressure. These measurements agreed with current densities calculated using measured plasma properties and estimated geometrical factors to within about ± 100%.

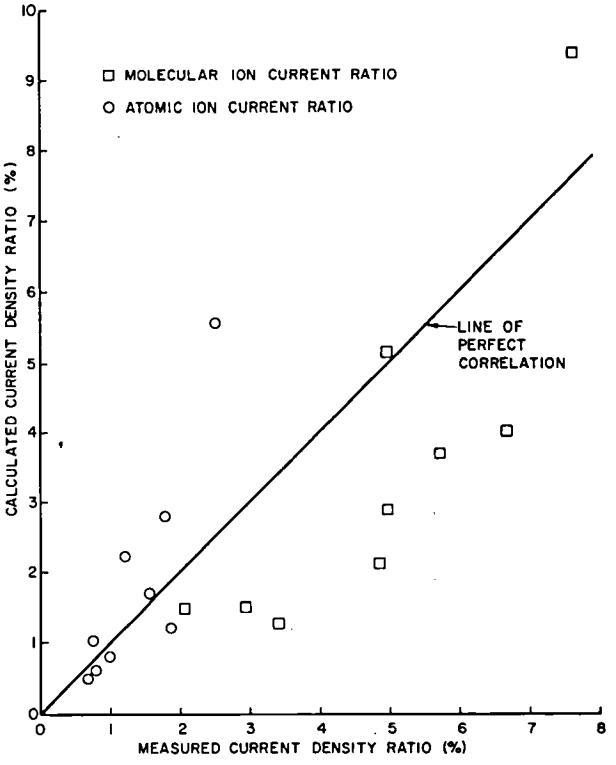

Figure 5. Correlation of Measured and Calculated Results

References

1. Rawlin, V. K. and M. A. Mantenieks, "Effect of Facility Background Gases on Internal Erosion of the 30-cm Hg Ion Thruster," AIAA Paper No. 78-665, April 1978.

2. Adams, D. L. and L. H. Germer, "The Adsorption of Nitrogen on W(100)," Surface Science, v.26, (1971), pp. 109-124.

3. Winters, H. F., "Ionic Adsorption and Dissociation Cross Section for Nitrogen," Jour. Chem. Phys., v. 44, No. 4, 15 Feb. 1966, pp. 1472-1476.

4. Winters, H. F. and D. E. Horne, "The Chemisorption of Nitrogen at Activated Sites on a Polycrystalline Tungsten Surface," Surface Science, v. 24, (1971), pp. 587-611.

5. Peters, R. R., "Double Ion Production in Mercury Thruster," NASA CR-135019, April 1976, p. 46.

6. Longhurst, G. R. and P. J. Wilbur, "Plasma Property and Performance Prediction for Mercury Ion Thrusters," AIAA Paper No. 79-2054, Nov. 1979.

7. Rapp, D. and P. Englander-Golden, "Total Cross Sections for Ionization and Attachment in Gases by Electron Impact, I. Positive Ionization," Jour. Chem. Phys., v. 43, No. 5, 1 Sept. 1965, pp. 1464-1479.

8. Rapp, D., et al., "Cross Sections for Dissociative Ionization of Molecules by Electron Impact," Jour. Chem. Phys., v. 42, No. 12, 15 June 1965, pp. 4081-4084.

9. Kieffer, L. J. and G. H. Dunn, "Electron Impact Ionization Cross-Section Data for Atoms, Atomic Ions, and Diatomic Molecules: I. Experimental Data," Rev. of Mod. Phys., v.38, No. 1, Jan. 1966.

10. Bechtel, R. T., et al., "Performance of a 15-centimeter Diameter Hollow-Cathode Kaufman Thruster," AIAA Paper No. 68-88, Jan. 1968.

11. Vahrenkamp, R. P., "Measurement of Doubly Ions in the Beam of a 30-cm Mercury Bombardment Thruster," AIAA Paper 73-1057, Oct. 1973.

12. Beattie, J. R., "Numerical Procedure for Analyzing Langmuir Probe Data," AIAA Journal, v. 13, No. 7, July 1975, pp. 950-952.

Appendix

On Board Nitrogen Mass Requirement for 30 cm Thruster Mission

The idea of carrying nitrogen on board a spacecraft to extend the lifetimes of discharge chamber components by increasing their sputter resistance could be of interest if it would not result in significant increase in spacecraft mass. Screen grid erosion rate data complied by Rawlin and Mantenieks[1] suggest that a substantial reduction in the erosion rate of molybdenum began to occur in ground based endurance tests of a 30 cm thruster operating at a 2 A beam current and a 36v discharge voltage when the facility pressure was about 1×10^{-6} torr. Equations (5), (6) and (7) of this paper can be combined to yield the following equation which can be used to calculate the molecular nitrogen flow rate into the thruster corresponding to this pressure.

$$\dot{n}_o = \frac{p_o A_a}{\sqrt{2 k T_o m \pi}} .$$

Using an assumed vacuum tank wall temperature T_o of 77°K, an accelerator grid open area of 0.0304 m^2, together with the facility pressure of 1×10^{-6} torr = 1.33×10^{-4} nt/m^2 one finds a nitrogen flow rate of $\dot{n}_o = 0.037$ A equiv. For a 10,000 hour mission this corresponds to supplying about 0.39kg of nitrogen directly into the discharge chamber. This corresponds to about 0.3% of the mercury mass required to operate the thruster.

Rate Factors for Nitrogen

Primary Electron Energy (eV)	P_2^{2+} (m^3/sec)	P_2^{+} (m^3/sec)	P_2^{1} (m^3/sec)	P_1^{+} (m^3/sec)
10	--	--	--	--
20	0.72×10^{-14}	--	2.31×10^{-14}	0.18×10^{-13}
30	3.31	0.05×10^{-14}	4.25	0.65
40	5.48	0.39	5.51	1.02
50	7.04	1.09	6.25	1.22
60	8.31	1.72	6.94	1.36
70	9.33	2.26	7.64	1.48

Maxwellian Electron Temp. (eV)	Q_2^{2+} (m^3/sec)	Q_2^{+} (m^3/sec)	Q_2^{1} (m^3/sec)	Q_1^{+} (m^3/sec)
3	0.009×10^{-14}	0.0003×10^{-15}	0.039×10^{-14}	0.024×10^{-14}
4	0.04	0.004	0.13	0.10
6	0.21	0.057	0.45	0.47
8	0.52	0.25	0.87	1.06
10	0.91	0.62	1.31	1.77
12	1.34	1.19	1.74	2.54

SPONSORED BY:
PRINCETON UNIVERSITY CONFERENCE
AMERICAN INSTITUTE OF AERONAUTICS AND ASTRONAUTICS (AIAA)
DEUTSCHE GESELLSCHAFT FUR LUFT-UND RAUMFAHRT (DGLR)

79-2114
The Screen Hole Plasma Sheath of an Ion Accelerator System

G. Aston and P. J. Wilbur,
Colorado State University, Fort Collins, Colo.

PRINCETON/AIAA/DGLR 14th INTERNATIONAL ELECTRIC PROPULSION CONFERENCE

Oct. 30-Nov. 1, 1979/Princeton, N.J.

THE SCREEN HOLE PLASMA SHEATH OF AN ION ACCELERATOR SYSTEM

Graeme Aston* and Paul J. Wilbur†
Colorado State University
Fort Collins, Colorado 80523

Abstract

Results of the first probing of the screen hole sheath of an ion accelerator system are presented. The screen hole sheath, represented as a set of equipotential contours, extends over a large distance within the discharge plasma. Under no conditions examined does the sheath enter the screen hole. Edge hole defocusing of multiaperture accelerator systems is due primarily to local plasma density variations rather than adjacent screen hole sheath interactions. The sheath boundary is independent of screen-to-accelerator grid spacing when the grid set is operated at the minimum ion beam divergence condition. Significant ion focusing effects occur in the sheath adjacent to the screen grid webbing leading to increased ion source beam current efficiency with decreasing screen-to-accelerator grid separation and/or screen grid thickness.

Nomenclature

ℓ_g = grid separation distance, mm

d_s = screen hole diameter, mm

d_a = accelerator hole diameter, mm

t_s = screen grid thickness, mm

t_a = accelerator grid thickness, mm

V_T = total accelerating voltage, volts

R = net-to-total accelerating voltage ratio

V_D = discharge voltage, volts

$\Delta\phi$ = potential variation through sheath, volts

T_e = Maxwellian electron temperature, eV

NP/H = normalized perveance per hole, amp/volt$^{3/2}$

Introduction

The ion beam divergence characteristics of ion accelerator systems have been studied experimentally by many workers in recent years.[1-6] Presently, the ion acceleration and focusing process is fairly well understood. Using the data available in Refs. 5 and 6, one can quite accurately predict the ion beam divergence characteristics of an arbitrary two or three-grid accelerator system at any specified operating condition. However, the process by which the accelerated ions are extracted from the plasma is not well understood. It is known that a plasma sheath is formed and that this sheath is a transition region separating the plasma from a region where ions are being accelerated through the screen hole(s) of the accelerator system. This screen hole plasma sheath varies in position and shape as a result of plasma density (i.e., beam current), grid geometry and grid accelerating potential variations. Consequently, changes in the physical characteristics of the screen hole plasma sheath affect directly such things as the divergence of the beam ions ejected from the accelerator system, direct ion impingement upon the accelerator grid with its associated erosion, ion re-combination over the screen grid surface and the associated lowering of ion source beam current efficiency, ion bombardment and erosion of the screen grid, and the limit to the ion current which can be extracted from the plasma.

Some theoretical and experimental work has been done on determining the physical characteristics of the screen hole plasma sheath.[7-9] However, the theoretical models treat the sheath as a single equipotential surface separating plasma from accelerated ions with no transition region. Similarly, the available experimental data is limited to a couple of idealized cases; being photographic in nature, it represents the sheath as a discontinuity and is of little use. Therefore, a thorough experimental investigation of the physical structure and behavior of the screen hole plasma sheath was undertaken. The basic physical phenomena uncovered would provide a better understanding of the ion extraction process and aid in the development of improved theoretical models.

Accelerator System Scaling

In order to make accurate measurements of the physical characteristics of the screen hole plasma sheath (i.e., position, shape and structure), it was necessary to use a large accelerator system so adequate spatial resolution could be achieved. This was done by increasing the screen hole diameter from a value of 2.06 mm, which is typical of ion thruster and ground application ion source accelerator systems, to a diameter of 12.7 mm. The other geometrical accelerator system parameters were also scaled directly by the ratio of these two diameters so geometric similarity was maintained. It was important to determine whether the maximum normalized perveance per hole[5] and ion beam divergence characteristics of such large accelerator systems were any different from the much smaller accelerator systems typical of most ion sources. Careful probing of the ion beam emerging from the large accelerator systems showed the divergence characteristics of these grid sets were identical, within experimental error, to those of the smaller accelerator systems. Also, tests determining the maximum normalized perveance per hole of the larger

* Research Assistant, Department of Physics, Student Member AIAA.

† Professor, Department of Mechanical Engineering, Member AIAA.

grid sets showed this limit to be equal to that obtained with the smaller accelerator systems. Details of these tests have been published previously.[10] In summary, scaling up ion accelerator grid systems to larger sizes does not appear to affect ion beam divergence characteristics or the maximum normalized perveance per hole as long as similar non-dimensionalized grid parameters are maintained.

Sheath Probing Technique

The screen hole plasma sheath was investigated at various grid geometry and accelerator system operating conditions. Figure 1 illustrates the manner in which these data were obtained. In Fig. 1a a cross sectional view of the large seven hole two-grid accelerator system used for this study is depicted. The probing volume surrounding the central screen hole is shown by the dotted rectangle in this figure. The probe origin was set at the downstream face of the screen grid and the sheath was probed a distance of one screen hole diameter back into the discharge chamber plasma from this point. The width of the probing region was 1.4 d_s (d_s = screen hole diameter) in order that sufficient data points could be taken to define the sheath overlap region adjacent to the screen grid webbing. Figure 1b indicates the manner in which the probe traversed the central screen hole. The sheath probe was set at each of the fifteen radial locations shown. At each location the probe was swept axially through the sheath and the variation in local plasma potential was recorded. In this way a full sheath profile, for a particular accelerator system geometry and operating condition, was characterized by an array of local plasma potential values.

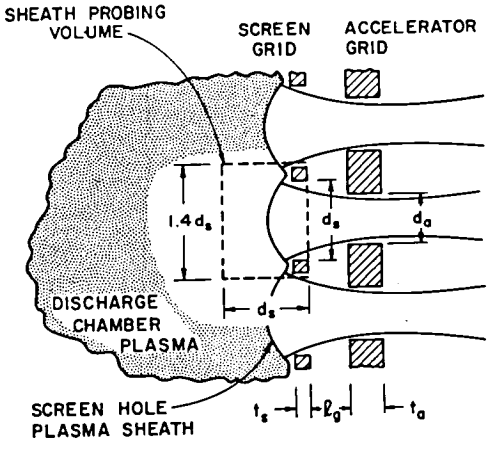

a)

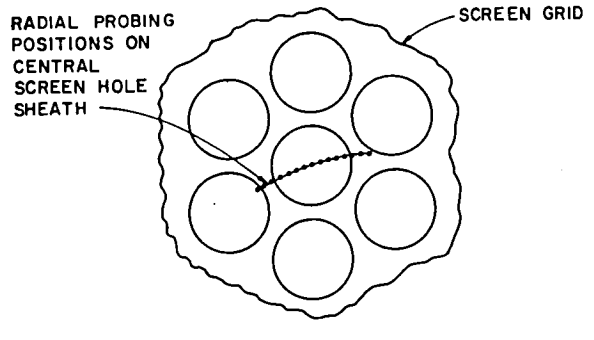

b)

Fig. 1. a) Sheath probing volume.
b) Sheath probe location.

The accelerator system depicted in Fig. 1 was positioned over a masked down discharge chamber of an 8-cm diameter electron bombardment ion source. This ion source had a mildly divergent magnetic field and used tungsten wire filaments as both the main and neutralizer cathode emitters. Argon propellant was used and all source operation was conducted in a 30-cm pyrex bell jar. Average bell jar pressure was 2.3 x 10^{-4} Torr.

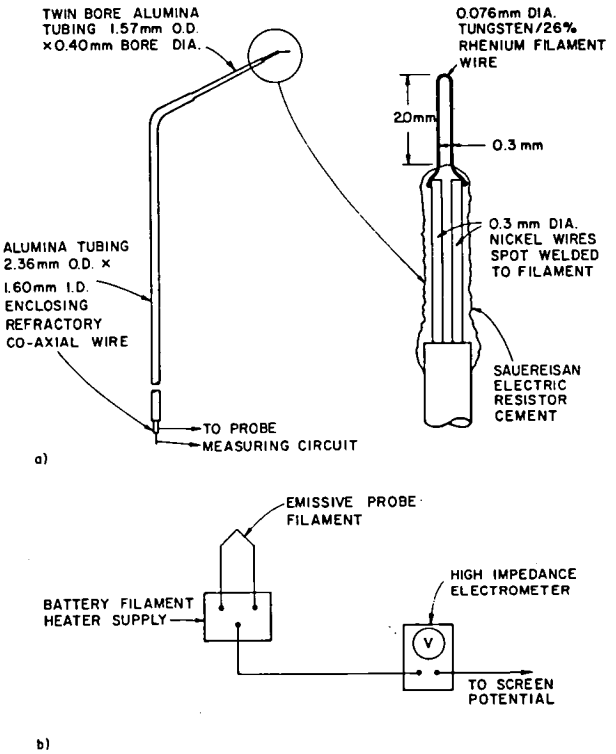

Fig. 2. a) Sheath probe design details.
b) Circuit schematic for floating potential measurements.

A floating emissive Langmuir probe was used to study the screen hole plasma sheath and is shown in Fig. 2a. This probe has a simple dog leg shape so it can be positioned off the axis of the central screen hole thereby permitting the probe tip to move radially as the probe is rotated. An enlarged drawing of the probe tip is also shown to detail the basic construction of the probe filament, its dimensions and its attachment to the support wires. The sheath probe is electrically isolated from the discharge chamber body and when the filament is heated to incandescence the filament floating potential becomes the local plasma potential. The instrumentation used to measure the probe floating potential is shown schematically in Fig. 2b. Briefly, an isolated battery supply provides heating power for the filament. The filament is connected through this battery supply to a high impedance electrometer set to measure voltage; the

low side of the electrometer is referenced to screen grid potential. The accuracy of the screen hole sheath emissive probe was checked by comparing its response to that of a small spherical Langmuir probe located within the discharge chamber plasma slightly off the ion source axis. This spherical probe was used to measure local plasma conditions just prior to entering the screen hole sheath region. Plasma potential measurements taken with the emissive and spherical Langmuir probes in the same location showed good agreement. Generally, the only source of error originating with the use of a floating emissive probe of the design shown in Fig. 2 is a small D.C. voltage extending along the length of the heated filament. This potential difference was approximately 0.5 volt in this experiment. A more detailed discussion of the operating characteristics of floating emissive Langmuir probes is presented by Kemp and Sellen.[11] The positioning error of the sheath emissive probe was ± 0.05 mm in the axial direction and ± 0.25 mm in the radial direction.

Sheath Contour Results

The screen hole sheath is really the set of equipotential lines that separate the region of homogeneous plasma from the region of accelerated ions where there are no electrons. These equipotential contours were computer drawn from the array of data obtained after probing each sheath profile. Figure 3 shows the screen hole sheath, represented as a set of equipotential contours, for the central screen hole of the large seven hole two-grid set shown in Fig. 1. Unless indicated otherwise, the following grid geometry and accelerator system operating conditions may be assumed:

center-to-center hole spacing = 14.7 mm
screen hole diameter, d_s = 12.7 mm
total accelerating voltage, V_T = 1100 volts
net-to-total accelerating voltage ratio, R= 0.7
screen grid thickness ratio, t_s/d_s= 0.17
accelerator hole diameter ratio, d_a/d_s = 0.64
accelerator grid thickness ratio, t_a/d_s= 0.37.

The central screen hole in Fig. 3 is shown in a cross sectional view and is drawn to scale as are the equipotential contours. It should be noted that the path traced out by the sheath probe in Fig. 1b crosses the webbing of the adjacent screen holes at different locations. These locations were not always the same as those shown in Fig. 1b because each grid geometry tested was not orientated in exactly the same way about the center line of the source. Consequently, the path traced out by the probe, although always passing through the screen hole center line and being set at the same radial positions, did vary somewhat relative to the adjacent screen holes. To indicate this variation the cross sectional view of the screen hole in Fig. 3 has the screen grid webbing artificially extended out to the extremities of the probing volume.

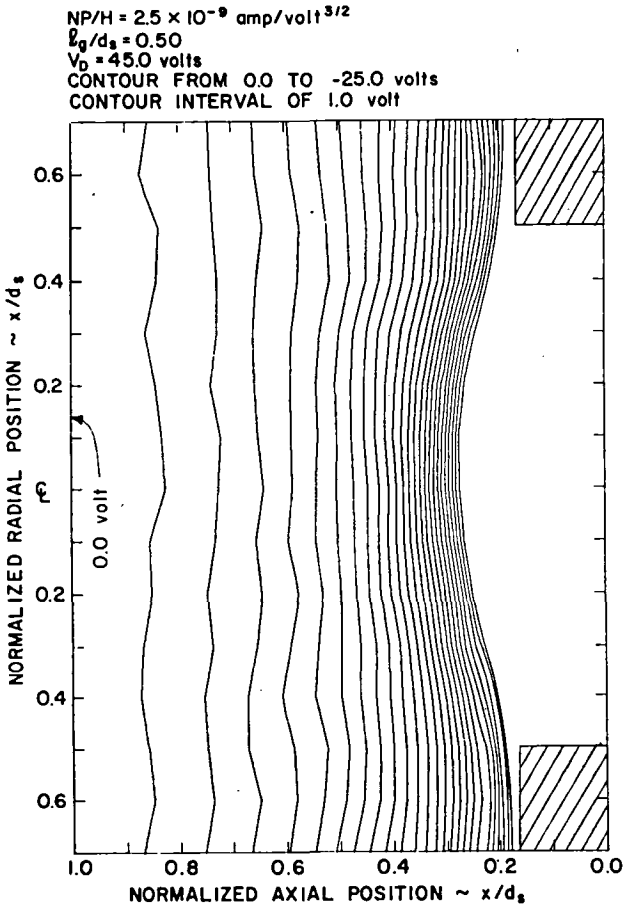

Fig. 3. Full screen hole sheath profile for standard grid set geometry and operating conditions.

The grid set used in Fig. 3 had an intermediate screen-to-accelerator grid separation ratio, ℓ_g/d_s = 0.50 and a discharge voltage, V_D, of 45.0 volts. This grid set was operated at a beam current or normalized perveance per hole value known to give the lowest ion beam divergence. The zero volt contour line shown in Fig. 3 is approximately equal to the equilibrium bulk plasma potential deep within the discharge chamber. Equipotential contours are plotted at one volt increments relative to this zero reference potential and are shown extending to -25.0 volts of this reference plasma potential. The -25.0 volt contour line is very close to the sheath boundary. Beyond this point the local electron density drops rapidly off to zero over a distance of the order of the probe axial resolution limit (~0.2mm). The sheath surrounding the central screen hole is fairly symmetrical; the slight asymmetry is believed to be due to the sheath probe entering different regions of the screen grid webbing at the extremities of its travel. In these regions the adjacent screen hole sheath interactions are slightly different. Perhaps the most important conclusion to draw from Fig. 3 is that the screen hole sheath extends over a large distance, influencing ion and electron trajectories deep within the discharge chamber plasma. To illustrate this point, the Debye length for the plasma condition shown in Fig. 3 was 0.6 mm whereas significant potential variations are evident over distances ten times this value.

Figure 4 makes a comparison between the sheath surrounding the central screen hole of the large seven hole two-grid set and the sheath that surrounds one of the edge holes of this grid set. For clarity, only the -5.0, -15.0 and -25.0 volt contours are plotted in each case. Again, an intermediate grid separation ratio was used while the grid set was operated at a normalized perveance per hole value known to give the minimum beam divergence. Sheath distortion is evident for the

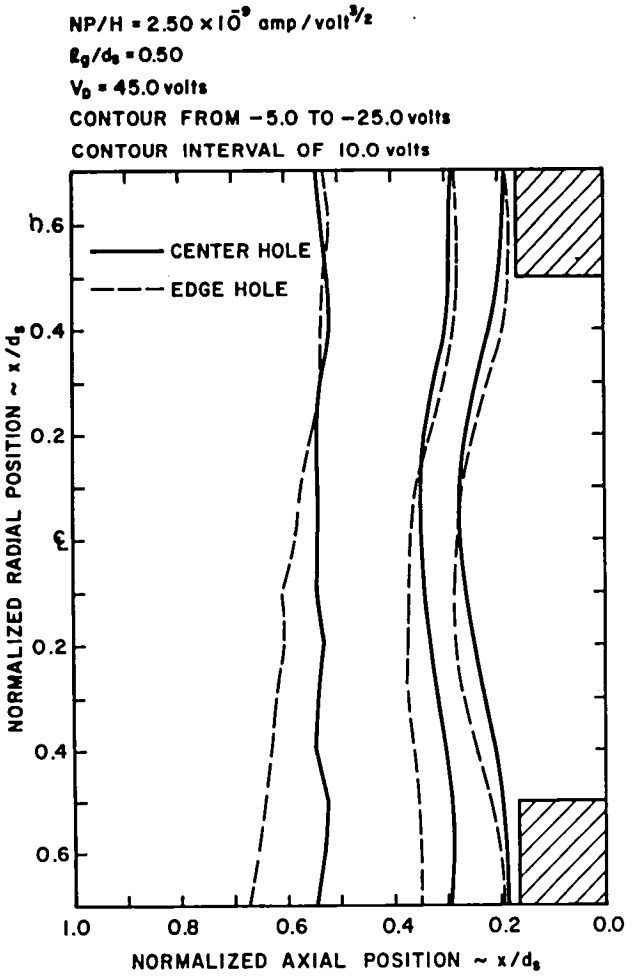

Fig. 4. Comparison of center and edge hole sheath equipotential lines (grid set edge towards bottom of figure).

edge hole. This distortion is tending to direct the initial ion trajectories to greater off-axis angles than those emerging from the central screen hole sheath. Plasma density variations across the edge hole were primarily responsible for the sheath distortion shown in Fig. 4. An edge hole was also probed in a region where the plasma density was uniform. Here, less significant sheath distortion was evident. It has been well documented by numerous workers in the field that those ions emerging from the outer ring of holes in a multi-aperture accelerator system have very divergent trajectories and are responsible for most of the accelerator grid erosion. The results of this study indicate that the decrease in plasma density which occurs as the discharge chamber edge is approached distorts the edge screen hole plasma sheath giving rise to more divergent ion trajectories. The lack of adjacent screen hole sheath interactions for an edge hole does not significantly contribute to this sheath distortion and ion focusing effect.

Figure 5 shows the effect on the screen hole plasma sheath when the grid set is operated at a very low and very high normalized perveance per hole. Since the central screen hole sheath is fairly symmetrical only half a sheath profile is being presented. As expected, increasing the normalized perveance per hole, or beam current, moves the sheath closer to the screen hole, the

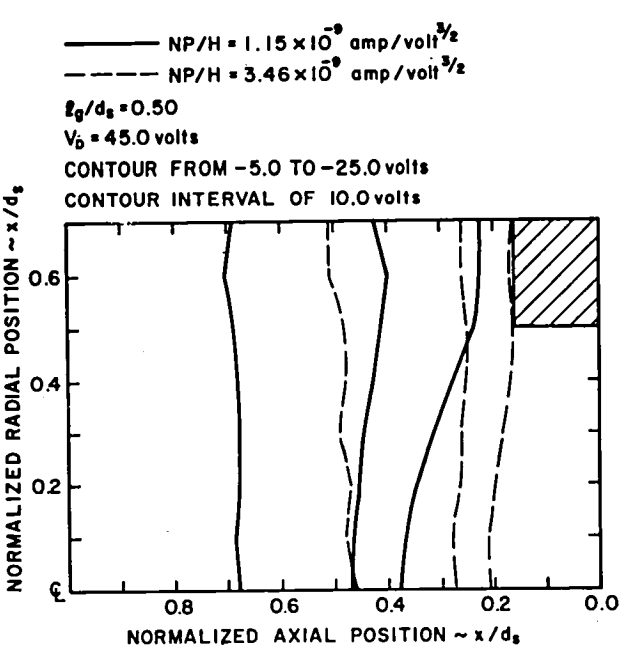

Fig. 5. Screen hole sheath movement and shape change with increasing beam current, or normalized perveance per hole, (half sheath profile).

sheath's bowed shape becoming more planar with this increase. An unexpected occurrence was that the screen hole sheath did not enter the screen hole even for a very large normalized perveance per hole. The maximum normalized perveance per hole condition pertaining to the dashed line of Fig. 5 was that one just below the onset of substantial accelerator grid impingement. It is noteworthy that the sheath has not been observed within the screen hole for any grid set or operating condition examined so far.

Figure 6 compares the effect on the screen hole sheath as the separation distance between the screen and accelerator grids was varied. In all cases the grid sets were operated at a normalized perveance per hole value known to give the lowest ion beam divergence for that particular grid separation. For clarity, only the -10.0 and -20.0 volt contour lines are plotted. Comparing the -20.0 volt contour lines shows that in all cases these lines were fairly coincident. The only significant departure from this similarity occurred for the closest grid separation tested (ℓ_g/d_s = 0.25) and then only towards the center of the screen hole. Since the -20.0 volt contour line is fairly close to the sheath boundary we can draw a tentative conclusion. Namely that to first order the screen hole sheath boundary has approximately the same position and shape for any screen-to-accelerator grid separation when the grid set is operated at its minimum beam divergence condition. We should note, however, that the sheath thickness is very different as evidenced by the variation in the separation between the -10v and -20v contours in the figure. Another interesting phenomenom apparent in Fig. 6 is that the sheath potentials around the webbing for the large grid separation (ℓ_g/d_s = 1.00 -solid line) tend to direct the plasma ions directly into the screen grid webbing. However, with decreasing grid separation these potential contours begin to direct ions away from the webbing and into the hole. This effect is illustrated by the electric field vectors shown in Fig. 6. This deflection of the

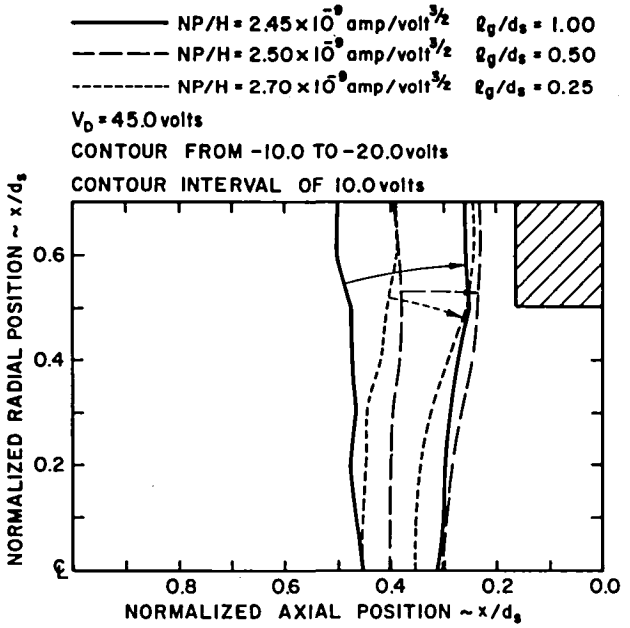

Fig. 6. Screen hole sheath movement and shape change with decreasing screen-to-accelerator grid separation ratio, ℓ_g/d_s, (half sheath profile).

ions away from the webbing as the grid separation is reduced would lead to reduced discharge losses. Such a reduction has been observed by other workers but it appears to be sensitive to screen open area fraction, a parameter that was held constant at 0.67 throughout these tests.

Figure 7a shows a half profile for the central screen hole of the standard grid set operating at a minimum beam divergence condition. Figure 7b shows the profiles for the same grid where the discharge voltage has been increased from 45.0 volts to 65.0 volt. As before, the last contour line plotted in both cases should be a good approximation to the sheath boundary. Comparing Figs. 7a and 7b one sees that the sheath potential contours have almost identical shapes, with the sheath boundary for the higher discharge voltage shifted slightly closer to the screen hole. The electric field gradients are significantly greater for the higher discharge voltage as shown by the closer spacing of the lines in Figure 7b. The profiles of these figures suggest that variations in ion velocities imparted significantly upstream of the aperture may be more important in accounting for the beam divergence changes associated with varying discharge voltages[5] than any gross change in the sheath shape near the screen grid. Figure 7c shows the effect of increasing the bell jar pressure by a factor of two over that pertaining to the results of Fig. 7a. With this large increase in neutral number density the small spherical probe used to monitor bulk plasma properties indicated that the primary-to-Maxwellian electron density ratio was approximately zero as compared to approximately 0.25 for the standard pressure condition. It is believed that this absence of primary electrons was responsible for the relative bunching of potential lines shown in Fig. 7c compared to those of Fig. 7a. Such a condition would be expected to occur when primary electrons were not present because the lower energy Maxwellian electrons would not penetrate far into

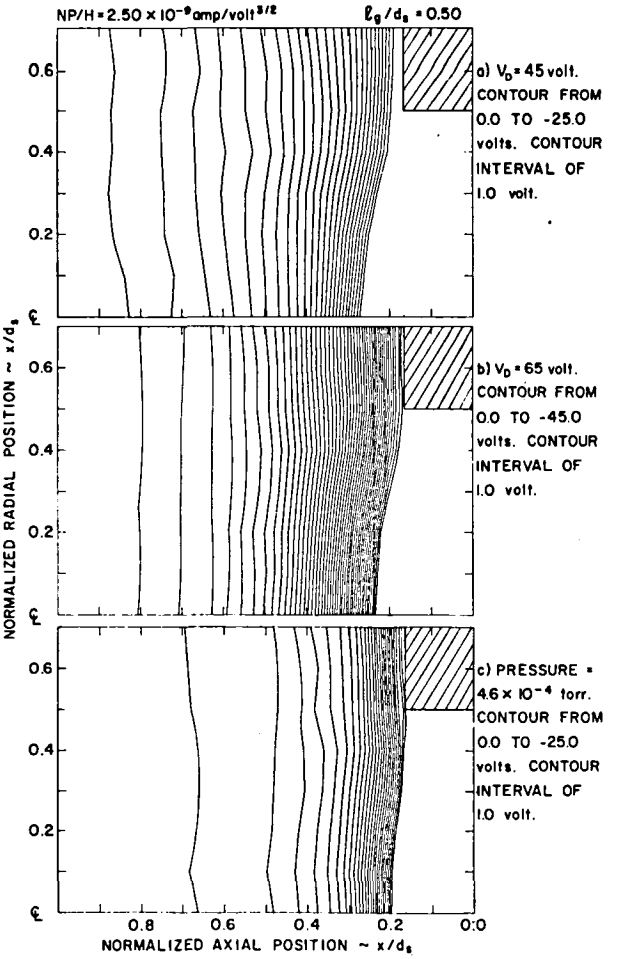

Fig. 7. Comparison of sheath half profile for standard grid set geometry and operating conditions (a) with sheath half profile for increased discharge voltage (b) and increased ion source operating pressure (c).

the sheath and the sheath potential gradients would therefore be expected to be steeper.

Figure 8 shows the result of decreasing the screen grid thickness while keeping all other parameters constant. Here, the -5.0, -15.0 and -25.0 volt contour lines are plotted for clarity. We note that the -5.0 and -15.0 volt contours are essentially coincident. However, the -25.0 volt contour line has followed the thinner screen grid at the webbing but is again coincident with the -25.0 volt line of the thicker grid at the sheath center. Examining electric field vectors in this webbing region, we note that as the screen grid is reduced in thickness, plasma ions are focused away from the webbing and into the screen hole. This focusing effect at the webbing would lead to decreased discharge chamber losses with the reduction in screen grid thickness. Such a reduction has been observed by other workers. The usual explanation given to account for this behavior is that the sheath is always located within the screen hole so that reducing the screen grid thickness results in less ion recombination on the inside screen hole edge. This does not appear to be the case however because all data obtained to date indicates the

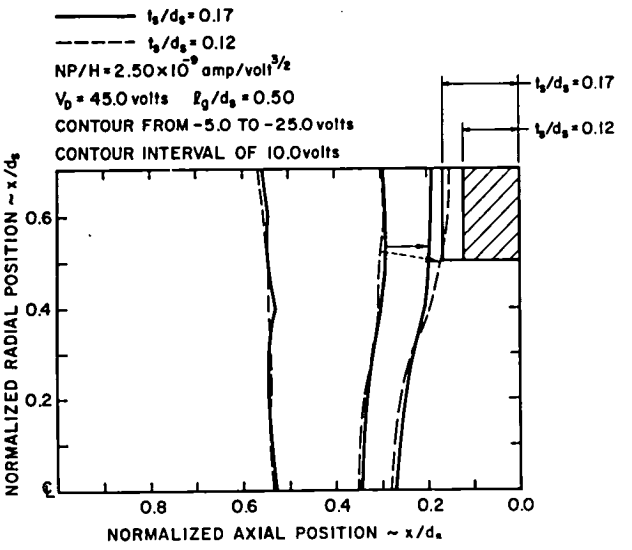

Fig. 8. Effect of screen grid thickness variations, t_s/d_s, on the screen hole plasma sheath (half sheath profile).

sheath does not enter the screen hole.

Figure 9 compares the screen hole plasma sheath obtained theoretically by Kaufman[12] using the digital computer program of Bogart and Richley[13] against the -25.0 volt contour line obtained experimentally at the same grid geometry and operating conditions. Qualitatively the shapes are similar but their positions are different. The theoretical screen hole sheath is a single equipotential surface at screen grid potential. Consequently, it terminates on the screen grid webbing and cannot account for the important web focusing effects brought out by this experimental study. Moreover, the theoretical sheath is a discontinuity separating the plasma from the region of accelerated ions.

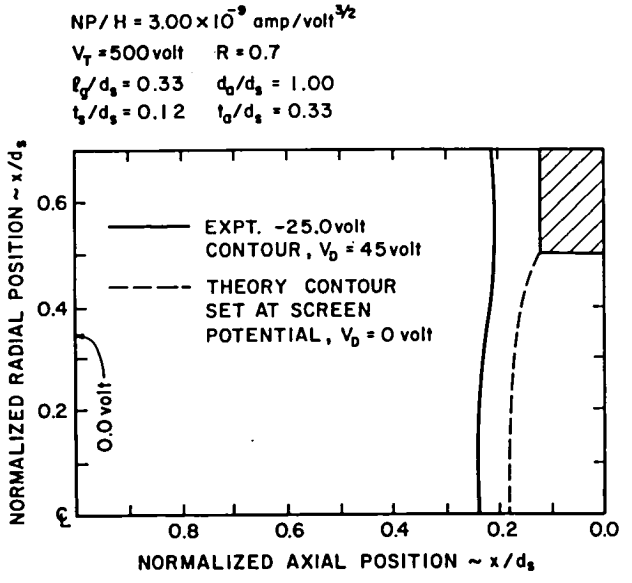

Fig. 9. Comparison of experimental and theoretical sheath potential contours (half sheath profile).

This is an oversimplified model since the experimental results indicate the sheath perturbs the plasma significantly back from the -25.0 volt contour line shown in Fig. 9. It is felt that these shortcomings in the theoretical sheath model are responsible for the poor agreement between theorectial ion beam divergence results and those obtained experimentally in previous studies.[5,6]

Sheath Plasma Density Variation

So far the sheath has been characterized by a set of equipotential contours. These contours define the extent over which the plasma is perturbed by the accelerator system potentials and are very useful in determining initial ion trajectories. Also useful is an understanding of the effect sheath potential gradients have on the local ion and electron densities. This information can be obtained directly from the sheath potential contours and the bulk plasma conditions. Briefly, a one dimensional model was developed incorporating Poissons' equation, the ion energy equation and conservation of ion flux. The ions were assumed to enter the collisionless sheath region with the modified Bohm velocity developed by Masek.[14,15] By taking the second derivative of the potential with respect to distance numerically through the sheath of the experimental data and using this as input to the model it was possible to calculate the ion and electron density variation through the sheath.

Figure 10 is a semi-log plot of the ion and electron number density, normalized by the bulk plasma density, for the centerline of the screen hole sheath shown in Fig. 3. Since the ions are being accelerated through the sheath their density drops off slowly. In contrast, the plasma electrons are being retarded as they enter the sheath region and their density drops off much more rapidly. Near the sheath extremity the finite thickness of the sheath probe (~0.2 mm) does not permit adequate spatial resolution to sense the last few potential contours necessary to send the electron number density to zero. As a first attempt at modelling these experimental results the plasma electrons are assumed to be in a Maxwell-Boltzman density distribution at a temperature T_e. The electron density is then given by the exponential expression shown in Fig. 10, where $\Delta\phi$ is the potential change through the sheath. Using this expression, a best fit to the experimental data was obtained with a Maxwellian electron temperature T_e = 11.0 eV. The small spherical Langmuir probe used to determine bulk plasma parameters indicated the Maxwellian electron temperature was 7.8 eV, considerably less than the temperature of the fitted curve. However, this same probe also indicated the ratio of primary (i.e., electrons which have undergone no ionizing collisions) to Maxwellian electrons was 0.25 for this plasma. Therefore the plasma electrons actually entering the sheath region comprised a Maxwellian population centered at 7.8 eV with a high energy primary distribution centered around 40-45 eV. Hence, if only a pure Maxwellian density distribution is assumed one would expect the effective electron temperature necessary to fit the experimental data to be higher than the experimentally observed Maxwellian electron temperature. This is indeed born out by test comparison shown in Fig. 10 where the necessary effective electron temperature was 11.0 eV while the measured Maxwellian electron temperature was only 7.8 eV.

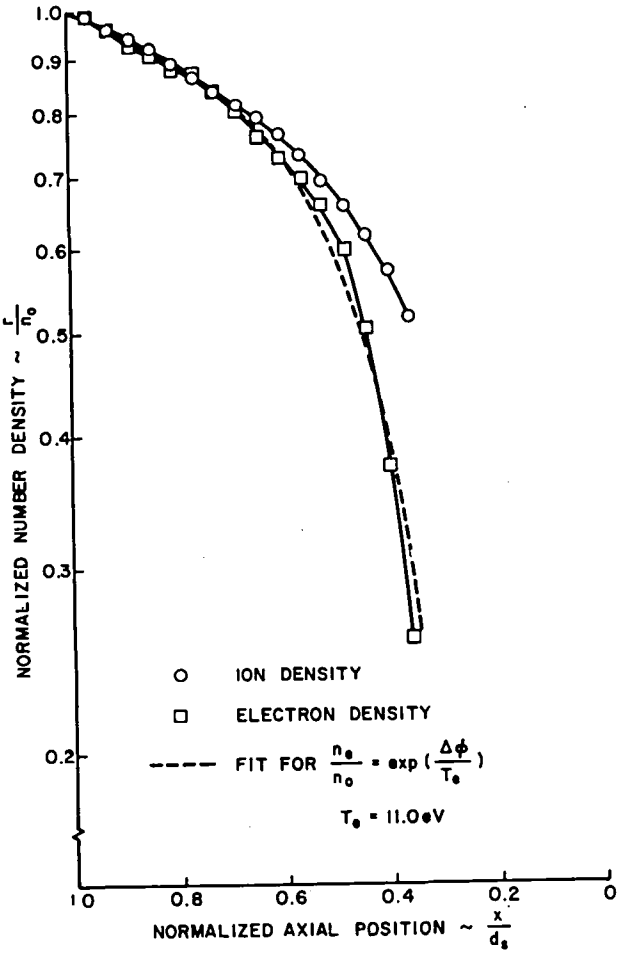

Fig. 10. Ion and electron density variation through a screen hole plasma sheath.

Further work is being done to define more realistic models to describe the observed ion and electron number density variations. It should be noted that to the authors' knowledge Fig. 9 contains the first experimental plots of the ion and electron density variation through any sheath. Some work was done by Goldan[16] in the late sixties on an experimental collisionless sheath investigation. However, he examined an idealized sheath on a planar electrode up to electric field strengths on order of magnitude less than those probed during this experiment.

Discussion

The results presented in this report detail the first probing of the screen hole sheath of an ion accelerator system. Initial results indicate that the screen hole sheath extends over a large distance, influencing ion and electron trajectories deep within the discharge plasma. Under no conditions examined so far does this sheath ever enter the screen hole. At low normalized perveance per hole values, the screen hole sheath bows out into the discharge chamber plasma. With increasing normalized perveance per hole the sheath moves closer to the screen hole and becomes more planar. Edge hole defocusing is due primarily to local plasma density variations rather than the lack of adjacent screen hole sheath interactions. The boundary of the screen hole plasma sheath has approximately the same position and shape, irrespective of the screen-to-accelerator grid spacing, if that grid set is operating at a normalized perveance per hole corresponding to its minimum beam divergence condition. Significant ion focusing effects occur in the sheath adjacent to the screen grid webbing. Decreasing both the screen-to-accelerator grid separation and the screen grid thickness enhance this focusing effect. This results in the deflection of more ions away from the screen grid webbing into the screen holes. This causes a subsequent gain in ion source beam current efficiency. Present theoretical models are inadequate to describe the many phenomena occurring in the sheath region. Further work is being done to define the screen hole sheath physical characteristics for more grid geometries and operating conditions.

Acknowledgment

This work was supported by NASA under Grant NGR-06-002-112. The author wishes to thank his wife, Martha Aston, for her help in taking the data contained in this report.

References

1. Coupland, J. R., Green, T. S., Hammond, D. P. and Riviere, A. C., "A Study of the Ion Beam Intensity and Divergence Obtained from a Single Aperture Three Electrode Extraction System," Rev. Sci. Instrum., Vol. 44, No. 9, Sept. 1973, pp. 1258-1270.

2. Alterburg, W., Freisinger, J., Häuser, J., Seibt, N., and Loeb, H. W., "Beam Formation in RF-Ion Thrusters," AIAA Paper No. 75-426, Nee Orleans, La., 1975.

3. Aston, G. and Kaufman, H. R., "The Ion-Optics of a Two-Grid Electron-Bombardment Thruster," AIAA Paper No. 76-1029, Key Biscayne, Fl., 1976.

4. Grisham, L. R., Tsai, C. C., Whealton, J. H. and Stirling, W. L., "Effect of Emission Aperture Shape Upon Ion Optics," Rev. Sci. Instrum., Vol. 48, No. 8, Aug. 1977, pp. 1037-1041.

5. Aston, G., Kaufman, H. R. and Wilbur, P. J., "Ion Beam Divergence Characteristics of Two-Grid Accelerator System," AIAA Journal, Vol. 16, No. 5, May 1978, pp. 516-524.

6. Aston, G. and Kaufman, H. R., "Ion Beam Divergence Characteristics of Three-Grid Accelerator Systems," AIAA Journal, Vol. 17, No. 1, Jan. 1979, pp. 64-70.

7. Harrison, E. R., "Investigation of the Perveances and Beam Profiles of an Aperture Disk Emission System," J. Appl. Phys., Vol. 29, No. 6, June 1958, pp. 909-913.

8. Hamza, V. and Richley, E. A., "Numerical Evaluation of Ion-Thruster Optics," NASA TN D-1665, May, 1963.

9. Goldin, D. S. and Cohen, E., "Plasma Extraction Optics Study," TRW Report No.14176-6001-TO-00, Sept., 1971.

10. Aston, G., "Screen Hole Plasma Sheath Investigation," Mercury Ion Thruster Research, edited by P. J. Wilbur, NASA CR-159485, Dec. 1978, pp. 38-49.

11. Kemp, R. F. and Sellen, Jr. J.M., "Plasma Potential Measurements by Electron Emissive Probes," Rev. Sci. Instrum., Vol. 37, No. 4, April 1966. pp. 455-461.

12. Kaufman, H. R., "Accelerator System Solutions for Broad Beam Ion Sources," AIAA Journal, Vol. 15, No. 7, July 1977, pp. 1025-1034.

13. Bogart, C. D. and Richley, E. A., "A Space-Charge-Flow Computer Program," NASA TN D-3394, 1966.

14. Bohm, D., "Minimum Ionic Kinetic Energy for a Stable Sheath," in The Characteristics of Electrical Discharges in Magnetic Fields, eds. A. Guthrie and R. K. Wakerling, McGraw-Hill, N.Y., 1949, pp. 77-86.

15. Masek, T. D., "Plasma Properties and Performance of Mercury Ion Thrusters," AIAA Paper No. 69-256, 1969.

16. Goldan, P. D., "Collisionless Sheath - An Experimental Investigation," Phys. Fluids, Vol. 13, No. 4, April 1970, pp. 1055-1059.

DISTRIBUTION LIST

	Copies
National Aeronautics and Space Administration Washington, DC 20546	
Attn: RS/Mr. Dell Williams, III	1
RTS-6/ Mr. Wayne Hudson	1
RTS-6/Mr. Jerome Mullin	1
MT/Mr. Ivan Bekey	1
National Aeronautics and Space Administration Lewis Research Center 21000 Brookpark Road Cleveland, OH 44135	
Attn: Research Support Procurement Section	
Mr. B. Shuman, MS 500-306	1
Technology Utilization Office, MS 3-19	1
Report Control Office, MS 5-5	1
Library, MS 60-3	2
Mr. N. Musial, MS 500-113	1
Mr. E. Davison, MS 3-3	1
Mr. W. E. Moeckel, Chief Scientist, MS 3-12	1
Space Propulsion and Power	
Mr. H. Douglass, MS 501-5	1
Dr. F. Teren, MS 501-5	1
Mr. R. Finke, MS 501-8	1
Mr. B. Banks, MS 501-8	1
Mr. D. Byers, MS 501-8	1
Mr. W. Hawersaat, MS 501-4	1
Mr. W. Kerslake, MS 501-8	30
National Aeronautics and Space Administration Lyndon B. Johnson Space Center Houston, TX 77058	
Attn: Mr. Hu Davis	1
National Aeronautics and Space Administration Marshall Space Flight Center Huntsville, AL 35812	
Attn: Mr. Jerry P. Hethcoate	1
Mr. John Harlow	1
Research and Technology Division Wright-Patterson AFB, OH 45433	
Attn: (ADTN) Lt. David A. Fromme	1
Mr. Everett E. Bailey	1
NASA Scientific and Technical Information Facility P. O. Box 8757 Baltimore, MD 21240	1
Attn: Accessioning Dept.	

	Copies
Case Western Reserve University 10900 Euclid Avenue Cleveland, OH 44106 Attn: Dr. Eli Reshotko	1
Royal Aircraft Establishment Space Department Farnborough, Hants ENGLAND Attn: Dr. D. G. Fearn	1
United Kingdom Atomic Energy Authority Culham Laboratory Abingdon, Berkshire ENGLAND Attn: Dr. P. J. Harbour Dr. M. F. A. Harrison	1 1
National Aeronautics and Space Administration Goddard Space Flight Center Greenbelt, MD 20771 Attn: Mr. W. Isley, Code 734 Mr. A. A. Vetman Dr. David H. Suddeth	1 1 1
COMSAT Laboratories P. O. Box 115 Clarksburg, MD 20734 Attn: Mr. B. Free Mr. O. Revesz	1 1
Comsat Corporation 950 L'Enfant Plaza, SW Washington, DC 20024 Attn: Mr. Sidney O. Metzger	1
Rocket Propulsion Laboratory Edwards AFB, CA 93523 Attn: LKDA/Mr. Tom Waddell LKDH/Dr. Robert Vondra	1 1
DFVLR - Institut fur Plasmadynamik Technische Universitat Stuttgart 7 Stuttgart-Vaihingen Allmandstr 124 West Germany Attn: Dr. G. Krulle	1

	Copies
DFVLR - Institut fur Plasmadynamik 33 Braunschweig Bienroder Weg 53 West Germany Attn: Mr. H. Bessling	1
Giessen University 1st Institute of Physics Giessen, West Germany Attn: Professor H. W. Loeb	1
Jet Propulsion Laboratory 4800 Oak Grove Drive Pasadena, California 91102 Attn: Dr. Kenneth Atkins Technical Library Mr. Eugene Pawlik Mr. James Graf Dr. Kevin Rudolph Mr. Dennis Fitzgerald	1 1 1 1 1 1
Electro-Optical Systems, Inc. 300 North Halstead Pasadena, California 91107 Attn: Dr. R. Worlock Mr. E. James Mr. W. Ramsey	1 1 1
TRW Inc. TRW Systems One Space Park Redondo Beach, California 90278 Attn: Dr. M. Huberman Mr. H. Ogawa Mr. Sid Zafran	1 1 1
National Aeronautics and Space Administration Ames Research Center Moffett Field, California 94035 Attn: Technical Library	1
National Aeronautics and Space Administration Langley Research Center Langley Field Station Hampton, Virginia 23365 Attn: Technical Library Mr. B. Z. Henry	1 1

	Copies
Hughes Research Laboratories 3011 Malibu Canyon Road Malibu, California 90265	
Attn: Mr. J. H. Molitor	1
Dr. R. L. Poeschel	1
Dr. Jay Hyman	1
Mr. R. Vahrenkamp	1
Dr. J. R. Beattie	1
Dr. W. S. Williamson	1
United States Air Force Office of Scientific Research Washington, DC 20025	
Attn: Mr. M. Slawsky	1
Princeton University Princeton, NJ 08540	
Attn: Mr. W. F. Von Jaskowsky	1
Dean R. G. Jahn	1
Dr. K. E. Clark	1
Joint Institute for Laboratory Astrophysics University of Colorado Boulder, Colorado 80302	
Attn: Dr. Gordon H. Dunn	1
Boeing Aerospace Co. P. O. Box 3999 Seattle, Washington 98124	
Attn: Mr. Donald Grim	1
Mr. Russell Dod	1
Lockheed Missiles and Space Co. Sunnyvale, California 94088	
Attn: Dr. William L. Owens Propulsion Systems, Dept. 62-13	1
Fairchild Republic Co. Farmingdale, New York 11735	
Attn: Dr. Domenic J. Palumbo	1
Electrotechnical Laboratory Tanashi Branch 5-4-1 Mukodai-Machi, Tanshi-Shi Tokyo, Japan	
Attn: Dr. Katsuva Nakayama	1
Bell Laboratories 600 Mountain Avenue Murray Hill, NJ 07974	
Attn: Dr. Edward G. Spencer	1
Dr. Paul H. Schmidt	1

	Copies
Sandia Laboratories Mail Code 5743 Albuquerque, NM 87115 Attn: Mr. Ralph R. Peters	1
Ion Tech, Inc. P. O. Box 1388 1807 E. Mulberry Fort Collins, Colorado 80522 Attn: Dr. Gerald C. Isaacson	1
EG & G Idaho P. O. Box 1625 Idaho Falls, Idaho 83401 Attn: Dr. G. R. Longhurst, TSA-104	1
The Aerospace Corporation P. O. Box 95085 Los Angeles, CA 90045 Attn: Dr. B. A. Haatunion Mr. A. H. Silva	1 1
Michigan State University East Lansing, MI 48824 Attn: Dr. J. Asmussen Dr. M. C. Hawley	1 1
General Dynamics Kearney Mesa Plant P. O. Box 1128 San Diego, CA 92112 Attn: Dr. W. Ketchum Dr. J. W. Stractman	1 1
Ford Aerospace Corp. 3939 Fabian Way Palo Alto, CA 94303 Attn: Mr. Robert C. Kelsa	1
Hughes Aircraft Co. Space and Communication Group P. O. Box 92919 Los Angeles, CA 90009 Attn: Dr. M. E. Ellison Dr. B. G. Herron	1 1

	Copies
The Aerospace Corporation Space Sciences Lab. P. O. Box 92957 Los Angeles, California 90009 Attn: Dr. Y. T. Chiu	1
The Takagi Research Laboratory Department of Electronics Kyoto University Yoshidahonmachi Sakyo-ku Kyoto 606 JAPAN Attn: Dr. Toshinori Takagi	1
Department of Aeronautics Faculty of Engineering University of Tokyo 7-3-1, Hongo, Bunkyo-ku Tokyo JAPAN Attn: Prof. Itsuro Kimura	1